

Universität Hamburg

DER FORSCHUNG | DER LEHRE | DER BILDUNG

Fakultät für Mathematik, Informatik und Naturwissenschaften

Fachbereich Physik | Institut für Experimentalphysik

Optics for XFI

Dissertation

zur Erlangung des Doktorgrades
an der Fakultät für Mathematik, Informatik und Naturwissenschaften
Fachbereich Physik
der Universität Hamburg

vorgelegt von:

Lukas Elbrecht

Hamburg
2026

Gutachter der Dissertation:	Prof. Dr. Florian Grüner Prof. Dr. Robert H. Blick
Zusammensetzung der Prüfungskommission:	Prof. Dr. Ludwig Mathey Prof. Dr. Florian Grüner Prof. Dr. Robert H. Blick Dr. habil. Theresa Staufer Dr. Michael Martins
Vorsitzender der Prüfungskommission:	Prof. Dr. Ludwig Mathey
Datum der Disputation:	12.10.2026
Vorsitzender des Fach-Promotionsausschusses PHYSIK:	Prof. Dr. Johannes Haller
Leiter des Fachbereichs PHYSIK:	Prof. Dr. Markus Drescher
Dekan der Fakultät MIN:	Prof. Dr.-Ing. Norbert Ritter

Diese Arbeit widme ich meinen Eltern,

die mir mit unerschütterlicher Liebe, Geduld und Vertrauen
den Weg bereitet und mich über all die Jahre getragen haben.

Ohne eure Unterstützung und euren Glauben an mich
wäre dieser Meilenstein nicht möglich gewesen.

Danke für alles!

Abstract

X-ray fluorescence imaging (XFI) is a modality that enables the quantitative, spatially resolved detection of small amounts of tracers, for example, in the form of functionalized nanoparticles that are taken up by tumors. To achieve spatial resolution, the fluorescence must be excited by tightly focused X-rays with an energy above the absorption edge and a small spectral width. Previous studies by our group have shown that these requirements are, up to now, only fulfilled by synchrotron X-rays. However, the corresponding systems are expensive and large, which makes them unsuitable for the clinical implementation and a wider adoption of XFI.
The described imaging method allows for slightly conical excitation beams and a spectral width of approximately 15 % FWHM. Therefore, other methods of X-ray generation can be employed. Using an X-ray tube in combination with a von Hámos optic, based on Bragg reflection from mosaic crystals, and employing strategically placed apertures in a compact laboratory setup is one possible alternative to synchrotrons. The von Hámos optics that our group uses for this purpose so far utilize graphite crystals for reflection. When combined with currently used X-ray tubes, they exhibit flux values of about $\Phi \approx 3.7 \times 10^8\,\mathrm{ph\,s^{-1}}$ at the focus at $E \approx 60\,\mathrm{keV}$. Such a flux however, is too low for in vivo measurements or other time-sensitive studies. One way to increase the flux is to advance the properties of the optics.

This work presents novel von Hámos optics, made from bent aluminum mosaic crystals, that achieve a flux at the focus more than five times higher than that achieved with the established graphite optics. A material study showed that a crystal thickness of 0.4 mm, paired with an etching surface treatment, and utilizing the aluminum (1 1 1) reflex, maximizes the novel optics' performance.
A dedicated characterization setup was designed and built, enabling spatially resolved measurements of the mosaic spread of the crystals, providing a detailed explanation of their focusing properties, and facilitating realistic ray tracing simulations. The same setup also enables a mapping of the relative reflectivity across an optic's surface, which revealed significant variations in the quality of the graphite optics. These results provide an explanation for the unstable flux values. They will be used to improve the optics' alignment and provide a benchmark for further optimizing the novel aluminum optics. The setup proved to be better suited for investigating the relevant properties of the specific samples than initially employed grazing incidence X-ray scattering measurements.
The focusing and energy-filtering properties of the von Hámos optics can also be utilized for a detector-sided use. Initial experiments demonstrate this capability by detecting the location and size of a 1 mm void in an aluminum sample, based on its Compton scattering signature. A future use of the novel aluminum optics is expected to enable a similar setup to be used for the spatially resolved detection of fluorescence signals.

Zusammenfassung

Die Röntgenfluoreszenz-Bildgebung (engl. XFI) ermöglicht den quantitativen, räumlich aufgelösten Nachweis kleiner Mengen von Tracern, wie etwa funktionalisierten Nanopartikeln, die von Tumoren aufgenommen werden. Um eine räumliche Auflösung zu erreichen, muss die Fluoreszenz durch stark gebündelte Röntgenstrahlung angeregt werden, deren Energie über der Absorptionskante liegt und deren spektrale Breite gering ist. Vorangegangene Studien unserer Gruppe haben gezeigt, dass diese Anforderungen bisher nur durch Synchrotron-Röntgenstrahlung erfüllt werden. Da die entsprechenden Anlagen teuer und groß sind, ist ihre Verwendung für eine klinische Etablierung und eine breitere Anwendung der Röntgenfluoreszenz-Bildgebung nicht geeignet.
XFI erlaubt jedoch auch leicht konische Anregungsstrahlen mit einer spektralen Breite von etwa 15 % FWHM. Dadurch kommen alternative Quellen zur Röntgenerzeugung infrage. Eine mögliche Alternative zu Synchrotronen ist der Einsatz einer Röntgenröhre in Kombination mit einer von Hámos-Optik, die auf Bragg-Reflexion an Mosaikkristallen basiert, sowie gezielt platzierten Blenden in einem kompakten Laboraufbau. Die bisher von unserer Gruppe dazu verwendeten von Hámos-Optiken basieren auf Graphitkristallen und erreichen mit der aktuell genutzten Röntgenröhre im Fokus einen Fluss von etwa $\Phi \approx 3.7 \times 10^8\,\mathrm{ph\,s^{-1}}$ bei $E \approx 60\,\mathrm{keV}$. Ein solcher Fluss ist jedoch zu gering für in-vivo-Messungen oder andere zeitkritische Studien. Eine Möglichkeit zur Steigerung des Flusses besteht in der Optimierung der Eigenschaften der Optik.

In dieser Arbeit wird eine neuartige von Hámos-Optik aus gebogenen Aluminium-Mosaikkristallen vorgestellt. Sie liefert im Fokus einen mehr als fünfmal höheren Fluss als die etablierten Graphitoptiken. Ergebnisse einer Materialstudie zeigen, dass die Reflektivität der neuartigen Optik durch eine Kristalldicke von 0.4 mm in Kombination mit einer Ätzbehandlung der Oberfläche und der Ausnutzung des Aluminium-(1 1 1)-Reflexes maximiert wird.
Es wurde ein Charakterisierungsaufbau entworfen und umgesetzt, der räumlich aufgelöste Messungen der Mosaikverteilung der Kristalle ermöglicht. Damit lassen sich ihre Fokussierungseigenschaften detailliert erklären und Raytracing-Simulationen der Optik präzisieren. Mit demselben Aufbau lässt sich zudem die relative Reflektivität über die gesamte Oberfläche einer Optik bestimmen. Dabei zeigte sich, dass die Qualität der Graphitoptiken entlang ihrer Oberfläche stark schwankt. Diese Ergebnisse liefern eine Erklärung für beobachtete, instabile Flusswerte. Sie werden zur verbesserten Ausrichtung der Optiken genutzt und dienen zukünftig als Maßstab für die weitere Optimierung der Aluminiumoptiken. Zudem erwies sich der Aufbau als geeigneter, um die relevanten Eigenschaften der untersuchten Proben zu bestimmen, als ursprünglich durchgeführte Streumessungen unter streifendem Einfall.
Die Fokussierungs- und Energiefiltereigenschaften der von Hámos-Optiken lassen sich auch detektorseitig nutzen. Dies wurde durch erste Experimente belegt, bei denen die Position und Größe einer 1 mm großen Lücke in einer Aluminiumprobe anhand ihres Compton-Streuungsprofils detektiert wurden. Es wird erwartet, dass die neuartige Aluminiumoptik zukünftig einen ähnlichen Aufbau zur räumlich aufgelösten Detektion von Fluoreszenzsignalen ermöglicht.

Contents

1 Introduction **1**

2 Principles of X-ray Diffraction **5**

2.1 Motivation for Diffraction-Based X-ray Optics 5

2.2 Interaction of X-rays with Matter 6

2.2.1 Absorption 6

2.2.2 Fluorescence 7

2.2.3 Compton Scattering 7

2.2.4 Classification of X-ray Scattering Processes 8

2.3 Fundamentals of X-ray Diffraction 9

2.3.1 Elastic Scattering by a Single Electron 9

2.3.2 Scattering by an Atom 14

2.3.3 Scattering by an Ensemble of Atoms 17

2.3.4 Scattering by a Bravais Lattice 17

2.3.5 Scattering by a Perfect Crystal 20

2.4 Quantitative Description of X-ray Diffraction in Crystals 21

2.4.1 Location of the Diffraction Peaks 21

2.4.2 Geometrical Description of Bragg Reflection 25

2.4.3 Bragg Reflection Intensity 26

2.4.4 Bragg Scattering Cross-Section 32

2.4.5 Bragg Reflection of Incoherent X-rays 38

2.4.6 Bragg Reflection by Mosaic Crystals 39

2.4.7 Justification and Limitations of the Mosaic Crystal Model 43

2.4.8 Extinction Effects and Corrections 44

2.4.9 Scherrer Broadening 45

2.4.10 Validity of the Adopted Diffraction Model 45

2.4.11 Bravais Lattice Classification 46

2.4.12 Selection Rules for X-ray Diffraction 48

3 Mosaic Crystal Optics **49**

3.1 Mosaic Focusing 49

3.2 Mosaic Defocusing Effects 51

3.2.1 Defocusing in the Bulk 51

3.2.2 Defocusing by Polychromatic Incidence 53

3.2.3 Azimuthal Defocusing 54

3.2.4 Distance-Dependence of Defocusing Effects 55

3.2.5 Focusing of Extended Sources 55

3.3 Requirements for Optics for Compact XFI Setups 57

3.4 Possible Optic Designs . . . 60
3.4.1 Von Hámos Geometry . . . 60
3.4.2 Johann and Johansson Geometry . . . 61
3.4.3 Transmission (Laue) Diffraction Focusing Optics . . . 62
3.4.4 Alternative X-ray Optics . . . 64
3.5 Von Hámos Optic Layout . . . 66
3.5.1 Orientation Gradient Effect . . . 69
3.5.2 Anticlastic Curvature and Quasi-Mosaicity . . . 70

4 Super Compact Optics-Based Tunable Testbed for Imaging (SCOTTI) 71
4.1 SCOTTI X-ray Tube . . . 72
4.2 SCOTTI Apertures . . . 73
4.3 Detectors . . . 74
4.3.1 Pixelated X-ray Detectors . . . 74
4.3.2 Energy-Resolved Detectors . . . 75

5 X-ray Tracing 76
5.1 Implementation of the SCOTTI Setup in `xrt` . . . 77
5.2 Comparison of Simulation and Experimental Results . . . 80

6 Implementation of a Novel Aluminum Mosaic Crystal Optic 83
6.1 Pyrolytic Graphite Optics . . . 83
6.2 Final Choice of Alternative Optic Materials . . . 87
6.3 Tile-Based Focusing Optics . . . 90
6.4 Focusing Optic Using Curved Crystals . . . 93
6.5 Experimental Optimization of Aluminum von Hámos Optics . . . 95

7 Optic Characterization Setup 108
7.1 Rocking Curve Measurements . . . 109
7.2 Concept of the Characterization Setup . . . 110
7.3 Design of the Setup . . . 111
7.4 Characterization Measurements . . . 115
7.4.1 Rocking Curve Measurements . . . 115
7.4.2 Rocking Curve Broadening Effects . . . 118
7.4.3 Rocking Curve Evaluation Procedure . . . 128
7.4.4 Crystal Scan Measurements . . . 129
7.5 Experimental Setup . . . 130
7.5.1 Rocking Curve Measurement Results . . . 132
7.5.2 Crystal Map Results . . . 140
7.6 Future Adaptations of the Characterization Setup . . . 146

8 Filtering Optics-Based X-ray Imaging (FOXI) 148
8.1 Test Scenario . . . 149
8.2 Ray Tracing-Based Feasibility and Performance Assessment . . . 150
8.2.1 Field of View (FOV) . . . 152
8.2.2 Evaluation Approach . . . 153

8.3 First Experimental Realization . . . 156
8.3.1 FOXI Alignment . . . 158
8.3.2 Measurements . . . 159
8.3.3 Future Improvements and Outlook . . . 170

9 Summary and Outlook **172**

List of Figures **I**

List of Tables **II**

Bibliography **III**

Appendix **A-1**
A.1 Use of Large Language Models . . . A-1
A.1.1 Coding . . . A-1
A.1.2 Research . . . A-2
A.1.3 Writing . . . A-2

1 Introduction

X-ray fluorescence imaging (XFI) is an imaging modality currently under development that detects the characteristic fluorescence emitted by tracer elements upon excitation with incident X-rays [1]. Typical targeted elements include gold, iodine, and palladium, whose K-shell fluorescence energies exceed 20 keV [1, 2].

In preclinical studies, tracer elements are commonly used in the form of functionalized nanoparticles with high tumor uptake [3] or as labeled pharmaceuticals, which makes XFI a promising method for imaging diagnostics and pharmacokinetics [1, 4]. The WHO's 2026 Global Status Report on Cancer states that cancer is one of the world's leading causes of death, with 10 million deaths per year, projected to rise in the coming centuries [5]. This underscores the persistent need to further develop diagnostics and pharmaceuticals.
Studies have shown that XFI can provide fluorescence imaging of in vitro samples and in vivo experiments on small animals [1, 6, 7]. Further studies demonstrate the feasibility of translating XFI to clinical applications for human-sized objects [8, 9]. However, this remains an active area of research in an early stage, with efforts focused on background reduction, developing compact, high-brilliance X-ray sources, and optimizing detectors [1]. Outside from medical applications, XFI is commonly referred to as XRF (X-ray fluorescence) and is widely applied in areas such as biology and materials science [10–12].

To achieve spatial resolution, the exciting X-rays must provide a small focal spot that is scanned over the area of interest [13–15]. Furthermore, the incident X-ray beam must have a small spectral width [1] and an energy above the absorption edge of the tracer to be excited, to ensure that the fluorescence signal is not masked by the excitation signal or Compton scattering [14]. Former XFI studies were therefore performed at synchrotron beamlines, as their properties of high brilliance, virtually no divergence, and quasi-monoenergetic X-rays after filtering make them well suited for XFI experiments [1].

Due to the size and cost of such facilities, a widespread use of XFI relying on synchrotron radiation is unfeasible. Therefore, XFI can only become widely established as an imaging technique if the size and cost of the radiation source are reduced.

One approach under development to achieve this goal is the study of laser-driven Thomson X-ray sources [16, 17]. However, they only produce pulsed X-rays [16], which restricts their average flux. Further development toward higher laser repetition rates and background reduction is necessary for a realistic application in XFI [1, 17].

For current XFI applications, the high flux values that can be achieved at synchrotron facilities such as the P21.1 beamline (PETRA III, DESY, Hamburg, Germany [18]), which delivers approximately $\Phi = 10^{11}\,\mathrm{ph\,s^{-1}}$ at a $1\,\mathrm{mm} \times 1\,\mathrm{mm}$ spot size at $53\,\mathrm{keV}$ [4, 19], are not fully usable and must be attenuated, because the used detector's input rates limit the tolerable incident flux [4]. Additionally, XFI measurements can also be realized using cone beams [2, 20], and allow for a spectral width of about $\Delta E/E = 15\,\%$ FWHM [9], which expands the range of possible X-ray sources for XFI.

X-ray tubes are a well-established, cost-effective source of radiation that are used in many traditional imaging techniques, such as Computed Tomography (CT) [21]. However, when used on their own, X-ray tubes have some intrinsic features that must be addressed to be suitable for XFI. They exhibit a broad spectrum consisting of Bremsstrahlung and characteristic lines, a high divergence, and do not provide an independent tuning of the excitation energy [22].
The resulting challenges for their application in XFI can be overcome by using a mosaic crystal-based optic that exploits the phenomenon of Bragg reflection [23], in addition to a number of sensitively adjusted apertures and beam stops [24]. From the intrinsic properties of an X-ray tube, requirements for a suitable optic can be derived. An optic must (in descending order of importance):

1. have a focusing effect to realize a focal point for scanning,
2. exhibit filtering properties to reduce the spectral broadness of the reflected spectrum,
3. provide an energy tunability to target different fluorescence markers,
4. have a high reflectivity to maximize the flux at the focal point,
5. keep the overall setup compact.

A compact XFI setup that satisfies all the above requirements, named Super Compact Optics-Based Tunable Testbed for Imaging (SCOTTI), was realized by utilizing an X-ray tube in combination with a von Hámos optic using graphite mosaic crystal materials [24, 25]. This setup proved to be suitable to perform XFI experiments, but it revealed challenges regarding the achievable flux of the focused X-rays of about $\Phi = 3.7 \times 10^{8}\,\mathrm{ph\,s^{-1}}$ in a $\approx 1\,\mathrm{mm} \times 1\,\mathrm{mm}$ focal spot. In addition, it was observed that the achievable values of Φ fluctuate across numerous alignments and different versions of the graphite optics.

In order to use the setup for in vivo measurements of mice, which can be anesthetized for a maximum of 60 min and have an upper local dose limit of 300 mGy that corresponds to $8.6 \times 10^9\,\mathrm{ph\,mm^{-2}}$ at $E = 53\,\mathrm{keV}$, an increase of the flux is necessary. A higher value of Φ also reduces the scan time of all other XFI experiments performed with SCOTTI [10] and enables more time-sensitive measurements.
To maximize the focused flux, either the X-ray tube or the optic must be improved.

This work focuses on a second-generation optic to enhance the SCOTTI setup's achievable flux and its consistency.

A material study was conducted in [26], based on simulations and diffraction measurements of flat samples at the P21.1 beamline (PETRA III, DESY, Hamburg, Germany [18]), to explore alternative materials for an improved optic. This study identified crystalline magnesium oxide and aluminum as the most promising candidates.

This work provides a detailed summary of the fundamentals of X-ray diffraction, including the quantitative description of diffraction in crystals, the Bragg reflection, and the mosaic crystal model in Chapter 2.
The subsequent Chapter 3 shows the focusing and defocusing effects that are inherent in mosaic crystals, defines the requirements for XFI optics, and evaluates various designs, thereby confirming the suitability of a von Hámos optic for the compact XFI setup.
Chapter 4 introduces the SCOTTI beamline as the compact XFI setup for which the novel optic is to be optimized.
The optic design considerations and later experiments rely on detailed ray tracing simulations of the focusing and defocusing properties of the Bragg-reflecting optics in conjunction with other SCOTTI beamline components. The corresponding code, custom adaptations, and a comparison between the simulated and experimental results are presented in Chapter 5.

Based on the results of [26], Chapter 6 explores potential second-generation designs for von Hámos optics using the identified alternative materials. The concepts are evaluated based on simulations of their expected performance, as well as their manufacturability, and are compared to the best-performing graphite optic. For the most promising option, which uses curved aluminum crystals, samples were manufactured in several iterations to identify the ideal specifications for a later full optic. This optimization led to an expected factor of 5.3 in flux improvement at the optic's focus, based on application-oriented benchmark measurements at the SCOTTI beamline.

Precise measurements of the intrinsic properties of the conventional graphite and the novel aluminum optics require a characterization setup designed specifically for this purpose. Such a setup was planned and implemented during this work and is presented in Chapter 7. The results enable more accurate simulations of the imaging properties, can be used to improve the optics' alignment, and provide a benchmark for the further optimization of the novel aluminum optics. In addition to the measurement of parameters that describe the crystals' intrinsic mosaic nature, the characterization setup reveals variations in quality across the surface of the graphite optics, which provides a possible explanation for the observed varying flux values.

Unlike when utilized to generate a focused, energy-filtered incident beam, the optics can also be used in a detector-sided application for the imaging itself. Chapter 8 presents a setup of such kind for identifying the location and size of a void inside a sample's bulk by using its Compton scattering signature. Demonstration measurements confirm the feasibility of the concept, which could also be used to measure fluorescence signals. Ray tracing simulations predict the theoretically possible resolution and field of view of this newly developed concept, named Filtering Optics-Based X-ray Imaging (FOXI).

2 Principles of X-ray Diffraction

Most conventional visible light optics rely on the principle of refraction. The following section demonstrates that this principle is not applicable to X-ray optics.

2.1 Motivation for Diffraction-Based X-ray Optics

When light passes from one medium to another medium with a different phase velocity v, it is refracted. The refraction at the interface between two media 1 and 2 can be quantified by the refractive index $n_{2\,1}$ of this transition [27]:

$$n_{2\,1} = \frac{v_1}{v_2}. \tag{2.1}$$

The refractive index in vacuum is one by definition.

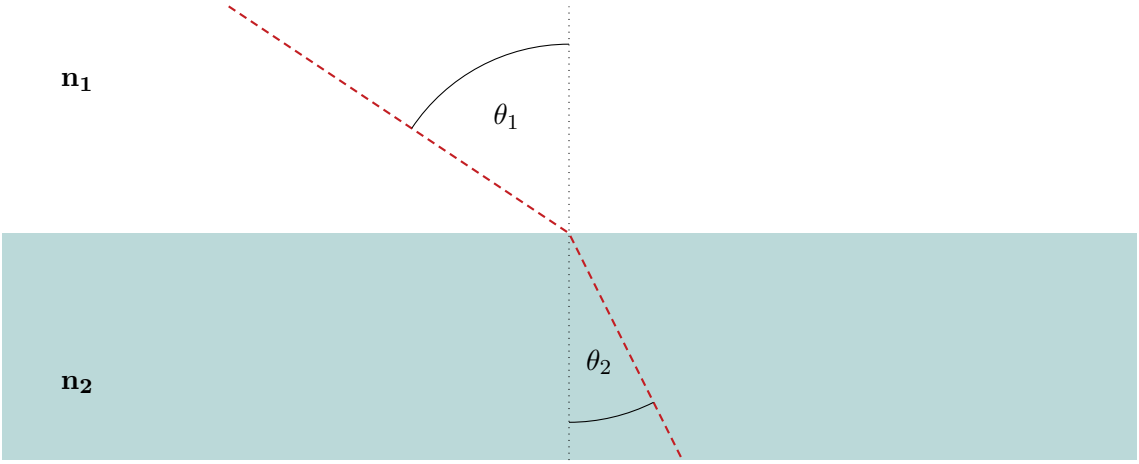


Figure 2.1: Refraction of visible light between two media of different refractive index ($n_{2\,1} > 1$), according to Snell's law [27].

If $n_{2\,1} > 1$, light undergoes refraction toward the normal of the transition. If $n_{2\,1} < 1$, it is refracted away from the normal, in accordance with Snell's law [27]:

$$n_1 \cdot \sin\theta_1 = n_2 \cdot \sin\theta_2. \tag{2.2}$$

The propagation direction only changes for non-normal incidence.
In the X-ray regime, the refractive index is commonly expressed by [22]:

$$n = 1 - \delta + i\beta, \tag{2.3}$$

where δ and β are small, positive values. They describe the scattering and absorption properties of the medium [22]. As an example, values of δ at $E = 20\,\text{keV}$ are about $\delta \approx 10^{-6}$ for graphite [28]. Values of β are typically smaller than δ [22]. Both quantities generally decrease with increasing photon energy. Therefore, the utilization of refractive optics like conventional lenses is not a viable option for X-rays.

According to the Fresnel equations, the intensity reflectivity R at normal incidence, given by [29, 30]:

$$R = \left|\frac{n-1}{n+1}\right|^2 \sim 10^{-13}, \tag{2.4}$$

is also very low for X-rays.
However, Equation 2.3 shows that their refractive index is slightly less than one. This implies that below a certain grazing incidence angle, referred to as the critical angle θ_c, X-rays undergo total external reflection, which drastically increases R. The critical angle in respect to the surface is given by $\theta_c = \sqrt{2\delta}$ [22]. As an example, at $E = 20\,\text{keV}$, the critical angle is about $\theta_c \approx 0.08°$ in graphite [28]. Again, higher energies lead to even smaller critical angles.
These small angles present a challenge for the application of total reflection in X-ray optics. Their suitability for the scope of this work is discussed in Section 3.4.4.

Due to the difficulties described in this section, X-ray optics, especially in the hard X-ray-regime[1], are often based on diffraction [22].

2.2 Interaction of X-rays with Matter

The interaction of X-rays with matter is dominated by electrons, which move much slower than the speed of light [22]. The subsequent section briefly summarizes the interactions that are most relevant for the newly developed X-ray optics.

2.2.1 Absorption

Processes that result in the attenuation of the transmitted X-rays are classified as part of absorption. These include, among others, inelastic scattering, fluorescence and thermal interactions [22]. The Lambert-Beer law is a quantitative expression of the absorption effects on the transmitted intensity I [32]:

$$I = I_0 \cdot e^{-\mu d}. \tag{2.5}$$

[1]Within the electromagnetic spectrum, a conventional categorization distinguishes between soft and hard X-rays. The former ranges from a few hundred eV to approximately 5 keV to 10 keV. X-rays with an energy above this threshold are classified as hard X-rays [22, 31]. This work focuses on hard, non-relativistic X-rays [22] of about 10 keV to 120 keV.

Here, I denotes the intensity at a depth d in the absorbing material, I_0 the intensity at the entrance surface ($d = 0$) and μ the linear absorption coefficient. The latter is material- and wavelength-dependent, and limits the X-ray reflectivity.

2.2.2 Fluorescence

Inelastic interactions between an incident photon and a bound electron can result in the ejection of the electron from the atom. The result of this process is an electron that is energetically excited and can undergo relaxation if an electron from a less bound shell transfers to the shell that was left by the ejected electron. In a fluorescence process, the release of energy can be observed through the emission of a fluorescence photon.
The energy of this photon is directly proportional to the difference in binding energies of the electron prior to and subsequent to relaxation. As the energies of the shells are discrete and dependent on the atom, the fluorescence energies are characteristic [22]. Therefore, the utilization of fluorescence enables the identification of atoms, which constitutes the fundamental principle of X-ray fluorescence imaging (XFI) [8].

2.2.3 Compton Scattering

The Compton effect is defined as an inelastic scattering process between a high-energy photon and a comparatively weakly bound electron [22, 33]. The collision between the photon and the electron results in the Compton electron being ejected from the atomic bond in a random direction, leading to the ionization of the atom.
Consequently, the energy of the photon is reduced and its trajectory might change. The angular distribution of Compton-scattered photons is described by the Klein-Nishina formula [34, 35]:

$$\frac{\mathrm{d}\sigma}{\mathrm{d}\Omega}^{\text{Klein-Nishina}} = \frac{{r_e}^2}{2}\left(\frac{E'}{E}\right)^2\left(\frac{E'}{E} + \frac{E}{E'} - \sin^2\varphi\right), \tag{2.6}$$

$$\frac{E'}{E} = \frac{1}{1 + \frac{E}{m_e c^2}(1 - \cos\varphi)}, \tag{2.7}$$

where r_e denotes the classical electron radius, E the energy of the incident photon, E' the energy of the scattered photon, m_e the mass of the electron and φ the angle between the direction of the incident and scattered photon. The higher the energy of the original photon in contrast to the binding energy of the electron, the less it changes its direction.

In XFI experiments using the laboratory setup described in Chapter 4, energies of about 60 keV are used. Figure 2.2 shows the angular dependence of the normalized differential Compton scattering probability at this energy. At these energies, forward scattering has the highest probability, but other scattering directions are also likely [35].

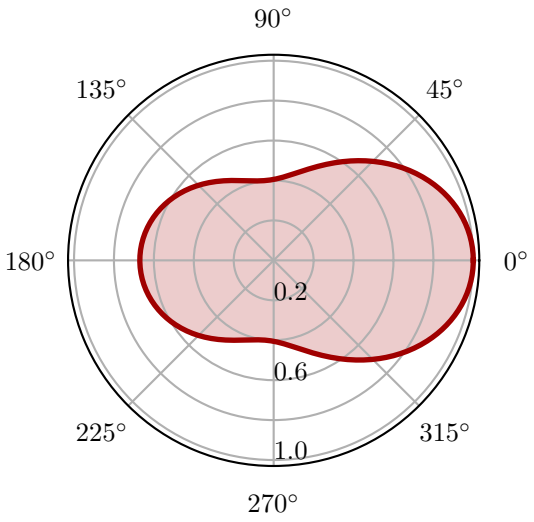


Figure 2.2: Angular dependence of the normalized differential scattering probability of a 60 keV photon undergoing Compton scattering by a free electron. Calculated using the Klein-Nishina equation 2.6.

2.2.4 Classification of X-ray Scattering Processes

In general, scattering describes an interaction between two objects, such as photons and electrons, which results in the deflection of at least one of the objects. If the total internal energy is conserved during the scattering process, it is referred to as elastic scattering. Otherwise, it is defined as an inelastic scattering process. In the latter case, part of the energy is converted. For instance, consider the excitation energy of an atom in the process of Compton scattering [22].

In instances where a scattering process can only be described by a wave model, as it is often the case with X-ray scattering, it is also frequently classified based on whether the incident and scattered waves have a phase relation or not. These processes are then classified as coherent or incoherent.
Compton scattering is a classic example of incoherent scattering, which is characterized by the randomness of energy transfer in this process. An example of coherent scattering is Thomson scattering, covered in Section 2.3.1.

If multiple waves are scattered coherently, the resulting wavefront can also be coherent. This coherency expresses the potential of waves to interfere with each other and produce direction-dependent events. [22, Sec. 1.5].

2.3 Fundamentals of X-ray Diffraction

The following section establishes the fundamentals of X-ray diffraction. The description is successively extended to increasingly complex scattering objects, from scattering by a single free electron to the diffraction of a perfect crystal.

2.3.1 Elastic Scattering by a Single Electron

X-rays are part of the electromagnetic spectrum and can therefore be described by a combination of electric and magnetic field vectors that are perpendicular to the propagation direction of the X-ray wave. The main interaction of X-rays with matter that is relevant for the developed X-ray optics is the interaction between the electric field and the electrons contained in atoms. The interactions of the magnetic field can be neglected because the corresponding Lorentz force is weaker than its electric counterpart by a factor of $v/c \ll 1$ for non-relativistic electrons [35].Consequently, magnetic scattering is typically more than four orders of magnitude weaker than charge scattering for hard X-rays [22]. Interactions with the nucleus are weak, but are taken into account, as will be shown in Section 2.3.2.

Thomson Scattering

This section explains the basis of X-ray-electron interaction, which lies in the process known as Thomson scattering, following [22, 27, 35–38].

The electric field component of an electromagnetic wave is defined as follows [27, 35]:

$$\vec{E} = E_0 \cdot \vec{p} \cdot e^{i(\vec{k}\cdot\vec{r}-\omega t)}. \tag{2.8}$$

Here, E_0 is the amplitude of the electric field, $\vec{p}$ is the polarization vector, ω denotes the angular frequency, and $\vec{k}$ is the wave vector. Since electromagnetic waves are transverse waves, it follows that: $\vec{p} \cdot \vec{k} = 0$.

When X-rays are incident on a free electron, they can be scattered, as explained below. The electron with mass m_e and charge e is assumed to have a velocity of v_{electron} that is much smaller than the speed of light c ($v_{\text{electron}} \ll c$). Thus, it is considered stationary. The magnetic contribution to the Lorentz force acting on the electron due to its interaction with the magnetic field vector can be neglected. The electric field part affects the electron via the corresponding term of the Lorentz force. Due to the wave-like nature of the electric field, this causes the electron to oscillate with a small amplitude, defined by the oscillator equation [35]:

$$\vec{F} = m_e \cdot \ddot{\vec{s}} = -e \cdot \vec{E}(t). \tag{2.9}$$

Field energy of the incident wave is transferred to the kinetic energy of the oscillating electron. This oscillation involves the accelerated movement of an electric charge and leads to the emission of a spherical wave. Outside the source region, the Maxwell equations describe the propagation of the emitted radiation under the assumption of a charge- and current-free vacuum [35]:

$$\frac{1}{c^2}\frac{\partial^2 \vec{E}}{\partial t^2} - \nabla^2 \vec{E} = 0. \tag{2.10}$$

In conclusion, the incident electromagnetic wave is absorbed and its energy is transferred to the kinetic energy of oscillation, which is then re-emitted. This process corresponds to the scattering of the wave by the electron, a phenomenon known as Thomson scattering. The Larmor formula describes the differential power per unit solid angle $\frac{\mathrm{d}P}{\mathrm{d}\Omega}$ that is radiated by an accelerated, non-relativistic electron [35, 39]:

$$\frac{\mathrm{d}P}{\mathrm{d}\Omega} = \frac{e^2}{16\pi^2\varepsilon_0 c}\dot{\beta}^2 \sin^2\theta. \tag{2.11}$$

Here, ε_0 denotes the electrical field constant, e is the charge of the electron, and $\dot{\beta}$ is the time derivative of its velocity v relative to the speed of light $\beta = \frac{v}{c}$. The angle between the acceleration vector and the observation point is denoted by θ.

The acceleration of an oscillating electron is not constant. Its time-averaged acceleration is given by $\langle\dot{\beta}\rangle = \frac{\langle\ddot{s}\rangle}{c}$.

Transforming Equation 2.9 to get $\langle\ddot{s}\rangle$ by using $\langle\vec{E}^2\rangle = \frac{{E_0}^2}{2}$ gives:

$$e^2\left\langle E^2\right\rangle = {m_e}^2\left\langle\ddot{s}^2\right\rangle \rightarrow \left\langle\ddot{s}^2\right\rangle = \frac{e^2E_0^2}{2m_e^2}. \tag{2.12}$$

Substituting this into Equation 2.11 yields the time-averaged radiated power per unit solid angle:

$$\frac{dP}{d\Omega} = \left(\frac{e^2}{4\pi\varepsilon_0 mc^2}\right)^2 \frac{\varepsilon_0 cE_0^2}{2}\sin^2\theta. \tag{2.13}$$

To obtain the cross-section of the Thomson scattering process, the total power of the scattered wave, expressed as a differential by Equation 2.13, must be divided by the total power of the incident wavefront or its time-averaged flux.

According to the definition of the Poynting vector, introduced by Poynting in 1884 [40], the latter is descibed by the time-averaged Poynting vector $\langle\vec{S}\rangle$ of an electromagnetic wave. It is given by [35]:

$$\langle S\rangle = \frac{\varepsilon_0 c}{2}E_0^2. \tag{2.14}$$

Dividing Equation 2.13 by Equation 2.14 yields an expression for the differential cross-section of the Thomson scattering:

$$\frac{d\sigma}{d\Omega} = \frac{\frac{dP}{d\Omega}}{\langle S\rangle} = \left(\frac{e^2}{4\pi\varepsilon_0 m_e c^2}\right)^2 \sin^2\theta. \tag{2.15}$$

Integrating over the solid angle yields the total scattering cross-section σ:

$$\sigma = \int_0^\pi \frac{d\sigma}{d\Omega} 2\pi \sin\theta d\theta = \frac{8\pi}{3} \left(\frac{e^2}{4\pi\varepsilon_0 m_e c^2} \right)^2 . \tag{2.16}$$

The polarization unit vector of the incident wave $\vec{p}$ is parallel to the electron's acceleration vector. The direction of the scattered wave is given by the unit vector $\vec{n}$. The angle θ in Equation 2.11 expresses the angle between the acceleration vector of the electron and the outgoing wave and can therefore be expressed via:

$$\cos\theta = \vec{p} \cdot \vec{n}. \tag{2.17}$$

So far, the incident wave was assumed to be linearly polarized. For the general case of Thomson scattering, Equation 2.15 must be generalized by using the correlation described in 2.17.

In addition to the polarization vector $\vec{p}$, the incident wave is also described by its wave vector $\vec{k}$, which is orthogonal to the polarization vector ($\vec{p} \perp \vec{k}$) for all transverse waves. The corresponding unit vector is $\vec{K} = \frac{\vec{k}}{k}$. To finalize an orthonormal system, a third vector $\vec{p} \times \vec{K}$ is defined. These three vectors fully describe the incident wave.

To describe the scattered wave with wave vector $\vec{n}$, two angles are introduced. φ is the angle between the incident direction $\vec{K}$ and the scattered direction $\vec{n}$. ψ is the azimuthal angle, which defines how the scattering plane is oriented relative to the polarization vector $\vec{p}$. This yields the definition of the unit vector $\vec{n}$:

$$\vec{n} = \sin\varphi\cos\psi\,\vec{p} + \sin\varphi\sin\psi\,\vec{p} \times \vec{K} + \cos\varphi\,\vec{K}. \tag{2.18}$$

Substituting this into Equation 2.17 yields:

$$\cos\theta = \vec{p} \cdot \vec{n} = \cos\psi\sin\varphi. \tag{2.19}$$

Using the Pythagorean identity $\sin^2 x + \cos^2 x = 1$ this can be adapted to:

$$\sin^2\theta = 1 - \cos^2\psi\,\sin^2\varphi. \tag{2.20}$$

In the case of an unpolarized incident wave, all possible azimuthal angles $\psi \in [0, 2\pi)$ are equally likely. This allows the average value of $\sin^2\theta$ to be calculated:

$$\overline{\sin^2\theta} = 1 - \overline{\cos^2\psi}\,\sin^2\varphi = 1 - \frac{\sin^2\varphi}{2} = \frac{1+\cos^2\varphi}{2}. \tag{2.21}$$

Substituting this into Equation 2.15 yields the differential cross-section for unpolarized incident waves:

$$\left(\frac{d\sigma}{d\Omega}\right)_{\text{unpolarized}} = \left(\frac{q^2}{4\pi\varepsilon_0 mc^2}\right)^2 \left(\frac{1+\cos^2\varphi}{2}\right). \tag{2.22}$$

Equation 2.22 shows, that within the Thomson limit, the differential cross-section of Thomson scattering is independent of the wavelength and is symmetric in forward and backward directions [35]. q denotes the scatterer's charge and m its mass.
Integrating over the entire solid angle yields the total cross-section [35]:

$$\begin{aligned}\sigma &= \int_0^{2\pi} d\psi \int_0^{\pi} d\varphi \left(\frac{q^2}{4\pi\varepsilon_0 mc^2}\right)^2 \frac{1+\cos^2\varphi}{2}\sin\varphi = \frac{8\pi}{3}\left(\frac{e^2}{4\pi\varepsilon_0 m_e c^2}\right)^2 \\ &= \sigma_{\text{Thomson}} = 6.65\times10^{-29}\ \text{m}^2.\end{aligned} \tag{2.23}$$

To represent scattering by an electron $q = e$ and $m = m_e$ was used. The result is the same as in Equation 2.16, which shows, that the total Thomson scattering cross-section is independent of the polarization of the incident wave. The quantity $\frac{e^2}{4\pi\varepsilon_0 m_e c^2}$ is the classical electron radius r_e.

Note that the foregoing considerations are only valid for stationary electrons.
If the energy of the incident photon is comparable to the rest mass of the scattering particle mc^2, the scattering becomes inelastic and part of the photon's energy is transferred to the scattering particle. This is the Compton effect, which is described in Section 2.2.3.
However, for small scattering angles φ, the ratio $\frac{E'}{E}$, defined in 2.6 is close to unity, which simplifies the Klein-Nishina formula 2.6 to the Thomson scattering formula 2.23. The same is true for small energies. Additionally, typical XFI energies are still much smaller than the rest mass of an electron $60\,\text{keV} < m_e c^2 = 511\,\text{keV}$. Therefore, both elastic and inelastic scattering processes do occur.

Furthermore, Compton scattering processes, as inelastic, incoherent scattering events, are inherently random and governed by probability distributions of the scattering direction and energy transfer in the process. Therefore, they do not meet the requirements for interference. As will be discussed in Section 2.4, interference is the operating principle of the presented X-ray optics.

Assume an incident wave with wave vector $\vec{k}_0$ and intensity I_0 that is scattered at the scattering angle $\varphi = 2\theta$. The intensity of the scattered wave I_e with wavevector $\vec{k}_s$ at the distance R is then given by Equation 2.24, following an inverse square distance law:

$$I_e\left(\vec{k}_s\right) = I_0 \frac{r_e^2}{R^2}\frac{1+\cos^2(2\theta)}{2}. \tag{2.24}$$

Geometric Phase Difference

In the context of X-ray scattering, it is often necessary to determine the relative phase difference between waves that are scattered at different points. The following section derives an expression for this phase difference caused by the path difference, based on [22, 41]. Consider two incident plane waves with identical wave vectors $\vec{k}_0$ and a relative phase offset α, which are scattered by two scattering sites, i and j, separated by the vector $\overrightarrow{r_{ij}}$. The waves scattered in a direction specified by the wavevector $\vec{k}_s$ will then exhibit a phase difference that is given by:

$$\Delta\Phi = 2\pi \left(\vec{k}_s - \vec{k}_0\right) \cdot \overrightarrow{r_{ij}} + \alpha. \tag{2.25}$$

By choosing one scattering site as a common origin, the positions of all scatterers are defined with respect to this origin via $\vec{r_j}$. The phase difference simplifies to:

$$\Delta\Phi_j = 2\pi \left(\vec{k}_s - \vec{k}_0\right) \cdot \vec{r_j} + \alpha. \tag{2.26}$$

The assumption that the waves share the same wavelength λ, the identity $\vec{s} = \lambda \cdot \vec{k}$ can be used, so that:

$$\Delta\Phi_j = 2\pi \frac{(\vec{s}_s - \vec{s}_0)}{\lambda} \cdot \vec{r_j} + \alpha, \tag{2.27}$$

where $\vec{s}$ denote dimensionless direction vectors. This relation implies that all points $\vec{r_j}$ that satisfy the condition

$$(\vec{s}_s - \vec{s}_0) \cdot \vec{r_j} = C, \tag{2.28}$$

with C being an arbitrary constant value, will share a common phase difference of:

$$\Delta\Phi = 2\pi \frac{C}{\lambda} + \alpha. \tag{2.29}$$

A phase difference of $\Delta\Phi$ between two waves of equal wavelength λ corresponds to an optical path difference of

$$\Delta x = \frac{\lambda}{2\pi} \Delta\Phi. \tag{2.30}$$

A phase difference of $\Delta\Phi = 2n\pi$ enables the formation of perfect constructive interference, while $\Delta\Phi = (2n+1)\pi$, where n is an integer, leads to perfect destructive interference [27]. The constructive interference of coherently scattered waves, whose relative phases are determined by the arrangement of the scattering sites in relation to each other, gives rise to the phenomenon of diffraction [41]. It is the underlying principle of a number of X-ray optics, which are discussed in this work.

2.3.2 Scattering by an Atom

When X-rays interact with matter, they are not only scattered by individual, free electrons, but rather an ensemble of bound electrons contained within the atoms. An atom is described by its atomic number Z. One could think, that the scattering power of an atom containing Z electrons is just Z times greater than that of a single electron.
However, the distance between individual electrons, or the ones contained in the electronic cloud of an atom, is on the order of magnitude of the wavelength of X-rays. As discussed previously, the underlying principle of Thomson scattering produces coherently scattered waves. Consequently, depending on their spatial distribution and number, some form of partial interference between the scattered waves of the individual electrons is anticipated. This will ultimately reduce the scattering power. The more diffuse the electronic distribution, the stronger the reduction. The following section briefly quantifies these considerations after [22]. It introduces the atomic form factor f, which expresses the ratio between the scattering amplitude of an atom and a single scattering electron.

The motion of bound electrons is significantly greater than the temporal variation of the electric field vector of the incident wave. As a result, their interaction takes place with the time-averaged electronic charge cloud of the atom instead of individual electrons. The corresponding charge distribution $\varrho(r)$ is initially assumed to be spherically symmetric. Consequently, it is determined solely by the radial distance r to the nucleus of the atom.

A single scattering event is described by the scattering vector $\vec{H} = \vec{k}_s - \vec{k}_0 = \frac{\vec{s}_s - \vec{s}_0}{\lambda}$, which is the difference between the scattered and incident wave vector. Figure 2.3 illustrates the definition of the propagation direction vectors $\vec{s}_0$ and $\vec{s}_s$. Using the scattering angle θ, it can also be expressed as $H = \left|\vec{H}\right| = 2\,\frac{\sin\theta}{\lambda}$ [36]. For forward scattering, it is therefore true that $H = 0$.

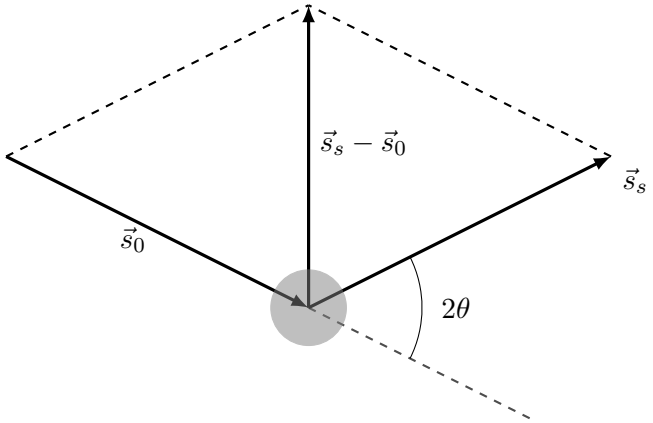


Figure 2.3: Definition of the incident and scattered propagation direction vectors $\vec{s}_0$ and $\vec{s}_s$, as well as the scattering angle θ for scattering by an atom [26].

The atomic scattering factor or atomic form factor f_0 is the Fourier transform of the atomic electron density $\varrho(r)$. It is a function of the scattering vector $\vec{H}$ [22]:

$$f_0(\vec{H}) = \int_V \varrho(\vec{r}) \mathrm{e}^{i\vec{H}\cdot\vec{r}} dV. \tag{2.31}$$

In the case of forward scattering ($\vec{H} \to \vec{0}$), the atomic scattering factor is equal to the atomic number, $f_0 = Z$. If $H \neq 0$, partial destructive interference between waves that are scattered by different electrons reduces the scattering amplitude.

Using Euler's formula, $\mathrm{e}^{i\vec{H}\cdot\vec{r}} = \cos(\vec{H}\cdot\vec{r}) + i\sin(\vec{H}\cdot\vec{r})$ corresponds to a unit circle in the complex plane, which represents the phase contribution of an electron that is located at $\vec{r}$. For large values of $\vec{H}$, the phase is much larger than 2π. The phase factors of different electrons will then fluctuate significantly around their unit circle. As a result, the integral in Equation 2.31 approaches zero, even for smooth distributions $\varrho(\vec{r})$.
This means that if the wavelength of the incoming radiation is small compared to the size of the atom, destructive interference occurs between the scattered waves of the individual electrons of the atom [22]. f_0 accounts for elastic, coherent scattering by bound electrons. It quantifies part of the deviation from an ideal Thomson scattering process.

Following the definitions of Chantler [42], the scattering differs even further from ideal Thomson scattering due to additional effects explained below. These effects are summarized in a more complex form of the atomic form factor, which can be expressed as a sum. Chantler's definition of f_0 [42] uses the ideal Thomson limit with a spherical symmetric electron distribution $\varrho(\vec{r}) = \varrho(r)$:

$$f_0(H) = 4\pi \int_0^\infty r^2 \varrho(r) \frac{\sin(Hr)}{Hr} dr, \tag{2.32}$$

$$f = f_0 + f_{\mathrm{NT}} + f' + if'', \tag{2.33}$$

$$f' = f_1 + f_{\mathrm{rel}}, \tag{2.34}$$

where f_{NT} represents the Thomson scattering by the atom's nucleus. It is defined as:

$$f_{\mathrm{NT}} \sim -Z^2 \frac{m_e}{M}, \tag{2.35}$$

with m_e representing the mass of an electron and M denoting the mass of the nucleus. Due to the significant difference between these two masses, f_{NT} is negligible as long as f_0 is much higher, which is the case for lighter elements, shallow reflection angles and X-ray energies below about 100 keV [43].

The term f' includes the dispersion correction and arises from resonant and dispersive effects near the absorption edges. It can be expressed as $f' = f_1 + f_{\mathrm{rel}}$, where f_{rel} represents relativistic corrections, which is significant for inner-shell electrons of high-Z elements that move at relativistic velocity. $f'(E)$ is energy-dependent and varies significantly near the absorption edges of an element. This is a decisive difference to f_0, which depends on the scattering angle. Both parts of f' are often tabulated as one value [43].
$f'(E)$ is related to the imaginary part of the form factor, $f''(E)$ via the Kramers-Kronig relation, which, in turn, is proportional to the photoelectric absorption [22]. $f''(E)$ is expressed by:

$$f''(E) = \frac{E\mu_{\mathrm{PE}}(E)}{2hcr_{\mathrm{e}}}, \tag{2.36}$$

with c denoting the speed of light, r_e the classical electron radius and h the Planck constant. It also depends on the energy as well as the material's photoelectric absorption coefficient $\mu_{\mathrm{PE}}(E)$. Values of $f''(E)$ are often tabulated together with $f'(E)$ [43].

Apart from the discussed factors, thermal vibrations also affect the elastic coherent scattering of an atom. The reduction in the scattering amplitude resulting from this effect is described by the Debye-Waller factor, which appears on the right-hand side of Equation 2.37 [22, 44]:

$$f(H) \cdot e^{-B_{\mathrm{iso}} \frac{\sin^2\theta}{\lambda^2}}. \tag{2.37}$$

The model assumes an isotropic vibration, $B_{\mathrm{iso}} = 8\pi^2 \left\langle u^2 \right\rangle$, where $\left\langle u^2 \right\rangle$, is the quadratic average amplitude of the thermal vibrations in the direction of $\vec{H}$. At room temperature, the Debye-Waller factor is close to one for crystalline solids.

Combining the described factors and corrections yields the modified expression 2.38 for the total scattering intensity of an atom $I(\vec{H})$:

$$I(\vec{H}) = I_e(\vec{H})\, |f(H)|^2\, e^{-2B_{\mathrm{iso}} \frac{\sin^2\theta}{\lambda^2}}. \tag{2.38}$$

Here, $I_e(\vec{H})$ denotes the theoretically scattered intensity of a single free electron in an ideal Thomson scattering process, as described in Section 2.3.1. The bound nature and spatial distribution of the electrons in an atom are represented by the atomic form factor $f_0(H)$. It modifies the scattering amplitude relative to the Thomson limit. The resulting elastic, coherent scattering of X-rays by atoms is commonly referred to as Rayleigh scattering [22]. It is further modified by the additional effects described above, which are quantified by f_{NT}, f' and f''. They are generally small compared to f_0 and become relevant in the vicinity of absorption edges [43].

2.3.3 Scattering by an Ensemble of Atoms

To represent the interaction of X-rays with matter, further specification as in the following section after [41, 45] is necessary.
The incident waves not only interact with indivudal atoms, but rather with an ensemble of atoms. However, the distances between the atoms as individual scattering sites are much larger than between the electrons inside the atom. It is therefore feasible to assume the atoms as point scatterers with scattering properties as described in Section 2.3.2. Individual scattering events can occur randomly at every atom within the irradiated volume. Therefore, the secondary (reflected) wavefront propagates in all directions, as quantified by Equation 2.38. Depending on the relative positions and the corresponding phase relations of the scattering sites, interferece effects can arise. This is referred to as internal interference.

In order to achieve pronounced constructive interference, the atomic arrangement within a material must exhibit a high degree of spatial order to ensure a phase relation among the scattered waves. This prerequisite is inherently satisfied by crystalline solids, which are defined by the International Union of Crystallography (IUCr) as such: "A solid is a crystal if its atoms, ions, and/or molecules form, on average, a long-range ordered arrangement. In most crystals, the arrangement is a periodic array that is governed by the rules of translational symmetry.[...]"[46].

This emphasizes that crystals are most suitable to make use of constructive interference to utilize the scattering for diffraction-based X-ray optics. Therefore, in the following sections, the scattering of X-rays by crystals is derived.

2.3.4 Scattering by a Bravais Lattice

This section describes the transition to X-ray scattering by crystals. First, it explains the interaction with a theoretically perfect lattice using the concept of Bravais lattices after [22, 45, 47–50].

A Bravais lattice is an idealized model of an infinite array of points, where every point has an identical environment. One point can be generated from another through a discrete translation operation along a translation vector. In three-dimensional space, such a translation can be described by three noncoplanar primitive vectors $\vec{a}$, $\vec{b}$ and $\vec{c}$ via Equation 2.39, where n_i are integer values [49, 51]:

$$\vec{R_j} = n_{j,1}\vec{a} + n_{j,2}\vec{b} + n_{j,3}\vec{c}. \tag{2.39}$$

The primitive translation vectors $\vec{a}$, $\vec{b}$ and $\vec{c}$ do not have to be orthogonal to each other and are not unique to the Bravais lattice.

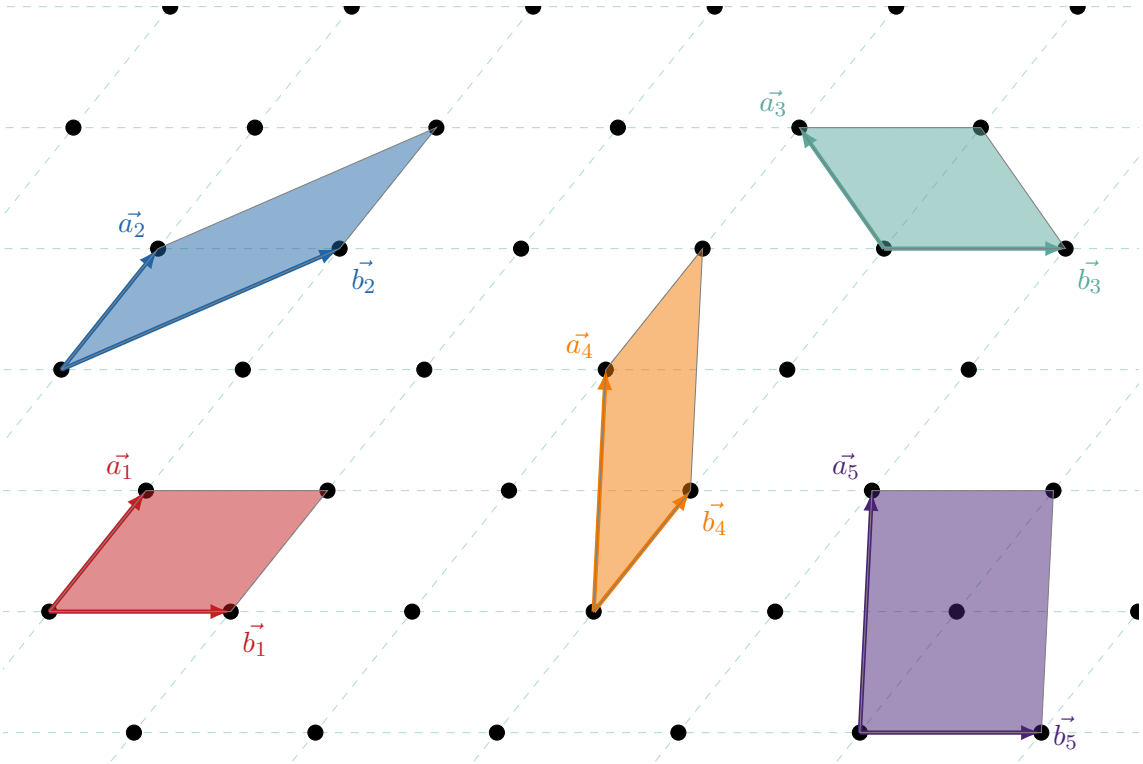


Figure 2.4: Four possible sets of primitive lattice vectors ($\vec{a}_{1-4}$, $\vec{b}_{1-4}$) and a possible set of conventional lattice vectors ($\vec{a}_5$, $\vec{b}_5$), according to the definition of Bravais [50].

Figure 2.4 shows a two-dimensional Bravais lattice with different sets of primitive lattice vectors. Any of these sets can be used to describe the same lattice. If the area or volume spanned by the vectors can be repeatedly translated by its associated primitive vectors to fill the entire lattice space without any overlap or voids, it is referred to as a unit cell [22]. Unit cells that minimize the area or volume are defined as primitive unit cells. All primitive unit cells of a Bravais lattice have the identical smallest possible area or volume and contain exactly one lattice point.

However, it is sometimes convenient to use unit cells larger than the primitive unit cell to describe a more complex lattice. These larger unit cells can contain more than one lattice point and are called conventional unit cells. Figure 2.4 shows examples of both types.

The following explanations consider a primitive unit cell and its primitive lattice vectors. Using Equation 2.39, the relative position of two atoms in a Bravais lattice $r_{\vec{n},\vec{n'}}$ can be expressed with:

$$\vec{r}_{n,n'} = \vec{R}_{n_1,n_2,n_3} - \vec{R}_{n'_1,n'_2,n'_3} = \left(n_1 - n'_1\right)\vec{a} + \left(n_2 - n'_2\right)\vec{b} + \left(n_3 - n'_3\right)\vec{c}. \tag{2.40}$$

Consider a single wave packet with an arbitrary initial phase, expressed by α in Equation 2.27. Within a wave packet, the waves are mutually coherent. Consequently, the relative phase differences can be set to zero when considering a wave packet. The diffraction of incoherent X-rays is further discussed in Section 2.4.5.

The total scattered intensity results from the superposition of the waves that are coherently scattered by the individual scattering sites. The phase of every individual contribution is given by 2.27. A scattering occurring at $\vec{r}_j$, relative to a common origin, has a scattering amplitude of $|f(H)|\, e^{-B_{\text{iso}} \frac{\sin^2\theta}{\lambda^2}}\, e^{i\Delta\Phi_j}$. The total scattered field is the sum of all individual scattering site contributions, and the measurable scattering intensity is proportional to the squared modulus of the total amplitude.

Therefore, the total scattered intensity can be expressed with a double sum:

$$I(\vec{H}) = I_e(\vec{H}) \sum_{n_1,n_2,n_3} \sum_{n_1',n_2',n_3'} e^{-(B_{\text{iso}\,j} + B_{\text{iso}\,j'}) \frac{\sin^2\theta}{\lambda^2}} f_j(H) f_{j'}^*(H) \exp\left[2\pi i \left(\vec{k}_s - \vec{k}_0\right) \cdot \vec{r}_{n,n'}\right], \tag{2.41}$$

where * denotes the complex conjugate. The double sum accounts for the intensity arising from the interference of all possible pairs of coherently scattered partial waves.
Assuming identical scattering sites, for example atoms of the same element with the same atomic form factor $f_j(H) = f_{j'}(H)$ and Debye-Waller factor $B_{\text{iso}\,j} = B_{\text{iso}\,j'}$, and substituting Equation 2.40 into Equation 2.41, this can be simplified to the Laue interference function for a finite Bravais lattice [41]:

$$I(\vec{H}) = I_e(\vec{H}) |f(H)|^2\, e^{-2B_{\text{iso}} \frac{\sin^2\theta}{\lambda^2}} \left(\frac{\sin^2(N_1 x_1)}{\sin^2 x_1}\right) \left(\frac{\sin^2(N_2 x_2)}{\sin^2 x_2}\right) \left(\frac{\sin^2(N_3 x_3)}{\sin^2 x_3}\right) \tag{2.42}$$

$$= I_e(\vec{H}) |f(H)|^2\, e^{-2B_{\text{iso}} \frac{\sin^2\theta}{\lambda^2}}\, I_l(\vec{H}), \tag{2.43}$$

$$x_1 = \pi \left(\vec{k}_s - \vec{k}_0\right) \cdot \vec{a}, \quad x_2 = \pi \left(\vec{k}_s - \vec{k}_0\right) \cdot \vec{b}, \quad x_3 = \pi \left(\vec{k}_s - \vec{k}_0\right) \cdot \vec{c}. \tag{2.44}$$

The total number of unit cells is $N_{tot} = N_1 N_2 N_3$. Equation 2.42 shows that the total scattered intensity is composed of three factors: the contribution of a single electron $I_e(\vec{H})$, the atomic form factor of the scattering atoms at the lattice points $|f(H)|$, and the influence of the lattice $I_l(\vec{H})$.
In the general case, it holds that $N_i \gg x_i$ and therefore $I_l \approx 0$ for most values of x_i. However, if x_i is an integer multiple of π, each corresponding factor of I_l reaches its maximum value of ${N_i}^2$. If this condition is met in all three directions, I_l attains its overall maximum of N^2. This means that at these points, the superposition of scattered waves results in strong intensity maxima, known as diffraction peaks.

The width of a peak is inversely related to the number of lattice points involved in its formation [49, 54]. This is discussed in detail in Section 2.4.2, and it can be determined experimentally by a rocking curve measurement, which is discussed in Section 7.1 [55].

2.3.5 Scattering by a Perfect Crystal

Following the definition of a crystal, given in Section 2.3.3, a crystal is composed of a periodic arrangement of unit cells that are defined by their unit vectors $\vec{a}$, $\vec{b}$ and $\vec{c}$. In its simplest form, a monoatomic lattice, every lattice point is occupied by exactly one atom. Therefore, the position of each atom is given by Equation 2.39.

More complex crystals also permit atoms that are not located exactly at a lattice point [47, 51]. The position of each atom within a unit cell is defined relative to the unit cell origin by:

$$\vec{r_k} = x_k\vec{a} + y_k\vec{b} + z_k\vec{c}, \tag{2.45}$$

and is referred to as the crystal basis [47]. For unit cells that are defined by positive unit cell vectors only, x_k, y_k and z_k lie between 0 and 1.
Therefore, the total position of every atom inside the crystal with respect to a common origin is given by the combination of lattice (Equation 2.39) and basis (Equation 2.45) translations [51]:

$$\overrightarrow{R_{jk}} = n_{j,1}\vec{a} + n_{j,2}\vec{b} + n_{j,3}\vec{c} + \overrightarrow{r_k}. \tag{2.46}$$

The existence of multiple atoms within a unit cell basis introduces a phase relationship between the scattered waves of these atoms, known as internal interference. To account for this, the total scattered intensity of a crystal is extended by the structure factor of the unit cell $F(\vec{H})$ [22]:

$$F(\vec{H}) = \sum_{k=1}^{n} f_k(H) e^{i\vec{H}\cdot\vec{r}_k}\, e^{-B_{\mathrm{iso}\,k}\frac{\sin^2\theta}{\lambda^2}}, \tag{2.47}$$

where f_k are the individual atomic form factors of the n atoms contained within one unit cell, and the exponential term expresses the relative phase. The corresponding intensity contribution is given by:

$$I_F(\vec{H}) = \left|F(\vec{H})\right|^2 = F(\vec{H})F(\vec{H})^*. \tag{2.48}$$

In its initial introduction in Section 2.3.4, the contribution of the Bravais lattice I_l to the total scattered intensity was derived under the assumption of a single, identical atom per unit cell. It therefore contained the atomic form factor $f(H)$ of this atom. In the extended model, the atomic form factor is now contained in the structure factor I_F instead.

Combining all contributions introduced so far, the total scattered intensity of a perfect crystal is given by Equation 2.49:

$$I(\vec{H}) = I_e(\vec{H}) I_l(\vec{H}) I_F(\vec{H}). \tag{2.49}$$

The direction of diffraction maxima for an incident wave of a given wavelength depends solely on the crystal's underlying Bragg lattice. Two crystals with the same lattice share the same set of peak positions. The diffraction intensity differs, because it is determined by the electron distribution, which is described by the structure factor $F(\vec{H})$ and especially the atomic form factors of the crystal's atoms [22].

2.4 Quantitative Description of X-ray Diffraction in Crystals

In the preceding Section 2.3, the underlying factors that give rise to the formation of diffraction maxima in a crystal were presented. This section derives quantitative statements on the position and strength of the diffraction peaks for both perfect and imperfect crystals.

2.4.1 Location of the Diffraction Peaks

As explained in Section 2.3.4, a crystal lattice can be defined by a set of translation vectors via $\vec{R}_{m_1,m_2,m_3} = m_1\vec{a} + m_2\vec{b} + m_3\vec{c}$. This lattice is referred to as the crystal's direct lattice [47]. Note again, that atoms do not have to be located exactly on these lattice points.

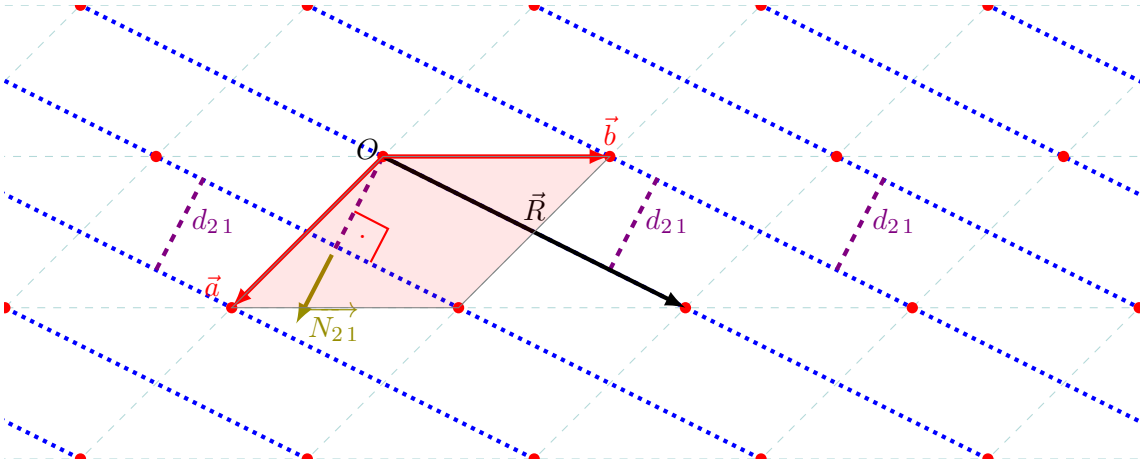


Figure 2.5: Geometric construction of a $\{2\,1\}$ lattice plane set (blue dotted lines) from a direct two-dimensional lattice, defined by $\vec{a}$ and $\vec{b}$, and the lattice set's normal vector $\overrightarrow{N_{2\,1}}$. Adapted from [22, Figure 5.2]

Figure 2.5 illustrates such a lattice in an exemplary 2D case after [22], which consequently has no m_3 nor $\vec{c}$ vector. Lattice points are marked with red dots, and a single unit cell, defined as a parallelogram by $\vec{a}$ and $\vec{b}$, is illustrated in light red.

In this lattice, it is now possible to define various sets of planes throughout the crystal on

which the unit cells or atoms, respectively, are arranged. Figure 2.5 shows an examplary set of lattice planes as dotted blue lines. The plane through the arbitrary origin O is constructed by connecting it to the point reached by the translation vector $\vec{R} = \vec{a} + 2\vec{b}$. Starting the construction from any other lattice point yields a plane that is parallel or identical to the one described. The exemplary lattice plane set is perpendicular to the sheet plane.

To reference a plane set, it is evaluated where the planes intersect the direct vectors of a single unit cell. In Figure 2.5, the constructed planes cut at $p\vec{a} = \frac{1}{2}\vec{a}$ and $q\vec{b} = 1\vec{b}$. In other words, in the direction $\vec{a}$, every $\frac{|\vec{a}|}{2}$ marks an interception point with a plane of the set. In the direction $\vec{b}$, the plane only cuts once at every unit cell border. The intercepts are located at $p\vec{a}, q\vec{b}, r\vec{c}$. The reciprocals of the factors $h = \frac{1}{p}$, $k = \frac{1}{q}$ and $l = \frac{1}{r}$, when reduced to the smallest integers, are the so-called Miller indices of the plane set [47, 48].

In the exemplary case in Figure 2.5, the Miller indices are $h = 2$ and $k = 1$. Consequently, the plane set is referred to as the $\{2\,1\}$ plane set.[2] The normal vector of the plane, denoted as $\vec{N}_{2\,1}$, is defined in the direction of $\vec{a}$ and $\vec{b}$. Therefore, the plane intersects at positive values along both vectors. By convention, if $\vec{N}$ was defined in the other direction, the plane set would be referred to as the $\{\overline{2}\,\overline{1}\}$ plane set, with an overline representing a negative Miller index [22]. In the illustrated case, the distances between the individual planes are denoted as $d_{hk} = d_{2\,1}$. Note again that the third dimension is not considered in this two-dimensional sample. A so-called reciprocal vector can then be defined in the direction of the plane normal via:

$$\vec{\sigma_{\mathrm{hkl}}}^{\,*} = \frac{\vec{N}_{\mathrm{hkl}}}{d_{\mathrm{hkl}}}, \tag{2.50}$$

for the exemplary case: $\vec{\sigma_{2\,1}}^{\,*} = \frac{\vec{N}_{2\,1}}{d_{2\,1}}$. This vector has the length of $\frac{1}{d_{hkl}}$, and by the definition, it follows that $\vec{R} \cdot \vec{\sigma_{\mathrm{hkl}}}^{\,*} = 0$. Similarly, any constructible lattice plane set can be transformed into a reciprocal vector. These vectors, constructed from an arbitrary origin, form a second grid referred to as the reciprocal lattice [51].[3]

In this context, reciprocal vectors resulting from the construction of plane sets that fully align with one of the direct lattice's unit cell planes play a distinctive role. Consider, for example, the plane set that coincides only with the planes spanned by the unit cell vectors of the direct lattice, $\vec{a}$ and $\vec{b}$. This plane divides the unit cell into one part ($r = 1$) in the direction of $\vec{c}$ and virtually infinite parts in the directions of $\vec{a}$ and $\vec{b}$, as it coincides with them ($p = q = \infty$). The Miller indices are obtained by the reciprocals of the intercepts. Therefore, it represents the $\{hkl\} = \{001\}$ lattice plane set. The corresponding reciprocal

[2] It is common practice to indicate a single lattice plane by $(h\,k\,l)$ and a lattice plane set by $\{h\,k\,l\}$. Directions are indicated by $[h\,k\,l]$ and sets of directions by $\langle h\,k\,l\rangle$.

[3] Note that throughout this work, reciprocal lattice vectors are defined without a factor 2π. The 2π convention as commonly used in quantum mechanical considerations, for example in [22], can be recovered by a simple rescaling of the reciprocal lattice vectors. Both definitions are common [47].

vector $\vec{\sigma_{001}}^{*} = \frac{\vec{N_{001}}}{d_{001}}$ is the new reciprocal lattice vector $\vec{c}^{*}$ [22, 51].

Analogously, the two other reciprocal lattice vectors $\vec{a}^{*}$ and $\vec{b}^{*}$ can be constructed. Note that the symbol $*$ denotes the reciprocal lattice. Following this definition, it is true that [56]:

$$\vec{c} \cdot \vec{c}^{*} = |\vec{c}| \; |\vec{c}^{*}| \cos\gamma = |\vec{c}| \; \frac{1}{d_{001}} \frac{d_{001}}{|\vec{c}|} = 1, \tag{2.51}$$

with γ denoting the angle between $\vec{N_{001}}$ and $\vec{c}$. The same is true for $\vec{a} \cdot \vec{a}^{*} = 1$ and $\vec{b} \cdot \vec{b}^{*} = 1$. Furthermore, the following correlations arise [56]:

$$\vec{a} \cdot \vec{b}^{*} = \vec{a} \cdot \vec{c}^{*} = \vec{b} \cdot \vec{a}^{*} = \vec{b} \cdot \vec{c}^{*} = \vec{c} \cdot \vec{a}^{*} = \vec{c} \cdot \vec{b}^{*} = 0. \tag{2.52}$$

A point in the newly formed reciprocal lattice can be constructed by translating along a vector $\vec{R}^{*}$ via:

$$\vec{R}^{*}_{hkl} = h\vec{a}^{*} + k\vec{b}^{*} + l\vec{c}^{*}, \tag{2.53}$$

with (hkl) being whole-numbered values, the Miller indices.
A reciprocal lattice point describes a plane set in the direct lattice with the interceptions $n\left(\frac{\vec{a}}{h}, \frac{\vec{b}}{k}, \frac{\vec{c}}{l}\right)$, where n is an arbitrary integer [47, 51]. The distance between them is given by the length of the reciprocal value of $\vec{R}^{*}$.

As derived in Chapter 2.3.4, diffraction maxima only occur at specific directions within a crystal lattice if $\vec{H} \cdot \vec{a}$, $\vec{H} \cdot \vec{b}$ and $\vec{H} \cdot \vec{c}$, with $\vec{H} = \frac{(\vec{s}_s - \vec{s}_0)}{\lambda}$, are all integer values. This is expressed by the Laue conditions in direct space:

$$\begin{aligned} \vec{H} \cdot \vec{a} &= h, \\ \vec{H} \cdot \vec{b} &= k, \\ \vec{H} \cdot \vec{c} &= l. \end{aligned} \tag{2.54}$$

Using the identities of the reciprocal lattice, expressed in Equations 2.51 and 2.52, this can be expressed using the reciprocal lattice vectors:

$$\vec{H} = h\,\vec{a}^{*} + k\,\vec{b}^{*} + l\,\vec{c}^{*} = \vec{G}_{hkl}. \tag{2.55}$$

This expression indicates that, in order for a diffraction maximum to occur, $\vec{H}$ must coincide with a reciprocal lattice vector $\vec{G}_{hkl}$, which defines a point in the reciprocal lattice. Ultimately, there must be a set of integer values (hkl), such that $\vec{H} = \vec{G}_{hkl}$. In the context of diffraction, (hkl) are referred to as the Laue indices [22]. They describe the existence of a diffraction maximum and are only defined in reciprocal space. Although they share the same numerical values as the Miller indices, which describe lattice plane sets in direct

space, the two concepts should not be confused. Their distinction is further explained below.

Using the definitions of the magnitude of the scattering vector $\vec{H}$ and of reciprocal lattice vectors, the wavelength that corresponds to a diffraction maximum can be deduced as in Equation 2.56 [41]:

$$\left|\vec{H}\right| = \frac{2\sin\theta_{hkl}}{\lambda} = \frac{|(\vec{s}_s - \vec{s}_0)|}{\lambda} = \left|\vec{G}_{hkl}\right| = \frac{1}{d_{hkl}} \tag{2.56}$$

$$\longrightarrow \lambda = 2d_{hkl}\sin\theta_{hkl}. \tag{2.57}$$

Since $\vec{G}_{hkl}$ corresponds to a plane set of distance d_{hkl} in real space, the expression demonstrates that successive planes diffract in phase. A plane that is m times further away has a plane distance of $m\,d_{hkl}$ and, therefore, a path difference of $m\lambda$, which translates to a phase difference of $2m\pi$.
Note again that the underlying principle of the formation of a diffraction maximum is the constructive interference of waves scattered by the regularly spaced lattice points. In principle, a series of higher orders can exist for every instance of constructive interference. However, depending on the crystal structure, their intensity may be greatly reduced or even disappear. These higher orders correspond to wavelengths that are integer fractions of the original wavelength. Therefore, Equation 2.56 must be adjusted to account for these higher orders [47]. The resulting Equation 2.58 is referred to as the Bragg condition with $2\theta_{hkl}$ denoting the angle between the incident and diffracted beam [47, 57]:

$$n\lambda = 2d_{hkl}\sin\theta_{hkl}. \tag{2.58}$$

Given that the angle is unique to a plane set with a given wavelength, it is often regarded as a characteristic of the plane set and is referred to as its Bragg angle.
The higher orders of reflection are considered by an integer multiple of the Laue indices. Consequently, the Miller and Laue indices are solely identical for the first order of interference ($n = 1$). For higher orders, the Miller index remains constant as it continues to represent the same set of planes in the direct lattice. In contrast, higher orders of diffraction are described by the Laue indices $(nh\,nk\,nl)$ [47].

Note that integer multiples of Miller indices, such as $\{1\,1\,1\}$ and $\{2\,2\,2\}$, are also possible if the crystal structure allows for it. Also note that depending on the crystal structure, certain planes may not generate a diffraction maximum, as the diffraction may be canceled out due to interference effects [22]. This will be further addressed in Section 2.4.12.
Using the requirements for the existence of a diffraction maximum and the definition of the reciprocal lattice introduced above, Equation 2.47 for the structure factor can be adapted.

By using $\frac{\vec{s}_s - \vec{s}_0}{\lambda} = \vec{H} = h\vec{a}^* + k\vec{b}^* + l\vec{c}^*$ and Equation 2.45 the structure factor can be written as:

$$F(\vec{H}) = \sum_{j=1}^{n} f_j(H) e^{2\pi i \vec{H}\cdot\vec{r}_j} e^{-B_{\mathrm{iso}\,j}\frac{\sin^2\theta}{\lambda^2}} = \sum_{j=1}^{n} f_j(H) e^{2\pi i\left(h\vec{a}^*+k\vec{b}^*+l\vec{c}^*\right)\cdot\left(x_j\vec{a}+y_j\vec{b}+z_j\vec{c}\right)} e^{-B_{\mathrm{iso}\,j}\frac{\sin^2\theta}{\lambda^2}}$$
$$= \sum_{j=1}^{n} f_j(H) e^{2\pi i(hx_j+ky_j+lz_j)} e^{-B_{\mathrm{iso}\,j}\frac{\sin^2\theta}{\lambda^2}}. \tag{2.59}$$

Here, f_j denotes the atomic scattering factor, defined by Equation 2.33.
Note again that the integer values (hkl) can also take negative values. They represent the direction of the plane normals and are expressed by a bar $[-h, -k, -l] = [\bar{h}, \bar{k}, \bar{l}]$.

2.4.2 Geometrical Description of Bragg Reflection

Equation 2.58 can also be derived and interpreted geometrically. The following derivation after [47] goes back to the original work of Bragg in 1913 [57].

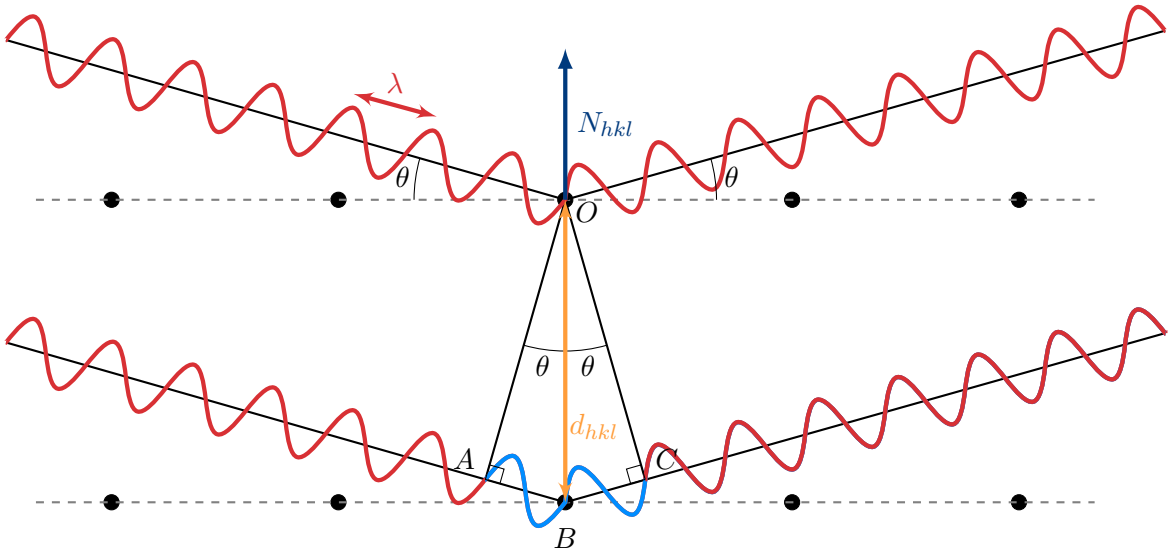


Figure 2.6: Geometric representation of a Bragg reflection after [57]. Two coherent waves are diffracted at two superimposed lattice points at the same angle. The path difference between the two paths is $\Delta = 2\lambda$.

Figure 2.6 shows a two-dimensional representation of a small section of a lattice with two planes drawn in dashed lines. The lattice sites, in this case, individual atoms, are represented by black dots. The lattice planes have a distance of d_{hkl}. An incident wavefront with the wavelength λ is illustrated from the left. It is scattered by the electrons contained within the atoms on the planes, as illustrated at O and B in Figure 2.6. Only the part that ist scattered at the same angle θ as the incoming wavefront is drawn here. The direction is the same for both scatterings. The lower pathway of the incident and subsequently reflected beam exhibits a geometric pathway difference of $\Delta = \overline{AB} + \overline{BC}$ with respect to

the upper pathway. Afterwards, both reflected wavefronts exhibit no phase difference.

Since the incident and reflection angles are identical in the illustration, it is clear that $\Delta = 2\overline{AB} = 2\overline{BC} = 2d_{hkl}\sin\theta$. Only if the phase difference is $\Phi = 0$, a constructive interference can occur. This corresponds to a geometric pathway difference that is an integer multiple of the wavelength $\Delta = n\lambda$, as discussed in Chapter 2.3.1, in the drawn case $n = 2$. This ultimately leads to the same equation for the existence of constructive interference in a lattice as derived in Section 2.4.1: $\Delta = n\lambda = 2d_{hkl}\sin\theta_{hkl}$.
The index θ_{hkl} is chosen to represent the fact that this specific angle is the only one at which the phenomenon can occur for a specific lattice plane distance d_{hkl} and integer multiples of the fitting wavelength. As discussed before, θ_{hkl} is referred to as the Bragg angle θ_B.

The explained model simplifies the formation process of diffraction maxima as a reflection with selection criteria concerning angle and wavelength for a given plane in a specific crystal.[4]

Note that the diffraction maxima are not perfectly discrete, as they arise from interference processes. They do have a certain range of acceptance, e.g., of angles at a given wavelength and plane set. This range of acceptance follows the so-called Darwin curve around the Bragg angle and is often characterized by its width, referred to as the Darwin width [54], which is given by Equation 2.91, and is described further in Section 2.4.4. The measurement of reflectivity over incident angles is a so-called rocking curve measurement, which is explained in detail in Section 7.1.

2.4.3 Bragg Reflection Intensity

After deriving the quantitative requirements for a Bragg reflection, this chapter aims to quantify the relation between the intensities of an incident beam I and its reflected component I', based on the work of Zachariasen and Darwin [49, 54, 58–61].
Bragg reflection processes are divided into two general cases, as illustrated in Figure 2.7. One is an overall reflection-like case, where the incident and reflected beams lie on the same side of the crystal. It is referred to as the Bragg case. The other one resembles an overall transmission, referred to as the Laue case. Both drawings in Figure 2.7 show an exemplary crystal plane as a dashed line. Illustrated is the respective underlying Bragg reflection at the Bragg angle θ_B, as well as the reflection angles relative to the crystal surface φ and φ'. For simplicity, only the incident and reflected beams are drawn.

[4] The Bragg model is central to the geometric relationships of X-ray diffraction on crystals. The simple reflection model described above is often sufficient. Therefore, the term “Bragg reflection” is commonly used in the literature and will be used in this work as well.

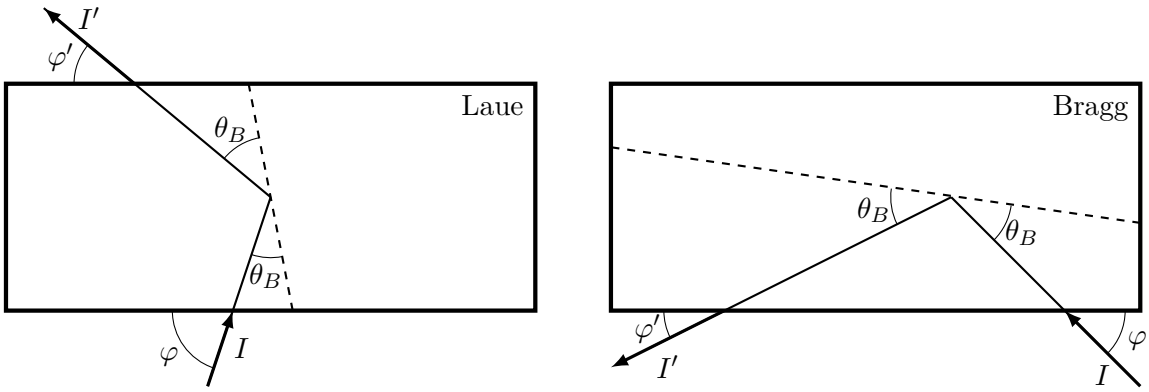


Figure 2.7: Laue and Bragg geometry, adapted from [58]. In both cases, the reflection from the crystal planes is characterized by the Bragg angle θ_B. In the Laue (transmission) geometry, the incident beam (I) and the Bragg-reflected beam (I') emerge on opposite sides of the crystal. In the Bragg (reflection) geometry, the incident and Bragg-reflected beams lie on the same side of the crystal. Angles with respect to the crystal surface are denoted by φ.

Apart from reflection itself, absorption plays a significant role in the overall reflected intensity. According to Zachariasen, the dominant part of absorption arises from "normal absorption," such as Compton scattering and photoelectric absorption, and it is quantified by the linear absorption coefficient μ [49, p. 102].
Coherent scattering is negligible outside the Darwin width, where the Laue conditions are not met, as indicated by the remarks in Section 2.4.4.
When the Laue conditions are satisfied, this leads to the formation of strong diffraction, which results in a reduction in the intensity of the incident beam due to the transfer of energy from the incident to the Bragg-reflected beam. Zachariasen refers to this as an extinction, which must be considered separately from normal absorption [49, p. 102].

The incident and the reflected beams are related through a coupled differential equation system, referred to as the Darwin equations 2.60 [58]:

$$\frac{\partial I(z)}{\partial z} = \frac{\sigma}{\sin\varphi'} I'(z) - \frac{\mu+\sigma}{\sin\varphi} I(z), \tag{2.60a}$$

$$\frac{\partial I'(z)}{\partial z} = \pm\frac{\sigma}{\sin\varphi'} I(z) - \frac{\mu+\sigma}{\sin\varphi} I'(z). \tag{2.60b}$$

In Equation 2.60b, (+) corresponds to the Laue and (-) to the Bragg case, as introduced in Figure 2.7. The equations account for the absorption effect and the build-up of Bragg-reflected intensity through the possibility of any number of plane reflections. σ is the coupling constant, which is the cross-section of the Bragg reflection per unit volume [58].

The Equations 2.61a and 2.61b provide boundary conditions for the differential equation systems.

To normalize the values, the intensity of the incident beam is set to $I(0) = 1$ [59]. The crystal's thickness is given by t. Therefore, the variable z, which represents the depth in the crystal at which the event occurs, is in the range $0 \leq z \leq t$.

$$I(0) = 1 \qquad I'(0) = 0 \qquad \text{Laue} \tag{2.61a}$$

$$I(0) = 1 \qquad I'(t) = 0 \qquad \text{Bragg} \tag{2.61b}$$

Furthermore, the overall reflectivity $R = \frac{I'}{I}$ and the transmissivity $T = I(t)$ as well as the absorptivity A are modeled by dimensionless variables. The conservation $R + T + A = 1$ applies [58].

The coupled intensity equations and their following solution correspond to the Darwin-Hamilton approach of the two-beam case of dynamical diffraction in a perfect crystal after [58].
A more general approach is given by the Takagi-Taupin equations, which describe the propagation of wavefield amplitudes inside a crystal. They also provide a solution for imperfect or distorted crystals. Refer to [54, 62–64] for these considerations. Section 2.4.10 discusses why the Darwin-Hamilton approach is sufficient for the scope of this work.

Auxiliary quantities are introduced in Equations 2.62a and 2.62b for the sake of clarity:

$$\begin{aligned} p &= \frac{(a+b)(1+\zeta)}{2}, \quad r = \sqrt{p^2 - \zeta b^2}, \\ q &= \frac{(a+b)(1-\zeta)}{2}, \quad s = \sqrt{q^2 + \zeta b^2}, \end{aligned} \tag{2.62a}$$

$$\begin{aligned} a &= \mu d, \\ b &= \sigma d, \\ \zeta &= \frac{\sin\varphi}{\sin\varphi'}, \end{aligned} \tag{2.62b}$$

where $d = \frac{t}{\sin\varphi}$ denotes the path length of the incident beam through the crystal. The general solution for the Laue case is given by:

$$I(z) = e^{-\frac{pz}{t}} \left(\cosh\left(\frac{sz}{t}\right) - \frac{q}{s} \sinh\left(\frac{sz}{t}\right) \right), \tag{2.63a}$$

$$I'(z) = e^{-\frac{pz}{t}} \left(\frac{b}{s} \sinh\left(\frac{sz}{t}\right) \right). \tag{2.63b}$$

Reflectivity R and transmissivity T are therefore given by:

$$R_{\text{Laue}} = e^{-p}\left(\frac{b}{s}\sinh(s)\right), \tag{2.64a}$$

$$T_{\text{Laue}} = e^{-p}\left(\cosh(s) - \frac{q}{s}\sinh(s)\right). \tag{2.64b}$$

The general solution for the Bragg case is given by:

$$I(z) = e^{-\frac{qz}{t}}\frac{r\cosh\left(r\left(1-\frac{z}{t}\right)\right) + p\sinh\left(r\left(1-\frac{z}{t}\right)\right)}{r\cosh(r) + p\sinh(r)}, \tag{2.65a}$$

$$I'(z) = e^{-\frac{qz}{t}}\frac{b\sinh\left(r\left(1-\frac{z}{t}\right)\right)}{r\cosh(r) + p\sinh(r)}. \tag{2.65b}$$

Reflectivity R and transmissivity T are therefore given by:

$$R_{\text{Bragg}} = \frac{b}{r\coth(r) + p}, \tag{2.66a}$$

$$T_{\text{Bragg}} = \frac{re^{-q}}{r\cosh(r) + p\sinh(r)}. \tag{2.66b}$$

Some special cases to these general solutions after [58] are presented in the following.

No Bragg Reflection

The first special case is the absence of a Bragg reflection, which is expressed by setting $\sigma = 0$. Consequently, the solutions for both Bragg- and Laue case simplify to Equation 2.67, which is identical to the Lambert-Beer law as presented in Equation 2.5.

$$R = 0, \tag{2.67a}$$

$$T = e^{-a} = e^{-\mu d}, \tag{2.67b}$$

$$A = 1 - T = 1 - e^{-\mu d} \tag{2.67c}$$

Symmetric Reflection Cases

The second special case occurs when the reflection is considered to be symmetrical. This means that $\varphi = \varphi'$ and therefore $\zeta = 1$. In the Laue case, this condition is met when the reflecting planes are perpendicular to the crystal's surface. In this case, reflectivity and transmissivity reduce to:

$$R = \frac{1}{2}e^{-a}\left(1 - e^{-2b}\right), \tag{2.68a}$$

$$T = \frac{1}{2}e^{-a}\left(1 + e^{-2b}\right). \tag{2.68b}$$

Therefore, $R + T = e^{-a}$ and consequently $A = 1 - (R + T) = 1 - e^{-a}$. Thus, the absorptivity in the symmetric Laue case is not influenced by the strength of a Bragg reflection [58].

In the Bragg case, a symmetric configuration occurs when the crystal planes are parallel to the crystal's surface. Here, reflectivity and transmissivity simplify to:

$$R = \frac{b}{\sqrt{a(a+2b)}\cosh(\sqrt{a(a+2b)}) + (a+b)}, \tag{2.69a}$$

$$T = \frac{\sqrt{a(a+2b)}}{\sqrt{a(a+2b)}\cosh(\sqrt{a(a+2b)}) + (a+b)\sinh(\sqrt{a(a+2b)})}. \tag{2.69b}$$

In this case, $R + T \neq e^{-a}$ and therefore $A \neq 1 - e^{-a}$. In contrast to the symmetric Laue reflection, the strength of a Bragg reflection in a symmetric Bragg case changes the absorptivity of the crystal [58]. This phenomenon is referred to as anomalous absorption.

In perfect crystals, the anomalous absorption originates from the Borrmann effect, which results from the formation of standing wavefields inside the crystal under dynamical diffraction conditions. Depending on the spatial distribution of the wavefield relative to the atomic planes, the Borrmann effect can lead to a strong reduction of the effective photoabsorption [54]. It can be recovered from the solution of the Takagi-Taupin equations for perfect crystals [54, 62–64].

For mosaic crystals, which are introduced in Chapter 2.4.6, the Darwin-Hamilton solution is sufficient as will be discussed in Section 2.4.10. In this class of crystals, long-range coherence is supressed by the misorientation of individual crystallites. Here, the anomalous absorption emerges from the Darwin-Hamilton formalism as described above. It is inherent to the nature of the Darwin equations [58]. The modified absorptivity then results from the coupled intensity transport between the incident and Bragg-reflected waves rather than from interference of the coherent wavefield.

Inserting Equation 2.62b into the solutions for the symmetric cases yields the reflectivities for the symmetric Lause and Bragg cases:

$$R_{\text{sym. Laue}} = \frac{1}{2}\left(1 - e^{-2\sigma\frac{t}{\sin\varphi}}\right)e^{-\mu\frac{t}{\sin\varphi}} \qquad \text{symmetric Laue case,} \tag{2.70a}$$

$$R_{\text{sym. Bragg}} = \frac{\sigma}{\sqrt{\mu(\mu+2\sigma)}\coth(\frac{t}{\sin\varphi}\sqrt{\mu(\mu+2\sigma)}) + (\mu+\sigma)} \qquad \text{symmetric Bragg case.} \tag{2.70b}$$

The reflectivity equations show, that the symmetric Bragg case reflectivity has a theoretical upper limit of $R_{\text{sym. Bragg}} < 1$. In contrast, the symmetric Laue case reflectivity has a theoretical upper limit of $R_{\text{sym. Laue}} < 0.5$.

Another key difference between both cases is the existence of a thickness t_{best} for maximum reflectivity in the Laue geometry, as can be derived from Equation 2.70a. With increasing thickness, the reflected intensity increases. At the same time, however, the absorptivity also increases. These two effects compete with each other, leading to the existence of an optimal reflectivity. For the symmetric Laue case, the thickness t_{best} that maximizes R is given by Equation 2.71.

$$t_{\text{best}} = \frac{\sin\varphi}{2\sigma} \ln\left(1 + \frac{2\sigma}{\mu}\right) \tag{2.71}$$

Conversely, an increase in thickness in the Bragg case results in an enhanced total reflectivity. However, the share of a layer in the total reflectivity decreases with the depth of the layer, as the incident beam intensity to deeper layers is already attenuated by the layers above. Tthis leads to a saturation of the reflectivity when the crystal thickness increases, as illsutrated by Figure 2.8.

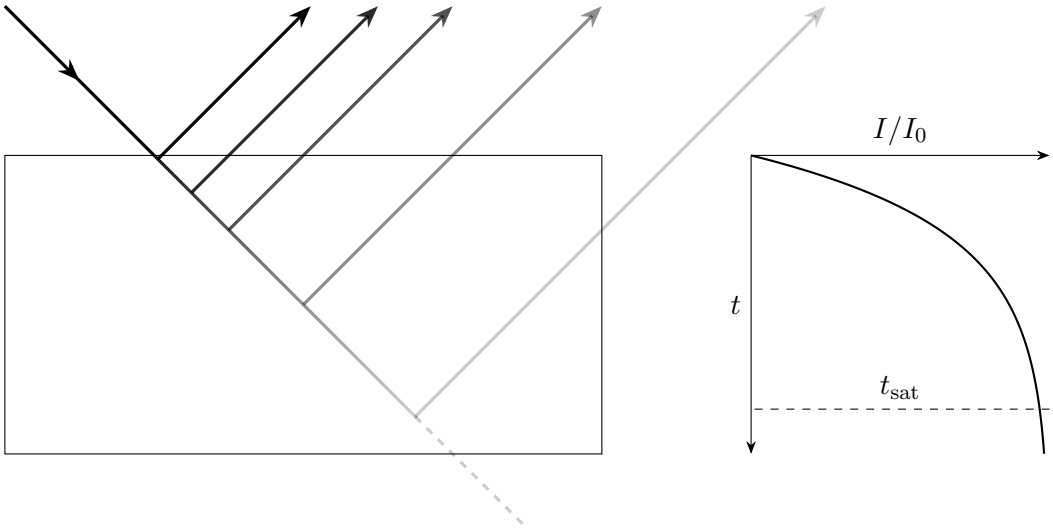


Figure 2.8: Decreasing share of the total reflecitivity for individual reflections at increasing depth t and overall reflectivity as a function of crystal thickness for a symmetric Bragg reflection case. The reflectivity saturates around t_{sat}.

The saturation thickness can be derived to Equation 2.72, where r is the value share of the maximum reflectivity. This is done to avoid overestimation due to the flattening of the

$R(t)$ curve. Consequently, $R = r \cdot R_{\max}$ is reached for a crystal of thickness t_{sat} under the assumptions of a symmetric reflection case and consistent values of μ and σ.

$$t_{\text{sat}} = \frac{\sin\varphi}{2q} \ln\left(\frac{(p+q) - r(p-q)}{(1-r)(p+q)}\right) \tag{2.72}$$

$$\text{with} \quad p = \mu + \sigma, \quad q = \sqrt{\mu(\mu + 2\sigma)}, \quad r = 0.9$$

Values for realistic XFI scenarios and the used crystals are below $t = 1\,\text{mm}$. Note that for relevant Bragg angles of well under $\theta_B = 10°$, the actual path length in a symmetric reflection $2d = \frac{2t}{\sin\theta_B}$ of a beam reflected after penetrating through a path of length d that is much larger than the crystal thickness t. This formula also applies to mosaic crystals, which are introduced in Chapter 2.4.6.

This chapter demonstrated that Bragg reflectivity depends on the principal geometry of the reflection, the absorptivity of the crystal material μ, and the cross-section per unit volume of the Bragg reflection σ. The following chapter focuses on calculating the latter value.

2.4.4 Bragg Scattering Cross-Section

To calculate σ following the Darwin-Hamilton approach, the crystal is modeled as being composed of many small perfect crystals, commonly referred to as crystallites [22].
For now, the crystallites are assumed to be perfectly aligned with the crystal surface, with no gaps in between. Therefore, the overall Bragg reflection can be described as the sum of only the symmetric Bragg reflections from these small crystallites.
To represent the general Bragg and Laue cases, the angles φ and φ' in Figure 2.7 are arbitrary within the described limits. The following derivation in Section 2.4.4 is based on Warren [45] and Zachariasen [49, 59].

Integral Reflectivity of a Small Perfect Crystal

To model the Bragg reflection of a small crystallite of a thickness t_0, the kinematic approximation is employed [59]. In this approximation, dynamical extinction effects are neglected, which is reasonable for small crystallites, with a thickness below their extinction length. Multiple scattering events within the crystallite are also neglected. Both assumptions are discussed further in Section 2.4.8. In the kinematic approximation applied for now, extinction and absorption effects, described by σ and μ, are not considered for individual crystallites, only in the entirety of crystallites forming the total crystal.

The equation system 2.60 is modeled by a zero-order approximation [59]. In the case of symmetric Bragg reflection, it therefore simplifies to 2.73.

$$\frac{\partial I(z)}{\partial z} \approx 0 \tag{2.73a}$$

$$\frac{\partial I'(z)}{\partial z} \approx \frac{\sigma}{\sin\varphi} I(z) \tag{2.73b}$$

The solutions are given by Equations 2.74a and 2.74b. Consequently, the reflectivity is given by Equation 2.74c.

$$I \approx I_0 \tag{2.74a}$$

$$I' \approx \sigma \frac{t_0}{\sin\varphi} I_0 \tag{2.74b}$$

$$R = \frac{I'}{I} \approx \sigma \frac{t_0}{\sin\varphi} \tag{2.74c}$$

Figure 2.9 illustrates the vectors, angles, etc., that will be used in the following derivation of the integral reflectivity of a small crystallite. It shows a symmetric Bragg reflection ($\varphi = \varphi'$), which maximizes the reflectivity.

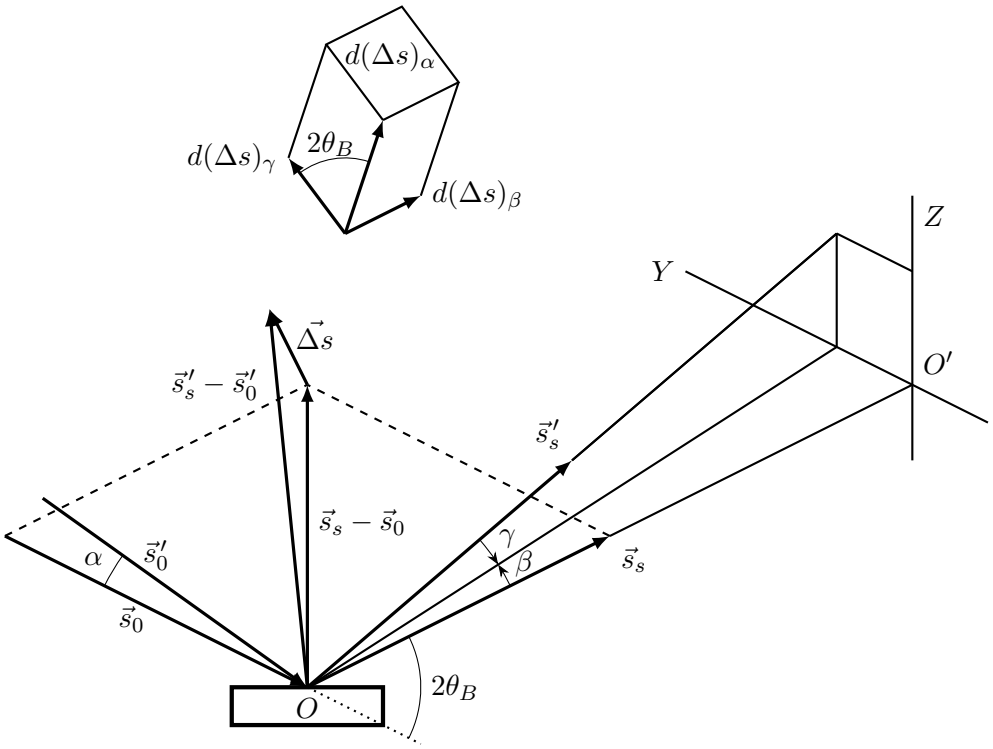


Figure 2.9: Bragg reflection by a small crystallite, adapted from [45, Figure 4.1]. A small variation in the angle of incidence at O, characterized by α, leads to a deviation in the Bragg reflection, characterized by γ. A variation by the azimuthal angle β merely results in a horizontal shift of the image point O'.

Therefore, the incident beam $\vec{s}_0$ meets the reflecting plane at the incidence point O exactly at θ_B, as defined by Equation 2.58. Consequently, the beam is reflected torwards $\vec{s}_s$ at a reflection angle of exactly $2\theta_B$ with respect to the incident beam. An imaginary detector

is placed in the distance R to the reflection point O. The point O is imaged to the point O' there.

As described in Section 2.4.2, a small deviation of the incidence angle from the reflectivity-maximizing Bragg angle, as for $\vec{s}_0'$, still leads to a reflection in the direction $\vec{s}_s'$, caused by an underlying diffraction. However, the resulting intensity will be smaller than for an incidence onto O at the exact Bragg angle.
To quantify the deviations from the ideal case, two angles are defined. In the paper plane, the difference between vectors $\vec{s}_0$ and $\vec{s}_0'$ is given by α. This difference causes a deviation between the respective reflection vectors $\vec{s}_s$ and $\vec{s}_s'$ which defines a second angle γ. The variation of direction in the vertical plane pointing into the paper is defined by β. Since the Bragg reflection can be modeled as a reflection at a plane, a variation of β only alters the position of O and, consequently, O'. However, the reflectivity as well as γ are invariant under the variation of the azimuthal angle β. Consequently, the reflection is also invariant under the rotation around the normal of the crystal plane.

β and γ span a plane at the imaginary detector at distance R. As described in Section 2.4.2, a Bragg reflection is only possible within the Darwin width, so for very small variations of α. Values for the Darwin width range from a fraction of an arcsecond up to tens of arcseconds.[5] Higher wavelengths and higher values of the structure factor increase the Darwin width [65].
Without applying instrumental resolution corrections, a rocking curve measurement of a perfect crystal, as outlined in Section 2.4.2, requires the divergence of an incident beam to be much smaller than the Darwin width [45]. Furthermore, crystals typically exhibit impurities or crystal defects, resulting, e.g., from their growth process [47], which alter the alignment of the reflecting crystal planes. Additionally, scattering broadens the beams. Therefore, a diffraction maximum will always have a certain width, which is further amplified by possible secondary reflections. In conclusion, the reflectivity of a crystal for exact values of α, β and γ is experimentally inaccessible. It can only be accessed as an integrated value. According to Warren, it is reasonable to calculate σ using the total power of the Bragg-reflected beam $\bar{P}$[45].
$\bar{P}$ can be obtained by integrating Equation 2.49 over α, β and γ:

$$\bar{P} = \iiint I(\vec{s}_s' - \vec{s}_0')\, d\alpha\, d\beta\, d\gamma. \tag{2.75}$$

As an alternative to using α, β and γ, a quantity $\Delta\vec{s}$ can be introduced to describe the deviation from a perfect Bragg reflection via Equation 2.76. In order to describe a Bragg

[5] One arcsecond is equivalent to $\frac{1}{3600}$ degree. Therefore, Darwin widths lie within the typical angular range of 10^{-5} to 10^{-3} degrees.

reflection as derived in Section 2.4.1, $\frac{\vec{s}_s - \vec{s}_0}{\lambda}$ must be equal to a reciprocal lattice vector $\vec{G}_{hkl}$:

$$\vec{s}'_s - \vec{s}'_0 = \vec{s}_s - \vec{s}_0 + \Delta\vec{s} = \lambda\vec{G}_{hkl} + \Delta\vec{s}. \tag{2.76}$$

Equation 2.42 showed, how the factor $I_l(\vec{s}'_s - \vec{s}'_0)$ determines the occurrence of a Bragg reflection. Since the three factors are similar for all directions, it is sufficient to first evaluate only direction $\vec{a}$. The Laue conditions 2.54 imply that $\frac{\pi}{\lambda}\lambda\vec{G}_{hkl} \cdot \vec{a} = h\pi$, where h is an integer. This simplifies Equation 2.77.

$$\frac{\sin^2\left(\frac{\pi}{\lambda}\left(\lambda\vec{G}_{hkl} + \Delta\vec{s}\right) \cdot N_1\vec{a}\right)}{\sin^2\left(\frac{\pi}{\lambda}\left(\lambda\vec{G}_{hkl} + \Delta\vec{s}\right) \cdot \vec{a}\right)} = \frac{\sin^2\left(\frac{\pi}{\lambda}\left(\Delta\vec{s}\right) \cdot N_1\vec{a}\right)}{\sin^2\left(\frac{\pi}{\lambda}\left(\Delta\vec{s}\right) \cdot \vec{a}\right)} \tag{2.77}$$

$\Delta\vec{s}$ is now expressed in reciprocal space as $\Delta\vec{s} = \lambda\left(p_1\vec{a}^* + p_2\vec{b}^* + p_3\vec{c}^*\right)$. The coefficients p_i represent the deviation of $\vec{\Delta s}$ from a point in reciprocal space that allows for Bragg reflection. Consequently, p_i must be small for reflection to be possible. Using the identities of the reciprocal lattice shown in 2.51 and 2.52, this yields:

$$\frac{\sin^2\left(\frac{\pi}{\lambda}\left(\Delta\vec{s}\right) \cdot N_1\vec{a}\right)}{\sin^2\left(\frac{\pi}{\lambda}\left(\Delta\vec{s}\right) \cdot \vec{a}\right)} = \frac{\sin^2\left(\frac{\pi}{\lambda}\left(\lambda\left(p_1\vec{a}^* + p_2\vec{b}^* + p_3\vec{c}^*\right)\right) \cdot N_1\vec{a}\right)}{\sin^2\left(\frac{\pi}{\lambda}\left(\lambda\left(p_1\vec{a}^* + p_2\vec{b}^* + p_3\vec{c}^*\right)\right) \cdot \vec{a}\right)} = \frac{\sin^2\left(\pi N_1 p_1\right)}{\sin^2\left(\pi p_1\right)}. \tag{2.78}$$

The same simplification can be done analogously for the other two directions $\vec{b}$ and $\vec{c}$. Combining the results of Equations 2.78, 2.49 and 2.75 this results in Equation 2.79. Note that I_e and F_{hkl} are independent of α, β or γ.

$$\bar{P} = R^2 I_e \left|F_{hkl}\right|^2 \iiint I(\vec{s}'_s - \vec{s}'_0)\frac{\sin^2\left(\pi N_1 p_1\right)}{\sin^2\left(\pi p_1\right)}\frac{\sin^2\left(\pi N_2 p_2\right)}{\sin^2\left(\pi p_2\right)}\frac{\sin^2\left(\pi N_3 p_3\right)}{\sin^2\left(\pi p_3\right)}\, d\alpha\, d\beta\, d\gamma \tag{2.79}$$

As shown in Figure 2.9, varying α, β and γ, varies $\Delta\vec{s}$. Therefore, the integration variables can be transformed to the components of $\Delta\vec{s}$ as follows:

$$\left|d(\Delta\vec{s})_\alpha\right| = d\alpha \quad \left|d(\Delta\vec{s})_\beta\right| = d\beta \quad \left|d(\Delta\vec{s})_\gamma\right| = d\gamma. \tag{2.80}$$

This defines a volume element:

$$dV = d(\Delta\vec{s})_\beta \cdot d(\Delta\vec{s})_\gamma \times d(\Delta\vec{s})_\alpha = \sin\left(2\theta_B\right)\, d\alpha\, d\beta\, d\gamma. \tag{2.81}$$

Figure 2.9 illustrates the volume element. Substituting Equation 2.81 into Equation 2.79 yields:

$$\bar{P} = R^2 I_e \left|F_{hkl}\right|^2 \frac{1}{\sin(2\theta_B)} \int_V I(\vec{s}'_s - \vec{s}'_0)\frac{\sin^2\left(\pi N_1 p_1\right)}{\sin^2\left(\pi p_1\right)}\frac{\sin^2\left(\pi N_2 p_2\right)}{\sin^2\left(\pi p_2\right)}\frac{\sin^2\left(\pi N_3 p_3\right)}{\sin^2\left(\pi p_3\right)} dV. \tag{2.82}$$

Using the definition of $\Delta\vec{s}$ in reciprocal space, dV can be expressed as follows:

$$dV = d(\Delta\vec{s})_\beta \cdot d(\Delta\vec{s})_\gamma \times d(\Delta\vec{s})_\alpha = (\lambda\vec{a}^* dp_1) \cdot \left(\lambda\vec{b}^* dp_2\right) \times (\lambda\vec{c}^* dp_3)\,. \tag{2.83}$$

$\vec{a}^*$, $\vec{b}^*$ and $\vec{c}^*$ are the reciprocal unit cell vectors. The volume of the reciprocal unit cell is given by the scalar triple product of these vectors. Using the definition of the reciprocal space, this can also be expressed as the inverse of the real space unit cell volume V [56]:

$$\vec{a}^* \cdot \left(\vec{b}^* \times \vec{c}^*\right) = V_{\text{rec}} = \frac{1}{V}. \tag{2.84}$$

Substituted into expression 2.83, it reduces to $dV = \frac{\lambda^3}{V} dp_1 dp_2 dp_3$.
As discussed above, p_1, p_2 and p_3 have to be small for a Bragg reflection to be possible. Therefore, the small angle approximation is applicable to the denominators in Equation 2.82, which gives expression 2.85 for the integrated power.

$$\begin{aligned}\bar{P} =& R^2 I_e \left|F_{hkl}\right|^2 \frac{\lambda^3}{V} \frac{1}{\sin(2\theta_B)} \\ & \iiint_{-\infty}^{\infty} I(\vec{s}_s' - \vec{s}_0') \frac{\sin^2(\pi N_1 p_1)}{(\pi p_1)^2} \frac{\sin^2(\pi N_2 p_2)}{(\pi p_2)^2} \frac{\sin^2(\pi N_3 p_3)}{(\pi p_3)^2}\, dp_1\, dp_2\, dp_3 \\ =& R^2 I_e \left|F_{hkl}\right|^2 \frac{\lambda^3}{V} \frac{1}{\sin(2\theta_B)} N\end{aligned} \tag{2.85}$$

$N = N_1 N_2 N_3$ is the total number of unit cells involved in the Bragg reflection process. Therefore, NV can be replaced with $NV = \delta V$, where δV is the total volume of a small crystallite hit by the beam. Using the expression 2.24 for I_e, this results in:

$$\bar{P} = I_0 \frac{r_e^2}{V^2} \left|F_{hkl}\right|^2 \lambda^3 \frac{1 + \cos^2(2\theta_B)}{2\sin(2\theta_B)} \delta V. \tag{2.86}$$

Equation 2.86 represents the reflecting power of the small crystallite. The Bragg-reflected intensity can then be calculated using Equation 2.87 by further defining the volume element δV.

$$\bar{I} = \frac{\bar{P}}{\delta A} = I_0 \frac{r_e^2}{V^2} \left|F_{hkl}\right|^2 \lambda^3 \frac{1 + \cos^2(2\theta_B)}{2\sin(2\theta_B)} \frac{\delta V}{\delta A} = I_0 \frac{r_e^2}{V^2} \left|F_{hkl}\right|^2 \lambda^3 \frac{1 + \cos^2(2\theta_B)}{2\sin(2\theta_B)} \frac{t_0}{\sin\varphi} \tag{2.87}$$

δA is the cross-sectional area perpendicular to the direction of the beam. $\frac{t_0}{\sin\varphi}$ is the path length through the crystallite, where t_0 is the crystallite's thickness. t_0 is assumed to be constant over the entire beam cross-sectional area δA, which corresponds to a parallelepiped-shaped crystallite.
It also means that the number of planes traversed by the beam is constant over δA. Due to its small size, extinction and coupling effects inside one crystallite are negligible. Most of the beam will pass through a single crystallite without interaction.

The preceding remarks are combined in expression 2.88 for the reflectivity of the crystallite at the considered plane set $R_{hkl} = \frac{\bar{I}}{I_0}$.

$$R_{hkl} = \frac{\bar{I}}{I_0} = \frac{r_e^2}{V^2} |F_{hkl}|^2 \lambda^3 \frac{1 + \cos^2(2\theta_B)}{2\sin(2\theta_B)} \frac{t_0}{\sin\varphi} \tag{2.88}$$

Comparing 2.88 and 2.74c reveals that for a single crystallite, σ is given by the Bragg-reflected power per unit volume and intensity, as expressed in Equation 2.89.

$$Q = r_e^2 \left| \frac{F_{hkl}}{V} \right|^2 \lambda^3 \frac{1 + \cos^2(2\theta_B)}{2\sin(2\theta_B)} \tag{2.89}$$

This value is referred to as the Q-value in kinematical diffraction theory. It can be calculated using tabulated quantities and values that are determined by the involved $\{hkl\}$ planes at a known wavelength λ [58]. Apart from the wavelength, the Q factor only contains values defined by the nature of a crystal and the set of involved crystal planes.
Note again that the shape of the crystallite was modeled to correspond to the symmetric Bragg case. Therefore, the path length through the crystallite is given by $\frac{t_0}{\sin\varphi} = \frac{t_0}{\sin\theta_B}$.

In total, the reflectivity of the small crystallite is given by:

$$R_{hkl} = Q \frac{t_0}{\sin\theta_B}. \tag{2.90}$$

For a perfect crystal, its reflectivity in the kinematic approximation is therefore given by inserting $\sigma = Q$ into Equation 2.64 and Equation 2.66, respectively.

Darwin Width

As discussed in Chapter 2.4.2, the reflectivity curve of a perfect crystal is generally not accessible by experiment. Several theories provide calculated estimates of the width of the diffraction profile of a perfect crystal [54].
A common model is the Darwin width, which was introduced by Sir Charles Galton Darwin in [60, 61]. It neglects the effects of extinction within a crystal. According to the model, the reflected intensity has a near-constant value over a width of ω_D around the exact Bragg angle. ω_D is the previously introduced Darwin width. It is defined by:

$$\omega_D = \frac{2r_e |F_{hkl}| \lambda^2}{\pi V \sin(2\theta_B)}, \tag{2.91}$$

where V denotes the volume of a single unit cell [22].

2.4.5 Bragg Reflection of Incoherent X-rays

Up to this point, all considerations have implicitly assumed coherent superposition of scattering amplitudes within a perfect crystal domain or crystallite. For instance, the considerations in 2.4.2 imply the need for coherency between the interacting beams. However, X-ray diffraction can also be observed when using incoherent sources, such as X-ray tubes. The reasons lie in the phenomena of self-coherence and local coherence, which are briefly introduced in the following section after [22].

Although the radiation of a thermal X-ray source is incoherent in its entirety, each wave packet or beam[6] that is emitted by an X-ray tube, for example, is coherent with itself over its coherence length. Therefore, scattering amplitudes originating from different sites within a volume, defined by the coherence length of a wave packet, can interfere.

From a quantum mechanical perspective, diffraction is the result of the superposition of probability amplitudes corresponding to all possible scattering paths. Every interaction can be regarded as a partial wave. The measured intensity at a given position is determined by the interference of these amplitudes [67]. Consequently, a wave packet that propagates along a direction that fulfills the Bragg or Laue conditions has a higher probability of detection than one propagation along other directions.

The spatial distances between atomic lattice planes are only a few Ångström, typically below 5 Å, leading to very small path distances under ≈ 1 Å between rays scattered by neighboring planes. The longitudinal coherence length of X-rays from an X-ray tube is in the nanometer range, which exceeds the path distances by orders of magnitude. For example, the tungsten K_α, $E \approx 60\,\mathrm{keV}$, which will be relevant later, has a spectral width of about $\Delta E \approx 40\,\mathrm{eV}$ [68]. Its longitudinal coherence length therefore is [27]:

$$L_c = \frac{\lambda^2}{\Delta\lambda} \approx \frac{hc}{\Delta E} \approx 30\,\mathrm{nm}, \tag{2.92}$$

where h denotes Planck's constant and c is the speed of light.
Consequently, the partial waves scattered by neighboring lattice planes remain mutually phase coherent within a wave packet. Despite the lack of coherence between different wave packets, constructive and destructive interference can still occur.
As the X-ray tube emits the wave packets with disordered phase, the intensities originating from independent emission events are ultimately superimposed on the detector [22]. Nevertheless, the maxima always occur at the same angles, which are determined by the underlying crystal's lattice geometry and the wave packets' wavelengths. Each wave

[6] Both terms wave packet and beam are common in literature in this context.

packet contributes intensity preferentially at these angles. Even when averaging over many incoherent emissions, an increased intensity accumulates at the Bragg angles. The reverse is true for diffraction minima.

Pathways that follow different directions or types of scattering contribute to the background scattering in the form of, e.g., diffuse scattering..

2.4.6 Bragg Reflection by Mosaic Crystals

Until now, the reflecting crystal was considered defect-free. Even the definition of crystallites was established for the derivation of the kinematic theory. In such a case, the long-distance order is represented by Equation 2.39.

The following chapter will demonstrate how crystal defects can affect the reflection properties of a crystal. It will be explained how these defects can be modeled and utilized for optics.

Mosaic Crystal Model

A common model to describe certain ordered crystal defects is the mosaic crystal model, which was introduced by Darwin in 1922 [22, 70]. This model employs the same definition of crystallites used in the derivation in Chapter 2.4.4. In conclusion, a crystallite is a small, perfect crystal, modeled in the shape of a parallelepiped with a thickness t_0.

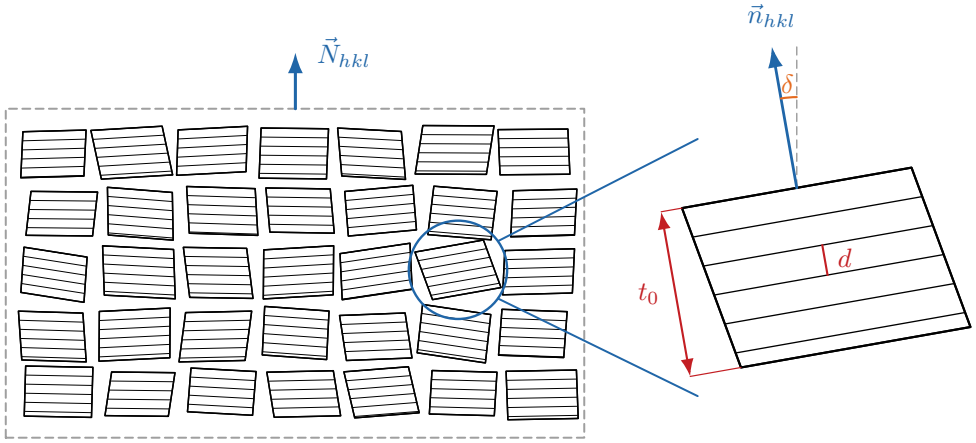


Figure 2.10: Mosaic crystal model (symmetric case), according to Darwin [70], showing individual parallelepiped-shaped crystallites of thickness t_0. The crystallites exhibit a tilt δ of their normal $\vec{n}_{hkl}$ with respect to the mean direction $\vec{N}_{hkl}$, indicated by the blue arrows. The lattice spacing d of the reflecting plane set is illustrated in red.

Unlike the explanations in Section 2.4.4, the mosaic crystal model assumes that the individual crystallites are slightly tilted relative to each other and have slightly different

shapes. Figure 2.10 shows an illustration of the mosaic crystal model. It is also referred to as the "perfectly imperfect" crystal model [45].
Figure 2.10 shows the crystallites inside a large crystal, which is outlined by the dashed rectangle. Note that, for reasons of clarity, the crystallites are drawn relatively large. Included in the crystallite drawings are lines representing an exemplary lattice plane set. According to the definition of crystallites as perfect crystals, all plane distances are equidistant. Again, for clarity, the distances are drawn large. Also illustrated is the exemplary crystallite thickness t_0 of one of the crystallites, measured along $\vec{n}_{hkl}$. The crystallite plane normals $\vec{n}_{hkl}$ are slightly tilted with respect to the mean normal $\vec{N}_{hkl}$. This tilt follows a Gaussian or Lorentzian distribution, as will be discussed in Section 2.4.6. The mean normal direction $\vec{N}_{hkl}$ of all crystallites in the illustration matches the surface normal of the overall crystal. This makes the drawn case a symmetric Bragg case (see Section 2.4.3). Further explanations also assume this symmetric case.

A single crystallite is defined by:

- its postion with respect to an arbitrary origin R_j.
- its tilt δ with respect to $\vec{N}_{hkl}$.
- its size, which is mainly decisive in the direction of the Bragg-reflected beam. In the symmetric case, it is modeled as the crystallite thickness $\overline{t_0}$

Crystallite Distribution

As previously mentioned, the individual crystallites are assumed to have a small, random tilt δ. Since they are assumed to be very small compared to a whole crystal, the mosaic crystal model assumes a discrete, continuous distribution function $W(\delta)$ of this tilt. The azimuthal angle of rotation of the individual crystallites is uniformly distributed. The mosaicity distribution $W(\delta)$ is assumed to have cylindrical symmetry [49]. That implies $W(\delta) = W(-\delta)$ and a uniform distribution in the azimuthal angle.

To represent a probability density, the distribution is naturally normalized:

$$\int W(\delta)\, d\delta = 1. \tag{2.93}$$

Depending on the crystal, $W(\delta)$ follows either a Lorentzian (Equation 2.94a) or Gaussian (Equation 2.94b) distribution [54, 71].

$$W(\delta) = \frac{1}{\pi} \frac{\frac{\beta}{2}}{\left(\frac{\beta}{2}\right)^2 + \delta^2} \qquad \text{Lorentzian distribution} \tag{2.94a}$$

$$W(\delta) = \frac{1}{\sqrt{2\pi}\,\eta} e^{-\frac{\delta^2}{2\eta^2}}, \qquad \eta = \frac{\beta}{2\sqrt{2\ln 2}} \qquad \text{Gaussian distribution} \tag{2.94b}$$

The crystal's individual disribution $W(\delta)$ is referred to as its mosaicity. Since the distributions are normalized, the mosaicity of a crystal is often described using the full width at half maximum (FWHM) of $W(\delta)$. In this context this value is referred to as the mosaic spread β [54].

Reflectivity of Mosaic Crystals

In the following, the reflectivity of a mosaic crystal is derived, based on [49].

Consider a perfect crystal and a mosaic crystal with a mosaic spread of β. In the used model, the perfect crystal can be modeled as having a mosaic spread of $\beta = 0$.
If a monochromatic, non-divergent, beam is incident on a perfect crystal at an angle φ, as shown in Figure 2.7, its incident angle onto the individual crystallites would only further depend on the angle between the crystal plane set's normal and the crystal normal. In a symmetric case, where surface and reflecting plane normals align perfectly, every crystallite would be met at the exact same angle φ.
If the case is not symmetric, the tilt of the planes normal ϕ would add to φ to form the crystallite incidence angle $\varphi_{\text{crystallite}}$. Following the previous derivation, the incident beam could then only be reflected by the crystallite if $\varphi_{\text{crystallite}}$ lies within the small margin of the Darwin width around the Bragg angle $\varphi_{\text{crystallite}} = \theta_B \pm \omega_D$ for the specific plane set and energy.

The same holds true if the beam is incident onto a mosaic crystal with $\beta \neq 0$. However, to determine the incident angle onto a crystallite $\varphi_{\text{crystallite}}$, its individual tilt δ must be taken into account. Consequently, not every crystallite, nor its reflecting plane set, is met at the same angle $\varphi_{\text{crystallite}}$. Again, only crystallites met at $\varphi_{\text{crystallite}} = \theta_B \pm \omega_D$ can be reflected.

Consider symmetrical cases for the perfect and the mosaic crystal. The planes of the perfect crystal and the mean crystallite normal of the mosaic crystal both align with the respective surface normal, which is met at an angle of exactly $\phi = \theta_B$. Only the mosaic crystal's crystallites with $\delta = 0 \pm \omega_D$ could reflect the beam. In the perfect crystal, the crystallites are all properly aligned and can contribute to the overall reflection, which allows for higher reflectivity.
If the crystals are met by beams with a certain divergence and/or energy bandwidth, only those with the right relation between energy and incidence can be reflected. However, the mosaic crystal can reflect a beam as long as it is incident on a crystallite tilted appropriately to its energy – incidence angle relationship. The perfect crystal can only reflect specific beams that fulfill the Bragg condition.

Consequently, the integral reflecting power of a mosaic crystal $\overline{P}_{\text{mos}}$, is higher than that of a perfect crystal when both are met by a divergent incidence and/or a certain energy bandwidth. Note that values for β are typically much greater than the Darwin width. Therefore, the latter one can usually be neglected for mosaic crystals. The reflecting power of a single hit crystallite is given by $\frac{I'}{I_0}\left(\varphi_{\text{crystallite}} - \theta_B\right)$. Note that the argument value of $\frac{I'}{I_0}$ corresponds to the deviation from the Bragg angle. Therefore, the reflection from a single crystallite is maximal when $\varphi_{\text{crystallite}} - \theta_B = 0$.
As explained above, in a symmetric case, the incident angle onto a crystallite can be expressed by $\varphi_{\text{crystallite}} = \overline{\varphi}_{\text{crystallite}} + \delta$, where $\overline{\varphi}_{\text{crystallite}}$ is the mean incident angle onto the crystallite.

Consequently, the reflecting power of all crystallites is given by:

$$\overline{P_{\text{mos}}} = \int W(\delta) \cdot \frac{I'}{I_0}\left(\overline{\varphi}_{\text{crystallite}} - \theta_B + \delta\right) d\delta. \tag{2.95}$$

As mentioned above, the mosaic spread of a mosaic crystal is usually much greater than its Darwin width. Therefore, $W(\delta)$ can be assumed to be constant over the angular range of δ for which $\frac{I'}{I_0}\left(\overline{\varphi}_{\text{crystallite}} - \theta_B + \delta\right) \neq 0$. Thus, the integral is dominated by values of $\delta = \theta_B - \overline{\varphi}_{\text{crystallite}}$. Therefore, the mosaic distribution $W(\delta)$ can be evaluated at $\delta = \theta_B - \overline{\varphi}_{\text{crystallite}}$ outside the integral:

$$\begin{aligned}\int W(\delta) \cdot \frac{I'}{I_0}\left(\overline{\varphi}_{\text{crystallite}} - \theta_B + \delta\right) d\delta &\approx W(\theta_B - \overline{\varphi}_{\text{crystallite}}) \int \frac{I'}{I_0}\left(\overline{\varphi}_{\text{crystallite}} - \theta_B + \delta\right) d\delta \\ &= W(\theta_B - \overline{\varphi}_{\text{crystallite}}) R_{hkl}.\end{aligned} \tag{2.96}$$

Consequently, the reflecting power of a thin crystal layer σdt can be expressed as:

$$\sigma dt = W(\delta) \frac{R_{hkl}}{\frac{t_0}{\sin \varphi_{\text{crystallite}}}}. \tag{2.97}$$

Assume the reflectivity optimum where $\varphi_{\text{crystallite}} = \theta_B$, with R_{hkl} given by Equation 2.90, and assume that Q and W are independent of depth. For a non-divergent beam this condition is fulfilled by crystallite tilted by δ. Therefore, 2.97 simplifies to:

$$\sigma = W(\delta) Q. \tag{2.98}$$

Note again, that $\delta = \theta_B - \overline{\varphi}_{\text{crystallite}}$ and Q is given by Equation 2.89, which shows again that the integrated reflectivity of a mosaic crystal over a range of incident angles is much higher than that of a perfect crystal. At the same time, its peak reflectivity, meaning the reflectivity at the exact the Bragg angle, is lower compared to a perfect crystal, as

less of the crystallites are oriented in a way that allows them to contribute to the overall reflection.
For the same reasons, the reflectivity as a function of the incident angle $R(\theta)$ depends on the mosaic spread β. As mentioned before, the corresponding curve $R(\theta)$ is referred to as the rocking curve. Its experimental determination is discussed in Chapter 7.1.

The same correlations can be used to discuss polychromatic incidence, as will be demonstrated in Chapter 3. For now, incident beams continue to be assumed monochromatic. Additionally, mosaicity leads to a number of imaging effects that are utilized in X-ray optics. These effects will also be discussed in Chapter 3.

2.4.7 Justification and Limitations of the Mosaic Crystal Model

Until now, it was assumed that a single crystallite is so small that the extinction effects within it are negligible. The derivations for Q and σ, 2.89 and 2.98, also followed this assumption. Therefore, the reflectivity was derived using a zero-order (kinematic) approximation, which corresponds to Darwin's model of an ideally imperfect crystal [45].

Depending on the overall thickness of the mosaic crystal and the size of the crystallites, the extinction within a crystallite due to diffraction is actually not negligible [45].
In the dynamical approach, the extinction length Λ_{ext} is defined as the depth within a perfect crystal at which the intensity of the incident beam is attenuated to $\frac{1}{e}$ of its original value due to dynamical diffraction. Following the remarks in [22] it is given by:

$$\Lambda_{\text{ext}} = \frac{1}{4}\left(\frac{m}{d}\right)\frac{v_c}{r_e|F|} \tag{2.99}$$

for the exact Bragg condition, where m is the order of reflection, d is the lattice plane spacing, v_c is the unit cell volume, r_e is the classical electron radius and F is the structure factor.
In the mosaic crystal model, this is accounted for by the introduction of two types of extinction, which are described in the following Section 2.4.8.

Most real-world crystals are imperfect. However, the mosaic crystal model is an oversimplification describing ideally imperfect crystals. Real crystals may contain defects caused by inhomogeneous strains or dislocations in the lattice, even without physical subdivision into individual crystallites. Nevertheless, the mosaic crystal model is widely used to describe imperfect crystals because it lends itself well to mathematical analysis [45]. Despite its simplifying assumptions, it remains the standard approach in simulating imperfect crystals, for example in well-established simulation codes like SHADOW/XOP [72, 73] by the Euro-

pean Synchrotron Radiation Facility (ESRF). A selection of simulation codes is presented in Chapter 5. Extended by the extinction correction in the following section, it gives good approximations of the macroscopic reflection properties of real-world imperfect crystals [45, 49].Therefore, the mosaic crystal model, extended by the extinction corrections described in Section 2.4.8, is used throughout this work.

2.4.8 Extinction Effects and Corrections

The Darwin-Hamilton approach distinguishes between two types of extinction, which are presented in the following after [22, 45, 49, 74].

If the crystallites are too large to neglect extinction effects within them, the integrated Bragg-reflected intensity of a single crystallite is lower than predicted by the kinematic theory. This is referred to as primary extinction. It is negligible if the crystallite thickness is small compared to the extinction length given by Equation 2.99, or if the structure factor for the reflection is very small [45]. Addressing this extinction will decrease σ.

A crystallite's reduced Bragg-reflected intensity may also result from shadowing by crystallites with identical orientations positioned above it. Due to foregoing diffraction by these crystallites, the intensity of a beam fulfilling the Bragg requirement is already reduced by the time it reaches the crystallite under observation. This extinction effect is referred to as secondary extinction. It is negligible for very thin crystals, very weak reflections, or high mosaic spreads because a broader range of disorientations reduces the likelihood that preceding crystallites have the same orientation.

The occurrence of both types of extinction depends on the thickness of the individual crystallites t_0. To address the extinctions, the derivations in Section 2.4.4 must be adjusted. Following Zachariasen in [49], this can be simplified by introducing an extinction correction factor $f(A) \leq 1$ to get a corrected Q-factor $Q' = Qf(A)$. All of the previously derived equations only need to be adjusted by replacing Q with Q' to account for extinction effects. The extinction correction factor is defined by Equations 2.100a and 2.100b for Bragg and Laue case [49].

$$f(A) = \frac{\tanh A + |\cos(2\theta_B)| \tanh\left(|A\cos(2\theta_B)|\right)}{A\left(1+\cos^2(2\theta_B)\right)} \qquad \text{Bragg} \qquad (2.100a)$$

$$f(A) = \frac{\sum_{n=0}^{\infty} J_{2n+1}(2A) + |\cos(2\theta_B)| \sum_{n=0}^{\infty} \left(2A\,|\cos(2\theta_B)|\right)}{A\left(1+\cos^2(2\theta_B)\right)} \qquad \text{Laue} \qquad (2.100b)$$

J_{2n+1} denotes the Bessel function of the first kind of order $2n+1$. A is given by [49]:

$$A = r_e \frac{\lambda\,|F_{\mathrm{hkl}}|\,t_0\left(1+|\cos(2\theta_B)|\right)}{V\sin^2\theta_B}. \qquad (2.101)$$

Therefore, an increasing crystallite thickness leads to stronger extinction effects. The secondary extinction is subsequently introduced by replacing Q with Q' in Equation 2.90. Applying the adapted derivation to Equation 2.98 yields the corrected expression:

$$\sigma = W(\delta)Q' = W(\delta)Qf(A). \tag{2.102}$$

Note that, despite the described improvements to the description of non-ideal, imperfect crystals, the corrections do not constitute a dynamical diffraction theory. It is still based on intensity transport rather than a dynamical wavefield description. However, the use of this model is justified in Section 2.4.10.

2.4.9 Scherrer Broadening

Very small crystallites lead to an additional broadening of the reflection profile, referred to as Scherrer broadening [45, 75]. The line broadening is quantified by the Scherrer equation [75]:

$$\Delta(2\theta) = \frac{K\lambda}{t_0 \cos\theta_B}. \tag{2.103}$$

Here, t_0 denotes the crystallite thickness and K is the Scherrer-form-factor. The latter is ≈ 1 for a crystallite. $\Delta(2\theta)$ is the FWHM of the broadening in radians caused by the Scherrer effect, and is of particular interest in powder diffraction. For mosaic crystals, especially when reflecting small wavelengths, the broadening effect caused by the Scherrer effect is usually much smaller than the effect caused by mosaicity and can therefore often be neglected.

However, for very small crystallites and / or long wavelengths, the reason for the broadening can be explained by Equation 2.42. Since very thin crystallites correspond to a small number of lattice planes, the assumption that $N_i \gg x_i$ is no longer valid. In agreement with the explanations in Chapter 2.3.4, this causes the diffraction peaks to broaden beyond the Darwin width.

2.4.10 Validity of the Adopted Diffraction Model

As mentioned in Section 2.4.3, this work employs the Darwin-Hamilton approach after [45, 58, 59]. It is an exact solution for the two-beam case, which includes one incident beam and one Bragg-reflected beam, and only considers coupled intensities. It uses the model of a perfect, stress-free crystal with a constant coupling σ and a constant absorption coefficient μ.

In contrast, the Takagi-Taupin equations describe the propagation of wavefield amplitudes inside a crystal. They provide a solution for coherent dynamical diffraction, which can also account for imperfect or distorted crystals [54, 62–65]
The Darwin-Hamilton approach is only valid for small, perfect crystals in the two-beam approximation. However, the mosaic crystal model, introduced in 2.4.6, accounts for the incoherent superposition of the X-rays scattered by individually lightly misoriented crystallites [65]. For these crystallites, the Darwin-Hamilton approach is valid. Therefore, the superposition approach is also valid for an overall perfectly imperfect mosaic crystal [49, 65]. The extinction corrections discussed in Section 2.4.8 further improve the description.

In the scope of this work, mosaic crystals with a mosaic spread much higher than the Darwin width, up to $\beta = 0.5°$, and a thickness of hundreds of μm are considered by experiment and ray tracing simulations. In theory, the Takagi-Taupin equations could be used to model each crystallite individually for a more exact solution, especially for very thick crystallites, small mosaic spreads, and crystallites under stress. However, since they can usually only be solved numerically and locally, their implementation is very computationally expensive [77]. As an example, the ray tracing code `xrt`, which is used in this work, advises to use Takagi-Taupin integrals for the diffraction of perfect crystals only up to 100 µm thickness and requires a graphics card due to the heavy computational load [78].
Therefore, it is common and sensible to limit the diffraction model to the Darwin-Hamilton approach.

2.4.11 Bravais Lattice Classification

The Bravais lattice system, defined by Auguste Bravais in 1850, aims to classify crystals by their greatest degree of symmetry [50]. The base level of classification distinguishes solely based on the unit cell vectors $\vec{a}$, $\vec{b}$ and $\vec{c}$, as well as the angles α, β, γ between them [48]. Figure 2.11 shows how these parameters define a crystal's unit cell.

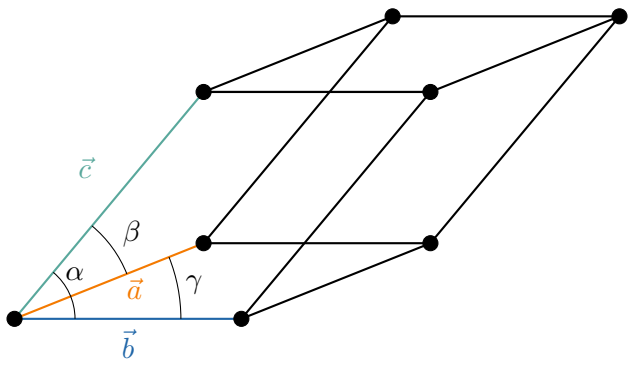


Figure 2.11: A primitive triclinic unit cell as the most general Bravais lattice with the definition of its unit cell vectors $\vec{a}$, $\vec{b}$ and $\vec{c}$, as well as the angles α, β, γ between them.

There are seven different lattice systems that can be distinguished by this first level of classification. They are listed with their respective relationships in Table 2.1.
The second level of classification is based on the presence of additional lattice points in the unit cell besides its corners.
A Bravais lattice is referred to as [48, 51]:

- **Primitive** if the lattice points are confined to the unit cell's corners.
- **Base-centered** if additionally the unit cell's horizontal faces, spanned by $\vec{a}$ and $\vec{b}$, contain a lattice point at their centers.
- **Body-centered** if an additional lattice point is located at the center of its unit cell.
- **Face-centered** if each face of the unit cell contains a lattice point at its center.

Not every second-level class exists for each lattice system. Table 2.1 shows the scheme with a checkmark ✓. The total classification defines 14 different Bravais lattice systems [48]. Note that this classification includes non-primitive unit cells, which may simplify the representation of a crystal's structure in some cases.

Lattice system	**Vector relation**	**Angle relation**	**Additional possible centerings**		
			Base-centered	Body-centered	Face-centered
Triclinic	$a \neq b \neq c$	$\alpha \neq \beta \neq \gamma \neq 90°$			
Monoclinic	$a \neq b \neq c$	$\alpha = \gamma = 90°$, $\beta \neq 90°$	✓		
Orthorhombic	$a \neq b \neq c$	$\alpha = \beta = \gamma = 90°$	✓	✓	✓
Tetragonal	$a = b \neq c$	$\alpha = \beta = \gamma = 90°$		✓	
Hexagonal	$a = b \neq c$	$\alpha = \beta = 90°$, $\gamma = 120°$			
Rhombohedral	$a = b = c$	$\alpha = \beta = \gamma \neq 90°$			
Cubic	$a = b = c$	$\alpha = \beta = \gamma = 90°$		✓	✓

Table 2.1: Overview of all possible Bravais lattices after [48]. Vector lengths are denoted by their magnitudes, e.g., $|\vec{a}| = a$.

Using the most general case, represented by the triclinic Bravais lattice, the volume of a unit cell is given by [48]:

$$V = abc\sqrt{1 - \cos^2\alpha - \cos^2\beta - \cos^2\gamma + 2\cos\alpha\cos\beta\cos\gamma}. \tag{2.104}$$

For the same general case, the interplanar spacing of a lattice plane set $\{hkl\}$ are given by Equation 2.105 [45].

$$\begin{aligned}\frac{1}{d_{hkl}^2} = \frac{1}{V^2}\Big(&h^2\big(b^2c^2\sin^2\alpha\big) + k^2\big(a^2c^2\sin^2\beta\big) + l^2\big(a^2b^2\sin^2\gamma\big) \\ &+ 2hk\big(abc^2(\cos\alpha\cos\beta - \cos\gamma)\big) + 2kl\big(a^2bc(\cos\beta\cos\gamma - \cos\alpha)\big) \\ &+ 2hl\big(ab^2c(\cos\gamma\cos\alpha - \cos\beta)\big)\Big).\end{aligned} \tag{2.105}$$

For more specific lattice systems, both expressions simplify. In the simplest case of a primitive cubic lattice, for example, to $V = a^3$ and $d_{hkl} = \frac{a}{\sqrt{h^2+k^2+l^2}}$.
The Bravais lattice classification is based solely on a crystal's translational symmetry. This classification can be expanded to define space groups by considering rotational, mirror, and inversion symmetries, as well as potential additional non-symmorphic symmetry operations. The International Union of Crystallography classifies 230 distinct space groups [48].
A crystal's basis completes its exact description by specifying the atom or set of atoms associated with each lattice point. For most known crystals, their full definitions as described above can be accessed via the "Crystallography Open Database" [79].
Note that if the crystal basis contains ions in addition to or instead of atoms, the calculation of f in Section 2.3.2 must be adapted to account for the number of electrons and the electron density of the ions.

2.4.12 Selection Rules for X-ray Diffraction

A crystal contains many possible lattice sets. Depending on the crystal's structure, constructive or destructive interference can occur between the reflections of different plane sets. For example, the n^{th} order reflection of a lattice plane set $\{hkl\}$ and the first-order reflection of a plane set $\{nh\ nk\ nl\}$, with n being an integer, will occur at the same Bragg angle [47, 57] and therefore overlap. Following the same principle, certain reflections from different plane sets can also cancel each other out completely.
This results in a set of reflections that are not visible in X-ray diffraction experiments, which defines selection rules. These selection rules depend on the Bravais lattice of a crystal because the relationships between its lattice planes remain consistent within a given Bravais lattice group [45].

The selection rules, with n being an arbitrary integer, are [45]:

1) **Primitive** unit cells can exhibit reflections for all lattice plane sets indexed by $\{hkl\}$.
2) **Body-centered** unit cells can exhibit reflections only if $h + k + l = 2n$.
3) **Face-centered** unit cells can exhibit reflections only if h, k and l are either all even or all odd.
4) **Hexagonal close-packed** unit cells exhibit no reflections if:
   a) l is odd and $h + 2k = 3n$
   b) l is odd and $2h + k = 3n$

The diffraction model used in this work implicitly includes these selection rules via the structure factor F. Note that there are even stricter selection rules for crystals with specific space groups [45].

3 Mosaic Crystal Optics

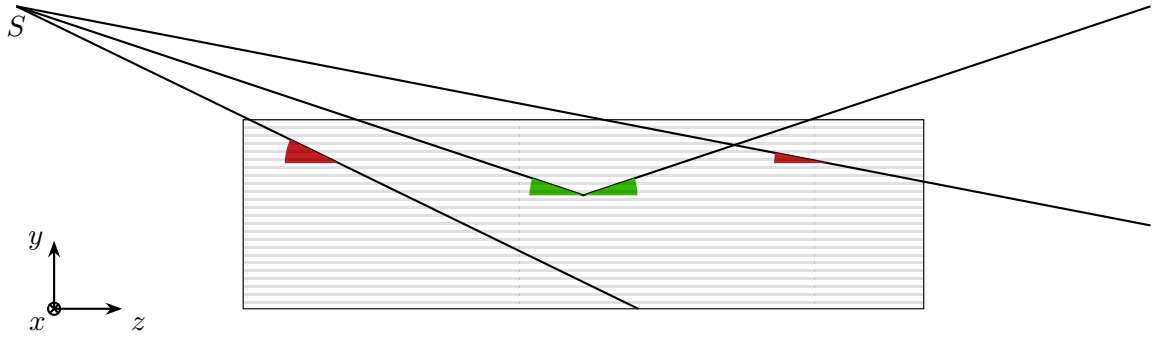
As discussed in Section 2.4.6, mosaic crystals are characterized by a higher integrated reflectivity than perfect crystals. This characteristic can be exploited for their use in X-ray optics. Their properties are particularly advantageous when X-ray tubes are used as the radiation source due to their high divergence and broad spectra.
This chapter summarizes the most important focusing and defocusing properties of mosaic crystals after [71, 82–84] and presents possible optical designs based on mosaic crystals as well as common alternatives. The presented types of X-ray optics are classified and evaluated in terms of their suitability as a focusing optic in a compact XFI configuration. Therefore, Section 3.3 summarizes the requirements for such an optic.
The explanations and figures in this chapter mostly use symmetric Bragg geometries, which means that the mean crystallite normal is identical to the surface normal.
Additionally, the basic optical effects of mosaic crystals are demonstrated at the example of two-dimensional models for Bragg reflections for the sake of simplicity. The third dimension is discussed in Section 3.2.3. For illustrative purposes, the figures in this chapter enlarge the angles and relative sizes of the crystallites with respect to the whole crystal size, which makes the focusing and defocusing effects appear stronger.
The use of Laue geometry-based optics is discussed in Section 3.4.3.

3.1 Mosaic Focusing

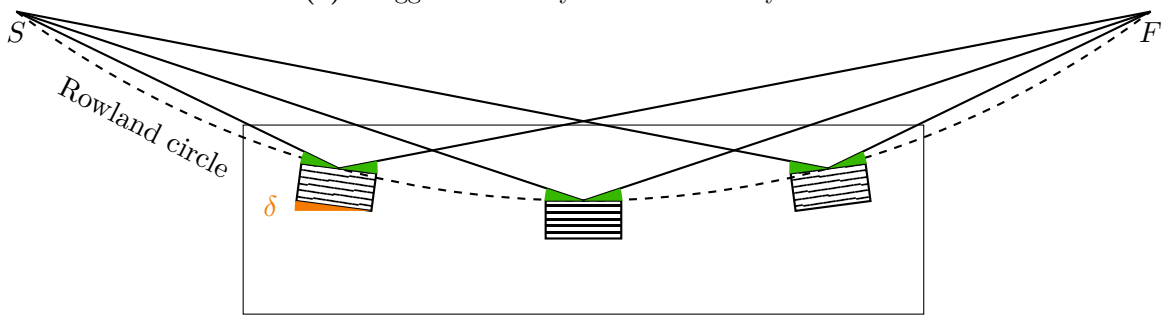
As demonstrated in Chapter 2.4.6, mosaic crystals exhibit a higher integrated reflectivity under divergent incidence than perfect crystals due to their higher angular acceptance for Bragg reflection. Additionally, the mosaicity causes a focusing effect, which will be derived in this section, referring to Figure 3.1 [82].

Figure 3.1 shows divergent, monochromatic X-ray beams that are incident on a perfect (3.1a) and a mosaic (3.1b) crystal. Both cases illustrate the plane sets by parallel lines. Three incident beams of the same wavelength but different incident angles are drawn in each case.
Figure 3.1a shows the case discussed in the derivation of the reflectivity of a perfect crystal in Chapter 2.4.4. Here, the central beam is incident on the crystal under the Bragg angle θ_B, which corresponds to its wavelength and the plane set spacing. According to the

Bragg reflection model, it can be reflected at the same angle, indicated by the green color. Note that this reflection and its modeled depth follow Equation 2.70b, which is derived in Section 2.4.3.



(a) Bragg reflection by a non-mosaic crystal



(b) Focusing effect of a mosaic crystal

Figure 3.1: Divergent incidence on a perfect and a mosaic crystal originating from a point source S. Incidence angles with respect to the lattice planes are marked green if they meet the Bragg condition and red if they do not. The mosaic crystal exhibits focusing properties to a focal point F for reflecting crystallites arranged on the Rowland circle.

The beams to the left and right of the central beam, which have the same wavelength, represent an incidence at steeper or flatter angles. Both angles of incidence lie outside the Darwin width of the shown crystal plane, indicated by the red angles, and can therefore not be reflected according to the Bragg reflection model.

Figure 3.1b shows a mosaic crystal that is struck by the same divergent, monoenergetic incident beams. Three crystallites, with the two outer ones tilted by an angle δ with respect to the crystal surface, are shown. The lattice planes of all three crystallites are parallel to their respective surfaces. According to the Bragg reflection model, a beam can be reflected if it is incident on a crystallite under the Bragg angle θ_B. All three incident beams fulfill this requirement, indicated by the green angles. This demonstrates the increased angular acceptance of mosaic crystals, which results in higher integrated reflectivity.
If the reflecting crystallites happen to be aligned on a segment of a circle that connects the point source and the points of incidence onto the crystallites, all of the reflected beams

will intersect at one point. This focal point also lies on the aforementioned arc, referred to as the Rowland circle [82, 85].
Hence, the focusing effect of mosaic crystals is demonstrated, which can be utilized for X-ray optics.

If the incident beams are polychromatic, each wavelength can be modeled separately, as described above. Each wavelength would correspond to a different Bragg angle. Again, a non-mosaic crystal would only reflect beams that are incident at their respective Bragg angles. For non-divergent beams, the perfect crystal would therefore function as a monochromator, a commonly used component in X-ray beamlines [86].
If the same polychromatic, non-divergent beams strike a mosaic crystal, different wavelengths can be reflected by tilted crystallites, if they are intersected at their respective Bragg angle, which also increases the integrated reflectivity for polychromatic incidence.

A divergent, polychromatic beam creates a spectrum of reflected beams in both cases presented in Figure 3.3. As this is especially relevant for X-ray tubes as a source, these cases are further discussed in Section 3.2.2.

3.2 Mosaic Defocusing Effects

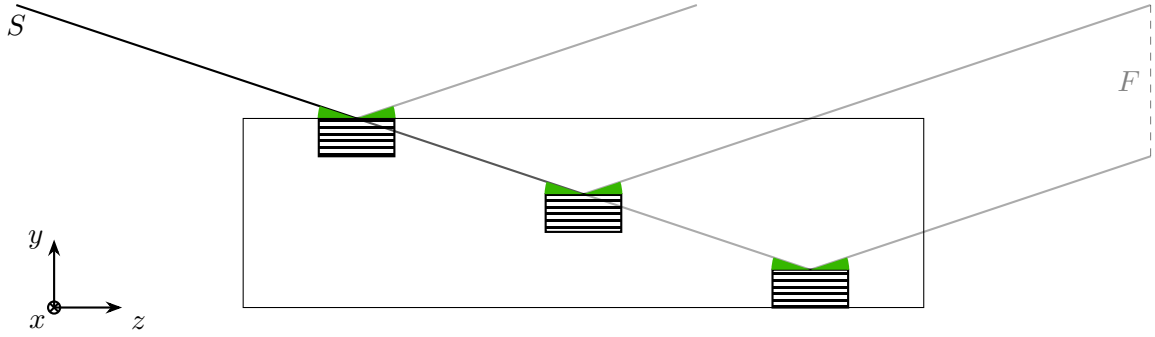
Apart from the focusing effects, the property of mosaicity also causes defocusing effects, which are described in the following sections.

3.2.1 Defocusing in the Bulk

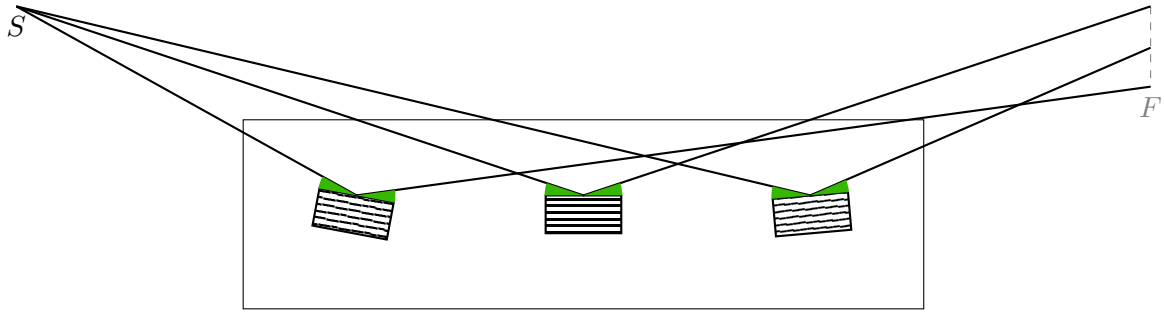
Section 3.1 described the focusing effect of crystallites aligned on a Rowland circle. However, since the tilt of the crystallites is distributed randomly, only a fraction of them are aligned this way. Despite their location outside the Rowland circle, these crystallites can also take part in the overall reflection when aligned suitably for fulfilling the Bragg condition, leading to a broadening of the focal point.

Figure 3.2a shows one possible case: A beam is incident on a crystallite at the Bragg angle. Part of the beam is reflected and exits the crystal. The non-reflected part of the beam propagates further into the crystal bulk, where it is incident on two other crystallites tilted the same way as the first one. Both deeper-lying crystallites also reflect and transmit part of the beam. Since the reflection angles of the second and third reflections are the same as the first, all reflected beams are parallel and cannot form a common focus.
The vertical distances of the reflecting crystallites correspond to the vertical distances of the reflected beams. This leads to a defocusing of the overall reflection to an enlarged

focus of size F, that has the same size as the crystal thickness. Note that for reasons of space, not the entire focal plane is drawn in Figure 3.2a.



(a) Defocusing by thickness.



(b) Defocusing by width.

Figure 3.2: Defocusing of beams from a point source S by the bulk in mosaic crystals, caused by identically tilted crystallites in different depths (a) or suitably tilted crystallites outside the Rowland circle (b). Incidence angles with respect to the lattice planes are marked green if they meet the Bragg condition. The bulk defocusing effect, shown in 3.2a, is also prominent in perfect crystals. Both effects lead to the formation of an extended focus F.

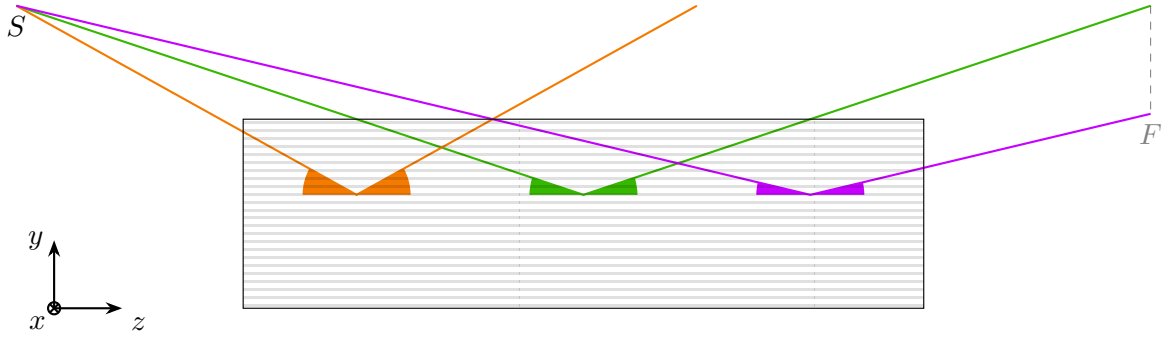
The described defocusing is generally limited by the penetration depth of the beams. For thin crystals, their thickness is the limiting factor.
Due to additional propagation inside the crystal, the pathways of the second and third reflected beams are longer overall. As described in Section 2.4.3, the possible reflectivity saturates at a certain crystal thickness. This corresponds to a maximal defocusing in the y-axis when the crystal's thickness exceeds its saturation thickness.

The other direction in which reflecting crystallites can be displaced from the Rowland circle in the two-dimensional case is shown in Figure 3.2b. Here, three reflecting crystallites lie at the same depth, but are displaced longitudinally. As before, all crystallites are tilted such that the incident beam strikes them at the Bragg angle, drawn in green. In the illustrated case, the reflected beams are pairwise convergent but will intercept at points different from the focal point shown in Figure 3.1. This effect blurs the focus, creating a defocusing effect.

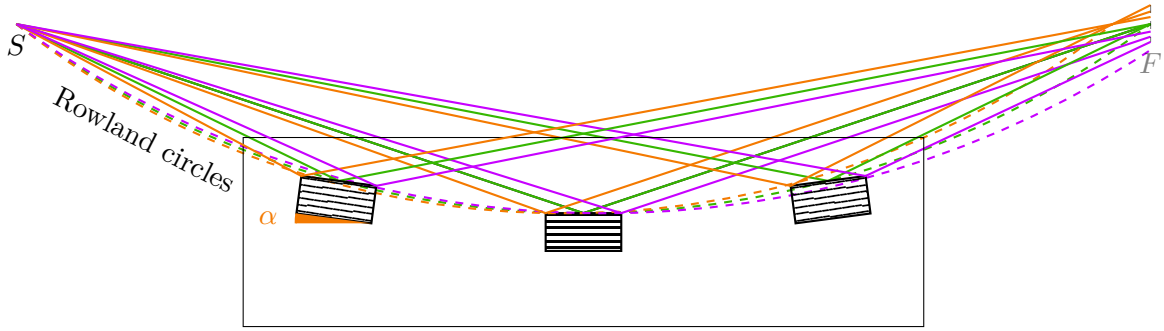
The further away the crystallite is displaced from the center, the greater its tilt must be in order to reflect the beam. Therefore, the defocusing effect is limited by either the longitudinal size of the crystal or the maximum tilt of the crystallites, characterized by the mosaic spread. Of two reflecting crystallites that are equidistant from a central, non-tilted crystallite, as shown in Figure 3.2b, the crystallite on the source side must be tilted more strongly in order to enable reflection. This results in a more prominent defocusing effect originating from this side (left in Figure 3.2b).

3.2.2 Defocusing by Polychromatic Incidence

Figure 3.3a illustrates a polychromatic incidence on a perfect crystal using different colored beams. Each wavelength corresponds to a different Bragg angle, quantized by Equation 2.58. Since perfect crystals can reflect only those rays that strike them within a small angular range around their respective Bragg angle, the reflectable energies are location dependent. The greater the wavelength, and therefore the Bragg angle, the closer the reflection point is to the source. This effect is applied in crystal spectrometers [87].



(a) Wavelength defocusing by a perfect crystal



(b) Wavelength defocusing by a mosaic crystal

Figure 3.3: Defocusing effect due to polychromatic incidence in perfect (a) and mosaic crystals (b). Both Figures show the reflection of three wavelengths $\lambda > \lambda > \lambda$. (b) additionally shows the Rowland circles and the focus points of all three wavelengths. Both effects lead to the formation of an extended focus F. In (b), the focal point for every wavelength lie on the same height but different horizontal positions.

The bandwidth of the reflected energy is limited by either the longitudinal size of the crystal, the bandwidth of the incident beam, or its divergence.

The same principle applies to mosaic crystals, as shown in Figure 3.3. However, due to the mosaicity, each crystallite can reflect a specific energy bandwidth. The green rays have the same wavelength as those in Figure 3.1b. The positions and tilts of the crystallites shown are also identical to those in Figure 3.1b. It is illustrated how the very same crystallites also reflect beams with both longer (orange) and shorter (purple) wavelengths. All three wavelengths define their individual Rowland circle. The corresponding foci lie above or below the original focus, which corresponds to a defocusing.
However, Figure 3.1b also shows that the mosaic crystal exhibits focusing properties for a range of wavelengths simultaneously. The reflected energetic bandwidth is limited by either the mosaicity of the crystal, its longitudinal size, the bandwidth of the incident beam, or its divergence. Note that the reflection bandwidth of the mosaic crystal in Figure 3.3b seems small because it is illustrated with the same three crystallites for all wavelengths. This limits the radii of the Rowland circles that can be drawn. If suitably tilted crystallites are present, Rowland circles with higher or lower radii, corresponding to the focusing of shorter or longer wavelengths than those illustrated, are possible.

3.2.3 Azimuthal Defocusing

So far, it was assumed that symmetric Bragg reflections were invariant under the azimuthal angle. This section demonstrates that this assumption only applies to non-tilted crystallites or perfect crystals. Since the mosaic distribution is rotation-invariant, the individual crystallites also exhibit a tilt in the direction perpendicular to the tilt shown, for example, in Figure 3.1b, which generally follows the same mosaicity. The result is a defocusing effect in the plane perpendicular to the diffraction plane [82], as illustrated in Figure 3.4.

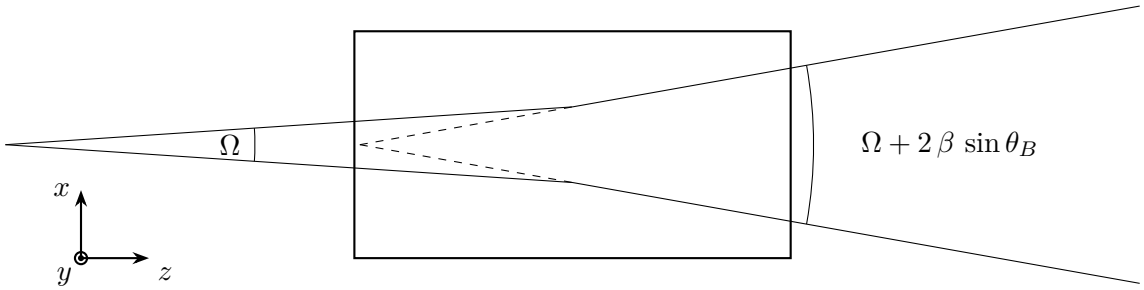


Figure 3.4: Azimuthal defocusing in the plane perpendicular to the diffraction plane, caused by the tilt of the crystallites perpendicular to the principal direction of propagation (z). The effect is illustrated at the top-view of a Bragg reflection at a plane crystal after [82, Figure 1].

Figure 3.4 shows a top view of the described lateral defocusing by a Bragg reflection on a plane mosaic crystal. This defocusing effect increases the angular divergence Ω in the

illustrated plane by a value of $2\beta \sin\theta_B$ [82]. However, typical values for the mosaic spread β are below 0.5°, and values for θ_B are well under 5° in the standard application of the presented optics. Therefore, the mosaic defocusing in this plane is much weaker than the other defocusing effects in the perpendicular plane, described in Sections 3.2.1 and 3.2.2. Additionally, the divergence Ω of an X-ray tube, e.g. [88], without further collimation, has a magnitude of tens of degrees and is therefore also well above the described widening.

3.2.4 Distance-Dependence of Defocusing Effects

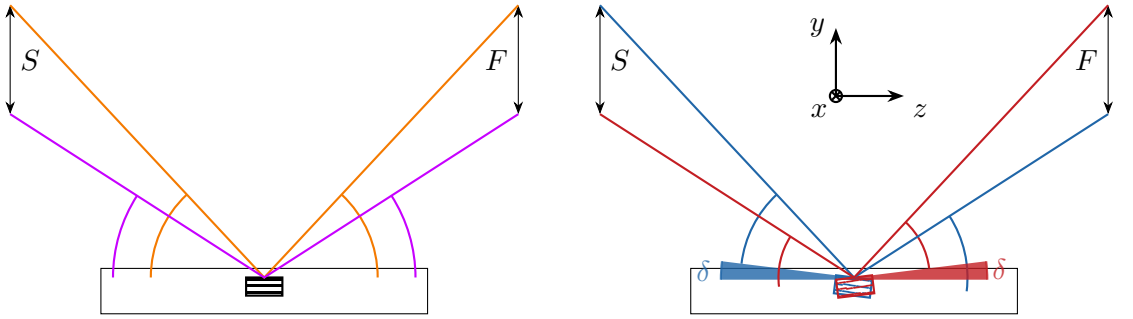
The focusing and defocusing effects described in the previous sections were conceptually discussed without any reference to the distances between the source, the crystal, and the focal point. This is sufficient for the demonstration of the effects, as they are solely angle-dependent. In concrete applications of the focusing and defocusing effects in an X-ray optic, as will be described in Section 3.5, a focusing can be realized for specific distances between source, crystal, and focal point.
In principle, focusing can be achieved at any distance between the source, the crystal, and the focal plane. If the energy to be focused, and thus the Bragg angle, as well as an experimentally feasible vertical distance between the crystal and the line connecting the source, and the focal point are specified, then the horizontal distances are uniquely determined by the Bragg condition. The resulting setup is scalable because it depends solely on the angles. With a doubled horizontal distance between the crystal and the line connecting the source and the focal point, the horizontal distances between the source and the crystal, and between the crystal and the focal plane, are also doubled, as is the length of the crystal.

The focusing described in Section 3.1 is independent of specific lengths and distances. The defocusing effects are also solely angle-dependent. However, greater distances also result in larger absolute defocusing values in the focal plane for all of the discussed defocusing effects, except for defocusing due to thickness, as illustrated in Figure 3.2a. To minimize the absolute values of the defocusing effects, a compact configuration is therefore preferable to a larger one, even though the focusing is independent of the size. The defocusing by thickness, illustrated in Figure 3.2a, is given by the crystal thickness or maximum depth of reflection, and is independent of the distances between the source, the crystal, and the focal plane.

3.2.5 Focusing of Extended Sources

Up to this point, the focusing and defocusing effects were discussed, assuming a point source to eliminate the contribution of the expansion of a real source with a certain focal

spot size. For a point source, the location of incidence on the surface of the optics can be directly associated with a specific angle of incidence. Figure 3.5 shows two beams from the edges of the focal spot size of a divergent source of extension S, that are incident on a single point of the optic, which shows that a direct association does not exist in this case.



(a) Focusing of an extended, divergent, polychromatic source with two drawn wavelengths $\lambda > \lambda$ under their respective Bragg angles at the same crystallite.

(b) Focusing of an extended, divergent, monochromatic source with two beams $\lambda = \lambda$ and their reflecting crystallites in the same color.

Figure 3.5: Focusing of a divergent source of extension S to a focus F. (a) shows how a single crystallite focuses the polychromatic, divergent incidence onto the focal plane. (b) shows how two divergent beams of the same wavelength of the extended source S can be focused onto a plane F by differently tilted crystallites located at the same z-position. The corresponding crystallites are illustrated in the same color as the reflected beam.

Figure 3.5a shows both beams incident on the same crystallite at their respective angles of incidence, which are determined by their points of origin at S. In this example, the two beams have different wavelengths, both of which satisfy the Bragg condition. For simplicity, only symmetrical reflections are illustrated. In the focal plane, the beams produce an image of the same size as the focal spot of the source $F = S$.

Figure 3.5b shows a case in which both beams have the same wavelength. In order to focus on the focal plane through F, they must be incident on differently tilted crystallites. Here, the crystallites are properly tilted for both beams at the same point to demonstrate the effect, despite the enlarged angles and sizes in the illustration. The respective incidence and reflection angles, shown in red and blue, are identical and match the Bragg angle. Unlike the effect illustrated in Figure 3.5a, this effect requires a mosaic crystal. The result is, once again, an image whose size corresponds to the focal spot of the source $F = S$, but which, unlike in the first case, is flipped.
Naturally, two crystallites cannot be located at the same position. However, two properly tilted crystallites might be located directly next to each other, which would, for small crystallites, only deviate slightly from the discussed case.

Both cases are edge cases. The actual focusing of an extended source depends on the origin of the beams in S and the wavelength relationship. It corresponds to a combination of the two discussed edge cases.
However, the analysis shows that, when using straight optics in the y-z plane, the lower limit of the focus size F is determined by the source size S. The focus size is further increased by the defocusing effects already discussed in this chapter.

3.3 Requirements for Optics for Compact XFI Setups

Section 3.1 demonstrates that mosaic crystals have focusing properties that can be used for X-ray optics. This section summarizes the requirements for an optic used in compact XFI setups, which leads to a discussion of possible concrete optical geometries in the following Section 3.4.

Conventionally, XFI experiments are performed at synchrotron beamlines [2], which provide highly collimated and monochromatic beams, characterized by a high brilliance[1] [22, 89]. Note that for a fixed incident energy, the scan time in such a setup is primarily limited by the flux of the beam, while the spatial resolution depends on the size of the focal spot on the sample [15].

Figure 3.6 shows a typical XFI spectrum obtained at the P21.1 beamline (PETRA III, DESY, Hamburg, Germany [18]) at an incident energy of 53 keV, and a simulation of the same setup. The examined sample is a Plexiglass cylinder with mouse dimensions, which contains an Eppendorf tube with a palladium solution. The simulation and measurement results are in good agreement, suggesting that the simulation accurately describes the physical processes. The majority of photons in the spectrum have undergone one or more Compton scatterings, as described in [91]. To minimize background contributions from multiple Compton scattering in the signal region, where the fluorescence lines of the examined element lie, the incident energy must be well above the fluorescence energy. For more detailed descriptions of typical XFI spectra, refer to [91].

By nature, X-ray tubes do not provide properties that are comparable to synchrotron sources because they are highly divergent and deliver a broad spectrum. To make them accessible as an X-ray source for XFI, an optic can be used. The requirements follow from the properties of an X-ray tube and can be listed as follows.

[1] The brilliance of a source is defined as the intensity in photons per second divided by the angular divergence in mrad times the source area in mm^2 times the spectral bandwidth relative to 0.1 %: Brilliance $= \frac{\text{Photons/second}}{(\text{mrad}^2)(\text{mm}^2\text{source area})(0.1\,\%\text{BW})}$ [22].

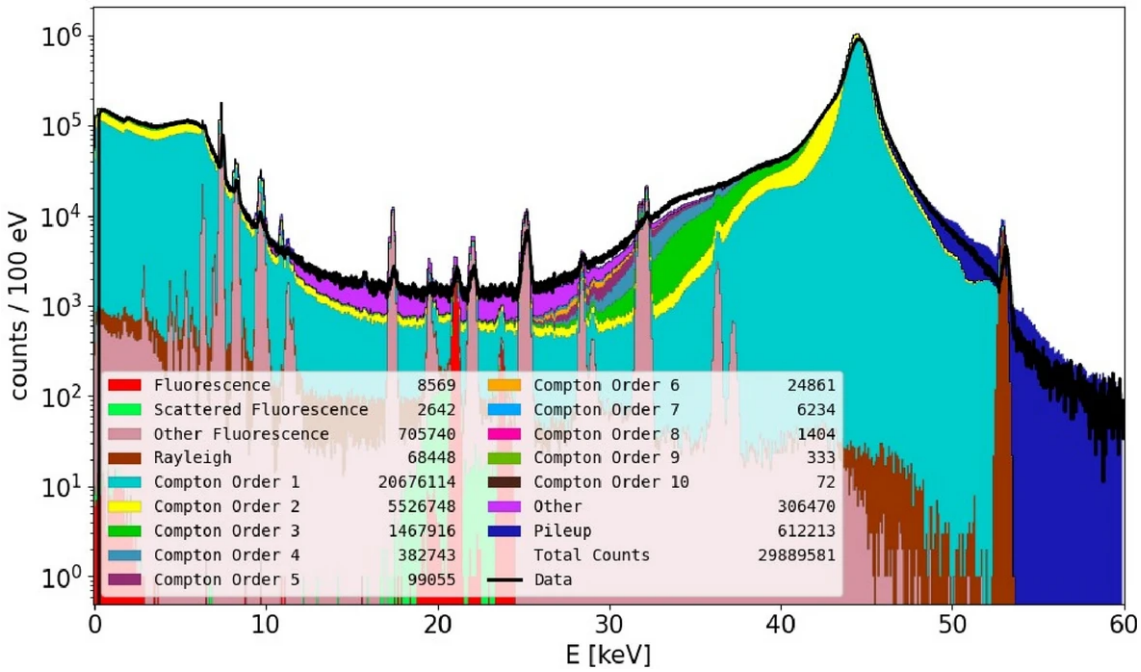


Figure 3.6: "Comparison of a typical simulated and measured (black line) XFI spectrum showing good agreement in all spectral regions. The setup consisted of a Plexiglass cylinder with mouse dimensions containing an Eppendorf tube with palladium solution and an X-ray detector with 0.5 mm sensor thickness (Amptek X123 FAST SDD [90]) at 60 mm distance and under an angle of 150°. One can clearly see that the majority of photons have been Compton scattered multiple times (number of Compton scattering events color coded) and the best possible signal energy range lies between 20 and 30 keV"[91]. The incident energy was 53 keV. Figure taken from [91].

The optic:

1. must produce a focal spot comparable to the focus of approximately 1 mm × 1 mm, achievable at the P21.1 beamline (PETRA III, DESY, Hamburg, Germany [18]), in order to provide sufficient resolution for XFI experiments,
2. must filter part of the spectrum energetically to minimize background contributions arising from multiple Compton scattering in the fluorescence energy region [15]. The bandwidth should not exceed 15 % FWHM [8],
3. should be energetically tunable between 30 keV and 85 keV to provide flexible energy for various experiments, including different sized objects,
4. should maximize the flux in the focal spot while meeting the requirements above in order to reduce scan time,
5. should leave the overall setup compact.

As demonstrated in Section 3.1, mosaic crystals can produce a focal spot when the crystallites are properly aligned on a Rowland circle. Section 3.2 demonstrates that various effects defocus this focal spot. Nevertheless, mosaic crystals remain suitable for providing requirement 1.

As explained in Section 3.2.2, a broader incidence spectrum results in defocusing. However, mosaic crystals also exhibit an energetic reflection bandwidth. Apart from material parameters and the width of the incidence spectrum, the reflection bandwidth is limited by the mosaicity of the crystal. Therefore, a crystal with the appropriate parameters can filter out part of the incident spectrum into the reflected spectrum, thereby satisfying condition 2.

As stated in Section 3.1, among all the beams with varying wavelengths that are incident on a perfect crystal or crystallite under a specific angle, only those whose corresponding Bragg angle is similar to their incidence angle can be reflected. In the two-dimensional examples of the preceding Figures 3.1 to 3.3 and 3.5, the angle is altered by changing the distance between the crystals horizontally or vertically. If, for example, the vertical distance remains constant, then the further away the crystal is, the flatter the incidence angles onto the crystallites become, and the smaller the wavelength of the corresponding beams that fulfill the Bragg condition must be. This corresponds to an energy tunability (requirement 3). Note that the energy bandwidth depends on the mosaicity of the crystal.

Requirement 4 can be satisfied by maximizing the reflectivity of a crystal within its energy bandwidth. As shown by Equation 2.90, different sets of reflecting planes provide different reflectivities. Additionally, higher-order reflections of a lattice plane set exhibit lower Bragg reflectivities. Therefore, the plane set with the highest reflectivity should be used in the first order of the Bragg reflection for a potential optic. This plane set should be aligned with the overall crystal surface to provide a symmetric reflection setup. Such a setup maximizes the reflectivity due to minimal beam pathways, and is the most convenient for alignment.
Additionally, the reflectivity is maximized when the crystal thickness is equal to or greater than the saturation thickness, as discussed in Section 2.4.3. Chapter 6 shows possible challenges for thick crystals in certain optics.

Requirement 4 also favors Bragg geometry reflection setups over Laue geometry. Figure 2.7 shows that the shortest possible pathway for a reflected beam in Bragg geometry is always shorter than in Laue geometry. Therefore, Bragg geometry is less susceptible to absorption, thus maximizing reflectivity. This is also reflected by Equations 2.70a and 2.70b.
Once the target energy and bandwidth are defined, a suitable crystal can be selected. This determines the Bragg angle at which the optic must operate. Various combinations of horizontal and vertical distances between the crystal and the source can achieve this angle, allowing adjustments to be made to the size of the overall setup. While a higher vertical extension may be more manageable, it also increases the horizontal size of the

setup. Section 6.1 discusses further limitations of a concrete implementation.

In conclusion, this section demonstrates that mosaic crystals can meet all the requirements for an XFI-optic.

3.4 Possible Optic Designs

In this section, the results of the explanations of Section 3.3 will be transformed into a three-dimensional optic. In the $\vec{x}$-$\vec{y}$ plane, this can be achieved by exploiting radial symmetry. When the basic geometry of Figure 3.1b is translated into 3D, the reflection remains unchanged with respect to the azimuthal angle. Therefore, it should be translated into a ring in the $\vec{x}$-$\vec{y}$ plane.

Several possible shapes in the $\vec{y}$-$\vec{z}$ or $\vec{x}$-$\vec{z}$ plane are conceivable for implementing the reflective optics. This section introduces some designs, followed by brief presentations of transmission optics and X-ray optics based on different physical principles. It does not aim to present all types of X-ray optics, but rather, the most common types to justify the design chosen for this work.

3.4.1 Von Hámos Geometry

The most simple three-dimensional optic that utilizes the radial symmetry of the azimuthal angle is the von Hámos geometry, which is also referred to as cylinder geometry in the following. First described by von Hámos [92], it is essentially a hollow cylinder where the inside is the reflecting surface. The central axis of the cylinder aligns with the imaginary line connecting the source and the detector. The crystal, which serves as the reflecting surface, is bent[2] so that the mean plane of the crystallites is aligned with the cylinder's inner surface, ensuring that the mean reflecting plane's normal always points toward the cylinder axis.
Therefore, the von Hámos geometry is an exact representation of the straight crystal slab in the Figures of Sections 3.1 and 3.2 for every azimuthal angle. Thus, the same focusing and defocusing principles discussed in Sections 3.1 and 3.2 apply [84]. It is suited to fulfill every requirement defined in Section 3.3.

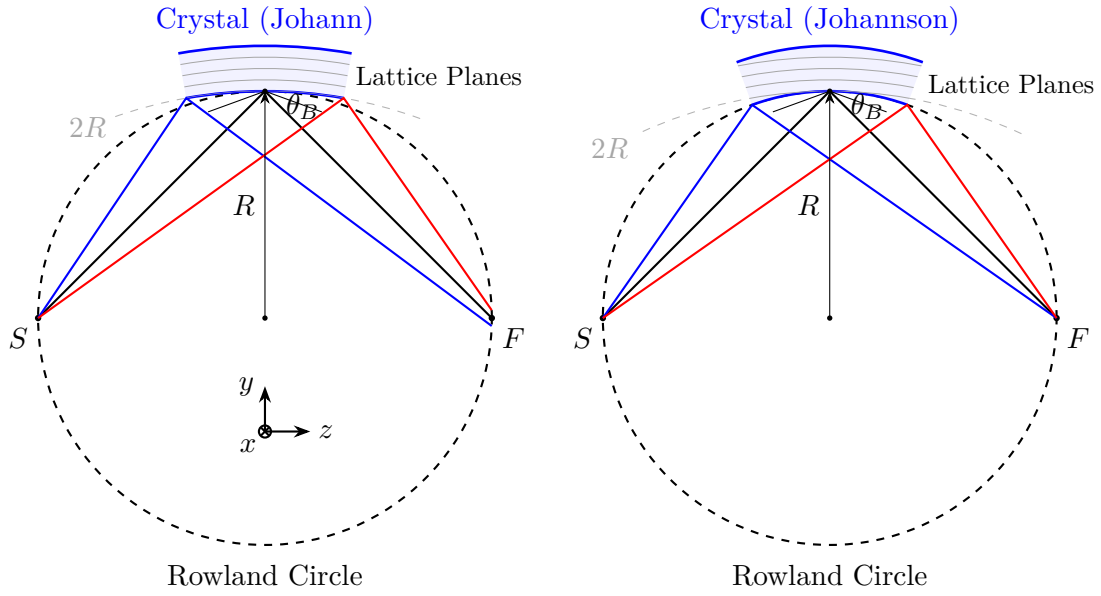
Compared to the other designs presented in the following sections, the von Hámos geometry is characterized by its simple geometry, good manufacturability, and, most importantly, its energy tunability. Section 3.5 provides insights into the design of a von Hámos geometry

[2]The reflective surface does not necessarily correspond to an entire crystal that has been bent. Various implementations are presented in Chapter 6.

for use in a compact XFI setup. Chapter 6 discusses the use of different mosaic crystals for such an optic and how the design must be adapted to accommodate their use.

3.4.2 Johann and Johansson Geometry

Besides using a mosaic crystal, the incidence angle onto the crystal planes in the z-direction can also be altered by bending the crystal and, therefore, its crystal planes. This gives rise to a number of reflection geometries, two prominent ones of which are the so-called Johann and Johansson geometries, which are briefly introduced in the following after [93–95]. Both concepts are shown in Figure 3.7.



(a) Johann optic design **(b)** Johansson optic design

Figure 3.7: Johann (a) and Johansson (b) optic designs using crystals curved to a radius of double the Rowland circle radius $2R$. Both designs feature reflecting crystal planes curved to the same radius $2R$. The Johansson optic (b) is additionally ground to the radius R, further improving focusing properties. Adapted from [93].

Both geometries are oriented on the Rowland circle, which connects a theoretical point source, the point of reflection, and the focus. This circle is defined by the Bragg angle of the reflection and has a unique radius R. Johann and Johansson geometries share an underlying crystal bending radius of $2R$ in order to fulfill the Bragg condition at every point on the bent surface. As shown in Figure 3.7, this radius optimizes the focusing properties of the optics. Compared to the focusing properties of a mosaic crystal, the bending replaces the mosaicity.

Due to its curvature, which has a radius of twice that of the Rowland circle, the Johann geometry only allows the central point to lie exactly on the Rowland circle. Consequently, only the beams reflected at this point converge on the Rowland circle at the focus position F. Therefore, beams that are incident on other positions of the Johann optic are focused

to a point that is slightly off with respect to the central focus F.

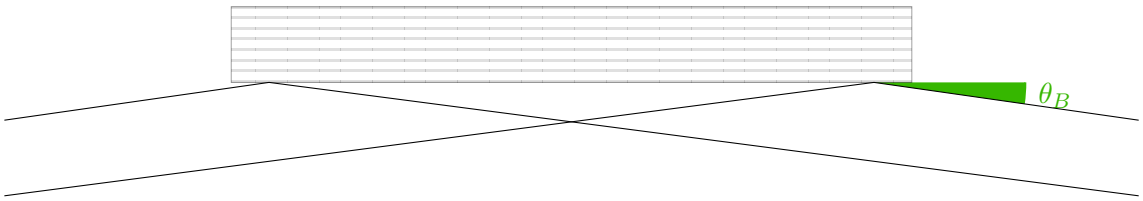
Johansson Optics compensate for this weakness through an additional grounding of the crystal to the single radius of the Rowland circle R. This allows the optic to image a monoenergetic point source perfectly onto a single point, but introduces an additional manufacturing step.

Both of the presented optics, especially the Johansson optic, exhibit excellent focusing properties for divergent, monochromatic beams. Using a perfect crystal as a base provides much higher integral reflectivity than a straight crystal slab. This design can also take advantage of radial symmetry in the azimuthal angle to build optics for higher dimensional focusing [96].

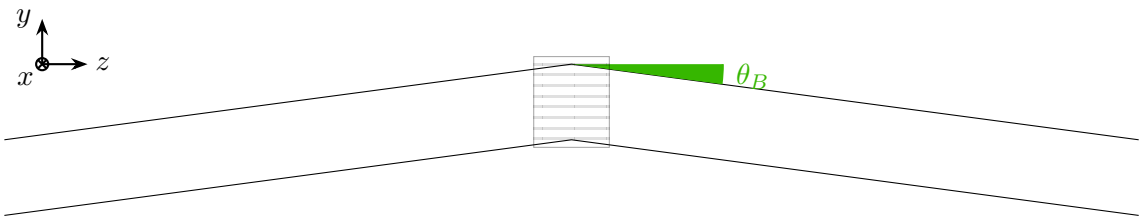
Johann and Johansson geometries are designed using the Rowland circle, which is specific to a given wavelength, crystal, and plane set. Therefore, they can only focus on this specific wavelength. These geometries cannot be tuned energetically by adjusting the distance between the source and detector, and can therefore not easily achieve requirement 3, defined in Section 3.3. The same is true for other optic designs using curved geometries in the y-z plane. However, for certain future XFI applications that require precise focusing of a small, constant energy bandwidth from a point-like origin with the highest possible reflectivity performance, Johann and Johansson geometries should be considered. For the scope of this work they are not further discussed.

3.4.3 Transmission (Laue) Diffraction Focusing Optics

Optics that rely on Bragg reflection can also be designed using the transmission (Laue) geometry, introduced in Section 2.4.3. One common application is the Laue lens, which is primarily used in astronomy [97, 98]. It can efficiently focus non-divergent, high-energy X-rays or soft γ-rays, up to about 1.5 MeV [99], and can also be realized using mosaic crystals [74].
A Laue lens is typically assembled from a number of small crystals, like the one illustrated in Figure 3.8b, aligned at concentric rings. Figure 3.8 shows how a Bragg-reflecting crystal in Laue geometry can focus a small portion of a non-divergent beam more efficiently with a significantly smaller crystal size in the z-direction than a crystal with the same Bragg angle in Bragg geometry.



(a) Parallel focusing by a perfect Bragg crystal



(b) Parallel focusing by a perfect Laue crystal

Figure 3.8: Focusing of identical non-divergent incident beams by the same crystal with the same reflecting crystal planes under the same Bragg angle, indicated in green; adapted from [74]. The focusing by a Bragg geometry (a) needs a crystal with a higher expansion in the z direction than the Laue geometry (b).

Classical Laue lenses cannot efficiently focus highly divergent incidence of constant wavelengths [74]. However, they can focus a certain wavelength bandwidth because every crystal can be reached by a certain range of incident angles, as illustrated in Figure 3.9.

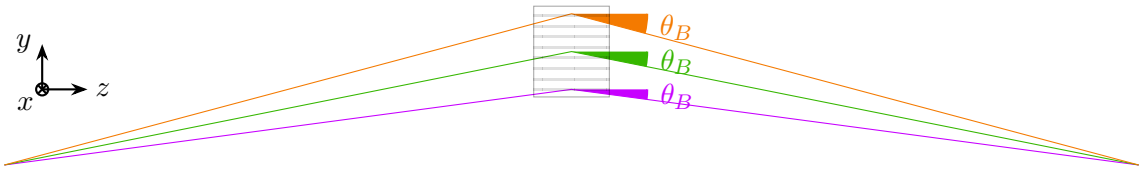


Figure 3.9: Focusing of polychromatic incidence in Laue geometry, featuring the reflection of three wavelengths $\lambda > \lambda > \lambda$. The Bragg angle θ_B of every wavelength is indicated in the respective color.

Since each angle corresponds to the Bragg angle of a specific wavelength, it acts as a wavelength filter, thus fulfilling condition 2, as defined in Section 3.3. However, the optic used for compact XFI setups should maximize the flux in the focal spot as expressed by condition 4 in Section 3.3. The source in this setup is an X-ray tube, which is presented in detail in Section 4.1. Naturally, its spectrum is not flat, it has strong characteristic lines above its bremsstrahlung spectrum. To maximize the flux to the focal spot, it is essential to maximize the solid angle coverage of possible reflection centers at the wavelength of a characteristic line. Since the Laue lens assigns a single incidence angle to every wavelength in its classical design, it cannot satisfy this requirement as effectively as the previously discussed reflection geometries.

To focus a divergent beam of constant wavelength using a Laue lens, the reflecting crystal planes must be aligned on a Rowland circle. This focusing condition arises solely from the underlying Bragg reflection, regardless of whether the geometry corresponds to an overall reflection (Bragg) or transmission (Laue) geometry. This would give the Laue optic essentially the same geometry as the Johann or Johansson optics presented in Section 3.4.2 or, if exploiting mosaic focusing, the von Hámos geometry presented in Section 3.4.1. The only difference would be the incidence of the beams on the front surface and the associated transmission, which would negate the advantage of requiring less crystal volume, as it is the case when focusing non-divergent beams.

For further explanations about Laue lenses and their concrete realization, refer to [74, 97].

3.4.4 Alternative X-ray Optics

Apart from Bragg reflection, alternative physical principles can be applied to X-ray optics. Some examples are presented in this section.

Refractive X-ray lenses

As demonstrated in Section 2.1, the refractive index of materials in the X-ray regime is given by $n = 1 - \delta + i\beta$, where δ and β are small, positive values. Therefore, the refractive index n is less than, but close to one, accounting for a weak refraction away from the normal of a transition from air to matter. As a result, X-ray lenses used for focusing must have a concave design with multiple individual lenses in series to produce significant focusing. Optical systems that use this design are referred to as compound refractive lenses (CRLs). A stack of N paraboloid-shaped lenses, each with a curvature of R at the apex and made of a material with a certain value of δ, has a focal length f of [100]:

$$f = \frac{R}{2N\delta}. \tag{3.1}$$

Up to $N = 300$ lenses are stacked [100]. Since δ has a strong wavelength dependence, $\delta \propto \lambda^2$ [22], the focal length f depends strongly on the energy E of the incident X-rays to be focused, $f \propto E^2$, which sets a possible challenge for achieving requirements 1 and 2, defined in Section 3.3. Furthermore, refractive X-ray lenses require a small divergence of the incident X-rays for tight focusing [101]. These lenses are used, for example, for microanalysis with a micrometer-range beam at synchrotron beamlines [101, 102]. However, they are not designed for focusing high-energy X-ray tube radiation.

Fresnel Zone Plates

Fresnel zone plates rely on the diffraction of X-rays at narrow slits that are arranged, for example, in concentric rings, and can focus X-rays onto a focal point.

However, even the focusing of X-rays as low as 8 keV, originating from a point-like source, already introduces major challenges for the thickness of the outermost ring of the zone plate, as well as stability issues for the high aspect ratio needed for focusing [103]. This would present fabrication challenges, which is why the maximum size of Fresnel zone plates at high energies lies in the 10th of µm range [104]. Therefore, zone plates manufactured to date cannot focus the spot of a conventional X-ray tube. Their high divergence and energy bandwidth would present additional challenges.
This is reflected by their application in, for example, X-ray microscopy, in combination with highly coherent X-ray sources and focusing energies of a maximum of 30 keV [10]. Fresnel zone plates are not discussed further as an alternative for compact XFI systems.

Total Reflection Optics

Various X-ray optics rely on total external reflection, which is introduced in Section 2.1, as the underlying principle. At 30 keV the total reflection angle in, e.g., graphite is $\theta_c \approx 0.04°$ [28]. Therefore, e.g., a von Hámos optic for this or even higher energies around 60 keV, relying on total external reflection, would be very large, which is not compatible with objective 5, defined in 3.3.

Total reflection optics are commonly used in applications in astrophysics [105], e.g., in Wolter optics [106, 107]. They additionally often rely on non-divergent incidence and are therefore not suited for the discussed use case.

At lower energies, total reflection optics are used, e.g., as polycapillary X-ray optics [108, 109]. The latter ones are used to focus X-rays up to 40 keV [10].

Other Reflection Optics

In addition to the geometries discussed in more detail in Sections 3.4.1 and 3.4.2, other geometries using either total external or Bragg reflection are also widespread. This section briefly mentions some of these geometries.

Kirkpatrick-Baez optics [105, 110] consist of two elliptically curved mirrors arranged one behind the other and perpendicular to each other. Montel optics [111, 112] are comparable to Kirkpatrick-Baez optics, but use the two elliptically curved mirrors in a nested

setup, directly next to each other. Both related types of X-ray optics are widely used in synchrotron beamlines, but are not useful for extended sources like X-ray tubes. They are also very large and heavy.

X-ray optics can also be constructed using multilayers instead of conventional crystals, which, e.g., allows for a precise control of the Bragg angle [113]. The current technological lower limit of a single layer thickness is about 8 Å [113]. At high energies around 60 keV, this would correspond to a Bragg angle below 1°, which poses a challenge to fulfilling condition 5, defined in Section 3.3. A multilayer approach does not enable the use of the focusing properties of mosaic crystals, presented in Section 3.1, but is an alternative to using perfect crystals. For further considerations of multilayer X-ray optics, refer to [113].

Therefore, Bragg reflection at mosaic crystals is the most promising option to fulfill all properties defined in 3.3.

3.5 Von Hámos Optic Layout

This section discusses the practical implementation of a von Hámos geometry for compact X-ray fluorescence imaging using mosaic crystals. It applies the mosaic crystal model presented and discussed in Chapter 2. Figure 3.10 shows all relevant geometric parameters.

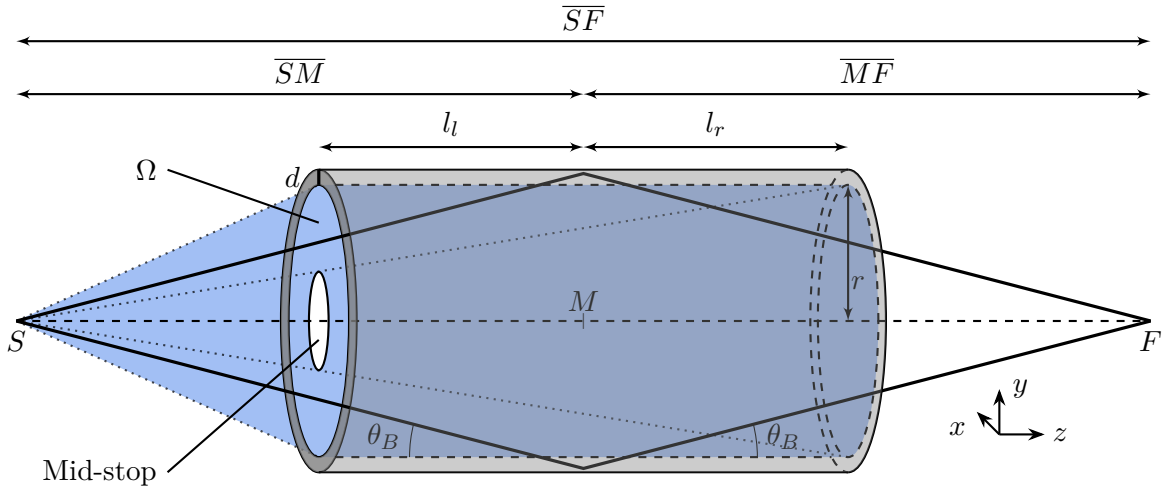


Figure 3.10: Von Hámos optic design utilizing a mosaic crystal. Illustrated are all relevant geometric parameters. The optic focuses a point source S to a focal point F and provides a solid angle coverage Ω that is dependent on the Bragg angle of the reflection and the spatial extent of the optic.

The von Hámos geometry has three main properties: its radius r, the reflecting material, and, for crystals, the set of reflecting lattice planes. The latter defines the Bragg angle for the reflection of an energy that will be focused, via Equation 2.58. As described in

Section 3.3, the radius r of the optic allows for a flexibility in its overall size. A larger radius corresponds to a longer distance $\overline{SF}$ between the source (S) and the focus point (F).

The point M is given by the middle of the Rowland circle segment of the underlying mosaic focusing, where the non-tilted crystallites exactly fulfill the Bragg condition for the wavelength to be focused. This is illustrated in Figure 3.1b. $\overline{SF}$ is exactly twice the horizontal distance from the source S to the point M where the beams have an incident angle of exactly θ_B:

$$\overline{SF} = 2\overline{SM} = 2r\cot\theta_B. \tag{3.2}$$

The center beam is reflected by crystallites with no tilt, $\delta = 0$. Since the tilt follows a Gaussian or Lorentzian distribution around $\delta = 0$, non-tilted crystallites are most common. Therefore, the center beams contribute the most to the overall reflectivity.
This is utilized by shifting the position of the optic on the central axis so that its center M matches the Bragg angle of the energy to be focused, thereby satisfying requirement 3 as specified in Section 3.3.
To maximize the flux, the optic should be tuned to a z-position such that the middle reflection corresponds to a high-flux part of the spectrum, i.e., a characteristic line of the X-ray anode in use.

Beams that are reflected at a point toward the source reach the optical surface at a steeper angle, while those reflected at a point toward the focus have a flatter angle of incidence. The corresponding crystallites must have the appropriate tilt δ. Since this tilt is expressed by the crystallite's mosaicity, this value limits the maximum incidence angles and energy-bandwidth that can be reflected. This provides a reasonable option to limit the length of the optic, based on the value of the crystal's mosaicity β, by setting the range of possible incidence angles θ onto the optic to $\theta_B - \beta \leq \theta \leq \theta_B + \beta$. Since the number of crystallites outside this range is very small, they would not significantly contribute to the reflectivity. Therefore, the lengths l_l and l_r can be calculated to:

$$l_l = r\left(\cot\theta_B - \cot\left(\theta_B + \beta\right)\right), \quad l_r = r\left(\cot\left(\theta_B - \beta\right) - \cot\theta_B\right). \tag{3.3}$$

Note that $l_r > l_l$, which is also reflected by Figure 3.2b and explained in Section 3.2.1.

The main objective of the optic is to maximize the intensity of the focused beam, which depends on the reflectivity of the optic and the number of photons that are incident on it.

The latter value is directly dependent on the solid angle coverage Ω of the optic, which is illustrated by the blue cone in Figure 3.10, and is given for a point source by:

$$\Omega = 4\pi \left(\sin^2 \left(\frac{\theta_{\text{front}}}{2} \right) - \sin^2 \left(\frac{\theta_{\text{back}}}{2} \right) \right), \tag{3.4}$$

$$= 2\pi \left(\cos \theta_{\text{back}} - \cos \theta_{\text{front}} \right), \tag{3.5}$$

where θ_{front} denotes the steepest geometrically possible incident angle at the front of the optic and θ_{back} denotes the flattest geometrically possible incident angle at the back of the optic. For an optic with a length as defined by Equation 3.3, these angles are given by $\theta_{\text{front}} = \theta_B + \beta$ and $\theta_{\text{back}} = \theta_B - \beta$. Note that the solid angle depends solely on the angles that define the optic. It does not depend on the radius of the optic. This once again illustrates the flexibility of the design's size.
However, as explained in Section 3.2.4, the absolute value of defocusing depends on the radius of the optic, which defines the distance between the reflecting crystal and the optical axis. Larger radii, and thus longer distances between the source, the optic, and the focus, lead to greater absolute values of defocusing. Depending on the specific proportions, this effect might not be significant since the absolute values of defocusing add to the minimal focus size, which is determined by the focal spot size of the source.

Theoretically, the maximum possible angle of reflection can be achieved by a beam that strikes the front surface of the optical element at an angle of θ_{front} and is reflected by a crystallite with the maximum possible positive tilt permitted by the underlying mosaicity. The corresponding energy of this beam, given by the Bragg condition, could only be reflected at the very front of the optic, since no other point would allow for this steep angle. Therefore, it would contribute very little to the overall reflectivity. It is therefore sufficient to consider only those energies whose corresponding Bragg angles fall within the range of possible angles of incidence on the optic, without taking the mosaicity into account. Thus, for all energies within the corresponding energy bandwidth ΔE, there is at least a 50 % coverage of the mosaic distribution of crystallites that can theoretically reflect the corresponding beams.
ΔE can therefore be estimated by the angles that define the optic via Equation 3.4 and results from Bragg's law (Equation 2.58) in first order:

$$\Delta E = \frac{hc}{2d_{hkl}} \left(\frac{1}{\sin \theta_{\text{back}}} - \frac{1}{\sin \theta_{\text{front}}} \right). \tag{3.6}$$

This bandwidth is a reasonable lower estimate. Although the actual range is higher for the reasons mentioned above, energies outside this range are significantly less likely to occur.

Apart from the optic itself, the bandwidth ΔE can be further reduced by suitable apertures, which are briefly described in Section 4.2. Higher-order reflections, as described in Section 2.4.1, can also be shielded in this way. The complete setup can therefore fulfill requirement 2, defined in Section 3.3 even when tuned to different wavelengths.

To provide the required filtering properties of the optic, only geometrically reflectable beams should be incident on the focus. Non-interacting photons should be blocked, which is accomplished with a mid-stop, illustrated by a white circle in Figure 3.10. The midstop can limit the flattest incidence angle for the reflection optic. Note that, in a concrete realization, the midstop expands along the z-axis and can be placed in different z-positions.

X-rays with steep angles that cannot interact with the optic or the midstop should also be absorbed by appropriate apertures. These apertures are part of a compact XFI beamline, which is presented in Section 4.2.

As mentioned in Section 3.4.1, the utilization of the cylinder geometry is essential for the focusing properties of the von Hámos optic. Transitioning from a flat to a curved hollow cylinder, with the cylinder axis lying on the connecting axis between the source and focal point, converts the source-angle mapping of a Bragg-reflective plate to a source-focal point mapping. Apart from this essential focusing, bending the diffracting crystal introduces additional optical properties that are not covered by the focusing and defocusing effects of flat mosaic crystals, which are explained in 3.1 and 3.2. These are explained in the following Sections 3.5.1 and 3.5.2 using von Hámos optics as an example. They are also relevant for all other optics that use curved crystals.

3.5.1 Orientation Gradient Effect

According to Chantler, bent crystals can be modeled as a stack of crystal lamellae with gradually changing orientations [114]. If a flat crystal is bent into a cylinder of radius R, only the inner lamellae will be bent to this curvature. The layers in depth t will be bent to a bending radius of $r(t) = R + t$. When paired with an extended source, this leads to an adopted combination of depth defocusing, explained in Section 3.2.1, and azimuthal defocusing, explained in Section 3.4.1.

When a beam originating from a point source is incident on a point on the cylinder's inner surface, a distinct incidence angle is defined. If the beam originates from an extended source of half-width w, the incidence angle onto a point on the cylinder can, when using small angle approximations, differ by roughly $\pm\frac{w}{d}$, where d is the distance between the source and the incidence point. The incidence angle can be divided into two angles: an

angle θ_n between the cylinder surface in the direction of the cylinder axis and the surface normal, and a second angle θ_p perpendicular to the first one.

If Figure 3.1 is considered as a cut of a von Hámos optic at its bottom, then θ_n corresponds to the angle part in the y-z plane and θ_p to the angle part in the x-z plane. θ_n adds to the incidence angle of the two-dimensional illustrations of the focusing and defocusing in the y-z plane in Sections 3.1 and 3.2. In the considered case of Figure 3.1 as a cut of the von Hámos optic, the angle θ_p expresses the dependence $x(z)$. After the beam is incident onto a point on the cylinder, it penetrates into the diffracting crystal's bulk, where it can ultimately be reflected if it satisfies the Bragg condition. As derived in Section 2.4.3, the effective depth of a possible Bragg reflection is not discrete. Depending on the depth of the reflection, it occurs at a layer that bends according to $r(t)$, as explained above. This results in the relative angle between the reflecting plane and the beam becoming a function of the reflecting depth and θ_p. It is complemented by the influence of the mosaic spread described in Section 3.2.3 and leads to a broadening of the focus.

The orientation gradient effect in bent crystals is particularly relevant for small cylinder radii, thick reflective crystals, and large source point extensions. The broadening effect by θ_p is perpendicular to the bulk defocusing effects, described in Section 3.2.1. Therefore, in the focal point of the entire von Hámos geometry, it cannot be distinguished from the bulk defocusing effects that originate from parts of the crystal with a relative offset of $\frac{\pi}{2}$ in the azimuthal angle.

3.5.2 Anticlastic Curvature and Quasi-Mosaicity

According to the Poisson effect, bending a thin plate along an axis causes lateral contraction, which leads to secondary deformation in the perpendicular direction, known as anticlastic curvature [115]. The plate then takes on a saddle shape, which can be prevented by using a suitable clamping device during the bending process.

A crystal's mechanical properties can be anisotropic depending on its structure. In this case, primary bending can lead to bending of the crystal lattice planes that are perpendicular to the main surface of the plate [81, 115]. This property is referred to as quasi-mosaicity because it cannot easily be distinguished from conventional mosaicity effects in the described direction. For further details, refer to [115].
Since the set of reflecting planes of a crystal bent for von Hámos optics is parallel to the main surface of the plate, it is unaffected by quasi-mosaicity. Therefore, the effect is not further discussed.

4 Super Compact Optics-Based Tunable Testbed for Imaging (SCOTTI)

The purpose of the von Hámos optic is to provide a focused beam with properties as comparable to a synchrotron beamline as possible, while using an X-ray tube as the source of radiation. Chapter 2 explains the underlying physical principle of the optic, which is X-ray diffraction by mosaic crystals. Chapter 3 discusses the implementation of these properties in a von Hámos optic, which can meet the requirements defined in Section 3.3. This chapter describes the implementation of the optic as the core of a laboratory measurement system. The system was given the name SCOTTI, and will be referred to as such in the following. Figure 4.1 shows the schematic of the SCOTTI setup, including the X-ray tube, the optic, a detector, and all apertures as well as an exemplary beam path. The distances, sizes and angles are not to scale.

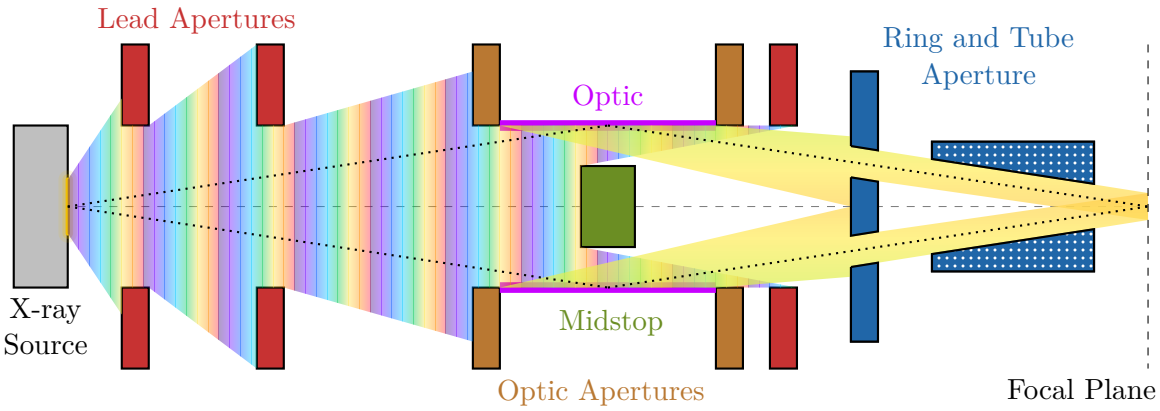


Figure 4.1: Conceptual illustration of the Super Compact Optics-Based Tunable Testbed for Imaging (SCOTTI) setup with possible beam paths. The radiation of the used X-ray tube has a large coverage of $40° \times 30°$ [88] and a broad spectrum, illustrated by the multiply colored area of beams from the left. It is shielded by lead apertures and the front optic aperture, which therefore define the geometrically possible incident beam paths onto a von Hámos optic (purple). The lead apertures not only shield the focal plane from the direct radiation of the X-ray tube, but also block unwanted background arising from scattering by the SCOTTI components. The beam is focused and energetically filtered by the von Hámos optic, illustrated by the remaining yellow area of possible beam paths. It is not exactly monochromatic, but rather has a narrow, focused bandwidth, which is illustrated by slightly different shades of yellow. The ring and the tube apertures, illustrated in blue, further energetically filter the beam by blocking specific focused beam paths. Detectors or further experimental setups can be placed in the focal plane (dashed line).

The focused energy of the SCOTTI beamline is defined by the distance between the X-ray tube and the used optic, as explained in Section 3.5. The energetic window in which the focused beam can lie is defined (downwards) by the minimum and maximum geometrically achievable distances between the individual components of the setup and, in the upper range, additionally by the X-ray tube itself. The SCOTTI setup is enclosed in a lead-shielded cabinet to ensure radiation safety.

All parts of the setup, except for the optic, starting with the used X-ray tube. For details about the optic, refer to Chapters 3 and 6.
For detailed descriptions about the aperture design, function and implementation, refer to [116], and for details about the control of the setup, refer to [117, 118].

4.1 SCOTTI X-ray Tube

In the SCOTTI setup, a Comet MXR-225HP/11, which is a commercial, water-cooled, unipolar X-ray tube with a tungsten anode and a (0.8 ± 0.1) mm beryllium filtering window [88], is used.

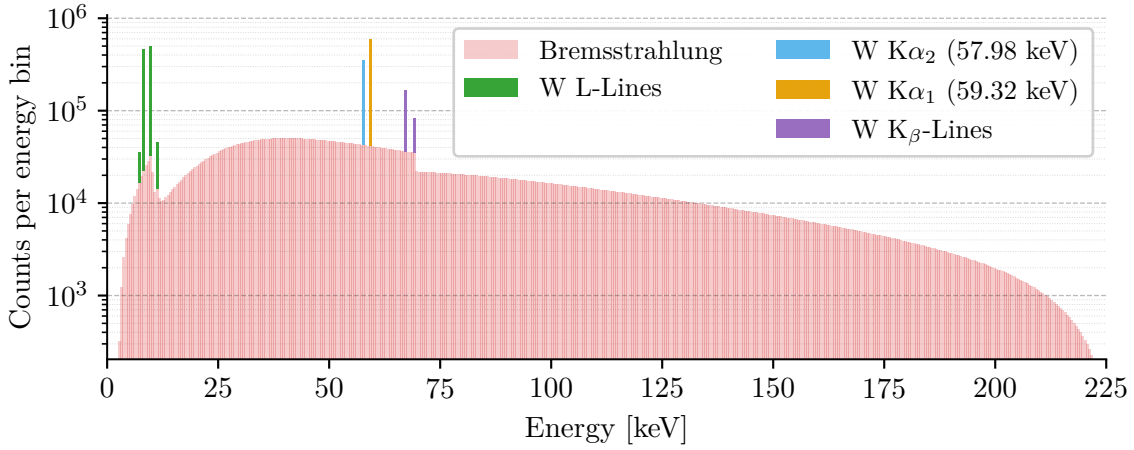


Figure 4.2: Simulated spectrum of the Comet MXR-225HP/11 [88] X-ray tube, used in the SCOTTI setup, at a voltage of 225 kVp, a current of 6.67 mA, and a focal spot size of 1 mm × 1 mm using the `SpekPy Python` package [119]. The characteristic lines and the Bremsstrahlung spectrum are plotted separately.

It provides two selectable focal spot sizes of approximately 0.4 mm × 0.4 mm and 1.0 mm × 1.0 mm and has a fixed anode angle of 11°. The tube operates at a maximum voltage of 225 kVp at a maximum continuous power rating of 800 W for the small and 1800 W for the large focal spot, enabling a high photon flux. Figure 4.2 shows the simulated spectrum of the X-ray tube after its beryllium filter at the maximum voltage of 225 kVp using the large focal spot of 1 mm × 1 mm and the corresponding maximum current of 6.67 mA. The spectrum was simulated using the `SpekPy Python` package [119]. It clearly

shows the characteristic tungsten lines and the continuous Bremsstrahlung spectrum. The strong $K_{\alpha 1}$ and $K_{\alpha 2}$ lines of tungsten are located at approximately 59.32 keV and 57.98 keV, respectively. The $K_{\alpha 1}$ line defines the central energy of the SCOTTI beam to which the optic is tuned in the standard operating mode, as described in Section 3.5. The so defined standard beam path is illustrated by the dotted lines in Figure 4.1.
Note that the used X-ray tube can generally be replaced by other models with different specifications, including the anode material. In the course of this work, only the presented tube was used.

The X-ray tube's broad spectrum of radiation and large radiation coverage of $40° \times 30°$ are illustrated by the multiple colored area of possible beam paths, originating on the left side of Figure 4.1.

4.2 SCOTTI Apertures

Several types of apertures are used in the SCOTTI setup. They fulfill different purposes, which are briefly described in the following.

Lead Apertures

The lead apertures, illustrated in red in Figure 4.1, are necessary to shield the setup from the part of the X-ray tube's emission that is not incident on the optic. Due to the X-ray tube's radiation coverage of $\geq 30\,\%$, it emits a significant amount of radiation in the direction of the focal plane. Without shielding, this would result in a strong background signal. Their beam path blocking effect is illustrated in Figure 4.1.

Optic Apertures

Densimet[1] apertures are placed directly before and after the optic to precisely define the possible incident beam paths onto the optic. In addition, they block photons in the vicinity of the optic that have been scattered by processes other than Bragg diffraction and originate from the optic itself, its housing, or its substrate. The optic apertures are illustrated in brown in Figure 4.1. Additionally, a Densimet midstop, illustrated in green, is necessary to block the direct radiation on the SCOTTI axis, which would otherwise interfere with the focused beam. The blocking effect of the optic apertures to the possible beam paths is visible in Figure 4.1.

[1] Densimet® is the trade name of a heavy alloy with $> 90\,$wt% tungsten, commonly used for radiation shielding and collimation [120].

Ring Aperture and Tube Aperture

The ring aperture, illustrated in blue, and the tube aperture, additionally illustrated with a dotted pattern in Figure 4.1, are placed between the SCOTTI optic and the focus. They do not interact with the direct, unreflected beams of the X-ray tube, since they are already blocked by the upstream apertures. This is illustrated by the yellow area of possible remaining beam paths in Figure 4.1. The small range of different shades of yellow color depicts the focused beam, which has a narrow energetic bandwidth. The purpose of the ring and the tube aperture is to precisely define the beam paths after the optic to further block unwanted scattering, and to be able to flexibly narrow down the energetic bandwidth of the focused beam to $\leq 15\,\%$ FWHM, to achieve requirement 2, defined in Section 3.3, independent of the focused part of the X-ray tube's spectrum.

The ring and tube aperture's function is based on the energetic defocusing properties of the optic, which are described in Section 3.2.2. As illustrated in Figure 3.3b, the energy-dependence of the Bragg angle leads to a spatial separation of different Bragg-reflected energies in the vicinity of the focal plane. This separation can be used to block specific beam paths and therefore filter out the respective wavelengths of the beams on these paths. This is illustrated by the blocking of parts of the yellow cones in Figure 4.1. Without the ring and tube apertures, the energetic bandwidth of the focused beam would only be defined by the optic's mosaicity, size, and position, and would not be as flexible.

Furthermore, as the ring and tube apertures filter part of the defocused beams of the optic, they also reduce the size of the focal spot.

4.3 Detectors

The wide range of experiments possible with SCOTTI requires the use of a variety of detectors. As part of this thesis, four different X-ray detectors were primarily used. These are briefly described in this section.

4.3.1 Pixelated X-ray Detectors

In this work, pixelated detectors are used for spatially resolved measurements of the SCOTTI beam, described in Section 6, for the optic-characterization setup, described in Section 7, and in the detector-sided application of the von Hámos optics, described in Section 8.3. This section briefly introduces the used pixelated detectors.

Actaeon FX5

The Actaeon FX5 detector from Direct Conversion was used for imaging the SCOTTI focus in Chapter 6, and as the detector for an experiment with a detector-sided optic, described in Chapter 8. The detector is based on a 2 mm thick CdTe-CMOS hybrid sensor and has an active area of approximately 52 mm × 26 mm with a pixel size of 100 µm × 100 µm. It enables an efficient detection over a range from 40 keV − 300 keV with added shielding, while supporting a frame rate of up to 2000 frames per second. The quantum efficiency lies above 80 % for energies ≤ 100 keV [121, 122].

Dectris PILATUS3 R 100K-M

As an alternative detector to the Actaeton FX5, a Dectris PILATUS3 R 100K-M hybrid photon-counting detector was used for some measurements of the SCOTTI beam focus, described in Chapter 6. It features a sensitive area of approximately 83.8 mm × 33.5 mm with a pixel size of 172 px × 172 px and is based on a 1 mm thick CdTe sensor. It is optimized for energies from a few keV up to several tens of keV [123].

Minipix

The characterization setup, explained in Section 7 is equipped with an Advacam MiniPIX EDU detector, which is based on a 0.5 mm thick silicon Medipix Timepix chip [124]. It features an active are of about 14 mm × 14 mm with a pixel size of 55 µm × 55 µm and is suited for detecting X-rays up to about 50 keV [125].

4.3.2 Energy-Resolved Detectors

In this work, non-pixelated, energy-resolving detectors are primarily used in the flux measurements of the SCOTTI beam, briefly described in Section 5.2. The detectors used for this purpose are briefly described below.

Amptek X-123 Silicon Drift Detector

The Amptek X-123 FAST SDD® is a silicon drift detector with a sensitive area of 70 mm^2 and a detector thickness of 0.5 mm. It is optimized for X-ray spectroscopy in the energy range from 2 keV − 30 keV and features a count rate of more than 2 million counts per second. The energy resolution is 123 eV FWHM at 5.9 keV [90]. It is commonly used in XFI experiments for detecting fluorescence markers in the respective energy range [8].

The use of potential detectors is not limited to those listed above. They are merely a selection. For more details on the choice of possible detectors for XFI, refer to [126].

5 X-ray Tracing

This thesis uses ray tracing simulations to investigate the effects of the geometric and crystallographic properties of the optics and apertures designed for use in SCOTTI, as well as to design experiments and predict their results.

XFI simulations are performed using the `GEANT4` toolkit [9, 23]. However, this software package is primarily designed for simulating particle transport and interactions with matter using a Monte Carlo approach [127].
While third-party extensions that allow for a simulation of basic Bragg reflections are available for `GEANT4` [128], its framework remains oriented toward particle-matter interaction rather than efficient ray tracing for X-ray optics. In particular, it does not include a native implementation for modeling X-ray optics based on Bragg or Laue diffraction that would be comparable to the specialized codes presented in the following. Since the simulations of the optics in this work focus on the behavior of mosaic crystals as X-ray optics, rather than relying on the combination of atomic particle simulations and X-ray tracing, a purpose-built ray tracing code was used.

Various open-source codes, specifically designed for X-ray tracing, have been tested for their suitability for the planned simulations, especially for simulating the von Hámos optics. The tested codes are: `SHADOW` [72], `McXtrace` [129], `mmpxrt` [130], and `xrt` [78]. In addition, a non-public ray tracing code from Technical University of Berlin was included in the comparison [131]. This code is based on an algorithm published by Schlesiger et al. in [132].

The ray tracing code `xrt`, short for `XRayTracer`, proved to be the best option, because it natively supports the integration of mosaic crystals into simulations, offers free choice of the surface geometry for optical elements, provides extensive options for placing apertures, and is easily customizable thanks to the use of `Python` as its programming language. It also provides fast computation, supports parallelization and batch processing, and can easily be run on the PHYSnet computing cluster at the University of Hamburg [133] for larger simulation studies. Therefore, all ray tracing simulations in this work were performed using `xrt`.

Note that none of the mentioned ray tracing codes generates a complete model of a mosaic crystal composed of individual crystallites, as it would be too computationally intensive to

simulate the interaction of every ray with every crystallite. All models sample individual crystallites with random orientations based on the mosaic structure at specific sampled points of interaction, or use a model based solely on the crystal‘s probabilities, such as the one used in `xrt`, which is presented in Section 5.1.

5.1 Implementation of the SCOTTI Setup in `xrt`

`xrt` does not provide the possibility to combine X-ray reflection processes with X-ray scattering processes. The simulations in this work are therefore idealized in the sense that only photons reflected by Bragg reflection or interacting with apertures and beam stops are taken into account. Other relevant scattering processes like scattering on the edges of apertures or non-coherent scattering at the optic are not included. These scattering processes are considered experimentally and by simulations in the dissertation of Jannis Haak [116] and require way more computationally intensive simulations, additionally performed with `GEANT4`.

However, many parts of the SCOTTI beamline apertures are designed to eliminate unwanted scattering anyway. Section 5.2 includes a comparison between an `xrt` ray tracing simulation and experimentally data of a focused SCOTTI beam. This comparison shows that, for the scope of this work, e.g., evaluating the optics' focusing properties, these simplifications are justified.

In the following section, the implementation of each individual component of the SCOTTI beamline, as introduced in Chapter 4, into xrt is discussed.

X-ray Source

The SCOTTI setup includes an X-ray tube with a peak voltage of 225 kV and a maximum current of 6.67 mA. For its implementation in the simulations, the `Python` package `SpekPy` [119] is used to simulate the spectrum of this source. By using this tool, the user can flexibly choose between any possible combination of voltage and current.
The focal spot of the X-ray tube is implemented to fit its available 0.4 mm × 0.4 mm and 1.0 mm × 1.0 mm spot sizes [88].

It is possible to only simulate rays under a certain range of emission angles. This is useful as only rays under a specific range of angles can geometrically be incident on the optic. By simulating no beams far outside the solid angle coverage of the optic, computing can be spared, which makes the simulation much quicker.

The generation of rays by the source is done using the `shine` function of `xrt`, which samples a direction and energy of every ray in accordance with the set properties of the source, which include the beam size, divergence, polarization, and number of rays to be generated.

Apertures and Beam Stops

All apertures and beam stops of the SCOTTI beamline are implemented as perfect apertures with no transmission. They are placed at the same positions as in the experimental SCOTTI setup. For details about their exact placing and design, refer to [116]. `xrt` does not provide the possibility to implement apertures with scattering or non-ideal absorption.

The interaction between apertures, beam stops, and rays is simulated using the `propagate` function of `xrt`, which first determines the point of incidence of the generated rays on the aperture's or beam stop's plane by using the sampled ray directions. Those rays whose point of incidence lies on the aperture are then marked with a `lost` flag. In the final result on a simulated detector, these rays are weighted with a factor of $w = 0$, and thus do not contribute to the simulated detector image or its flux.

Optic

`xrt` has the possibility to compute X-ray reflections following a Monte Carlo ray tracing approach. Therefore, a crystalline material is defined by its crystal basis and lattice, as described in Section 2.4.11, using data from the "Crystallography Open Database" [79] and employing the `CrystalFromCell` function of `xrt`. The crystal plane set that should be respected for the simulation, as well as its main orientation to the surface of the optical element, are defined. Additionally, the mosaic spread and the thickness of the reflecting crystal layer are defined. Finally, the type of reflection (Bragg reflected / transmitted or Laue reflected / transmitted) is set.

The shape of the von Hámos optic is defined as a `SurfaceOfRevolution` optical element, using the defined crystal as its material. For mosaic crystals, the default reflection calculation follows a model that is based on the approach of Zachariasen, as explained in Section 2.4.6. However, `xrt` only supports a basic approach that does not consider extinction effects or their corrections by default.
Based on this, the underlying computation was adapted throughout this work to align with the diffraction descriptions of mosaic crystals in the Section 2.4.6, especially with respect to extinction effects and their corrections, as explained in Section 2.4.8. The adapted model also provides the option to define a Lorentzian mosaic distribution, in addition to the Gaussian mosaicity that is included in the default reflection model. The

custom adaptations of the base code are controllable via additional input parameters to the `CrystalFromCell` function.

In a reflection calculation using the adapted `reflect` function of `xrt`, the exact point and angle of incidence onto the optic's surface is calculated for every ray, using its sampled direction. The relative angle between the incident angle and the mean orientation of the lattice planes defines the tilt a crystallite would have to have in order to reflect the ray in accordance with the Bragg condition. As the tilt of the crystallites follows the defined mosaic distribution of the crystal, this implies a certain probability of a suitably aligned crystallite within the ray's pathway. The reflectivity of a ray is calculated by integrating the reflectivity of a thin crystal layer, as expressed by Equation 2.97, over the pathway of the ray. The ray is subsequently weighted by a factor w that corresponds to the calculated reflectivity, as an expression of its reflection probability. The interaction depth is sampled in accordance with the remarks in Section 2.4.3 with respect to the decreasing probability of reflection due to absorption effects. This way, the simulations include the bulk defocusing effects of mosaic crystals, as explained in Section 3.2.1.
Regardless of whether this is possible given the defined mosaicity, the propagation direction from the sampled interaction point is determined as if the ray were incident on a crystallite tilted by the appropriate angle. Reflections that are impossible due to a mismatch between the required tilt and the crystal's mosaicity are accounted for by a weighting factor of $w = 0$.

Note that the sampling of an interaction point describes the Darwin-Hamilton approach and does not reflect the wave-nature of the underlying interaction. The justification of this model is discussed in Section 2.4.10.

The adapted reflection model includes all focusing and defocusing properties, described in Chapter 3, as well as the saturation effect, described in Section 2.4.3.

The model of Zachariasen does not include the possibility of multiple successive Bragg reflections. Since `xrt` uses this model with the described adaptations, a ray tracing simulation performed with `xrt` does not include this possibility either. Each ray is transmitted, absorbed or reflected once. Schlesiger et al. propose a reflection model for mosaic crystals as an alternative to the established model by Zachariasen, which allows for multiple reflections [132]. Like the described adapted model in `xrt`, it also includes a possible depth penetration into the reflecting crystal. Multiple reflections introduce an additional source of defocusing as they can cause a lateral displacement of the reflection point. When considering focusing diffraction optics this ultimately causes an enlarged focus. Schlesiger et al. compared measures results to their multiple-reflection model and a single-reflection

Zachariasen model that does not consider a depth penetration. The comparison showed deviations in the simulated spectrum and detector image of about 15 % between the basic Zachariasen model and the experiment in regions away from the intensity maximum of the focus, whereas their reflection model showed $< 5\,\%$ deviation [132]. It is not possible to distinguish between the part of the deviation attributable to depth penetration and the part attributable to including multiple reflections. Since deep penetration is accounted for in the adjusted model in `xrt`, it can be assumed that the corresponding deviation from `xrt` is also smaller.

Additionally, the larger deviation occurs only for reflected X-rays away from the intensity maximum, while the peak intensity remains largely unaffected. Therefore, the deviation of integrated reflectivity predicted by both models is less than 0.7 % [132].
Thus, it can be assumed that no significant errors arise from limiting the adapted reflection model used in `xrt` to a single possible Bragg reflection.

Detector

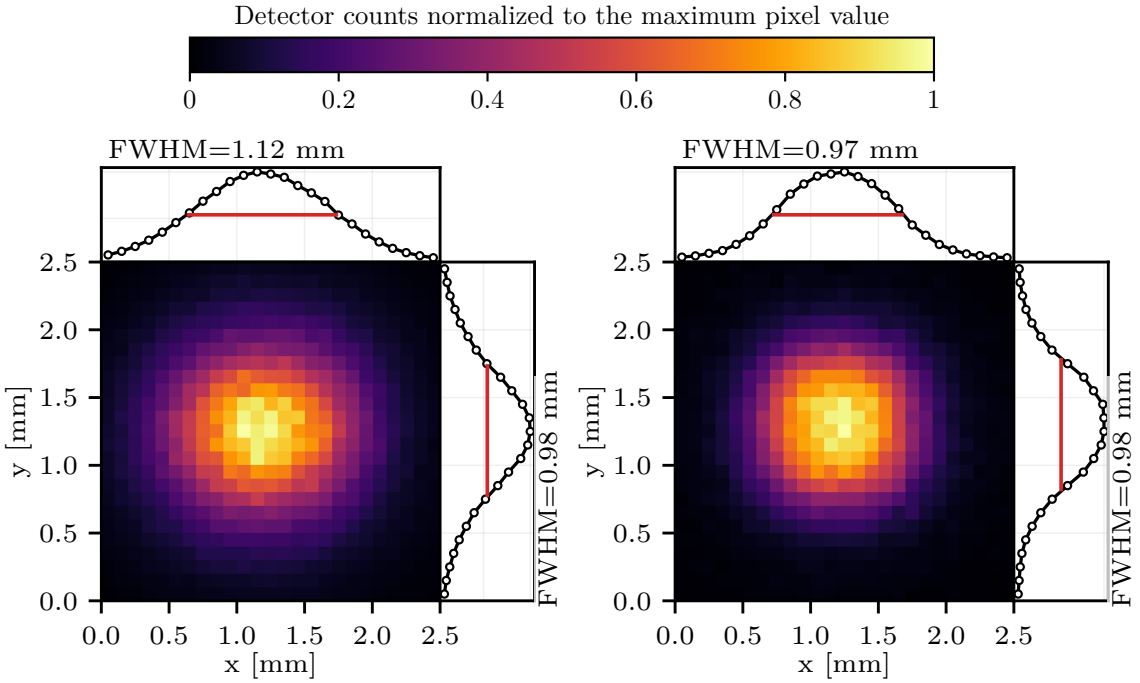
The detectors used in `xrt` are idealized, pixelated detectors without any detector effects, which can be defined with arbitrary pixel counts and sizes. For simulations, serving as a comparison to experiments, the detectors were matched to the pixel sizes and numbers of the respective detectors.

In `xrt`, the `expose` function is used to calculate the exact impact of the rays onto the defined screen and plot the resulting image. The expected number of counts is then calculated by summing up all rays that are incident onto the defined detector, multiplied by their respective weighting factors.

5.2 Comparison of Simulation and Experimental Results

To test the validity of the `xrt` simulations, the focus of the SCOTTI setup, using the K_α lines as the central energy to be focused, was simulated and compared to measurements of the focus. The comparison is done using the bigger available spot size of the X-ray tube, specified by Comet with a size of $1\,\text{mm} \times 1\,\text{mm}$ [88]. For most of the measurements performed with the SCOTTI setup so far, a von Hámos optic with a radius of 10 mm and a reflecting crystal layer thickness of 200 µm of Highly Oriented Pyrolytic Graphite (HOPG)[15] with a mosaic spread of $\beta \approx 0.46°$ was used. The optic is presented in detail in Section 6.1.
Figure 5.1a shows a measured, and Figure 5.1b the simulated focus of the SCOTTI setup including all apertures. The used detector is an Actaeon FX5 pixelated detector, which

is described in Section 4.3.1. The creation and evaluation of the focus is part of every alignment process of the SCOTTI beamline before every measurement and is described in detail in Section 6.5.



(a) Measured SCOTTI focus **(b)** Simulated SCOTTI focus

Figure 5.1: Measured (a) SCOTTI focus using an Actaeon FX5 detector, and a simulated (b) SCOTTI focus using `xrt`, including marginal projections onto the x and y axes. Both images show the normalized focus of a von Hámos optic with a radius of 10 mm, a reflecting crystal layer thickness of 200 µm using HOPG with a mosaic spread of $\beta \approx 0.46°$ as the Bragg-reflecting crystal. The foci are comparable in shape and size, although the measured focus is slightly wider in x, likely caused by an asymmetrical shape of the focal spot of the X-ray tube used in SCOTTI, or to an asymmetry in the optics or their mount. The measured focus has a broader background at the edges due to additional scattering throughout the SCOTTI beamline, which was not included in the simulation.

The total counts given as the simulation result and the total counts measured by the detector used in the experiment cannot be directly compared because the shown experimental results are not corrected for detector effects and efficiency. Additionally, due to the simulation model used in `xrt`, a simulated detector hit carries the weighting factor $w \leq 1$ as its contribution to the total count rate. Therefore, the detector counts for both foci illustrated in Figure 5.1 are normalized to their respective highest pixel counts.

Both foci are comparable in shape and size, although the measured focus is slightly wider in x and has a broader background at the edges, as can be seen in the projections of the foci onto the x and y axis in Figure 5.1. The focus size in y is similar. The asymmetrical shape of the measured focus, which has been observed in all alignments to date, is caused

by an asymmetrical shape of the focal spot of the X-ray tube used in SCOTTI [134]. Additional asymmetry in the optics or their mount can enhance this effect. The slightly broader background in the measured focus in comparison to the idealized simulations is likely caused by scattering, radiation background and imperfect shielding of the apertures. After every alignment process of the SCOTTI beamline, every focus is also evaluated in terms of the achieved count rate, measured in $\mathrm{ph\,s^{-1}}$. The achieved count rate in the focus varies depending on the quality of the alignment. As described by requirement 4 in Section 3.3, a higher count rate is desirable and indicates proper alignment of all SCOTTI beamline components.
Using the described HOPG optic, a maximum count rate of $\Phi_{\mathrm{exp}} \approx 5 \times 10^8\,\mathrm{ph\,s^{-1}}$ has been achieved in multiple alignments, and is used as a reference in the following. The count rate is measured using an established method, which utilizes multiple precisely characterized fluorescence targets in combination with an Amptek FAST SDD®, described in Section 4.3.2. For details about the measurement procedure, refer to [4, 135].

The ray tracing simulation of the setup results in a count rate of $\Phi_{\mathrm{sim}} \approx 5.5 \times 10^8\,\mathrm{ph\,s^{-1}}$ in the focus, which is in good agreement with the maximum experimentally achieved count rate. The good comparability of both foci and count rates confirms the suitability of the chosen simulation model. The simulated count rate is highly dependent on the used crystal's properties, which define its reflectivity. The simulation model assumes a mosaic spread of $\beta = 0.46°$ and a crystallite thickness of $t_0 = 3.19\,\mu\mathrm{m}$. Both values were measured in a characterization measurement of a flat, solid HOPG crystal at the P21.1 beamline (PETRA III, DESY [18]) as part of a material study in [26]. They are discussed in Chapter 6.

However, the actual properties may differ from these assumed values. A deviation of about $\Delta\beta = 0.1°$ in the mosaic spread or $\Delta t_0 = 0.5\,\mu\mathrm{m}$ in the crystallite thickness from the assumed values already causes a deviation of about 15 % in the simulated count rate. Note that the count rate does not scale linearly with the mosaic spread or crystallite thickness. Additionally, the mosaicity determines the focusing and defocusing characteristics of the optic, as explained in Chapter 3. For samples apart from unbent crystal slabs, the mosaic spread is usually not precisely given by the manufacturers. This underscores the need of a characterization setup tailored to the von Hámos optics described in this work and used in the SCOTTI setup, which is introduced in Chapter 7.

It should also be noted again, that the simulations use a computational model that does not account for the microscopic properties of the crystal and may therefore lead to discrepancies. Section 2.4.7 justifies the use of the model and summarizes its limitations.

6 Implementation of a Novel Aluminum Mosaic Crystal Optic

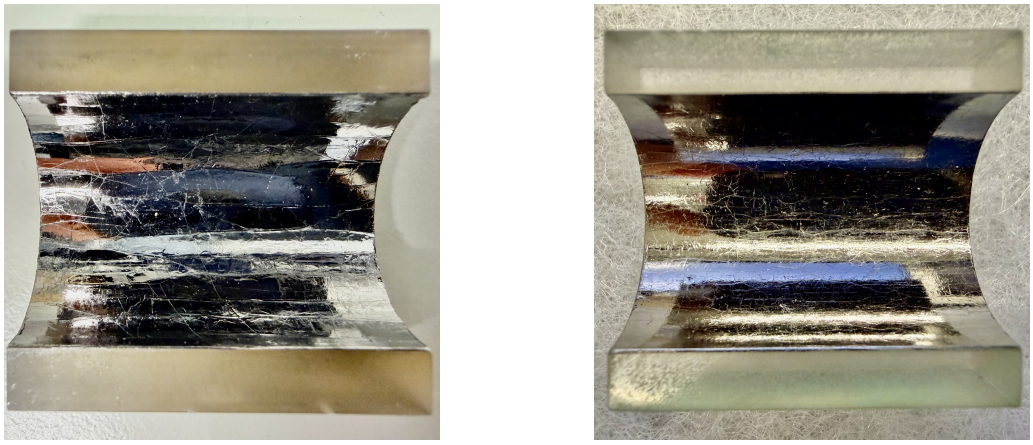
In [26], that preceded this work, 117 different crystalline materials were compared in a numerical study to determine their suitability for use in a von Hámos optic designed for the SCOTTI beamline. The material being searched for should serve as a suitable alternative to graphite-based optics, which are described in detail in Section 6.1. Section 6.2 summarizes the most important results of the material study and evaluates the most promising materials, crystalline aluminum and magnesium oxide, based on their properties and manufacturability.
Concrete concepts for the realization of von Hámos optics using these materials are discussed in Sections 6.3 and 6.4. Section 6.5 first presents samples of a novel aluminum optic, summarizes the results of their testing at the SCOTTI beamline, and finally compares the samples to the graphite optics currently in use.

All estimates in this chapter assume that mosaicity is independent of depth because the models used in this study do not account for depth-dependent mosaicities. Measurements of material probes similar to those used in the currently employed graphite-based optics suggest that the mosaic spread of these optics increases with greater produced thicknesses [136]. However, their provided specifications do not include a concrete depth dependence. If such a connection exists, the mosaic spread would be an average over depth, with deeper regions contributing less to total reflection. Section 7.6 presents a potential measurement to study the depth dependence. In order to account for such behavior, the simulation model would need to be adjusted.

6.1 Pyrolytic Graphite Optics

Von Hámos optics using mosaic crystals, as conceptually presented in Section 3.5, are already in use as part of the SCOTTI beamline. These optics utilize mosaic crystal materials called Highly Annealed Pyrolytic Graphite (HAPG) and Highly Oriented Pyrolytic Graphite (HOPG)[15]. HAPG is the further development of HOPG with a less pronounced mosaic structure [71, 84]. These graphite optics were initially designed together with the Analytical X-ray Physics Group at the Technical University of Berlin, headed by Prof. Dr. Birgit Kanngießer [137], and were built by the Optigraph GmbH [136]. Each of these optics

consists of two half cylinders, which are mounted together to form a full von Hámos optic. Figure 6.1 shows a top view of one half of an HOPG optic and one half of an HAPG optic.



(a) HOPG optic **(b)** HAPG optic

Figure 6.1: Photos of a 200 µm HOPG-coated optic half (a) and a 50 µm HAPG-coated optic half (b). Both feature a respective length of 33 mm and an inner radius of the substrate of 10 mm. Both photos were taken from above and show the uneven inner surface coating of the materials. HOPG shows a more uneven surface with more creases when compared to HAPG. The discoloration of the substrate of the HOPG optic appeared over time.

An optic using pyrolytic graphite can be manufactured by first growing an HOPG or HAPG crystal, from which thin layers between 5 and 20 µm thickness are then removed via an exfoliation process and applied to a polished substrate [138]. Multiple films can be stacked on top of one another to increase the total thickness of an optic's reflecting layer. Bonding to the substrate and between the films occurs purely through adhesion and cohesion, requiring no adhesive. This allows the films to be applied to substrates of arbitrary shape, which gives these optics great flexibility. By applying them to a suitable substrate, a von Hámos optic, as presented in Section 3.5, can be manufactured. The here presented graphite optics utilize a polished glass substrate with a cylindrical inner surface, which is coated with the exfoliated graphite films, as shown in Figure 6.1.

Graphite has a hexagonal Bravais lattice. Its strongest Bragg reflex is the $(h\,k\,l) = (0\,0\,2)$ reflex, which is utilized in the optics by exfoliating and bonding the crystal films so that the corresponding mean crystal planes are parallel to the surface of the optic. At the $K_{\alpha\,1}$ line of tungsten at $E = 59.32\,\text{keV}$, which is used as the central energy in SCOTTI, graphite exhibits a Bragg angle of $\theta_B = 1.79°$.

Despite the basic similarities of the graphite materials, HAPG and HOPG exhibit different properties in terms of their manufacturability and mosaic structure. The well-established HOPG is characterized by a Gaussian mosaicity with a mosaic spread of $\beta \approx (0.4 \pm 0.1)\,°$ at a thickness of 100 µm [139]. Optigraph can produce HOPG optics in thicknesses of up

to 500 µm with the described process [136]. However, the measured Rocking curve width of HOPG samples, which is primarily determined by the mosaic spread, increases sharply with increasing thickness to a value of up to $\beta \approx 0.7°$ to $\beta \approx 1.3°$ at 300 µm thickness, depending on the type of HOPG used. Optigraph sells the described type of HOPG under the name HOPG-flex, which stands for Flexible Highly Oriented Graphite [136].
As described in Section 2.4.6, the mosaic spread is a crucial parameter for a mosaic crystal's integral reflectivity, as it determines the range of angles or energies over which the crystal can reflect incident X-rays. A greater mosaic spread increases the range of angles or energies that can be reflected, but also decreases the peak reflectivity at the Bragg angle because the reflected intensity is distributed over a wider range of angles. Additionally, an increased mosaic spread leads to higher degrees of defocusing, as explained in Section 3.2. When paired with an X-ray tube and apertures, as in the SCOTTI beamline, both effects can ultimately lead to a decreased intensity of the optic's focus. Therefore, the mosaic crystal properties are always a trade-off between the basis of focusing and achievable reflectivity.
Depending on other crystal properties, like modeled crystallite thickness and Bragg angle, the mosaic spread of a crystal for the use in SCOTTI should not exceed about $\beta \approx 0.5°$.

As measured by Optigraph, the integral reflectivity of HOPG samples saturates at around 200 µm to 300 µm total thickness [136], which confirms that the reflectivity of this material strongly deteriorates as layer thickness increases. This is also consistent with experiences from the Analytical X-ray Physics Group at the Technical University of Berlin [131]. Therefore, the HOPG von Hámos optics use a maximum layer thickness of 200 µm.

In [26], a flat, solid HOPG crystal was characterized among other samples at the P21.1 beamline (PETRA III, DESY, Hamburg, Germany [18]) to precisely determine the mosaicity and modeled crystallite thickness of the samples as part of a material study. The results provide a baseline for the properties of the respective materials when used in a von Hámos optic and are listed in Table 6.1. The HOPG sample was characterized to have a Gaussian mosaicity with a mosaic spread of $\beta \approx 0.46°$, which is in good agreement with the values provided by Optigraph. Using the same measurements, the modeled crystallite thickness was calculated to be $t_0 \approx 3.2\,\mu m$, which is consistent with orders of magnitude in the micrometer range that are reported in literature [140, 141].
Based on these values, the saturation thickness of HOPG, as introduced in Section 2.4.3, can be estimated to be about $d_{\text{sat.}} \approx 800\,\mu m$ at the central energy $E = 59.32\,keV$, which is well above the employed maximum total thickness of the HOPG layers of 200 µm. This indicates, that the reflectivities of the HOPG optics are limited by the achievable layer thickness and apparent deterioration at greater thicknesses to about 50 % of the theo-

retically achievable reflectivity. The estimated maximum possible reflectivity could be achieved by increasing the layer thickness beyond the saturation thickness without altering the crystal properties.

The second type of graphite material used in the current optics is HAPG. It exhibits a Lorentzian mosaicity with a mosaic spread of $\beta \approx 0.1°$ to $\beta \approx 0.2°$, depending on the used substrate [136]. For optically polished glass substrates, like the ones used for the HAPG optics presented in this chapter, the expected mosaicity is $\beta \approx 0.1°$ [136], which is therefore used for the simulations in this chapter. The manufacturing process of an optic coating made of HAPG is mostly similar to that of HOPG. However, the producible total layer thickness of HAPG is limited to 100 µm [136]. This value is well below the saturation thickness of HAPG at $E = 59.32\,\text{keV}$, which is estimated to be about $d_{\text{sat.}} \approx 300\,\mu\text{m}$ the same way as for HOPG. The discrepancy indicates, that the reflectivity of the HAPG optics is limited by the achievable layer thickness to about 35 % of the theoretically achievable reflectivity if the layer thickness could be increased above the saturation thickness without changing the crystal properties. This effect is even more pronounced compared to HOPG, which is confirmed by the fact that a higher count rate can be achieved with the HOPG optics than with the HAPG optics in SCOTTI.

The geometrical dimension of the current graphite optics was fitted to the parameters of HAPG, as explained in Section 3.5, with a radius of 10 mm, and an assumed mosaicity of $\beta = 0.1°$. This results in a length of the optics of $l = 33\,\text{mm}$. This length does not fully utilize the mosaicity of HOPG, as its more pronounced mosaicity would correspond to a bigger optic when applying Equation 3.3.
However, an increased length would also significantly increase the defocusing effects, as indicated in Section 3.2, as well as the energetic bandwidth. Together with the already high defocusing by the high mosaic spread of $\beta \approx 0.46°$, the resulting focal spot would have to be limited in size by an aperture to achieve requirement 1, defined in Section 3.3. These apertures are already included in the SCOTTI beamline. Ray tracing simulations show, that an HOPG optic, which is virtually elongated to twice the size of the current optic, so to 66 mm, would increase the count rate in a $1\,\text{mm} \times 1\,\text{mm}$ focus area by about 35 %. Extending the optic beyond this point would not result in an increased count rate at the focal point.

The optic radius of 10 mm and the Bragg angle of $\theta_B = 1.79°$ at the central energy of $E = 59.32\,\text{keV}$ determine a source to focus distance of about 640 mm. As explained in Section3.2.4, greater radii and the resulting larger source-to-focus distances lead to extended defocusing. In contrast, smaller radii and the resulting smaller source-to-focus distances make it difficult to place all the components shown in Section 4 along the SCOTTI

beamline, especially when tuning the setup to lower energies. The radius of 10 mm is therefore a good compromise.

The achieved count rates in the foci vary depending on the quality of the alignment. The established method for determining the flux in SCOTTI uses multiple fluorescence targets for measurement, and is described in detail in [135].
Using the HOPG optics with a crystal layer thickness of 200 µm, a photon flux between $\Phi \approx 3.5 \times 10^8\,\mathrm{ph\,s^{-1}}$ and $\Phi \approx 5 \times 10^8\,\mathrm{ph\,s^{-1}}$ has been achieved across different optics and multiple independent alignments over several years. Using the HAPG optics with a crystal layer thickness of 100 µm, the reproducible count rates vary between $\approx 2 \times 10^8\,\mathrm{ph\,s^{-1}}$ and $\approx 3 \times 10^8\,\mathrm{ph\,s^{-1}}$, depending on the respective optic.
The reported ranges reflect both differences between individual optics and variations obtained with the same optic after repeated alignments. Thus, the quality of both types of optics appears to vary when comparing different optics, as well as across the surface of individual optics. Possible explanations for the varying count rates are given in Section 7.5.2. As discussed above, the lower count rate when using HAPG is mainly caused by the thinner reflecting layer.
To represent an upper estimate of the performance of the graphite optics, the maximum achieved value of $\Phi \approx 5 \times 10^8\,\mathrm{ph\,s^{-1}}$ is used as a benchmark for the evaluation of alternative designs in this chapter.
As specified by requirement 4 in Section 3.3, a higher count rate is desirable for XFI experiments at the SCOTTI beamline, which is why the HOPG optics were used as the default focusing optics until now. However, HAPG optics can still be beneficial for applications that do not rely on maximum integral reflectivity, but rather on narrower reflected energy bandwidths. For their potential use cases, all optics should be characterized by their crystal properties and quality, to explore the cause of their apparent fluctuations in performance. A setup for this purpose is presented in Chapter 7.

6.2 Final Choice of Alternative Optic Materials

Of the 117 materials examined for their properties through simulations and calculations, five possible candidates, in addition to HAPG and HOPG, were identified [26]. Generally, the Bragg reflectivity of possible materials scales linearly with the atomic number Z, while the absorption scales with Z^4 [142]. Therefore, crystals consisting of low-Z elements exhibit a higher Bragg reflectivity.

The identified alternatives are copper (Cu), magnesium oxide (MgO), aluminum (Al), zinc oxide (ZnO), and yttrium-stabilized zirconia (YSZ).

Note that all considerations in the following refer to the crystalline forms and apply the mosaic crystal model. Unbent slabs of these crystals were produced by the MaTecK Material-Technologie & Kristalle GmbH [143] and examined in an experiment at the P21.1 beamline (PETRA III, DESY [18]) regarding their mosaicity and modeled crystallite size.

The crystals were first ranked by their reflectivities using the results of these characterizations. Two candidates stood out: aluminum and magnesium oxide. The zinc oxide and YSZ samples showed a significantly lower reflectivity, likely caused by extinction effects in the crystal.
Copper also showed a much lower reflectivity and a high mosaicity, making it not well-suited for the planned application. The study and subsequent simulations of the optics employed the respective reflecting crystal plane with the highest reflectivity.
The strongest reflexes are the (1 1 1) reflex for the examined crystals with a cubic lattice structure, aluminum, magnesium oxide, copper, and yttrium stabilized zirconia, and (0 0 2) for zinc oxide and HOPG/HAPG with a hexagonal lattice structure. The results of the mosaic spread and the modeled crystallite thickness of the remaining relevant materials are listed in Table 6.1.

Crystal	**Main reflex**	**Mosaicity**	**Mean mosaic spread $\overline{\beta}$ in °**	**$\overline{t_0}$ in µm**
HOPG	(0 0 2)	Gaussian	0.461	3.19
MgO	(0 0 2)	Lorentzian	0.026	9.9
Al	(1 1 1)	Lorentzian	0.195	7.5

Table 6.1: Experimentally obtained mosaic spread and modeled crystallite size of relevant materials for use in a von Hámos optic for the SCOTTI beamline. The values are obtained from the characterization of flat crystal slabs at the P21.1 beamline (PETRA III, DESY, Hamburg, Germany [18]). The results are taken from [26].

Ray tracing simulations of the optics were performed to test the theoretical suitability of the materials for use in a von Hámos optic designed for SCOTTI. These simulations were based on crystal parameters obtained from characterization measurements, and also took geometric effects, such as solid angle coverage, into account. Crystals with a greater Bragg angle at the standard focused energy of SCOTTI of 59.32 keV, have a reduced distance between source and optic, and therefore maximize the solid angle coverage of the optic. Furthermore, a steeper incident angle to be reflected leads to the rays traversing more crystallites and therefore reaching the saturation thickness faster.
Conversely, very shallow Bragg angles can lead to geometrical paths where the rays cannot reach sufficient depths over the relevant length of the optic, which sacrifices potential integrated reflectivity. These considerations also led to the identification of aluminum and magnesium oxide as promising alternatives to graphite-based optics.

In the final step, the manufacturability of the materials was discussed in detail with MaTecK [144]. Magnesium oxide is hard to produce with consistently quality. It is also a very brittle material, making it nearly impossible to bend to small radii without breaking. It is therefore only suited for an optic design, using tiles to approximate the cylindrical shape of a von Hámos optic. Such a design is presented in Section 6.3.

The characterized magnesium oxide sample exhibited a small measured mosaic spread of 0.026°, which shows the near-perfect crystallinity of the probe. However, since the mosaicity is the fundamental principle behind the focusing of the optic, a very small mosaic spread of $\beta \lessapprox 0.05°$ leads to less pronounced focusing properties in a von Hámos optic. Also, the integral reflectivity is directly related to the mosaic spread, as described in Section 2.4.6. It was discussed with MaTecK that the mosaicity of magnesium oxide could potentially be increased by doping the material during crystal growth, if it were chosen as an alternative to graphite-based optics [144].
To reflect this possibility and to be able to compare the performance of an optic using magnesium oxide to the other optics, a mosaic spread of $\beta = 0.195°$, which matches the measured mosaicity of aluminum, is assumed for the simulations of the magnesium oxide optics in the following sections. Note that this is a purely hypothetical value, and it is not clear if this could be achieved in practice.

Aluminum on the other hand is a well-known material, that is easy to produce and handle. Aluminum crystals are not as brittle as magnesium oxide, making it theoretically possible to bend them to small radii [144]. However, this had never been done before by MaTecK. It was not clear to which radii an aluminum crystal could be bent without breaking. Additionally, it was unknown which thicknesses of crystal slabs could be bent. Accordingly, both properties needed to be tested.

Therefore, aluminum is considered for both optic designs: A focusing optic using tiles, described in Section 6.3, and a focusing optic using a crystal, bent to a radius of 10 mm, see Section 6.4.
Additionally, a design using aluminum tiles, that are bent, not to a radius of 10 mm, but rather to larger radii up to 1000 mm, making the bending easier and less likely to break the crystal, is also considered in Section 6.4. All following considerations of the optics used to plan the samples to be produced are based on simulations performed with `xrt` using the experimentally obtained crystal parameters of the flat crystal samples in Table 6.1.

6.3 Tile-Based Focusing Optics

To use unbent crystals in a von Hámos optic, the individual crystal slabs, in the following referred to as tiles, must be arranged in a way, that they approximate the cylindrical shape. Figure 6.2 shows the basic design of such an optic, with a length l, an approximated radius r, a tile width w and a tile thickness of t. The number of tiles is set to 10 in the exemplary illustration. In an actual implementation of the concept, the tiles would need to be arranged by a construction device that holds them in place.

The cylindrical shape is best approximated by using as many tiles as possible. At the same time, narrower tiles are more challenging to produce and harder to align precisely to the approximated cylindrical shape.

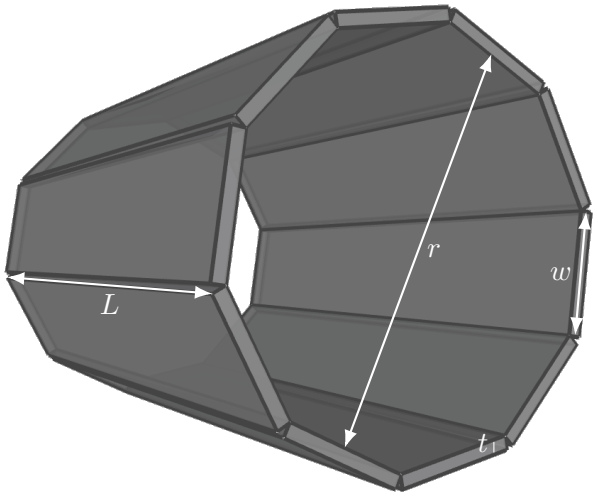


Figure 6.2: Tile optic approximating a von Hámos optic. The illustrated example is made up by ten individual, unbent crystal tiles. The design is not generally limited to ten tiles. Illustrated is the length of the optic L, the approximated radius r, the tile width w and the tile thickness t.

`xrt` simulations using aluminum and magnesium oxide were performed to determine the minimum number of tiles required for the optic to achieve the same performance level as the HOPG optic. The simulated number of counts per second at the focal point of an adapted SCOTTI setup is used as a measure of the optic's performance. Using this performance value instead of pure reflectivity takes into account geometrical effects, such as the solid angle coverage of the respective optic.
Figure 6.3 shows the reflectivity of the two tile optics as a function of the number of tiles.

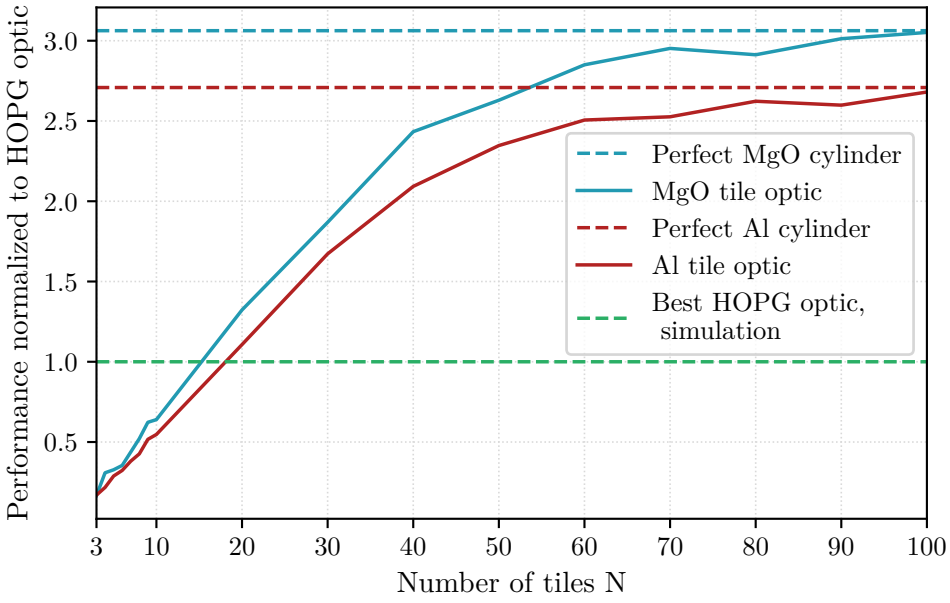


Figure 6.3: Simulated performance of aluminum (Al) and magnesium oxide (MgO) tile optics that approximate a von Hámos optic as a function of the number of used tiles, compared to the performance of an ideal von Hámos optic made of the same materials. The number of counts per second in the respective optic's focus is used as a measure of performance. This value is normalized to the performance of the most suited 200 µm HOPG optic. The thickness of the Al and MgO crystals is set to 1 mm, which is greater than the saturation thickness of both crystals. The mosaicity of MgO is set to match that of aluminum of 0.195°.

All count rates are normalized to the rate achieved with the highest-performing HOPG optic, which serves as the baseline for optic performance. Additionally, the graph shows the theoretical limit of an ideal von Hámos optic made of the respective materials for comparison. The thickness of the crystals is set to 1 mm, which is greater than the saturation thickness of both crystals. For convenience, the length is set to 33 mm, which uses the entire crystal for reflection in both cases. The approximate radius is set to 10 mm because this size has proven ideal for handling optics in the SCOTTI beamline. It also aligns well with the overall length of the beamline.

The width of the tiles w is given by:

$$w = 2r \tan\left(\frac{\pi}{N}\right), \tag{6.1}$$

with N being the number of tiles.

Figure 6.3 shows that, with the use of either crystals, the achievable count rate is already higher than that of the best-performing HOPG optic if about 15 to 20 tiles are used in the described optic concept. The theoretical limit of both crystals is about three times higher than that of the best-performing HOPG optic.

The graphs also show that, for both crystals, the reflectivity of the respective tile-based optic saturates after the use of about 70 tiles. Using more tiles would only further increase the reflectivity by about 5 %. However, note that using more tiles makes the optics harder to produce and align.

The optic using magnesium oxide has an about 10 % higher reflectivity than the one using aluminum. This is caused by a slightly better reflectivity of the material, and a greater Bragg angle of the main reflection, which increases the solid angle coverage of a possible optic. However, note that the mosaicity of magnesium oxide was adjusted to match that of aluminum of 0.195° in order to compare their performance. If the mosaicity of magnesium oxide was as low as measured in the flat crystal sample, the performance of the magnesium oxide optic would not exceed about 60 % of that of the HOPG optic. However, magnesium oxide cannot be bent, so it is limited to the presented design of flat tiles. Section 6.4 explores how curved crystals contribute to a higher reflectivity. To match the performance of a theoretically perfect aluminum optic, about 50 tiles would be needed, requiring a complex assembly and alignment process.

A study by Bartkoski et al. shows that a von Hámos optic can be built using aluminum tiles, and describes the challenges associated with this design [142]. Unlike the optic design presented in this section, their design uses three intercepted approximated cylinder optics. All three parts use different Miller indices in ascending order toward larger radii for reflection. Therefore, the larger rings exhibit a steeper Bragg angle. The largest ring has a diameter of $\approx 10\,\mathrm{cm}$. The sizes of inner rings are not given in the paper, but are optimized to achieve a single focal point for the three rings of the optic. Each concentric ring is composed of about 60 tiles. The length of the individual cylinders is limited by the design, as the outer-lying rings should not be shaded by a ring of smaller diameter.
This design presents additional challenges as all cylinders have to be tuned to each other. Additionally, the divergence of the focused beam from the outer ring is greater. Unfortunately, Bartkoski et al. do not provide a reflectivity or flux measurement at the focal point for comparison with the experiments presented in this thesis.

The reflectivity of Bragg reflections at crystal planes with higher-order Miller indices is generally lower than that of lower-order Miller indices. Thus, the respective rings do not contribute equally to the overall reflectivity of the optic. The results of the study led Bartkoski et al. to conclude that, in a future refinement, the implementation of a solitary cylinder and the subsequent extension of that cylinder should be prioritized over their current design using multiple reflecting rings [142]. This approximated single cylinder would utilize the strongest reflection, which also corresponds to the design presented in this

section. The study of Bartkoski et al. shows that it is possible to construct and operate a tile-based optical system that approximates a von Hámos optic.

6.4 Focusing Optic Using Curved Crystals

Of the materials identified as possible alternatives to the conventionally used HOPG / HAPG optics, only aluminum is bendable in theory. Therefore, this section only considers aluminum. In the following, perfectly bent tiles are assumed. Thus, the number of bent crystals forming a full von Hámos optic is not important for the simulation, as long as their bending radius matches the radius of the optic. However, the number of tiles is of interest for reasons of manufacturability. Additionally, more parts make the final alignment to a full cylinder more complex. Thus, the number of parts should be minimized, ideally to one part or two half cylinders, as in the currently used graphite optics.
Figure 6.4 shows the simulated performance of this optic as a function of its layer thickness, compared to the best-performing 200 µm HOPG optic. The simulation uses the same crystal parameters obtained experimentally for the flat crystal samples in [26], as described in Section 6.3 and listed in Table 6.1. The crystal's length is set to 33 mm and its radius to 10 mm for the same reasons described in Section 6.3.

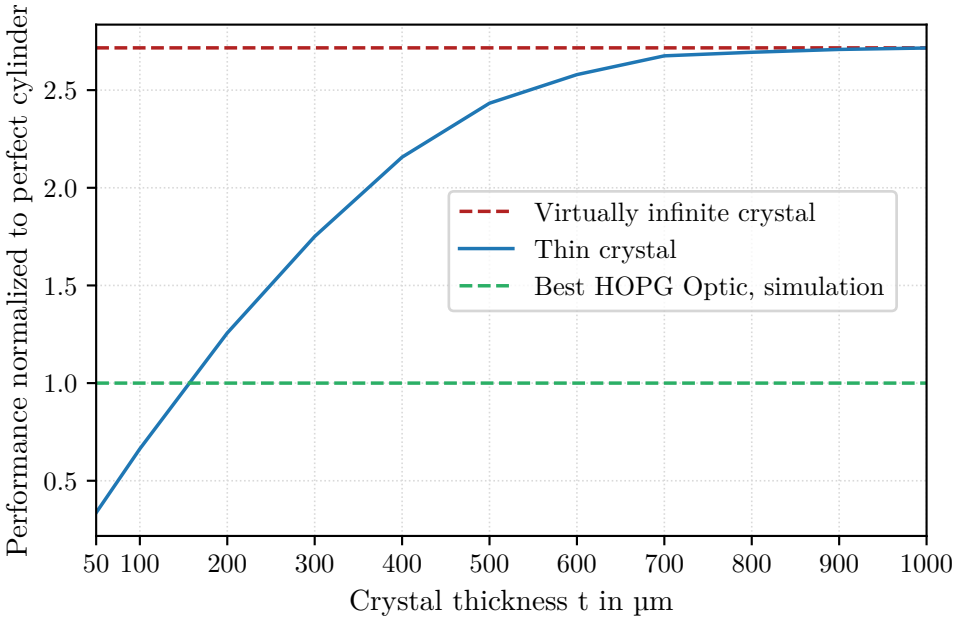


Figure 6.4: Simulated performance of an aluminum von Hámos optic as a function of the used layer thickness, compared and normalized to the best-performing 200 µm HOPG optic. The red line shows the simulated maximum performance of an aluminum optic, if the thickness was not limited, which corresponds to the maximum possible reflectivity. Plotted in blue is the simulated performance of an aluminum von Hámos optic as a function of the crystal thickness t, which shows a saturation to the maximum reflectivity at about $t = 700\,\mu m$.

Figure 6.4 clearly shows that the reflectivity saturates at a crystal thickness of about 700 µm. Note that the reflectivity curve as a function of crystal thickness depends heavily on the mosaic spread and modeled crystallite thickness. Therefore, the plot shown in Figure 6.4 reflects the relation for the measured values of the flat aluminum crystal sample, which is given in Table 6.1. Furthermore, the values are assumed to be independent of the bending of the crystal.

Initially, it was unclear if aluminum could be bent to an inner radius of 10 mm. To test whether an optic could also benefit from higher bending radii, an additional `xrt` simulation was conducted using a tile optic with slightly bent tiles instead of straight ones. Figure 6.5 shows the performance of this special tile optic as a function of the bending radius R of the tiles. The simulated optic uses 30 tiles, resulting in a width of approximately 2.1 mm, which is consistent with the order of magnitude used by Bartkoski et al. [142]. They demonstrated that tiles with a width of few mm are still manufacturable and manageable. The concrete size of their tiles is not given in [142]. For comparison, the simulated values for a perfectly cylindrical aluminum optic and the best-performing HOPG optic are given.

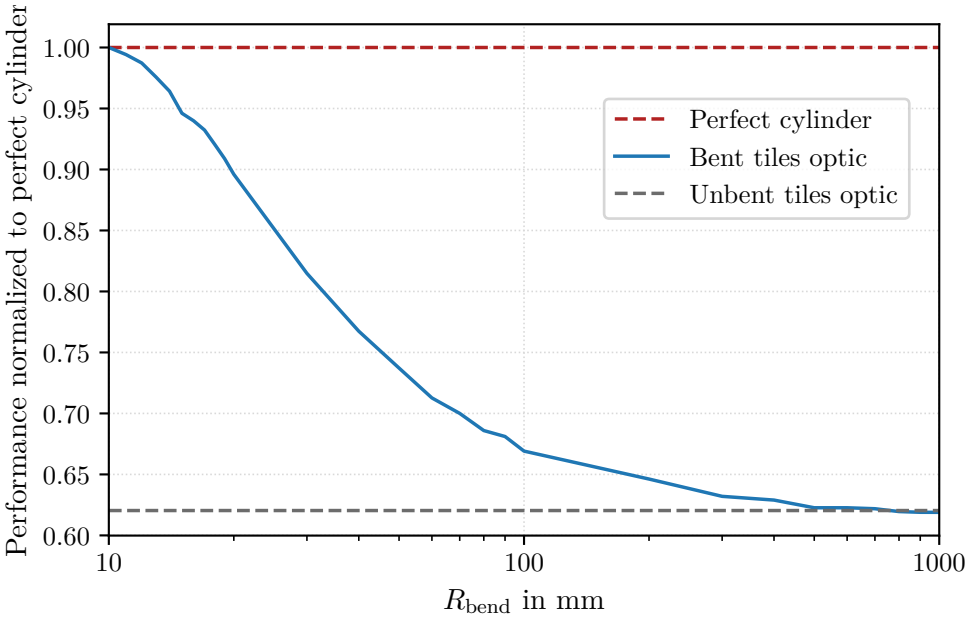


Figure 6.5: Performances of a von Hámos optic approximated by 30 bent tiles, and a von Hámos optic approximated by 30 straight tiles, plotted against the performance of a perfect von Hámos optic.

Figure 6.5 shows that the reflectivity already benefits from slightly bent tiles. A bending radius of less than 80 mm increases the reflectivity by about 10 %. Using bent aluminum tiles instead of straight magnesium oxide tiles would result in a greater achieved performance for this 30-tile optic. Note again that magnesium oxide cannot be bent.

The benefit of bending decreases as the number of tiles increases. However, more tiles eventually lead to a greater chance of misalignment, which reduces reflectivity.

In conclusion, the simulations show that a bent aluminum optic could significantly increase the performance compared to the HOPG optics currently in use, even if bending to a radius of 10 mm is not possible.
Based on the results of the simulations, the first step in producing a prototype was to attempt to bend aluminum crystals to a 10 mm radius. If the crystals showed signs of breaking, the bending radius would be increased. The calculated saturation thickness of 700 µm,based on the assumed crystal parameters, was chosen as a starting point for the samples.

6.5 Experimental Optimization of Aluminum von Hámos Optics

This section describes a stepwise study involving various samples, the purpose of which is to experimentally determine the ideal crystal and production parameters for a prototype of a von Hámos optic.
The experimental study is based on the results of the simulations described in the preceding sections. For the tests, samples measuring 33 mm in length and 15 mm in width, with varying thicknesses t, were manufactured. If bent to the desired radius of 10 mm, a sample of this size is roughly a fourth of a full cylinder, which gives a good indication of the performance of a whole von Hámos optic and is sufficient to produce a focus when used in the SCOTTI beamline.

MaTecK developed a device to bend the samples reliably and reproducible. It is designed to suppress anticlastic curvature, as described in Section 3.5.2 [145]. Based on the results presented in this chapter, the device was improved between the production of different samples. The improvements are outlined in Section 6.5.
Furthermore, the relative direction of bending remained constant among all samples to guarantee reproducibility. Therefore, the crystals are cut in a way, that the normal of the crystal plane set indexed by $\{1\,1\,1\}$ is parallel to the normal of the crystal's largest face to provide a focusing at this plane set. The normal of the face of the crystal with the dimension 15 mm $\times\, t$ is parallel to the $\{1\,1\,-2\}$ crystal planes' normal. Thus, the normal of the face of the crystal with the dimension 33 mm $\times\, t$ is parallel to the $\{1\,-1\,0\}$ crystal planes' normal [145].
Additionally, the $\{1\,1\,1\}$ orientation of cubic crystals like aluminum is highly resistant to elastic bending because its elastic properties are rotationally symmetric about the $[1\,1\,1]$ axis [146].

In the first iteration, two bent crystals were produced by first cutting flat slabs from a grown aluminum crystal, performing a surface treatment afterwards, and finally bending it to the desired radius. Both samples feature a thickness of 700 µm and an inner bending radius of 10 mm. Assuming a mosaicity of $\beta < 0.2°$, as given in Table 6.1, the sample's length of 33 mm is sufficient to use the whole length of the optic for reflection without sacrificing reflectivity. Additionally, this length is already established by the current graphite optics and multiple parts of the SCOTTI beamline are designed to fit this length.

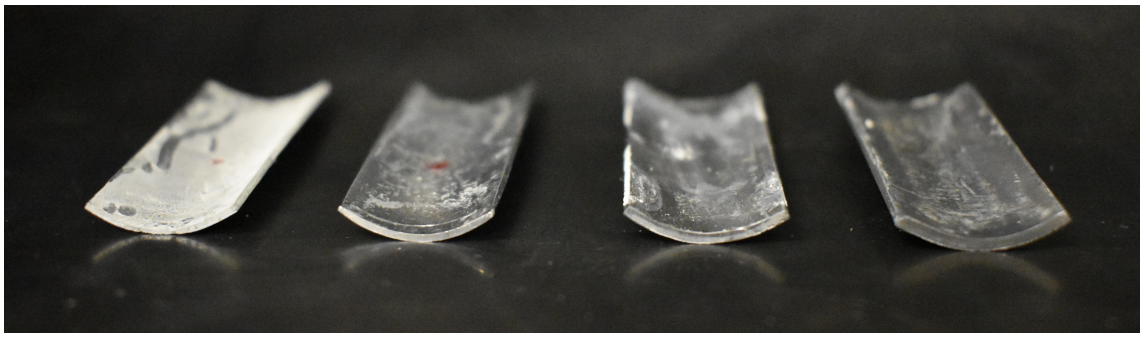


Figure 6.6: Photo (from left to right) of bent aluminum samples 1 to 4. All samples feature an inner bending radius of 10 mm. Samples 1 to 3 feature a thickness of 700 µm, sample 4 has a thickness of 1000 µm. Sample 1 underwent a different surface treatment processes, using a different etching method, than samples 2 to 4.

The two crystals underwent different surface treatments involving two different etching processes to investigate which of them would produce a more intense focus. The exact processes are a trade secret of MaTecK.
Both crystals are self-supporting and do not need a substrate. Figure 6.6 shows a photo of the two bent samples of this first batch on the left.

All samples presented in this chapter were tested in the SCOTTI beamline, employing the same alignment procedure as the currently used HOPG/HAPG optics, to determine their performance and compare it to the current optics. This alignment procedure starts with the alignment of the optic in the $x-$, $y-$, $z-$, $\omega-$ and $\phi-$ directions[1] to focus the beam onto a detector that is initially placed at about double the focal length of the optic. The count rate in the focus and the shape of the focus are used as a measure of the quality of the alignment. This process is partly automated [118]. The maximum count rate is achieved at a position where the K_α line of the used X-ray source at 59.32 keV is best focused. Then, the position of the detector in the $x-$, $y-$ and $z-$directions is fine-tuned to minimize the size of the focus. In an XFI scan, this point marks the optimal location of a sample to be measured. The alignment is typically performed using an Actaeon pixel detector, described in Section 4.3.1.

[1]The $\omega-$ and ϕ angles correspond to the rotation around the y axis and the x axis.

This first step of the alignment is performed without the ring and tube apertures, described in Section 4.2.
After the initial alignment, the apertures are placed one after another in the beam path, and their positioning is optimized. The count rate served as the criterion for this optimization.

The same apertures and mid-stops that were already available for the HAPG and HOPG optics were used in the tests of the samples because the exact values of the influencing parameters, such as the mosaic spread, were unknown at that time. This led to a slightly suboptimal setup of the beamline for the aluminum optics because the apertures block more of the focused beams than when paired with the graphite optics. However, in the case of the ring aperture the loss in flux is only about 10 % higher than for HOPG / HAPG. The current design of the tube aperture is not compatible with the geometry of the aluminum optics. Therefore, it was not used in testing the aluminum samples. However, previous measurements of the graphite optics with the tube aperture included show that its use does not significantly influence the flux in the SCOTTI focus. Therefore, excluding the tube aperture from the test measurements did not lead to an overestimation of the results.

After alignment, the focus flux is measured using fluorescence measurements, as described in detail in [135]. All experimentally obtained flux values in this chapter are given as a mean value from using palladium, rubidium iodide, and silver reference targets in three separate measurements. This procedure has been established for measuring the SCOTTI flux. Therefore, the results can be compared to those achieved with the HAPG and HOPG optics.

Figure 6.7 shows the obtained foci using a Dectris PILATUS pixel detector. The reason for using this detector is described below. It is noted again, that these foci are only produced by about a fourth of a full cylinder optic. The total counts shown in Figure 6.7 are summed detector counts with an integration time[2] of 1 s. These values should not be confused with the measured flux, as the detector images were acquired at a lower X-ray tube current to protect the detector. Additionally, the images were not corrected for detector effects. However, the counts can be used for a relative comparison between the samples in Figure 6.7.

Samples 1 and 2 show a comparable focus size, shape and detector count rate, which indicates that both crystals have a comparable bending radius. The slight deviation in the count rates is assumed to be caused by the different surface treatments. After the alignment, the flux measurements were performed. Sample 1 showed a mean flux of $\Phi \approx (2.4 \pm 0.3) \times 10^8\,\mathrm{ph\,s^{-1}}$, and sample 2 a mean flux of $\Phi \approx (3.0 \pm 0.3) \times 10^8\,\mathrm{ph\,s^{-1}}$.

[2] In the context of this thesis, the integration time is the period during which the detector collects the signal. All detector counts within this time interval are accumulated.

Due to the higher achieved flux of sample 2, the surface treatment used on that sample was selected for future sample iterations and the later optics.

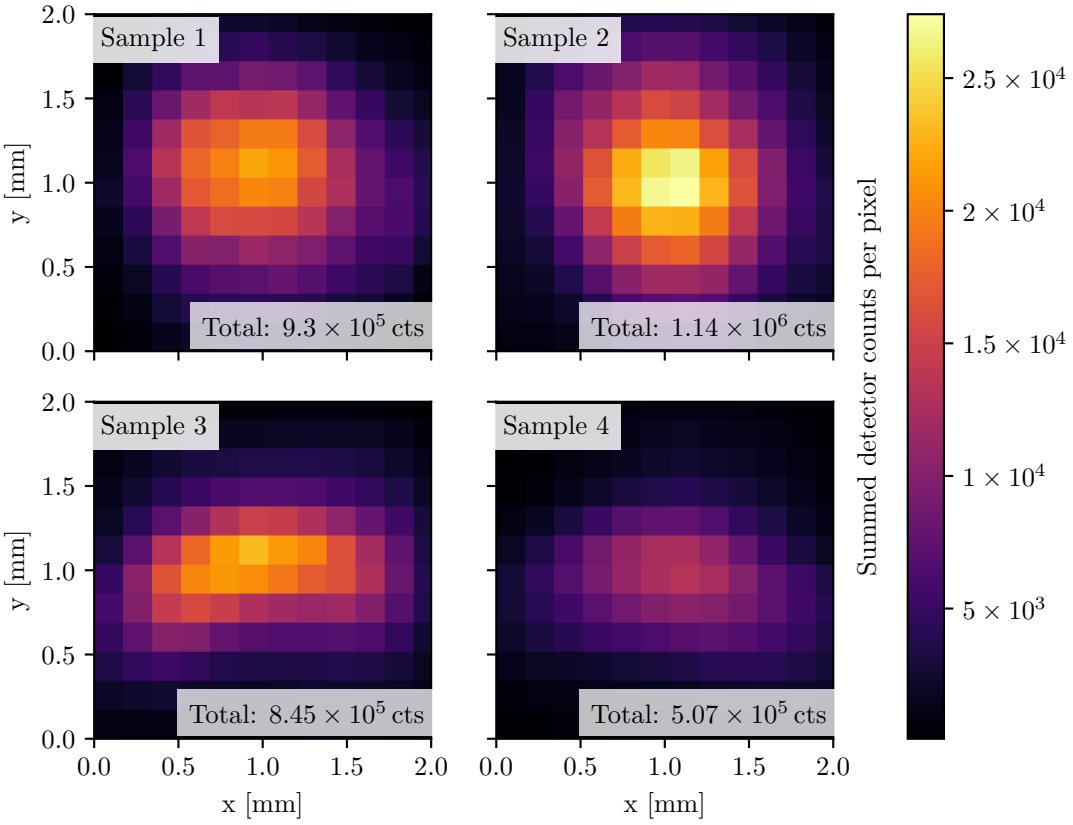


Figure 6.7: Foci produced by bent aluminum crystal samples 1 to 4, measured with a Dectris PILATUS pixel detector with an integration time of 1 s. The different shapes and total counts (cts), which are calculated as the sum of the detector counts of all pixels in a plot, imply a strong effect of the surface treatment process and sample thickness, as well as a variation in the bending quality of the samples.

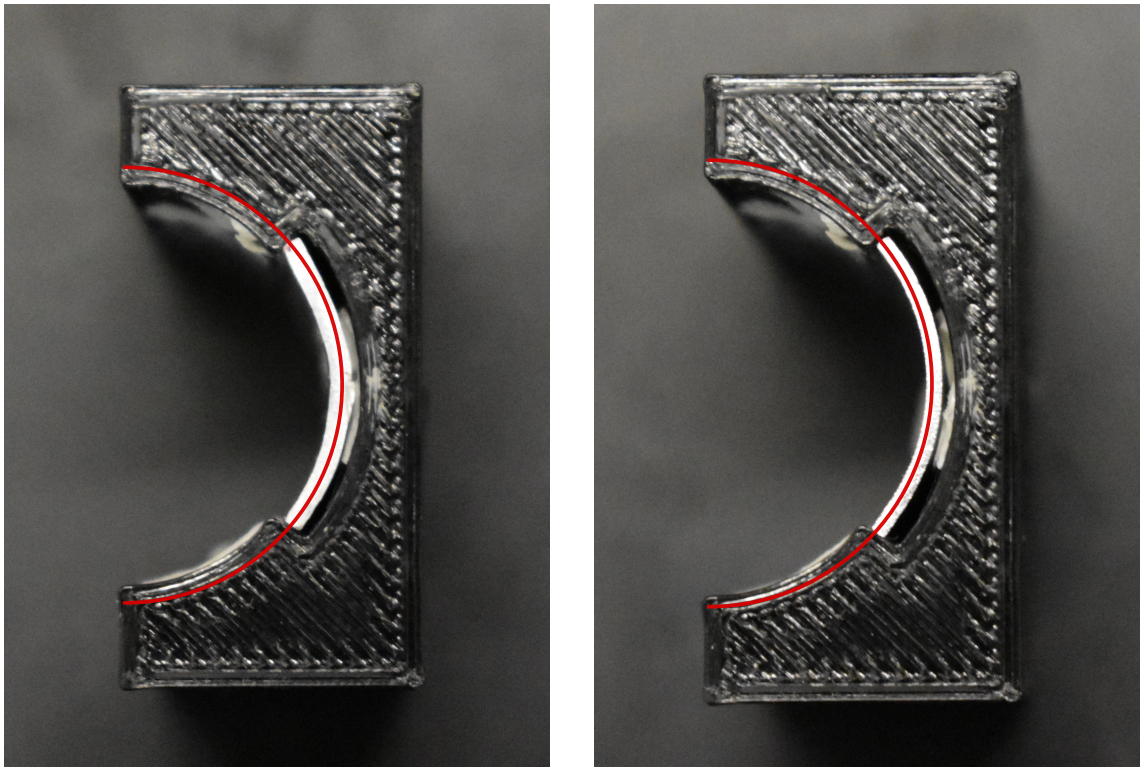
Following these results, two additional crystal samples were manufactured in a second batch, both using the assumed more suitable surface treatment of sample 2. Sample 3 was produced to match the specifications of the so far best-performing sample 2 to study the reproducibility.

Sample 4 was produced with a thickness of 1 mm, which exceeds the expected saturation thickness of 700 µm. Therefore, it was expected to produce similar results to samples 2 and 3 because, in theory, a thickness greater than the saturation thickness does not enhance reflectivity. However, a thicker sample is expected to be more susceptible to potential damage introduced by the bending process, which could affect the reflectivity. Note that the samples 1 to 4 were all cut from the same grown crystal.

In the measurements of the second batch, the Actaeon detector was not available. The Dectris PILATUS pixel detector, described in Section 4.3.1, was used as an alternative. To ensure comparability, the measurements of batch 1 were repeated during the measurement

of batch 2 using this alternative detector. Therefore, Figure 6.7 shows the foci obtained with the Dectris PILATUS detector. The repeated alignment of the samples of batch 1 showed no differences in the quality of alignment between the use of the two different detectors. However, the Actaeon detector is to be preferred because its smaller pixel size makes the focus shape easier to perceive, which therefore makes the alignment easier.

In contrast to expectations, both samples from the second batch exhibited poorer focusing properties, which resulted in a visibly more uneven focus profile. This observation is confirmed by the flux measurements, which yielded a value of $\Phi \approx (2.1 \pm 0.3) \times 10^8\,\mathrm{ph\,s^{-1}}$ for sample 3, and a value of $\Phi \approx (1.5 \pm 0.2) \times 10^8\,\mathrm{ph\,s^{-1}}$ for sample 4. Therefore, sample 3 performs about 30 % worse than sample 2, even though they were manufactured essentially the same way. They have the same thickness and surface treatment and were cut from the same original crystal. However, an apparently imperfect bending was observed in all four samples of batches 1 and 2. This reduces the performance of the optics and their ability to form a focus, and made their alignment difficult. Hence, the described bending setup was significantly improved in order to minimize its impact on the results [145].



(a) Bent Al sample 4 **(b)** Bent Al sample 8

Figure 6.8: Photo of samples 4 and 8 taken from above, looking down at the sample holder. Sample 4 was bent using the first iteration of the bending setup, and sample 8 with the second iteration of the bending setup built by MaTecK [143].

Figure 6.8a shows a photo of sample 4, which was bent using the first iteration of the bending setup, taken from above. The sample is shown inserted in the sample holder. Figure 6.8b shows a photo of sample 8, which was bent using the second iteration of the

bending setup. It has a visibly better fit with the cylindrical shape of the inner surface of the sample holder than sample 4. The difference is particularly evident when looking at the upper ends of both samples. Sample 4 deviates from the red curve, which follows the intended circular shape of the end face of the bent samples.

Furthermore, a significant drop in the performance of the thicker sample 4 was observed when compared to the 700 µm thick samples. Since the samples 1 to 4 were all cut from the same crystal before bending and theory suggests that increasing the thickness of an unbent crystal beyond its saturation thickness does not lead to deterioration of diffraction properties, sample 4's poorer performance must be due to the bending process.
It can be concluded that the associated deterioration of the crystal's focusing properties due to bending may already be noticeable at thicknesses below 700 µm. Given that the calculation of the saturation thickness is based on values acquired using different samples, the ideal thickness for the aluminum optics may be well below the initially calculated saturation thickness of 700 µm.

To test this hypothesis, a third batch with four samples of different thicknesses was produced. All samples in batch 3 were bent using the improved setup. As with the first four samples, a new crystal was grown from which all samples of batch 3 were cut prior to bending. Figure 6.9 shows a photo of all samples of the third batch.

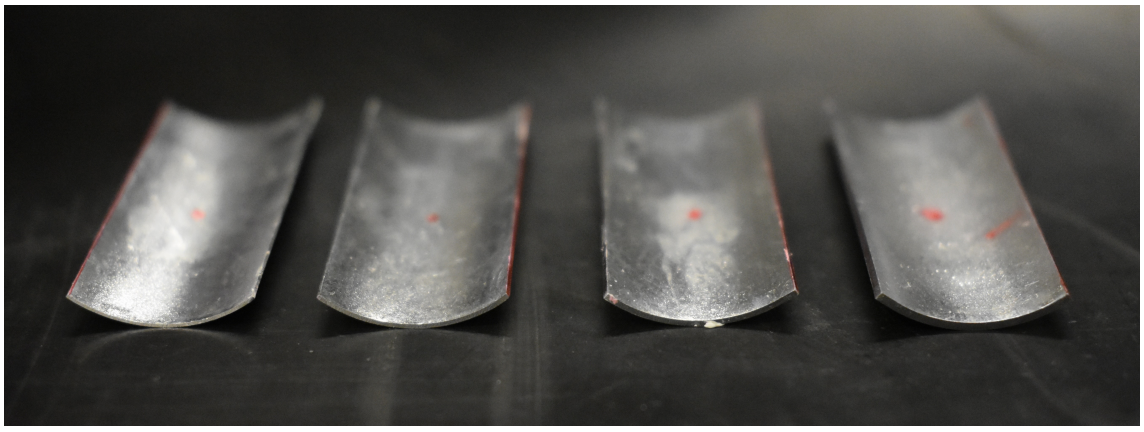


Figure 6.9: Photo of bent aluminum samples 5 to 8 (from left to right). The samples feature thicknesses of (from left to right) 300 µm, 400 µm, 500 µm, 700 µm. All samples have an inner bending radius of 10 mm, and underwent the same surface treatment process. The manufacturer marks the visible red dots during the cutting process to show the middle of the samples. The red lines on the outside indicate the edges along which the crystal was cut. These red marks do not alter the properties and are therefore not removed.

The thicknesses of samples 5 to 8 are: 300 µm, 400 µm, 500 µm, 700 µm. The latter dimension was included again to test the reproducibility of the so far highest achieved flux, measured with sample 2. The bending of all crystals of batch 3 is visibly better that in the first two batches.

The foci, which were recorded after a similar alignment procedure as for the samples 1 to 4, are plotted in Figure 6.10.

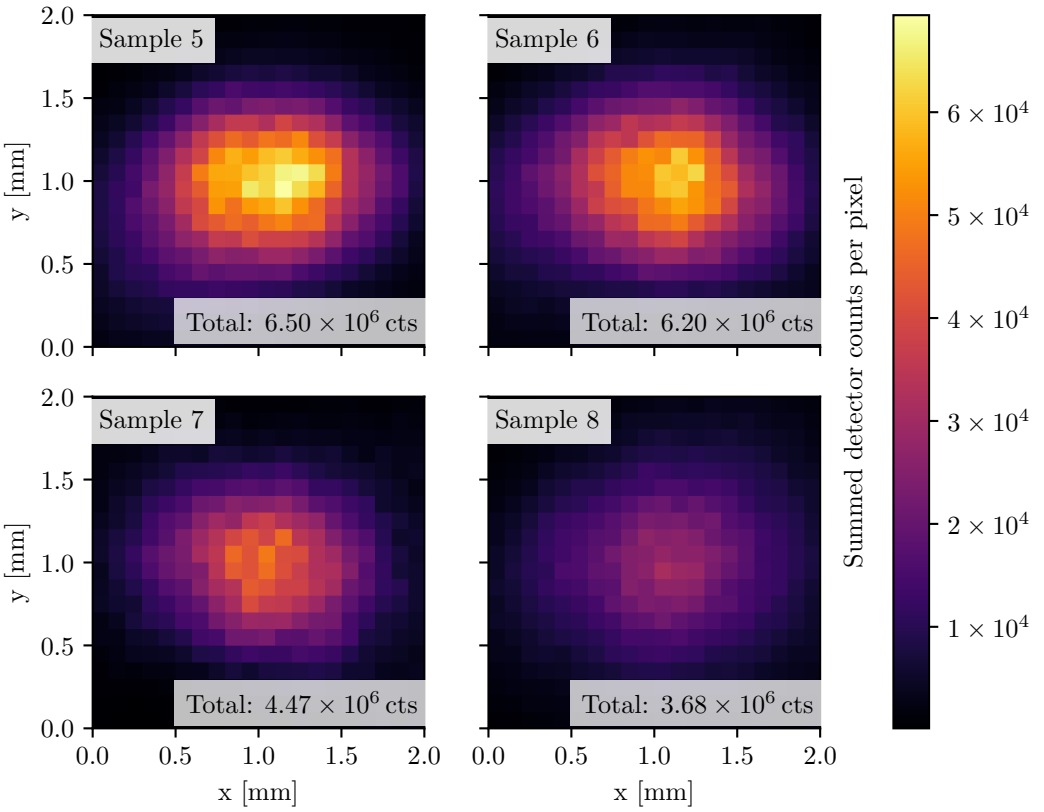


Figure 6.10: Foci produced by bent aluminum crystal samples 5 to 8, measured with an Actaeon pixel detector with an integration time of 2 s. All foci are comparable in size and shape. The varying total counts are calculated as the sum of the detector counts of all pixels in a plot and are caused by the different samples thicknesses of 300 µm, 400 µm, 500 µm, 700 µm (from sample 5 to 8).

Note that for samples 5 to 8, the preferred detector for alignment, an Actaeon pixel detector, was used. Therefore, the shown summed detector counts can only be compared between samples 5 to 8. However, the general shape of the foci can also be compared to those of samples 1 to 4, shown in Figure 6.7. All samples 5 to 8 exhibit good focusing properties, which made the alignment process easier than for samples 1 to 4. All foci are comparable in size and show a more uniform shape than the foci of samples 3 and 4.

The flux measurements of the foci taken after alignment yielded significantly higher values than for the first two batches. Table 6.2 lists the obtained values for all samples 1 to 8.

Sample number	**Crystal number**	**Sample thickness in µm**	**Measured flux in ph s^{-1}**
1	1	700	$(2.4 \pm 0.3) \times 10^8$
2	1	700	$(3.0 \pm 0.3) \times 10^8$
3	1	700	$(2.1 \pm 0.3) \times 10^8$
4	1	1000	$(1.5 \pm 0.2) \times 10^8$
5	2	300	$(4.4 \pm 0.5) \times 10^8$
6	2	400	$(4.5 \pm 0.5) \times 10^8$
7	2	500	$(3.5 \pm 0.3) \times 10^8$
8	2	700	$(3.2 \pm 0.3) \times 10^8$

Table 6.2: Mean reconstructed flux in the focus of all bent aluminum samples, acquired with a fluorescence measurement using palladium, rubidium iodide, and silver reference targets. Also listed are the respective sample thicknesses, and the crystal from which the sample was cut before bending.

Samples 2, 3 and 8 were produced with identical specifications. As discussed above, sample 3 exhibited worse focusing properties, and a lower flux in the focus than sample 2. Due to the unexpected performance of sample 3, sample 8 was manufactured with the same dimensions to once again assess the reproducibility of its good focusing properties and high flux. Both mean measured flux values of sample 2 and 8 are comparable, which confirms the reproducibility thanks to the improved bending setup. This suggests that sample 3 was likely impacted by a single manufacturing imperfection.

The flux measurements with the samples of the third batch reveal a clear, systematic relationship between the crystal thickness and the achieved values of Φ. Figure 6.11 illustrates this trend by plotting the measured flux of samples 4 to 8 against their thickness. As the thickness increases beyond $t = 400\,\mu\text{m}$, the crystals exhibit an increasingly lower flux, supporting the hypothesis formulated after measuring batch 2.
Therefore, the bending of the crystals appears to significantly influence the samples' properties. This is likely due to the occurrence of larger defects, tensile and compressive stresses, alteration of the underlying crystal lattice, or possible broadening of the mosaic distribution.

The impact of these effects on the focusing properties of the crystals can be characterized using the setup described in following Chapter 7.
Due to time discrepancies between completing the setup described in the following chapter and receiving the samples from batch 3, characterization measurements for batch 3 are not included in this work. Consequently, this work does not address the detailed examination

of the microscopic effects caused by the bending that could explain the thickness-dependent performance of the aluminum samples. However, the macroscopic effects on the achievable count rate was measured as described.

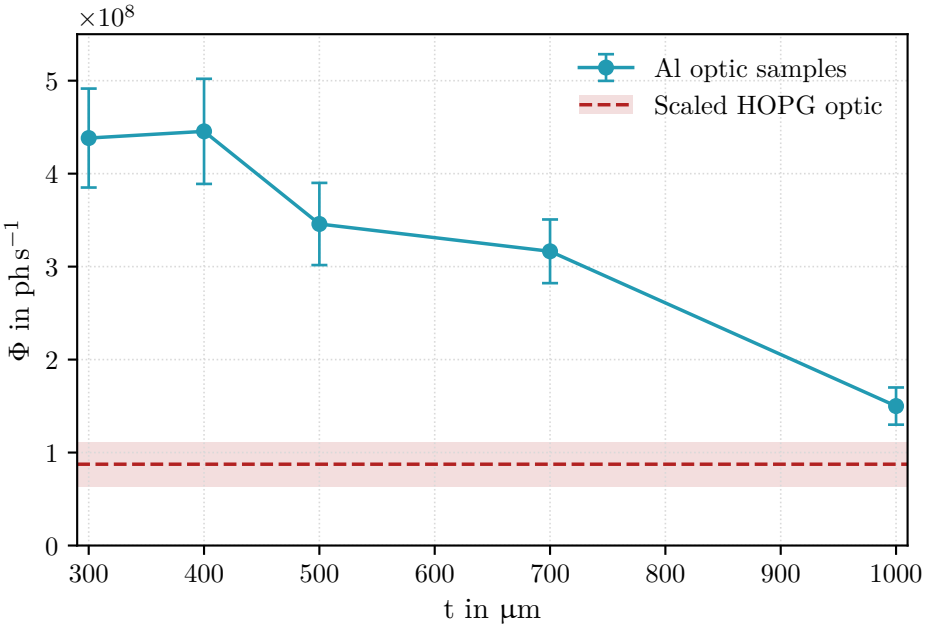


Figure 6.11: Mean measured flux in the foci of aluminum von Hámos optic samples plotted against the respective thickness of the samples. For comparison, the flux of the best-performing HOPG optic, measured immediately before the aluminum samples, scaled down to the same size as the samples, is also provided. The error bars and the pale red area indicate the standard deviations of the flux measurements.

By respecting the sample width of 15 mm and the achieved desired bending radius of 10 mm, the results of the flux measurements of the best-performing sample 6 can be extrapolated to an expected flux in the focus of a total von Hámos optic used in the SCOTTI beamline of:

$$\Phi_{\text{total}} = \frac{2\pi\,10\,\text{mm}}{15\,\text{mm}}\,\Phi_{\text{Sample 6}} \approx \underline{\underline{(1.9 \pm 0.2) \times 10^9\,\text{ph}\,\text{s}^{-1}}}, \tag{6.2}$$

when manufactured to the same 400 µm thickness.

This value exceeds the maximum calculated value of approximately $1.4 \times 10^9\,\text{ph}\,\text{s}^{-1}$, which was based on the assumed crystal parameters listed in Table 6.1. Additionally, the optimal crystal thickness for achieving the brightest focus is significantly lower than the previously assumed 700 µm. Besides the detrimental effects of bending, this has to be accounted to crystal parameters that deviate from the ones given in Table 6.1.

It is assumed that bending can increase the mosaic spread of the crystals at most, but does not reduce it [144]. Therefore, the samples must have a lower value for the model parameter of crystallite thickness than was initially expected. Assuming the same mosaic spread of approximately 0.2°, as measured for a flat aluminum sample from MaTecK in [26],

`xrt` simulations suggest a required crystallite thickness of $t_0 \lessapprox 3.5\,\mu\text{m}$. Note that the reflectivity does not scale linearly with the model parameter of crystallite thickness.
In terms of reflectivity, the grown crystals that are used to prepare the samples seem to be of higher quality than the flat aluminum sample measured in [26], which showed signs of a crack inside the crystal. The crack was originally assumed to not alter the crystal's reflectivity properties, which apparently was an incorrect assumption. It is therefore possible that the estimate of t_0 in [26] was slightly inaccurate due to the crack in the sample.
Future aluminum crystals for optics will be grown in the same way as batches 1 to 3. The comparable count rates achieved by samples 2 and 8, which were cut from different crystals, also confirm the reproducibility of the initial crystal.

Figure 6.11 and the values listed in Table 6.2 show that the measured fluxes for sample 5 and 6 are comparable, which indicates a plateau in the performance of the aluminum von Hámos optic as a function of the crystal thickness.

It can be assumed that the ideal thickness of the crystal is in the range of about 300 µm to 400 µm. No improvement in performance is expected below a thickness of 300 µm, since even with the hypothetical crystal parameters adjusted as described, the thickness would then lie below the saturation thickness. Furthermore, the stability of the samples, and thus of a subsequent whole optic, would suffer if even thinner crystals were used.

To conclude, the results of the measurements exceeded the initial expectations. Even the sample 6 alone, which is roughly a fourth of a full von Hámos optic, achieved a flux of $4.5 \times 10^8\,\text{ph}\,\text{s}^{-1}$, which is in the range of the flux values achieved with the so far best-performing HOPG optic. Extrapolated to a full von Hámos optic, the expected flux of approximately $1.9 \times 10^9\,\text{ph}\,\text{s}^{-1}$ is about 3.8 to 5.5 times higher than that achieved with best-performing HOPG optic, depending on the measured flux value used for comparison.

To rule out any potential systematic errors in the comparison, the best-performing HOPG optic was precisely aligned, and a flux measurement of the resulting focus was performed immediately before the measurements of the aluminum samples of batch 3. The exact same alignment procedure, and the same flux measurement setup with the identical fluorescence targets and data analysis as for the aluminum samples was used. If a systematic error is present, it must therefore be present for all values. A flux of $(3.7 \pm 0.3) \times 10^8\,\text{ph}\,\text{s}^{-1}$ was measured, which is comparable to values determined during the six months prior to the measurements. Using this value for comparison suggests an improvement factor of the extrapolated aluminum optic of approximately 5.2.

Chapter 7 presents a hypothesis for the strong variation in the measured flux using the HOPG optics, which is based on a characterization of the varying reflectivity across the surface of the crystals.

A comparison of the foci in Figure 6.10 and 5.1a shows that they are comparable in shape, which indicates expected similarities between the HOPG focus shape and the focus shape of a full aluminum optic. However, the focus sizes and shape of an HOPG optic can not be exactly compared to the results presented in this chapter, as this would be an unfair comparison between a full optic and an optic part.

According to Equation 3.6, the expected spectral width of the optics at a central energy of 59.32 keV, without the use of apertures that can limit this width if the planned experiment is dependent on it, is $\Delta E_{\mathrm{FWHM}} \approx 9\,\mathrm{keV}$. This corresponds to a relative spectral width of approximately 15 %, when considering a flat incidence spectrum. Since the K_α lines are very prominent in the real incident spectrum in SCOTTI, the count-corrected energy bandwidth is much lower and can additionally be reduced by the ring and the tube apertures.

Figure 6.12 shows the `xrt`-simulated spectra of an HOPG optic with a total flux scaled to the measured value of $(3.7 \pm 0.3) \times 10^8\,\mathrm{ph\,s^{-1}}$ in comparison to the simulated spectrum of the extrapolated full aluminum von Hámos optic.

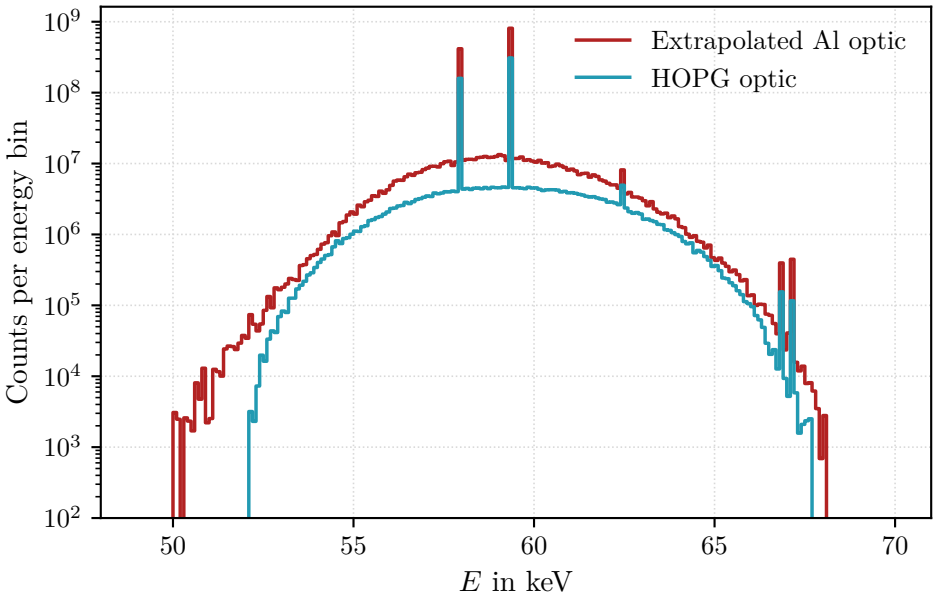


Figure 6.12: Simulated spectra (logarithmic representation) of the best-performing HOPG (blue) and the extrapolated aluminum optic (red) in combination with the ring aperture, designed for the use with an HOPG optic. The optics are tuned to the $\mathrm{K}_{\alpha\,1}$ line of tungsten at $E = 59.32\,\mathrm{keV}$.

Both spectra arise from the optic being tuned to the $K_{\alpha 1}$ line of tungsten at $E = 59.32\,\mathrm{keV}$, and use the same ring aperture as in the measurements described in this section, which is tailored to the use in combination with an HOPG optic. The Gaussian-like components of the spectra originate from the reflection of the Bremsstrahlung background and have widths of $\mathrm{FWHM}_{\mathrm{HOPG}} \approx 6\,\mathrm{keV}$ and $\mathrm{FWHM}_{\mathrm{aluminum}} \approx 5\,\mathrm{keV}$. These values are well below the relative limit of 15 %, set by requirement 2 in Section 3.3, for both types of optics, thanks to the use of the aperture. Although the FWHM of the background is comparable in both spectra, the aluminum optic's spectrum extends further toward higher values. Consequently, when displayed on a logarithmic scale with identical y-axis limits, the aluminum optic's spectrum appears broader because its low-intensity tails remain visible over a wider range. Additionally, the current, unoptimized design of the ring aperture blocks more high-energy wavelengths than low-energy wavelengths from the aluminum optic's spectrum.

The ring aperture is designed to allow as many focused photons with the desired central energy as possible to pass through. Therefore, it is dimensioned to the length of the optic in order to utilize the reflections from its full angular coverage. The aluminum optic has the same length as the graphite optics and is tuned to the same energy. However, it is positioned at a distance that is 1.4 times smaller due to its 1.4-fold Bragg angle. This corresponds to a wider angular coverage of possible incident beams and a wider spectral width.
However, the slightly larger spectral width primarily relates to the comparatively weak background caused by the reflection of the X-ray tube's Bremsstrahlung spectrum. Adjusting the ring aperture for the novel aluminum optic to cover all crystallites located on the Rowland circle, and thereby increasing the flux by an estimated 10 %, also leads to a broadening of this background. If this is not acceptable for the planned experiment, this width can also be reduced by adjusting the ring aperture. As a result, the expected flux also decreases. For further details on the design of the apertures, refer to [116].

A full aluminum von Hámos optic, paired with suited apertures, is expected to fulfill all requirements of an optic for the use in the SCOTTI beamline, as defined in Section 3.3. The extent to which the expected performance exceeds that of the previously used graphite optics across the entire energy range to be achieved depends on the exact mosaic spread of the optic and the design of the apertures. Compared to the highest-performing HOPG optics, an improvement factor of between 2.5 and 7, also depending on the comparative value, is expected in the range from 30 keV to 85 keV, with greater improvements at higher energies.

The use of the novel aluminum optic is therefore expected to be beneficial across the entire desired energy range, set by requirement 3 in Section 3.3.

The desired bending radius of 10 mm could be achieved in the test measurements. Due to the about 1.4 times greater Bragg angle of the aluminum (1 1 1) reflex compared to the graphite (0 0 2) reflex, the entire setup is thus much more compact in length.
To avoid potential problems when positioning all the apertures at lower energies, it makes sense to manufacture optics with larger radii, e.g., 15 mm for the use in low-energy focusing. This is not expected to result in any significant changes in the fundamental behavior of the optics or major difficulties in manufacturing.

For higher energies, the flux can benefit from an increase in length, as can be explained by Equation 3.3. To take advantage of this effect, two complete aluminum von Hámos optics can be combined using a suitable holder to form a single optical system of twice the length. Depending on the experiment, it must be considered whether this approach is worthwhile for increasing the flux, despite the associated higher spectral width.

Since the best option among the possible optic designs using aluminum or magnesium oxide, presented in Sections 6.3 and 6.4, has been successfully realized, the other concepts are not further pursued. This includes a von Hámos optic made from magnesium oxide, for which an artificial extension of the mosaicity would have to be realized.

Based on the results of the study presented in this chapter, a whole aluminum von Hámos optic is currently manufactured. To optimize the setup, the ring and tube apertures in the SCOTTI beamline will be redesigned to match the new aluminum optic.
Since the Bragg angles of the novel aluminum optics are about 1.4 times greater than those of the graphite optics, the focused beam will widen quicker by the same factor when moving away from the focus point. This must be considered when evaluating XFI experiments.

The characterization setup, which is introduced in the following Chapter 7, will be used to study the microscopic effects of the bending process on the crystal parameters.
Accurately characterizing the optics using this setup is also crucial for further improving the aluminum optics and other components of the SCOTTI beamline. For example, the sufficient length of the optic is a function of the crystal's mosaic spread, as quantified by Equation 3.3.

7 Optic Characterization Setup

Due to the possible variations in the manufacturing process of the presented HOPG, HAPG, and aluminum optics, such as produced layer thickness, bending, and surface treatment, significant variations in their observable focusing abilities may occur. For example, the performance of different HAPG optics was found to vary by 50 %, as described in Section 6.1. With the SCOTTI setup, optics can only be characterized by their performance with regard to their focusing abilities and the achievable flux in a focus.

In order to bring the simulation models as close as possible to reality, improve the manufacturing processes, and precisely dimension other parts of the SCOTTI beamline, such as apertures, it is crucial to know the properties of the reflecting crystals used for the optic. The mosaicity profile is particularly important because it establishes the basis for the focusing properties of Hámos optics. Such mosaicity profiles can be determined by recording a rocking curve, the concept of which is briefly described in Section 7.1. However, established characterization methods for these types of measurements are only designed for flat samples or very small areas on a crystal. To the best of the author's knowledge, no methods tailored specifically to von Hámos optics for measuring rocking curves exist. This chapter presents a setup, which is dedicated to the von Hámos optics discussed in this work, and is capable of measuring rocking curves as well as quantitatively characterizing the uniformity of an optic's reflectivity across its entire surface.

As explained in Chapter 6, the production of the novel aluminum optics by MaTecK starts by cutting a flat slab out of a grown crystal with the desired $\{1\,1\,1\}$ crystal plane set oriented parallel to the slab's surface. Therefore, the most obvious way of characterizing the sample would be to measure spatially-resolved rocking curves before the subsequent bending. However, the results of Section 6.5 imply that the bending might alter the mosaicity of a sample. Therefore, the characterization should be performed after the bending process.

The design and implementation of the setup, as well as the development of the control software, were carried out in a joint project with members of the Analytical X-ray Physics Group at the Technical University of Berlin [147].

7.1 Rocking Curve Measurements

The reflectivity of a crystalline sample as a function of the incidence angle is referred to as a rocking curve [55]. It is conventionally recorded by using an ideally monoenergetic, non-divergent beam that is incident on a sample under a certain angle. This angle is then altered by rotating the sample, which is referred to as "rocking". Depending on the properties of the crystalline sample, the width of the measured function is determined by different underlying properties [55]. In line with the definition of the mosaic spread β, the FWHM of such a curve is referred to as the rocking curve width. In measurements like those presented in this chapter, the reflectivity becomes measurable as the intensity of the reflected beam on a detector.

If the sample is an ideally perfect crystal, and the beam used for characterization is monoenergetic and non-divergent, the resulting rocking curve width would be determined solely by the Darwin width ω_D of the crystal, which is described in Section 2.4.4. The mean of the curve would lie exactly at the Bragg angle of a respective crystal plane set, as defined by Bragg's law (Equation 2.58).
In a realistic rocking curve experiment, the recorded width is the result of the convolution of the beam's divergence and the Darwin width. Therefore, the value of ω_D is generally not accessible by experiment, as its order of magnitude lies in the range of arcseconds.

If the sample is a mosaic crystal, the mosaic spread usually far exceeds the Darwin width, as it lies in the order of tenths of a degree. As a result, the rocking curve width is then also mainly determined by the mosaic spread of the sample. Nevertheless, even in the case of a rocking curve measurement of a mosaic crystal, the determined width is subject to broadening due to the divergence or spectral width of the beam used for characterization. The extent of the broadening depends on the ratio between the mosaic spread and the beam properties.
Furthermore, additional parameters of the measurement setup or the sample that affect the effective divergence or spectral width can influence the obtained rocking curve width. Those effects, relevant to the setup described in this chapter, are summarized in Section 7.4.2.

Strains in bent crystal samples can lead to a broadening of the measured rocking curve [55]. With the characterization setup presented in this chapter, a rocking curve broadening due to a strain cannot be distinguished from the intrinsic mosaicity. Depending on the actual effect of the strain, the obtained values of the mosaic spread might therefore be overestimated. As the potential broadening would be a systematic effect in the sample itself, it would also affect the focusing properties of the optic when used in the SCOTTI setup. Therefore, it is actually beneficial to include the effect of a potential strain in the

final estimate of the mosaic spread, to obtain a more realistic estimate of the effective focusing properties of an optic.
However, the results presented in Section 7.5.1 imply that the effect of mosaicity is stronger than the effect of strains in the samples because the obtained estimates of β are comparable between bent and unbent HOPG and aluminum samples.

Lastly, samples that consist of very small grains, especially powders, can be subject to Scherrer broadening, which is explained in Section 2.4.9. This mechanism of rocking curve broadening is not relevant for the samples measured in this work.

7.2 Concept of the Characterization Setup

The characterization measurements should be as close as possible to the working conditions of the optics in the SCOTTI setup. Therefore, they also rely on Bragg reflection at the inner surface of the crystal cylinder.

The Bragg angle at the standard central energy in the SCOTTI beamline (59.32 keV) is about $\theta_B = 2.6°$ for the aluminum (1 1 1) reflex and about $\theta_B = 1.8°$ for the graphite (0 0 2) reflex. The expected values of mosaic spreads are about $\beta = 0.2°$ for the aluminum optics [26], $\beta = 0.1°$ to $\beta = 0.2°$ for the HAPG optics [136], and $\beta = 0.4°$ to $\beta = 0.7°$ for the HOPG optics [136].
As outlined in Section 7.1, a rocking curve measurement benefits from a small divergence of the used beam, which is easier to achieve if the absolute values of the incidence angles that are relevant for the range of the respective rocking curve are steeper. As given by Bragg's law, this corresponds to a lower energy that is used for the characterization.
The setup should be compact and inexpensive, which limits the possible X-ray source to the use of an X-ray tube. The evaluated part of its incident spectrum should also be as close to being monoenergetic as possible, which speaks for the use of an intense characteristic line in the spectrum of the used X-ray tube. To additionally suppress the defocusing effect by an extended source, as described in Section 3.2.5, which would increase the effective divergence of the beam used for the characterization, the focal spot should be small.
These requirements can not be met by the tungsten anode X-ray tube of the SCOTTI setup. Instead, a rhodium anode microfocus X-ray tube, which has a strong characteristic $K_{\alpha 1}$ line at 20.21 keV is capable of providing these properties and is used in the setup [148]. The Bragg angle at this energy is $\theta_B = 7.54°$ for the aluminum (1 1 1) reflex and $\theta_B = 5.24°$ for the graphite (0 0 2) reflex.
The used X-ray tube model is a MCBI 50B-50 Rh 40°, manufactured by rtw Röntgen-Technik Dr. Warrikhoff GmbH & Co. KG, which has a focal spot size of 50 µm × 50 µm [148].

The basic idea of the setup is to use a collimated, cone-shaped X-ray beam from the microfocus X-ray tube to illuminate a circular part of the crystal optic. The exposed part of the crystal can then be varied in the course of a characterization scan, which is realized by using movable apertures. Depending on the part of the optic that is illuminated, the geometrically possible range of incident and reflection angles varies. The K_α line of the used rhodium X-ray tube is strong enough to produce a measurable signal after the Bragg reflection from a restricted part of the whole optic.

Throughout a scan, the detector records the reflected intensity as the range of geometrically available angles onto the crystal surface varies. Therefore, the scan results can be evaluated to produce a rocking curve of the optic. Section 7.4.1 shows in detail how such scan is realized using the described setup.
Section 7.4.4 describes a second type of measurement using the setup, which can be used to qualitatively characterize the homogeneity of an optic.

7.3 Design of the Setup

Figure 7.1 shows the basic design concept of the characterization setup. The illustration uses enlarged angles for clarity to explain the working principle. This section describes the concept using an idealized setup, whereas the practical deviations in the experimental realization are subsequently explained in Section 7.4.2.

In a first step, a monoenergetic point source at S is assumed for the following explanations. Its energy is consistent with the characteristic K_α of rhodium at 20.21 keV that should be employed for the characterization, and is assumed to be monoenergetic for now. Therefore, the Bragg angle with respect to the reflecting crystal plane set of the optic to be characterized is constant for all beams. Later descriptions dispel the assumption of a monoenergetic source and take into account the entire spectrum of the X-ray tube.
On the axis between the source and the detector lies an aperture designed as a hollow cylinder with a cutout. In the following, only ray paths under a single azimuthal angle are considered. This is permissible due to the rotational symmetry of the optic, which therefore underlies the same negligible azimuthal defocusing as explained in Section 3.2.3.

Above the aperture cutout, the crystal sample to be scanned is placed. The currently used graphite-based optics and the novel aluminum-based optics are designed as two half-cylinders that are mounted together to form a full cylinder. The setup can characterize optic parts of up to such a half cylinder, or optic samples, which constitute a smaller portion of a cylinder, such as the aluminum samples described in Section 6.5. All considered

von Hámos optic designs utilize a crystal or substrate curved to a specific radius. This curvature radius defines a rotational symmetry.

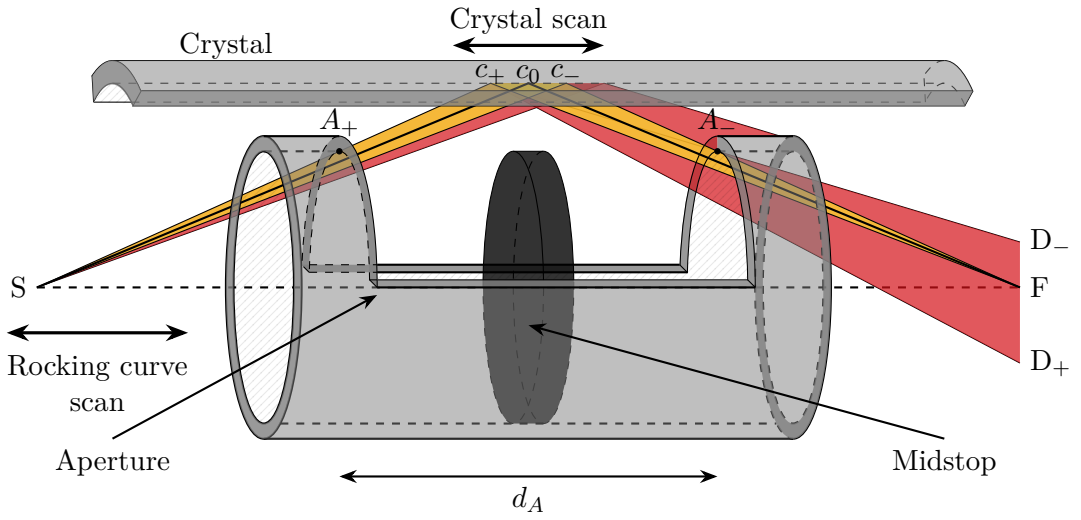


Figure 7.1: Schematic illustration of a characterization setup for measuring spatially-resolved rocking curves, and spatially-resolved intensity scans (crystal scans) of mosaic crystal von Hámos optics. The crystal scans can be used to rate the relative quality of the optics across their entire size.
The setup includes a microfocus X-ray tube S, an aperture with a flexible cutout with a width of d_A between its limits A_+ and A_-, a midstop, and a detector placed either at the focal point F, for a focused setup, or behind F, for a defocused setup. A crystal sample is placed above the aperture cutout, which limits the geometrically possible incidence and reflection angles (yellow cone) that can lead to a focusing onto F, resulting in a limited exposure of the sample surface over a distance $\overline{c_+c_-}$. A characteristic line doublet of the X-ray tube is used for the evaluation of the focused yellow cone. The red cones show the reflected Bremsstrahlung background and defocused characteristic line doublet.

Accordingly, a sample to be scanned is placed so that the axis of its curvature lies on the same axis as the source S and the cylindrical aperture. In Figure 7.1 the axis is illustrated by the dashed horizontal line.
The aperture radius must be smaller than the sample radius. All current optics and samples feature a radius of about 10 mm. Thus, the radius of the aperture was set to 8.5 mm.

As illustrated in Figure 7.1, the point A_+ of the aperture limits the steepest incidence angle onto the optic. This corresponds to a projected point on the sample, which is marked with c_+ in Figure 7.1. A beam with this incident angle can only be reflected if it strikes a crystallite tilted in such a way that the incident angle corresponds to the Bragg angle. The Bragg angle is defined by the crystal plane set and the beam's energy. If the so-defined necessary tilt δ lies in the range of the mosaic distribution of the crystal of the sample, the beam can be reflected toward F.

Figure 7.1 shows a case where the symmetric reflection is fulfilled. The central beam is incident onto the crystal surface at c_0 with exactly the Bragg angle as its incidence angle. Following the focusing abilities of a mosaic crystal, it is focused onto the focal point F. The reflecting crystallites at c_0 that focus the beam onto F are not tilted with respect to the crystal surface.
All optics are designed in a way that the mean normal directions of the crystallites align with the normal of the optics' surface. Therefore, a crystallite most likely has no tilt. Thus, the illustrated situation in Figure 7.1 shows the state of maximum reflectivity, which is referred to as the reference configuration for all scans in the following.

Following the geometrically possible incident points onto the crystal in a direction toward F, the incidence angles become more flat. Again, the respective incident beams can only be reflected toward F, if they strike a crystallite which is tilted suitably.
A reflected beam can only finally reach F if it is not absorbed by the right side of the aperture beyond A_-. Therefore, A_- defines the flattest reflection angle that contributes to the intensity in F. This corresponds to the definition of a point c_- on the crystal, which is the farthest point from the source from which rays can be focused onto F. Hence, c_+ and c_- define an angular range.

The yellow cones in Figure 7.1 illustrate the angular range $\Delta\theta$ of beams with the target energy that are reflected and propagate up to the focal point F. These beams exactly show the ideal mosaic focusing, as explained in Section 3.1, which is only fulfilled by crystallites that lie on the Rowland circle.
A part of the incident beams undergo all kinds of mosaic defocusing effects, as explained in Section 3.2, which causes them to lie outside the yellow range and within the red-colored angular range.

Additionally, the described limits are only valid as long as the angular range between c_+ and c_- is smaller than the width of the crystal's mosaic distribution, because the setup assumes that every angle inside this range corresponds to an existing, suited crystallite. If the angular range is too wide, the (non-)existence of suitably tilted crystallites limits the steepest and flattest incidence angles that still lead to a Bragg reflection.
Therefore, the distance between A_+ and A_-, indicated as d_A, limits the minimal width of the mosaic distribution that can be assessed by the characterization setup, and should consequently be small. Note that the width of the mosaic distribution discussed here corresponds to the total width, not the FWHM of the mosaic distribution, which is referred to as the mosaic spread β.

The setup also includes a midstop, which is connected to the aperture, and blocks direct beams from reaching the focal point.

Since the concept is experimentally realized using an X-ray tube, the incident beams are not monochromatic, but show a broad spectrum. Therefore, other energies apart from the K_α line have to be considered.

The steepest angle onto the crystal surface is independent on the energy, and is limited by A_+. At the corresponding incidence point on the crystal surface, c_+, the crystallites on which the beams are incident are tilted according to the mosaic distribution. Those crystallites at c_+ that exhibit the maximum tilt toward S, defined by the mosaic distribution, correspond to the steepest possible incidence angle α_+ onto a crystallite. If a Bragg reflection follows, the reflection angle of this beam with respect to the crystallite will also be α_+. This corresponds to the maximum possible reflection angle, illustrated by the lower limit of the red angular range. At the distance of the focal point F, this defines a lower limit D_+ of possible beam paths. The maximum reflection angle also limits the minimum energy that can be reflected by means of Bragg's Law.
Note that because of the low number of crystallites with maximum tilt, these reflections are relatively weak. Additionally, sets of crystal planes other than the main set are not considered because their reflectivity is typically much lower, and they cannot fulfill the Bragg condition for the K_α lines under consideration at the same time as the main set. The same is true for higher-order reflections of the $\{1\,1\,1\}$ crystal plane set.

Flatter reflection angles are achieved when the incidence points on the crystal lie closer toward F, combined with a maximally tilted crystallite normal. However, as indicated by the upper part of the red angular range near the crystal surface, a significant part of these beams is blocked by the right side of the aperture beyond A_-. Note that not all incidence points that are geometrically reachable are illustrated in Figure 7.1, and that in the practical implementation, the right end of the aperture is longer than illustrated.

The flattest reflection angle under which a beam can still traverse through the aperture is defined by A_- in combination with c_+ as the point of reflection. Thus, this angle also limits the maximum energy that can be incident on the detector plane through F following Bragg's law. It also defines an upper limit D_- of possible beam paths at the focal distance of the optic. This shows how d_A limits the energy range that reaches the detector. A small value of d_A is beneficial, because a small energy range is desired for the rocking curve measurement, as described in Section 7.4.1.

Both F and D_- can be defined by the connection of A_- with c_- and c_+, respectively. A small value of d_A therefore corresponds to a small distance between D_- and F and to a small energetic difference between the beams that reach these points.
In contrast to that, D_+ is solely defined by the maximum available tilt of crystallites at c_+. Therefore, the distance between F and D_+ is usually higher than the distance between F and D_-, which also corresponds to a higher energetic difference. Thus, the energetic background on the detector will mainly be defined by energies that are lower than the energy focused onto F. Note again, that the red angular range also includes the beams of the central energy that are subject to mosaic defocusing. The plane through D_-, F and D_+ defines the focal plane.

The size of the aperture cutout d_A can be adjusted to be able to precisely scan different samples with different radii and Bragg angles.

7.4 Characterization Measurements

Section 7.3 explains how the characterization setup can be used to "cut out" a part of the optic that is illuminated. The aperture and the sample itself are movable, which allows for two possible scan methods that are explained in this section.

As described in Chapter 6, the measured flux values for the graphite optics vary significantly. One explanation for this lies in possible inhomogeneities of the reflection properties and fabrication quality across the crystal.
Therefore, spatially resolving the characterization of the crystal is desirable.

7.4.1 Rocking Curve Measurements

Using the described setup, a rocking curve measurement is realized by varying the distance between the aperture and the source S.

To achieve a spatial resolution in the azimuthal direction, it is possible to place the detector at a defocused position behind the focal point F. Thus, the focus of the optic diverges into an image of the illuminated area. A semi-cylindrical optic, for example, results in an imaged semi-circle. Figure 7.2 shows the defocused detector image during a rocking curve scan of an HAPG sample.
Using only a part of this semi-circle for the rocking curve evaluation and assigning it to an azimuthal point on the exposed strip of the optic achieves a spatial resolution along this axis. The region of interest (ROI) for the evaluation is therefore an annular sector as

illustrated by the red area in Figure 7.2. The defocused image of F is referred to as F' in the following.

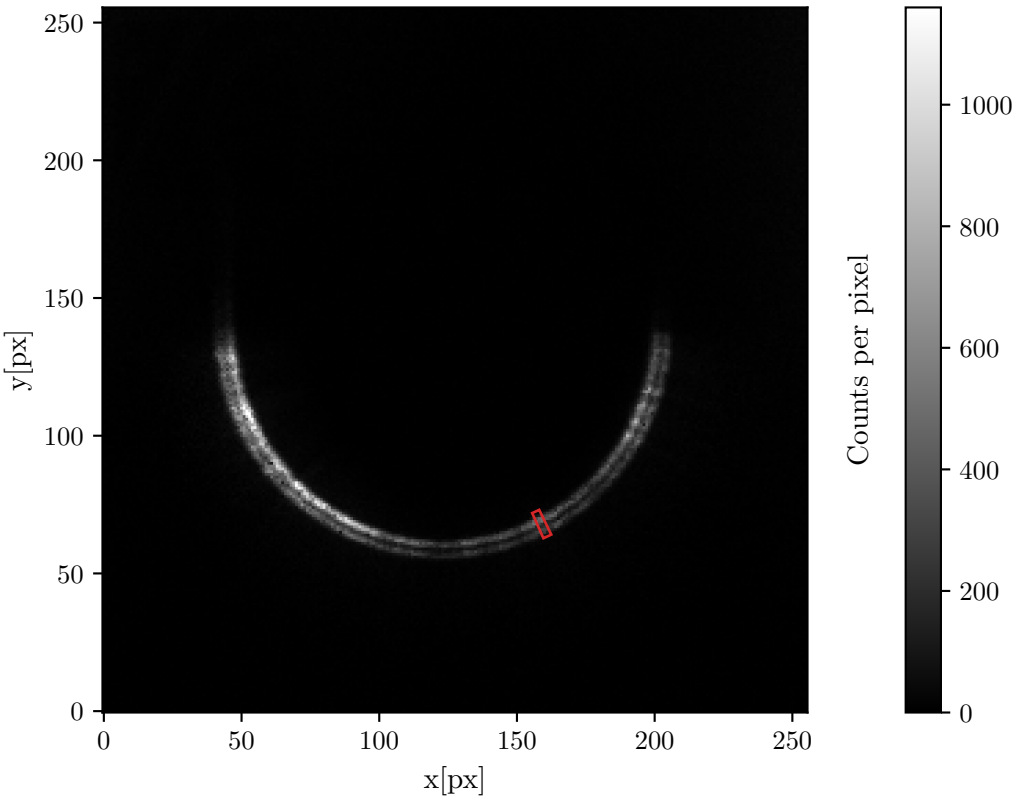


Figure 7.2: Detector image during a defocused rocking curve measurement of an HAPG optic sample using the characterization setup. The aperture was tuned such that the illuminated area of the optic has a width of 1.5 mm, which corresponds to an angular range of 0.07°. The inner ring is the image of the reflection of the $K_{\alpha 1}$ line with $E(K_{\alpha 1}) = 20.22\,\text{keV}$, and the outer ring is produced by the $K_{\alpha 2}$ line with $E(K_{\alpha 2}) = 20.07\,\text{keV}$.

The used rhodium X-ray tube has a $K_{\alpha 1}$ and a $K_{\alpha 2}$ line, arising from the two slightly different relaxation effects in the X-ray tube's anode. They have an intensity ratio of $I(K_{\alpha 1}) : I(K_{\alpha 2}) \approx 2 : 1$ [119]. Their exact energies are $E(K_{\alpha 1}) = 20.22\,\text{keV}$ and $E(K_{\alpha 2}) = 20.07\,\text{keV}$.

In a defocused setup, the existence of this doublet leads to a visible double circle structure, which is a strong indicator for F', and makes the identification of the ROI easier.
Section 7.4.2 further explores the benefits of employing the defocused setup. In order to use the described setup, the detector's pixel size must be small enough to resolve the doublet. The used detector is an Advacam MiniPIX EDU pixelated X-ray detector [125], described in Section 4.3.1, which has a sufficiently small pixel size of $55\,\mu\text{m} \times 55\,\mu\text{m}$.

In the following, the procedure of a rocking curve measurement is described in detail. As the first step, the above mentioned reference configuration is established in a focused setup.

Therefore, d_A is chosen relatively large, to ensure an illuminated ring at the optic that has a length of about $\overline{c_+c_-} \approx 5\,\mathrm{mm}$. As the Bragg angle of the optic is known beforehand, the motors can be moved to a state that roughly represents the reference configuration. A focus point should be visible. Otherwise, the detector distance to the optic and the optic's relative position to the central axis must be varied.

Crystal and aperture are always moved together in the rocking curve scan mode, while the detector and the source have a fixed position throughout a measurement. The combined position of the sample and the aperture is tuned to a point, where the flux around F is maximized, by defining an ROI around the visible focus. In this optimized state, the K_α line is reflected by the maximum number of crystallites. As these have a tilt of $\delta = 0°$, this point marks the reference configuration of the setup, which is completely defined by the Bragg angle, d_A and the radii of the aperture and the optic to be characterized.
The motor positions of the crystal and the aperture can now be used as a reference value. This way, all relative position values of the motors to this reference in the later scan can be transformed to absolute distances in the setup, which are ultimately used to calculate the current range of incidence angles at a certain scan point.

In the next step, the optic and the aperture are moved together in a coarse scan, while the setup is still in the focused condition. During this scan, the focus point should not move but only vary in intensity, which confirms a correct alignment. If the focus point moves, a mismatch between the optic's axis and the characterization setup's axis is present, and the optic has to be realigned.

Afterwards, the detector is moved out of the focal plane to make use of the defocused setup. The width d_A is now gradually reduced until the double-ring structure is just discernible across the entire width of the image. This way, d_A can be optimally reduced to the smallest value that is experimentally achievable to still be able to perform a scan. The determined width d_A is used in the analysis to calculate the width of the illuminated area $\overline{c_+c_-}$ and, consequently, the angular range at a scan point. Section 7.4.2 explains how the translation is done.

For the actual scan, the position of the crystal and the aperture are moved step by step along the central axis of the setup, in the following referred to as the z-axis, in both directions from the initial position. A movement toward the X-ray tube corresponds to steeper incidence angles. Therefore, the crystallites need to have a higher tilt of their normal toward the detector in order to take part in the reflection of the K_α lines. As long as beams with the characteristic line wavelength meet crystallites that are tilted suitably,

and lie on the Rowland circle, they are focused to the initial focal point F. In the defocused setup, they are ultimately incident on the detector at F', which is visible as the described double ring structure. The same is true for the scan direction toward the source, with the only difference being that, in this case, the crystallites have to be tilted in the opposite direction.
This way, the intensity in F' reflects the number of crystallites that are available for reflection in the current scan point. As the scan starts from the reference configuration, the z-offset of crystal and aperture to this case can be translated to an incident angular range onto the crystal.

Although the length of the illuminated area $\overline{c_+c_-}$ remains constant throughout a scan, the width of the angular range and the solid angle coverage change. The scan has to be corrected to this change, which is explained in Section 7.4.2.

Different scan points in the rocking curve measurement correspond to different mean reflection angles. In a focused scan, all beams originating from reflections on the Rowland circle are exactly incident on F. In a defocused scan, the varying reflection angle leads to a variation of the radius of the defocused image, e.g., the half ring in Figure 7.2. Therefore, the radii of the sector that define the ROI change, while the ROI's angular coverage in the azimuthal direction has to remain constant in an evaluation of the scan.

By changing the position of the optic relative to the aperture before a scan, the illuminated area of the optic is shifted. This allows for rocking curves to be recorded at different axial points of the optic, which provides a spatial resolution of the measurement in this direction.

7.4.2 Rocking Curve Broadening Effects

The measurement setup introduces various broadening effects of the rocking curve. These effects have to be accounted for in order to obtain the intrinsic mosaic distribution of a measured sample. In this section, all major contributions to the detuning and broadening of the measured rocking curves, as well as limitations of the setup, are discussed. To put the effects into perspective, the impact of every broadening effect is estimated. These estimations use the same crystal parameters as the estimations in Section 6, and are listed in Table 6.1.

In the following, the convolution of top-hat functions with width W and Gaussian or Lorentzian distribution will be used. It is common to replace a top-hat function with a Gaussian of equal variance [149]:

$$\sigma_{\mathrm{rect}}^2 = \frac{W^2}{12}. \tag{7.1}$$

A Gaussian distribution has the known connection $\mathrm{FWHM}_{\mathrm{Gauss}} = 2\sqrt{2ln(2)}\,\sigma$ between its FWHM and its variance σ [150]. This leads to a Gaussian equivalent FWHM of the top hat function of:

$$\mathrm{FWHM}_{\mathrm{equiv.}} = 2\sqrt{2ln(2)}\frac{W}{\sqrt{12}} \approx 0.68W. \tag{7.2}$$

Focal Size

The X-ray tube used in the characterization setup is not an ideal point source. Therefore, it introduces an uncertainty of the incidence angle onto a certain point on the optic. Depending on the size of the focal spot, beams originating from the upper or lower side can reach the same reflection point at slightly different angles. The angle variation to a certain point in radiant can be estimated by

$$\Delta W_{\mathrm{source}} \approx \frac{w_{\mathrm{spot}}}{L}, \tag{7.3}$$

where L denotes the z-distance between the source and optic. The broadening due to the focal size motivates the use of a microfocus X-ray tube. For the focal spot size of 50 µm, this corresponds to an angle variation of:

$$\Delta W_{\mathrm{source}} \approx \frac{50\,\mu\mathrm{m}}{109.0\,\mathrm{mm}} = 4.6 \times 10^{-4}\,\mathrm{rad} = 0.026^\circ \quad \rightarrow \mathrm{FWHM}_{\mathrm{equiv.}} \approx 0.018^\circ \mathrm{Graphite}, \tag{7.4a}$$

$$\Delta W_{\mathrm{source}} \approx \frac{50\,\mu\mathrm{m}}{75.5\,\mathrm{mm}} = 6.6 \times 10^{-4}\,\mathrm{rad} = 0.037^\circ \quad \rightarrow \mathrm{FWHM}_{\mathrm{equiv.}} \approx 0.025^\circ \mathrm{Aluminum}. \tag{7.4b}$$

The mosaicity of the reflecting crystal convolutes with $\Delta W_{\mathrm{source}}$ to the measurable rocking curve. The convolution differs depending on whether the mosaicity is Gaussian or Lorentzian. For Gaussian mosaicities like HOPG the convolution leads to:

$$\mathrm{FWHM}_{\mathrm{total}} = \sqrt{\beta^2 + \mathrm{FWHM}^2_{\mathrm{equiv.}}}. \tag{7.5}$$

Since HOPG is expected to have a rather high mosaic spread of about $\beta \approx 0.46^\circ$, the broadening of the rocking curve by this effect is negligible.

The convolution with a Lorentzian distribution takes the form of a Voigt distribution. Its FWHM can be approximated by using the Olivero-Longbothum approximation [151]:

$$\mathrm{FWHM}_{\mathrm{total}} \approx 0.5346 \cdot \Gamma + \sqrt{0.2166 \cdot \Gamma^2 + \delta^2}, \tag{7.6}$$

where δ is the FWHM of the Gaussian contribution, and Γ is the FWHM of the Lorentzian contribution. In the case of HAPG with an expected mosaicity of $\beta \approx 0.1° = \Gamma$ and $\text{FWHM}_{\text{equiv.}} \approx 0.018° = \delta$ this convolutes to $\text{FWHM}_{\text{total}} \approx 0.105°$.
For aluminum with an expected mosaicity of $\beta \approx 0.195° = \Gamma$ and $\text{FWHM}_{\text{equiv.}} \approx 0.025° = \delta$, this convolutes to $\text{FWHM}_{\text{total}} \approx 0.198°$.

The effect is below the acceptable level of accuracy of 0.01° and can therefore be neglected if the mosaicities are close to the estimated values. Thus, based solely on the broadening described above, there is no need to use a Voigt fit instead of a Lorentz fit for rocking curves of crystals with a Lorentzian mosaicity.
Note that even if no other broadening effects were present, the focal spot size of the X-ray tube would present a lower limit of the size of F.

Divergence of Incident Beams

The original divergence of the beam affects the width of the measurable rocking curve because it allows crystallites with different tilts to participate in the reflection. It acts like "cutting out" part of the mosaic distribution. The divergence of the incident beams with respect to the K_α line is defined by the aperture. It is equivalent to the angular range discussed in Section 7.4.1, $\delta = \Delta\theta$.

The angular range has the form of a top-hat function. By measuring the size of the aperture d_A, the exposed area on the optic $\overline{c_+c_-}$ is exactly known.
In combination with the calculation of the exact position of the aperture by using the described reference configuration as the reference, the angular range $\Delta\theta = \theta_+ - \theta_-$ can be calculated. The borders of the angular range are given by:

$$\theta_+ = \arctan\left(\frac{r}{\overline{Sc_+}}\right), \tag{7.7}$$

$$\theta_- = \arctan\left(\frac{r}{\overline{Sc_-}}\right), \tag{7.8}$$

where r denotes the radius of the optic and $\overline{Sc_+}$ and $\overline{Sc_-}$ denote the distances along the central axis of the setup between the source and the borders of the illuminated area. The calculations of $\overline{Sc_+}$ and $\overline{Sc_-}$ are described in Section 7.4.2.

Due to the mosaic crystal properties of the optics, each incident ray within the range has a certain probability of being reflected. Therefore, it is problematic to assign an average incident angle to an angular range at a scan point in order to plot the results of a rocking curve scan. The average angle would have to be treated as a center of gravity

of the reflection probabilities. Additionally, the resulting rocking curve would need to be deconvolved with the angular range.

Alternatively, the rocking curve measurements can be treated as bin-averaged measurements. The observable intensity I_{meas} on the screen at a scan point i is given by the integrated intrinsic intensity:

$$I_{\text{meas,i}} = \frac{1}{\Delta\theta_i} \int_{\theta_{i-}}^{\theta_{i+}} I_{\text{true}}(\theta)\mathrm{d}\theta, \tag{7.9}$$

where I_{true} denotes the intensity of the rocking curve at the scan point i for a discrete incidence angle θ. $I_{\text{true}}(\theta)$ has the form of a Lorentzian or Gaussian distribution. If no other broadeing effects are considered, $I_{\text{true}}(\theta)$ is the intrinsic mosaic distribution of the crystal.
Using Equation 7.9 as the model to which the data is fitted, essentially converts the continious fit model to a binned model. Kipping et. al. discussed in [152] that such an approach is effective for fitting a model on binned data when the underlying context varies within a bin.

The integral can be solved analytically. In the following, the fit is briefly explained for an underlying Lorentzian fit function, which is defined by:

$$f(\theta_i) = \hat{A}\frac{\gamma^2}{(\theta_i - \theta_0)^2 + \gamma^2}, \tag{7.10}$$

where $\hat{A}$ denotes the amplitude, γ the halfwidth at half maximum ($2\gamma = \Gamma$), and θ_0 the mean value of the function.
Integrating Equation 7.10 as given by Equation 7.9 yields:

$$M_i = \hat{A}\frac{\gamma}{\theta_{i+} - \theta_{i-}} \left[\arctan\left(\frac{\theta_{i+} - \theta_0}{\gamma}\right) - \arctan\left(\frac{\theta_{i-} - \theta_0}{\gamma}\right)\right], \tag{7.11}$$

where M_i expresses the value of the fit model at scan point i. The fit then minimizes $r_i = I_{\text{meas,i}} - M_i$ by varying $\hat{A}$, γ, and θ_0. No further correction by deconvolution is necessary for the resulting fit.
The same procedure is followed for Gaussian mosaic spreads. All fit-calculations of this chapter are performed using the least squares method included in the `curve_fit` function of the `scipy` `Python`-package [153].

To ensure a good fit, the intervals in θ should still be minimzed to supress the other rocking curve boradening effects discussed in this chapter.

Probing Depth

The reflection sites inside the crystal bulk are randomly distributed and can occur in the whole volume traversed by the incident beams. However, the incidence angles are relatively small, paired with the small angular range permitted by the aperture. Therefore, the effective depth reached by a beam which is reflected toward F is limited. For a length of the exposed crystal surface of $\overline{c_+c_-}$, the maximum depth is reached for a beam that enters the crystal at c_+ and exits at c_-. Expressed with the measureable value of d_A, the maximum depth is given by:

$$d_{\max} = \frac{d_A}{2} \tan(\theta_B) - \left(R_{\text{inner}} - R_{\text{Ap}}\right), \tag{7.12}$$

with R_{inner} denoting the inner radius of the optic sample, and R_{Ap} denoting the aperture's inner radius, which is set to $R_{\text{Ap}} = 8.5\,\text{mm}$ in the current setup. All graphite optics use glass substrates with a radius of 10 mm. The optics' inner radius is therefore additionally defined by their layer thickness t via $R_{\text{inner}} = 10\,\text{mm} - t$.

The reference configuration, illustrated in Figure 7.1, is fulfilled if c_0 lies in depth $d_{\max}$, and is exactly met under the Bragg angle θ_B. This defines the z-distance between source S and c_0 to:

$$\overline{S\,c_0} = \cot\theta_B\,(R_{\text{inner}} + d_{\max}) = \overline{S\,A_0} = 2\,\overline{S\,F}, \tag{7.13}$$

which is equal to the z-distance between the source and the middle of the aperture $\overline{S\,A_0}$ in the reference configuration. It also corresponds to half the length of the focus point in a focused setup. Therefore, the setup is fully defined. Note again, that the z-direction is defined by the central axis of the setup. Both sides of the aperture cutout have an equal z-distance to A_0 of $\overline{A_+A_0} = \overline{A_0A_-} = \frac{d_A}{2}$, which defines:

$$\overline{SA_0} = \cot\theta_B\,(R_{\text{inner}} + d_{\max}) - \frac{d_A}{2} = \overline{A_0F}. \tag{7.14}$$

The borders of the illuminated area are a projection of S via A_+ and a projection of F via A_-:

$$\overline{Sc_+} = \frac{\overline{SA_+}}{R_{\text{Ap}}} R_{\text{inner}} \tag{7.15}$$

$$\overline{Sc_-} = \overline{SF} - \frac{\overline{A_-F}}{R_{\text{Ap}}} R_{\text{inner}} \tag{7.16}$$

All lengths are given as distances in z.

During a rocking curve scan, the aperture and the crystal are moved relative to the reference configuration, while the location of S and F remain constant. Moving the aperture toward

the source also moves A_+ and A_- toward the source. Thereby note that F is used in the focused mode for the calculations, even if the defocused setup is used.
The length of the illuminated area is given by $\overline{c_+c_-} = \overline{Sc_-} - \overline{Sc_+}$, and remains constant over a crystal scan. Therefore, $\overline{Sc_-}$ can also be calculated via $\overline{Sc_-} = \overline{Sc_+} + \overline{c_+c_-}$, once $\overline{c_+c_-}$ is known.

The described maximum probing depth reaches values of about $50-100\,\mu\text{m}$ with the values of d_A that were achieved during the alignments of the so-far measured samples. These maximum depths are well below the saturation thicknesses for all crystals of the characterized optics, and therefore lie in the linear correlation part of the crystals' reflectivity as a function of thickness, as shown and discussed in Section 2.4.3.

The maximum reached depth reached shows that the presented measurement approach is surface-sensitive and cannot be used to study the deeper parts of the crystal. Therefore, only the effects of bending on the upper layers can be studied. Section 7.6 briefly discusses alternative approaches for studying a possible depth-dependence using the characterization setup.

As illustrated in Figure 3.1, the Rowland circle, which defines the crystal's focusing properties, establishes a depth within the crystal that the beams must reach to enable mosaic focusing. The maximum depth is defined by the case where the non-tilted crystallites cause the reflection. This case corresponds to the defined reference case of the described characterization setup.

As described in Section 7.1, the aperture length d_A is reduced during the alignment of a scan until the K_α doublet is just discernible. This is only possible if the necessary underlying reflection still reaches the Rowland circle. To ensure a probing depth corresponding to at least the maximum depth of the Rowland circle, it is important to set the final value of d_A at the reference case of the setup.

Characteristic Line Width and Multiplicity

The characteristic lines of an X-ray tube have a certain energetic width. However, as this width lies in the eV range [68], its effect on the rocking curve broadening can be neglected when scanning mosaic crystals.

The used rhodium X-ray tube has a $K_{\alpha1}$ and a $K_{\alpha2}$ line, with an intensity ratio of $I(K_{\alpha1}) : I(K_{\alpha2}) \approx 2:1$ [119]. Their energy differences correspond to differences in their

Bragg angles of $\Delta\theta_B \approx 0.056°$ for aluminum and $\Delta\theta_B \approx 0.039°$ for graphite. Both values are smaller than the mosaic spread of the samples.
Therefore, the existence of these two lines results in a weighted overlap of two rocking curves for every line. Separating the two lines would result in a very small ROI per line and an increased susceptibility to noise. Furthermore, the boundaries between the two lines cannot always be clearly distinguished on the screen.
Thus, the ROI's definition over the whole doublet is retained.

The result is an overlap of two contributions to the measured rocking curve originating from both K_α lines with amplitudes A_1 of the $K_{\alpha 1}$ line and A_2 of the $K_{\alpha 2}$ line. In the following, the resulting broadening is estimated for the case of Gaussian mosaic distributions.
The ratio between both amplitudes is defined as:

$$r = \frac{A_2}{A_1}. \tag{7.17}$$

The mean of the resulting overlap of both Gaussians is:

$$\bar{\mu} = w_1\mu_1 + w_2\mu_2, \tag{7.18}$$

with:

$$w_1 = \frac{A_1}{A_1 + A_2} = \frac{1}{1+r}, \tag{7.19}$$

$$w_2 = \frac{A_2}{A_1 + A_2} = \frac{r}{1+r}. \tag{7.20}$$

The weights w_1 and w_2 add up to $w_1 + w_2 = 1$. $\Delta\theta_B$ is defined by:

$$\Delta\theta_B = \mu_2 - \mu_1. \tag{7.21}$$

The variance σ^2 of a distribution is generally defined as $\sigma^2 = E\left[(X-\mu)^2\right]$, with E denoting the expected value, X the random variable, and μ the mean of the distribution [154]. Both Gaussians have the same variance in this case.
For an arbitary point of reference a, it holds that $E\left[(X-a)^2\right] = \sigma^2 + (\mu - a)^2$. Using the mean of the added Gaussians $\bar{\mu}$ as the arbitary point of reference for both indivdual Gaussians yields:

$$\sigma_{\text{eff}}^2 = w_1\left[\sigma^2 + (\mu_1 - \bar{\mu})^2\right] + w_2\left[\sigma^2 + (\mu_2 - \bar{\mu})^2\right], \tag{7.22}$$

which can be transformed to:

$$\sigma_{\text{eff}}^2 = \sigma^2 + w_1 w_2 {\Delta\theta_B}^2. \tag{7.23}$$

Taking $w_1 w_2 = \frac{1}{1+r}\frac{r}{1+r} = \frac{r}{(1+r)^2}$ then yields:

$$\sigma_{\text{eff}}^2 = \sigma^2 + \frac{r}{(1+r)^2}{\Delta\theta_B}^2. \tag{7.24}$$

Considering the connection between FWHM and the variance, this can be transformed to:

$$\text{FWHM}_{\text{eff}} = \sqrt{\beta^2 + 8\ln 2\frac{r}{(1+r)^2}{\Delta\theta_B}^2}. \tag{7.25}$$

A similar analytical derivation for Lorentzian distributions is not possible in this form since no variance is defined for them. Therefore, the same width is assumed for Lorentzian distributions in the following. Analytical tests of the overlap between two Lorentzian functions showed that the resulting deviation from the actual width is less than 10 %.

This effect brings the rocking curve widths to:
$\text{FWHM}_{\text{total, HOPG}} \approx 0.462°$, $\text{FWHM}_{\text{total, HAPG}} \approx 0.11°$ and $\text{FWHM}_{\text{total, Aluminum}} \approx 0.205°$. Thus, the broadening is relatively weak, and conventional Gaussian or Lorentzian distributions can still be used for fitting of the data. This is confirmed by the results in Section 7.5.1, that show a good resulting fits using these distibutions.

Solid Angle Coverage

The length of the exposed crystal area remains constant during a rocking curve scan. In contrast to that, the solid angle covered by the illuminated area is different for every scan point. Since the solid angle coverage is directly connected to the flux from the X-ray tube that reaches the exposed area, steeper angles are favored over flatter angles in the resulting rocking curve. As a result, the measurements have to be corrected with a normalization factor.

The solid angle Ω of the exposed area is given by:

$$\Omega = 2\pi\left(\cos\theta_- - \cos\theta_+\right), \tag{7.26}$$

in accordance with Equation 3.4. The borders of the angular range are given by Equations (7.7) and (7.8). To account for the varying solid angle coverage, a normalization factor, N_Ω, is applied to the recorded rocking curves prior to fitting. This factor normalizes

the recorded counts with respect to the solid angle covered in the reference configuration of the scan, and is given for a specific scan point i as:

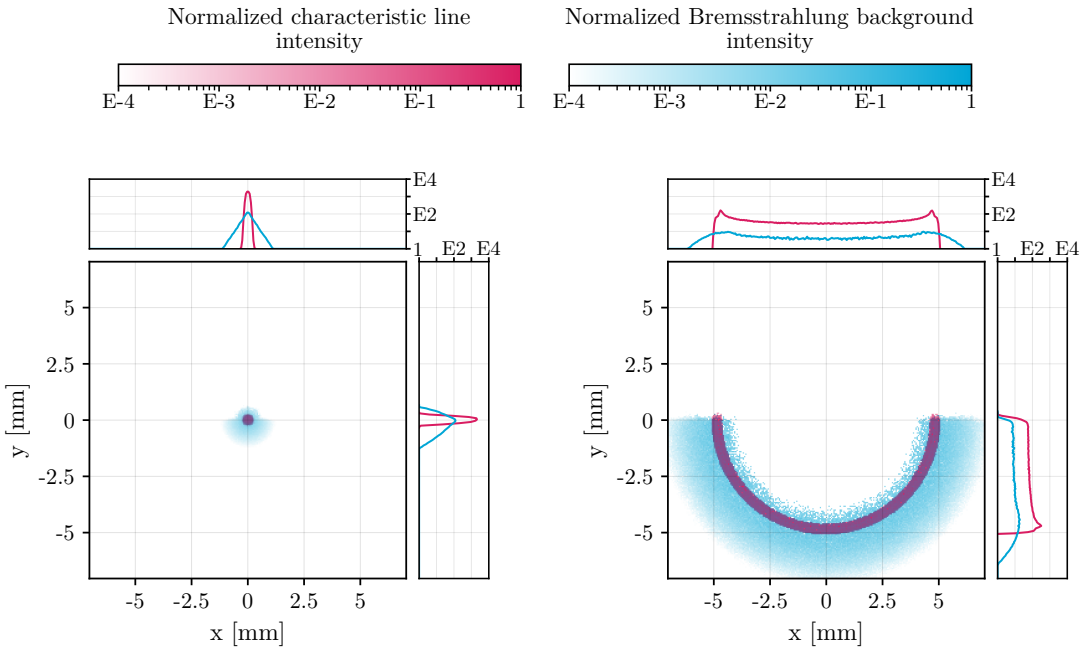
$$N_{\Omega,i} = \frac{\Omega_i}{\Omega_{\text{in}}}, \tag{7.27}$$

where Ω_{in} denotes the solid angle coverage in the reference configuration.

Bremsstrahlung Background

In addition to the characteristic lines, the spectrum of the used X-ray tube has a continuous Bremsstrahlung background. As a result, every energy up to the operating voltage of the tube, which was set to 50 kV, is present in the spectrum.
Therefore, each point during a rocking curve scan creates a setting in which the exposed crystal area exhibits a perfect reflection geometry for a particular energy. For scan points closer to the X-ray tube, the aperture and crystal positions result in a lower best-focused energy. In the other direction, the best-focused energy increases.
In a focused setup, the best-focused energy of the Bremsstrahlung background could form a focal point around F that could be mistaken for the focus of the K_α lines. This is particularly relevant when the alignment begins far from the scenario in which the characteristic lines are best focused. This highlights the advantage of the defocused setup, as the identification of the double line structure ensures that only the K_α lines are evaluated.

Figure 7.3 shows the focus during a simulated rocking curve measurement of an HOPG sample at a scan point 5 mm away from the reference configuration. Figure 7.3a uses a focused setup, while Figure 7.3b uses a defocused setup.
Both plots show the contribution of the characteristic line to the total flux in the focus in blue, and the Bremsstrahlung background in red. Overlapping contributions are illustrated by additive color mixing. Since the background is weaker than the characteristic lines, approximately 87 % of the total flux originates from the contribution of the K_α doublet. To depict the Bremsstrahlung background contribution, the plots are logarithmic.
Note that the K_α doublet is not differentiable on a logarithmic scale. The brightness of the colors indicate the intensity of each contribution. Both contributions are normalized to the highest flux per pixel in their respective setups. Marginal projections of the detector image of the foci onto the x and y axes show the relative contribution of the characteristic lines and the Bremsstrahlung background on a logarithmic scale.
Figure 7.3a, shows that in a focused setup, the majority of the background is also focused in a round shape around the focus of the characteristic lines, which makes both contributions hard to distinguish in a real, not energy-resolved measurement. Therefore, the determination of the ROI is particulary prone to errors.



(a) Focused setup **(b)** Defocused setup

Figure 7.3: Comparison of simulated detector images of a focused (a) and a defocused (b) setup at an exemplary scan point during a rocking curve measurement. Red indicates the characteristic K_α lines' contribution to the total flux on the detector, blue the Bremsstrahlung background. The detector images and their marginal projections are in logarithmic scale, making the K_α doublet non-separable. While the focused setup concentrates both contributions in the same region, the defocused setup spreads the background over a larger detector area, thereby facilitating the ROI definition.

In contrast, Figure 7.3b shows that, in a defocused setup, the background is spread across a larger area of the detector. Additionally, as shown in Figure 7.2, the K_α doublet is visible using a linear scale, which simplifies the definition of the ROI in a defocused setup.

The results of the simulations of this scan point also show, that even if the ROIs are defined ideally in a way that, in both cases, the ROIs are precisely limited only to the region corresponding to the reflected K_α lines (red area) about 55 % of all Bremsstrahlung photons are incident on the ROI in the focused setup, and 33 % of all Bremsstrahlung photons are incident on the ROI in the defocused setup. This demostrates the benefits of the defocused setup, even for a perfect ROI definition.

For a reliable recording of a rocking curve, it is essential to limit the evaluated energy range as much as possible. In the defocused setup, this is achieved by restricting the analysis to the discernible double structure of the K_α lines. If, for example, the entire unrestricted detector signal was evaluated, the result would be a broad rocking curve with an overlying peak, arising from the K_α lines, that would be difficult to resolve.

Additionally, the defocused setup is more resistant to possible inaccuracies of the alignment of the setup's and the optic's axes. If the alignment is not exact, the different parts of the illuminated area along the azimuthal direction would reach their best alignment to the Bragg condition slightly after each other. The detector image of the circle segment, as shown in Figure 7.2, would become progressively lighter in an azimuthal direction.
Using the focused setup, the sequential ideal focusing would lead to a rocking curve that is broadened by the angle between the optic's and the setup's axes. Since the mosaic spreads to be measured are well under 1°, the alignment would have to be very precise.
By using the defocused setup and only evaluating a segment of the detector image, the measured rocking curve is not substantially broadened by a possible slight misalignment between both described axes.

Despite the described choice of the ROI in the defocused setup, reflected spectral regions of the Bremsstrahlung spectrum, particularly those with energies close to the analyzed characteristic lines, may also be included in the ROI. This results in an unavoidable broadening of the rocking curve that is difficult to estimate analytically as it depends on the size of the ROI. This broadening is minimized by a narrow definition of the ROI and the use of the maximum tube voltage of 50 kV, which maximizes the fraction of the total flux contained in the characteristic lines.

The remaining broadening suggests that the measured, solid angle-corrected rocking curve is an overestimation of the mosaicity of the characterized optic. Due to the use of a non-energy-resolved pixel detector, the broadening effect caused by the background is difficult to distinguish from the other discussed broadening effects.

7.4.3 Rocking Curve Evaluation Procedure

To improve the estimate of β, the respective setups with the achieved aperture settings are simulated using `xrt` ray tracing for various mosaic spreads on the order of magnitude of the measured rocking curve width. These simulations are then evaluated in the same manner as the experimental scans. The simulation results are subject to the same broadening effects discussed in Section 7.4.2.
Therefore, if the rocking curve width obtained through the evaluation of the corresponding simulation matches the width that was determined experimentally, the mosaic spread β_{sim} that underlies the simulation can be used as a good estimate for the intrinsic value of the mosaic spread β of the sample. As shown in Section 7.5.1, the deviation between the rocking curve widths and the estimated mosaic spread is less than 0.02°.

Since the simulation also accounts for the focal size broadening, the broadening by the characteristic line width, and the effect of the line multiplicity, no further corrections of these effects are necessary when using the described approach. Nevertheless, the knowledge of their order of magnitude is important for suppressing their broadening effects and improving the estimate.
The most significant reduction of the broadening effects comes from using the binned model for fitting, minimizing the aperture width d_A, and using a microfocus X-ray tube.

Additionally, minor inaccuracies in the alignment or the definition of reference configuration, as well as possible scattering in the setup, can lead to a rocking curve broadening background. Since the simulations do not account these sources of broadening, the final result of the mosaic spread always remains an upper estimate.

7.4.4 Crystal Scan Measurements

Apart from the mosaic distribution, another important information for the evaluation of an optic is its relative overall reflection quality. An ideal optic would have the same reflectivity and mean crystallite alignment over its whole reflecting surface.

This property is tested using the same defocused setup in the reference configuration as described in Section 7.4.1. The obtained image resolves the azimuthal angle of the illuminated optic part involved in the reflection. Since the reference configuration is used, the visible doublet has its maximum brightness. Ideally, the intensity remains constant across the entire detector image, indicating a consistent optical quality. As visible in Figure 7.2 this is not the case for the measured samples. The brightness of the image varies along the azimuthal direction.

During a crystal scan, the positions of the source, the aperture, and the detector remain constant. Only the optic is moved above the aperture, along the central axis of the setup. This way, every scan point corresponds to a different part of the optic being illuminated. The ROI is defined as the entire ring segment showing the K_α doublet in an obtained detector image. This definition corresponds to the entire semi-circle in Figure 7.2 being the ROI for the corresponding scan point, while the radial width of the ROI is defined in the same way as for the rocking curve measurements.
The counts in the ROI are integrated along the radial axis. This is done, because the focus of the K_α doublet is produced by the whole width of the illuminated part $\overline{c_+c_-}$. A single scan point has no spatial resolution in the axial direction. In contrast, the azimuthal direction is resolved for the same reason as described in Section 7.4.1.

Between scan points, the position of the optic, and therefore the illuminated area on the crystal, is shifted by a fixed step width w. For the measurements presented in this chapter, a step width of $w = 1\,\text{mm}$ is chosen. The step width specifies the resolution in the axial direction. The individual results per scan point are combined to form a map of the entire crystal surface, which can be matched to the exact surface area of the optic. This way, the overall crystal quality can be evaluated, and possible defects can be identified.
$\overline{c_+c_-}$ limits the sensitivity[1] in the axial direction of a single scan point, while the sensitivity in the azimuthal direction is only limited by the pixel size of the detector. The resolution in the azimuthal direction is similar to the sensitivity in this axis.

If the step width w is smaller than $\overline{c_+c_-}$, the individual results per scan point overlap. Therefore, in the resulting map, the value is averaged from all scan points that contribute to a strip of width w. As an example, if $\overline{c_+c_-} = 3\,\text{mm}$ and $w = 1\,\text{mm}$, every 1 mm strip in the final map is the result of averaging over 3 scan points. Thus, the resolution of the resulting map is given by w, while the sensitivity of the scan is given by $\overline{c_+c_-}$.

Together with the rocking curve scan, the described crystal scan gives the opportunity to compare different optics. It is resistant to detuning because it produces reliable results even when the reference configuration is not perfectly met.
Note that the detector image is flipped with respect to the optic in all defocused measurements, where F' lies behind F. This should be considered when matching the results to the optic's surface.

7.5 Experimental Setup

Figure 7.4 shows a photo of the experimental setup during the measurement of an aluminum sample. The aperture is positioned at the minimum distance from the X-ray tube. Therefore, Figure 7.4 shows the end of the respective scan.

The X-ray tube is mounted on two motors to make its position adjustable. This allows it to be precisely aligned with the optical axis of the setup.
The optics to be measured are placed on a suspension that fits semi-cylindrical optical parts with a length of up to 33 mm. Optic parts that are less than a half cylinder can also be measured using appropriate adapters, as shown for the aluminum samples in Figures 7.4 and 6.8. The aperture and the optics can be moved together or separately along the optical axis using linear guides, which enables both discussed measurement options.

[1] The sensitivity describes the ability of a measurement to detect small changes in the measured intensity, while the resolution describes the spatial resolution of the resulting map.

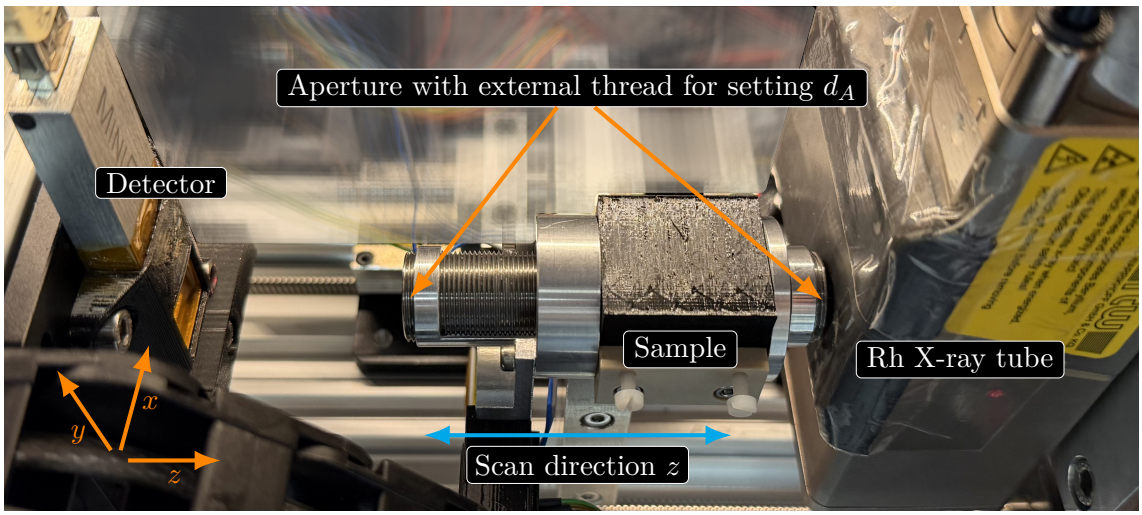


Figure 7.4: Experimental characterization setup during a scan of an aluminum sample. The aperture and the sample are positioned at the minimum distance from the X-ray tube. The gap, d_A, between both sides of the aperture and the midstop lie underneath the sample. Both are not visible in the photo.

In the expiremental setup, d_A is controlable by using two hollow cylinders with an external thread, visible in Figure 7.4, as the aperture. In combination with a mounting bracket featuring the corresponding internal thread, this allows for a precise control of the distance between both sides of the aperture.
Due to the small angles of reflection, d_A is significantly larger than $\overline{c_+c_-}$, which simplifies the fine-tuning of the illuminated area by varying d_A. For example, when characterizing a 50 µm-thick HAPG optic, a width of $d_A = 34.0\,\text{mm}$ corresponds to an exposed area on the optic with a length of $\overline{c_+c_-} = 2.6\,\text{mm}$.
The gap d_A between both sides of the aperture and the midstop are not visible in Figure 7.4 as they lie underneath the sample.

To show the desired focus, the detector can be moved along the central axis, as well as in the x- and y-planes.
The setup is shielded by placing it inside an X-ray protection cabin. The aperture and the midstop are made of stainless steel, and the midstop is additionally lined with lead to maximize its absorption capability.

In the following, the results of selected samples are presented to demonstrate the suitability of the setup, and to highlight current weaknesses. This includes an HAPG optic with a crystal layer thickness of $t = 50\,\mu\text{m}$, which is the thinnest SCOTTI optic produced so far. The expected mosaic spread lies between $\beta \approx 0.1°$ to $\beta \approx 0.2°$ [136], with a Lorentzian mosaicity.
The second presented sample is an optic-half with a $t = 200\,\mu\text{m}$ thick HOPG layer, with an expected mosaic spread between $\beta \approx 0.4°$ and $\beta \approx 0.7°$ [136], and a Gaussian mosaicity.

This sample's geometric properties are comparable to those of the best-performing HOPG optic, which was used in SCOTTI during the measurements presented in this chapter and was therefore unavailable for characterization. However, the characterized optic showed about 20 % less flux when used as the focusing optic in SCOTTI.
Finally, a first measurement of an aluminum optic sample of batch 2 was performed. Due to the non-ideal bending of the samples from batches 1 and 2, a complete characterization was not possible. The aluminum optic samples from batch 3 were delivered only after the latest characterization measurements in Berlin, and were therefore not characterized during the study presented in this chapter.

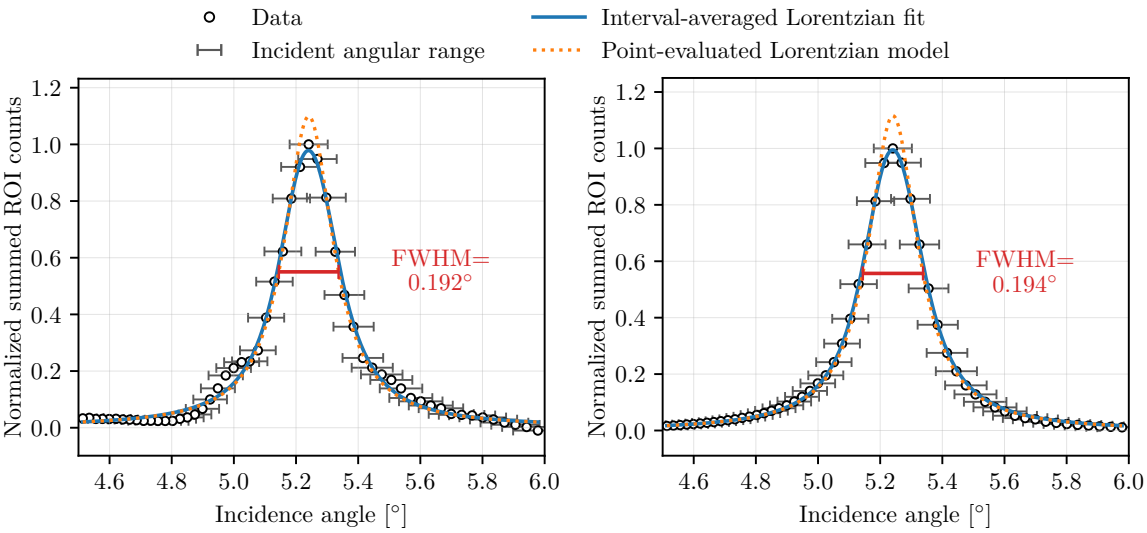
7.5.1 Rocking Curve Measurement Results

In the following, the results of the first rocking curve measurements are presented. As explained in Section 7.4.2, the evaluation includes a simulation of the setup, the results of which are also presented.

Additionally, a rocking curve measurement performed without an optic revealed a light background signal. This manifests as a linear relationship between angle and background in a rocking curve measurement, which rises at steeper angles that correspond to scan points toward the X-ray tube. This suggests that the background signal originates from scattering at the aperture and the optic mount. The linear background was subtracted from the data presented in the following.

HAPG Optic Sample

During the alignment of the HAPG sample with a thickness of 50 µm, an aperture width of $d_A = 33.8\,\text{mm}$ could be achived, which corresponds to a width of the illuminted area of $\overline{c_+c_-} \approx 2.4\,\text{mm}$. Figure 7.5a shows the experimentally obtained rocking curve, and Figure 7.5b the best-fitting simulation of the setup.
Both curves are corrected for the solid angle coverage. Furthermore, both datasets are normalized to their respective highest summed detector counts inside the ROI. As the goal of this part of the characterization is to measure the width of the fits, no information is contained within the absolut values of the summed counts.
The used ROI has an angular coverage of 2°, which was empirically found to be a good compromise between flux inside the ROI and spatial resolution in the azimuthal direction. Both plots show the fit of the respective experimental or simulated data using a binned fit model with an underlying Lorentzian, which is described in Section 7.4.2. The horizontal line at each point shows the angular width that is covered at the respective scan point.



(a) Measured rocking curve **(b)** Simulated rocking curve

Figure 7.5: Experimentally (a) obtained rocking curve and rocking curve obtained by evaluating an `xrt` simulation (b) of the same setup. The evaluated ROI was defined as a sector of the half circle, as shown in Figure 7.2, with an angular coverage of 2°, and a radial coverage defined such that the K_α doublet is contained in every scan point. Both datasets were corrected for solid angle coverage and normalized to their respective highest sum of counts in the ROI.
The evaluations use a binned Lorentzian model. For every scan point, the respective angular coverage is drawn as a horizontal line. The blue line shows the interval-averaged Lorentzian fit of the data, while the orange dotted line shows the plot of a Lorentzian using the paramters obtained by the interval-averaged fit, evaluated at discrete values of the incidence angle instead of angular ranges. The FWHM of the point-evaluated Lorentzian, illustrated in red, is the rocking curve width of the scan.

Both plots show a good consistency with the performed fit. The measured or simulated value at a scan point is always a mean value over the respective range of incidence angles, as described by the integral in Equation 7.9.

The results of the fit for the function parameters can also be used to plot a point-evaluated Lorentzian model. In contrast to the interval-averaged model it shows the calculated rocking curve as a function of discrete values of the incidence angle. Thus, the plotted dashed orange curve shows the model's estimation of a rocking curve if an incident beam with a virtually constant incidence angle was used. The FWHM of the point-evaluated Lorentzian model is the resulting rocking curve width without the influence of the broadening effect of the finite angular coverage at a scan point, and is therefore used as the result of the measurement.

The deviation between the interval-averaged fit and the point-evaluated model arises from the averaging effect of the angular range. Only at the mean of a rocking curve, its value drops on both sides of the respective angular range in respect to the value at its center. Therefore, the averaging at this point results in a significantly lower value.

At all other points, one side of the angular range is located at a higher value, and one side at a lower value than the center of the respective range. Along a single scan point's angular range, the underlying Lorentzian is nearly linear, which results in a good agreement between the interval-averaged fit and the point-evaluated model.
This underscores the importance of the presented binned evaluation method, especially for samples with a low mosaic spread, which show a significant difference between the signal at the center and the edges of an angular range at the mean of the rocking curve. Even without a simulation for comparison, the point-evaluated model provides a good upper estimate of the intrinsic mosaicity profile.

Both point-evaluated models in Figure 7.5 have a comparable rocking curve width of $(0.192 \pm 0.005)^\circ$ for the experiment, and $(0.194 \pm 0.001)^\circ$ for the simulation, where the reported inaccuracies are the 1σ-errors of the fit. The simulation uses an underlying mosaic spread of $\beta = 0.180^\circ$, which is therefore identified as the final experimental estimate of the mosaic spread of the sample at the analyzed location.

The small discrepancy between the rocking curve width and the mosaic spread indicates that only a slight broadening of the rocking curve occurred due to the effects described in Section 7.4.2, meaning that they were successfully minimized. The result of $\beta \approx 0.18^\circ$ falls within the range specified by Optigraph for different susbtrates of $0.1^\circ \lessapprox \beta \lessapprox 0.2^\circ$, but is greater than the originally expected value of $\beta \approx 0.1^\circ$, which was used for simuations of the HAPG optics.
This expected mosaic spread of $\beta \approx 0.1^\circ$ was based on the general specifications of Optigraph for HAPG optics using optically polished glass substrates [136] to account for the theoretically resulting high peak reflectivity. However, Optigraph performed a characterization of an HAPG optic sample with similar specifications as the measured 50 µm HAPG sample, which yielded a value of $\beta \approx 0.17^\circ$ [155]. This value is comparable to the mosaic spread measured with the presented characterization setup. The measurement of Optigraph was performed on 5 points on the sample. Therefore, their measurement does not provide the high potential spatial resolution as the presented characterization setup.

The measurement and the fitted rocking curve show a slight deviation at the left edge, which could have been caused by additional scattering into the evaluated ROI. It is also possible that some X-rays were reflected to the ROI from an illuminated crystal region with a shape that deviates from the basic shape of the optic. In addition, the location of the illuminated area changes slightly over the course of a scan. If a crystal region with slightly different properties is located right next to an evaluated region, this can also cause the rocking curve to deviate from a perfect Lorentzian profile. Section 7.6 describes how

the setup can be improved to reliably study such effects.

The analysis of other ROIs along the azimuthal axis of the scan reveals mosaic spreads ranging from $\beta = 0.17°$ to $\beta = 0.19°$.

The 50 µm HAPG optic sample is the thinnest optic produced so far. To demonstrate the suitability of the design across the entire range of optics used in SCOTTI, the thickest graphite-based optic, a 200 µm HOPG optic, is characterized in the follwing.

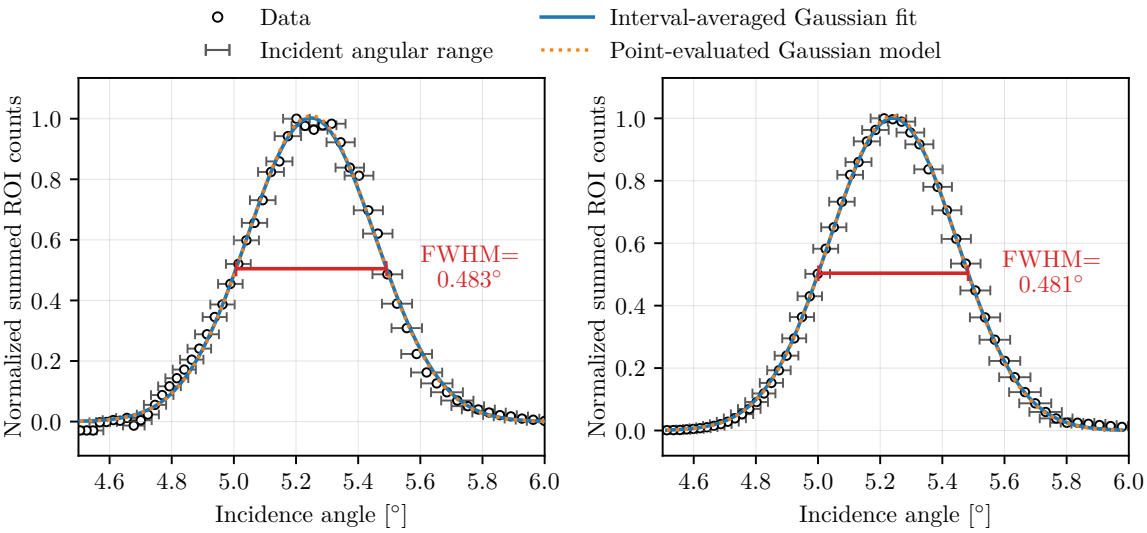
HOPG Optic Sample

In the alignment of the 200 µm HOPG sample, an aperture width of $d_A = 29.9\,\text{mm}$ could be achieved, which corresponds to an illuminated area width of $\overline{c_+c_-} = 1.1\,\text{mm}$. Note that the different achievable values of d_A are attributable to different layer thicknesses and the resulting different inner radii, as well as different reflectivities, which results in higher required values for $\overline{c_+c_-}$ in order to be able to distinguish the line doublet from the background.

Figure 7.6a shows the experimentally obtained rocking curve, and Figure 7.6b the best-fitting simulation of the setup. The evaluation was performed in the same way as explained for the HAPG sample, but with using a binned Gaussian model for fitting. The fit of the binned Gaussian model, illustrated in blue in Figure 7.6, and the point-evaluated model, illustated as the dotted orange line, show no visible deviation. The reason lies in the high mosaic spread of the HOPG sample compared to the HAPG sample, and the smaller achieved length of $\overline{c_+c_-}$. As a result, the normalized summed ROI counts remain nearly constant across the angular range of a single scan point. Thus, the significantly lower amplitude caused by averaging, as seen in the evaluation of the HAPG sample, does not occur here.

Both curves have a comparable rocking curve width of $(0.483 \pm 0.006)°$ for the experiment, and $(0.481 \pm 0.002)°$ for the simulation. The simulation used an underlying mosaic spread of $\beta = 0.480°$, which is therefore the final experimental estimate of the mosaic spread of the sample at the analyzed location.
The rocking curve width and the intrinsic mosaic spread are nearly identical in the case of HOPG, which is caused by the high mosaic spread and the resulting negligible broadening by the effects discussed in Section 7.4.2.

The measured mosaic spread lies within the expected range between $\beta \approx 0.4°$ and $\beta \approx 0.7°$ [136], and shows the expected Gaussian mosaicity.



(a) Measured rocking curve **(b)** Simulated rocking curve

Figure 7.6: Experimentally (a) obtained rocking curve and rocking curve obtained by evaluating an `xrt` simulation (b) of the same setup. The evaluated ROI was defined as a sector of the half circle, as shown in Figure 7.2, with an angular coverage of 2°, and a radial coverage defined such that the K_α doublet is contained in every scan point. Both datasets were corrected for solid angle coverage and normalized to their respective highest sum of counts in the ROI.
The evaluations use a binned Gaussian model. For every scan point, the respective angular coverage is drawn as a horizontal line. The blue lines show the interval-averaged Gaussian fits of the data, while the orange dotted lines plot a Gaussian using the same paramters obtained by the fit, evaluated at discrete values of the incidence angle instead of angular ranges. The FWHM of the point-evaluated Gaussian, illustrated in red, is the rocking width of the scan. Due to the high mosaic spread, the normalized summed ROI counts are nearly constant over an angular coverage of a scan point, which is why the blue and the orange line are nearly identical.

The result is also comparable to the experimental value obtained in the characterization measurement of an unbent HOPG slab in [26] of $\beta = 0.461°$, measured at the P21.1 beamline (PETRA III, DESY, Hamburg [18]). This comparability suggests that the mosaic spread, up to the probing depth, is not significantly altered by the manufacturing process, which is described in Section 6.1. It also implies, that a rocking curve broadening due to possible strains in the bent samples is negligible for HOPG.

The analysis of other ROIs along the azimuthal axis of the scan revealed mosaic spreads ranging from $\beta = 0.47°$ to $\beta = 0.53°$.

Figure 7.7 shows a part of a detector image taken during the described defocused rocking curve scan of the HOPG sample. Compared to Figure 7.2, Figure 7.7 shows the semi-circle being composed of straight segments while still retaining the visible double structure of the K_α doublet. One explanation of this effect is that it is caused by the rougher surface of HOPG compared to HAPG, which results in larger areas that do not exactly follow

the curvature of the substrate. The other possible explanation is that small parts of the crystal majorly contribute to the reflection, while directly neigboured parts contribute less to the overall reflection. The result is an image that is mainly caused by reflections at single points that lie on the illuminated half-ring.

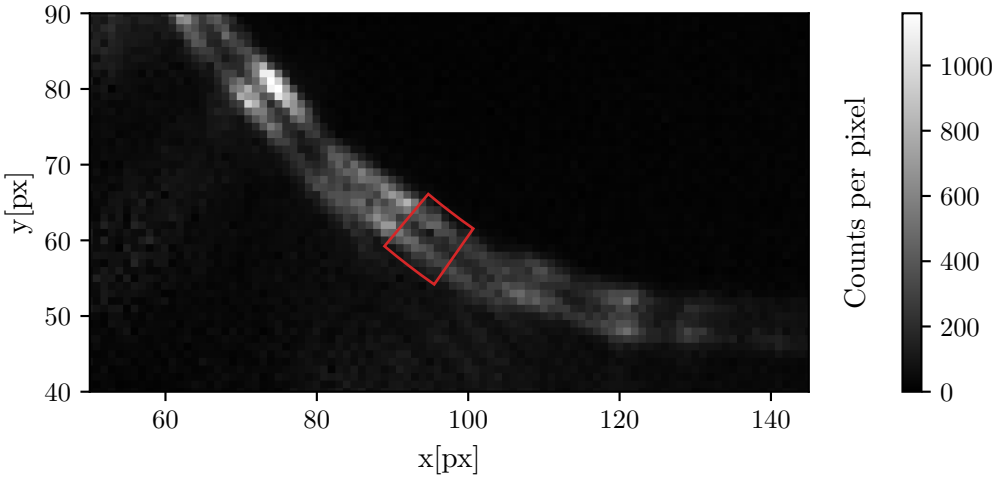


Figure 7.7: Zoomed detector image during the rocking curve measurement of an HOPG optic sample using the defocused characterization setup, showing the semi-circle being composed of straight segments. An exemplary ROI with an angular range of 2° is shown to illustrate that only a single straight segment lies within the evaluated ROI.

Both explanations, combined with the high mosaic spread of HOPG, account for an increased relevance of the azimuthal defocusing described in Section 3.2.3. In the evaluation of the aluminum sample, that is presented in the following, this effect is even further enhanced, as only a single point at the surface takes part in the reflection, resulting in a single, straight K_α doublet on the screen.

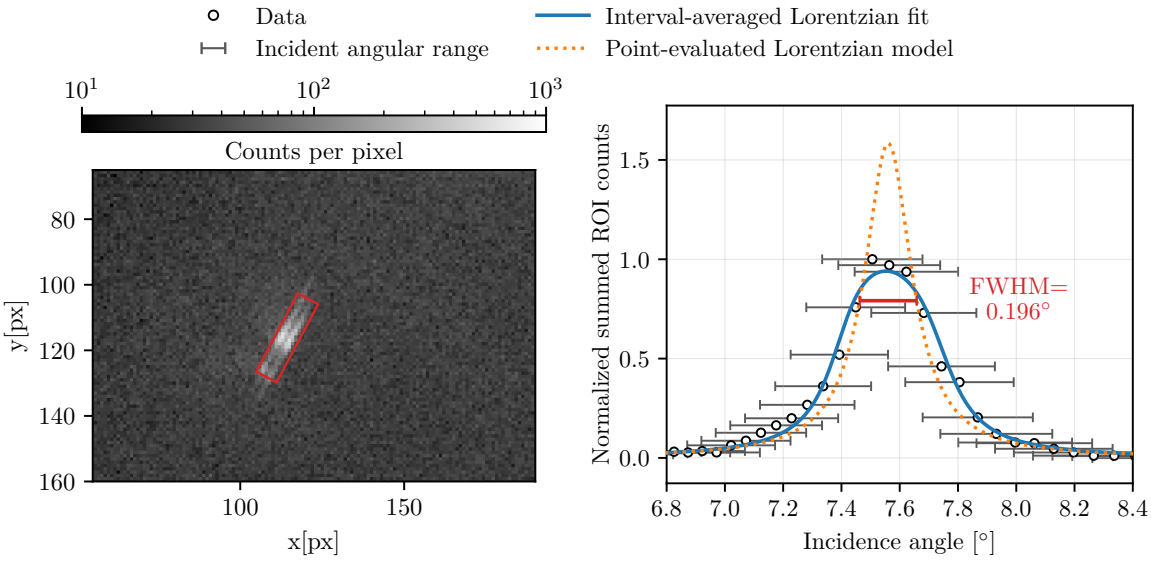
The enhanced azimuthal defocusing can result in reflected X-rays from adjacent areas entering the analyzed ROI. This effect is a possible explanation for the small deviations between data and fit around the mean of the rocking curve in Figure 7.6a. Figure 7.7 shows an exemplary ROI with an angular range of 2° to illustrate that only a single straight segment lies within the evaluated ROI.
When defining an ROI in a sample that shows the described behavior, it is essential to ensure that it does not fall on the boundary between two segments. Otherwise, the evaluated rocking curve will show the overlapping behavior of both segments, which reduces the spatial resolution and can lead to a broadening of the rocking curve.

Aluminum Optic Sample

At the time of the most recent measurements, only the aluminum samples from batches 1 and 2, described in Section 6.5, had been produced. As shown in Figure 6.8, these samples did not exhibit a precise curvature.

The characterization setup, and in particular the described method for achieving the smallest possible width of d_A, relies on the sample being uniformly curved along the azimuthal axis.
Sample 3, which is the best-curved sample from batches 1 and 2, was therefore used for the measurements presented in the following.

Furthermore, to convert d_A to the angular range of each scan point, it is essential to know the exact distance between the sample surface and the axis of the setup, which is difficult to determine if the sample is curved unevenly. Due to the imperfect bending of the sample, it was therefore not possible to produce the image of a complete semi-circle in the alignment. An aperture width of $d_A = 25.6\,\text{mm}$ could be achieved, which corresponds to a width of the illuminated area of $\overline{c_+c_-} = 3.5\,\text{mm}$, assuming an inner radius of $R_{\text{inner}} = 10\,\text{mm}$. Only a small section of the optic sample could be illuminated in such a way that the K_α doublet was visible in the reflection. Figure 7.8a shows the zoomed detector image with a visible K_α doublet. It is plotted logarithmically to improve the visibility of the weak signal.



(a) Detector image and selected ROI **(b)** Angular scan and Lorentzian fit

Figure 7.8: Zoomed detector image (a), captured during the rocking curve scan of the aluminum optic sample 3, with the selected ROI (red square), and the corresponding rocking curve (b). (a) shows a logarithmic representation of the detector image. Due to imperfect bending, only a fraction of the sample is illuminated, leading to a weak reflection and the K_α doublet being imaged as straight lines.
The evaluation of the data in (b) uses a binned Lorentzian model. For every scan point, the respective angular coverage is drawn as a horizontal line. The blue line shows the interval-averaged Lorentzian fit of the data, while the orange dotted line shows the plot of a Lorentzian using the same paramters obtained by the fit, evaluated at discrete values of the incidence angle instead of angular ranges. The FWHM of the point-evaluated Lorentzian, illustrated in red, is used as a rough upper estimate of the underlying intrinsic mosaic spread at the iluminated point on the crystal.

The lines appear straight, with no curvature, and an intensity maximum in the center. Since the reflection originates from a single point, it is subject to the azimuthal defocusing discussed in Section 3.2.3. In a complete optic, this effect is normally no longer visible. It is also conceivable that the aluminum samples of batch 1 and 2 have an even rougher surface than the HOPG samples, which also showed straight lines originating from non-bent parts on their surface.

As a result, the data can not be fully evaluated as done for the HAPG and the HOPG samples, because a simulation of the setup is not reasonable as it always assumes a perfect curvature. Nevertheless, the data is evaluated using the binned Lorentzian fit, as was done for the HAPG sample, and assuming an inner radius of the sample of $R_{\text{inner}} = 10\,\text{mm}$. This way, the origin of the visible refection is assumed to be a point on the bent crystal that has a distance of 10 mm to the axis of the setup.
The ROI is defined as a constant area over the doublet and is illustrated in red in Figure 7.8a.

Figure 7.8b shows the resulting rocking curve and the fit using the binned Lorentzian model. The achieved minimal aperture width accounts for a higher angular range per scan point. As a result, the point-evaluated Lorentzian, illustrated in blue, and the interval-averaged Lorentzian fit, illustrated in orange, differ significantly, as the model assumes an integration over the relatively large angular range.
The FWHM of the plot is illustrated in red and has a value of $(0.196 \pm 0.016)^\circ$.

The result should only be treated as a rough upper estimate of the intrinsic mosaic spread, especially because the achieved minimal angular range per scan point is high, compared to the HAPG and HOPG samples.
However, the resulting estimate of the mosaic spread is comparable to the experimental value obtained in the characterization measurement of a straight aluminum slab of $\beta = 0.195^\circ$ in [26], measured at the P21.1 beamline (PETRA III, DESY [18]). The comparablility suggests that the mosaic spread at the evaluated point is not significantly altered by the bending or a possible strain in the bent sample. However, as only a single point on the bent crystal was used for this measurement, a defintive statement is not possible. The comparability could also result from the evaluated point remaining locally straight, as opposed to being bent.

Nevertheless, this initial measurement demonstrates that characterizing aluminum samples is generally possible with the presented setup. This is not naturally given, as the steeper Bragg angles of the (1 1 1) reflex of aluminum, compared to the (0 0 2) reflex of graphite, account for smaller distances between the parts of the setup.

It can be assumed that future measurements of the far better bent aluminum samples of batch 3 will be significantly easier to align, allowing for a full characterization.

7.5.2 Crystal Map Results

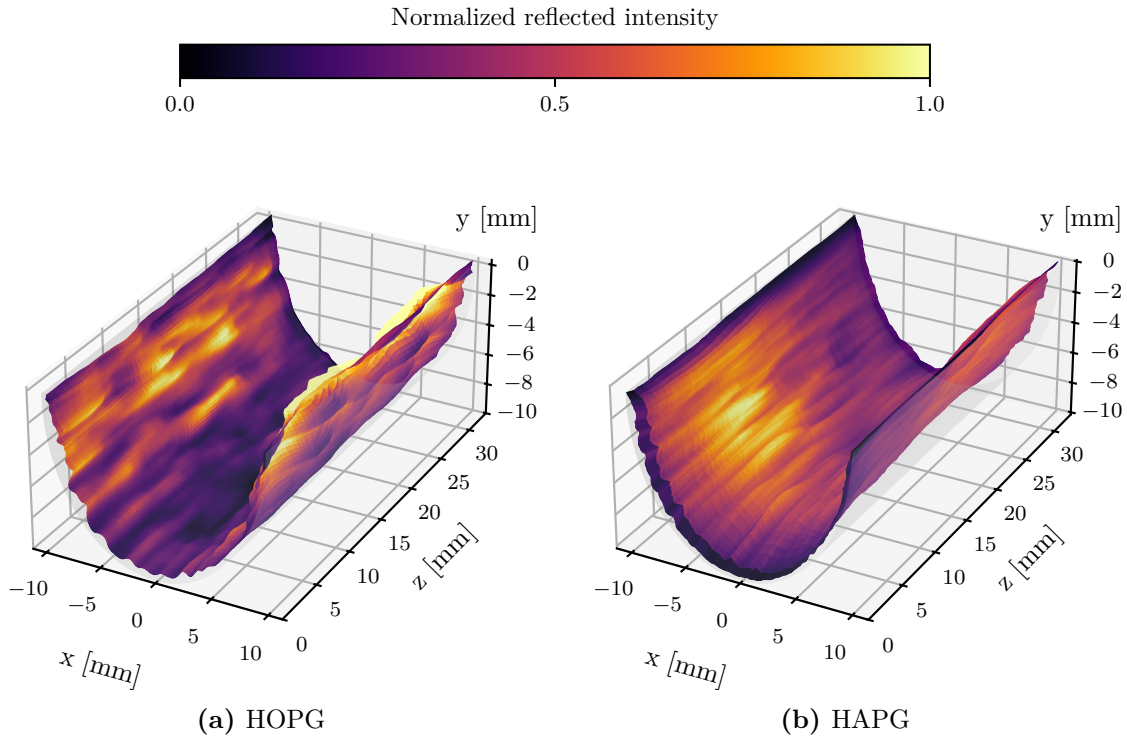
The second type of characterization that is possible with the described setup is a surface scan of the entire crystal, as explained in Section 7.4.4. Therefore, the aperture is tuned to a width of d_A so that the entire ring segment exhibits a comparable brightness. This ensures, that the width of the illuminated area $\overline{c_+c_-}$ is comparable along the azimuthal axis of the crystal. Otherwise, areas where the illuminated area is broader, would show a higher signal in the resulting map which could be mistaken for an effect of the crystal.
As the value of $\overline{c_+c_-}$ increases, the possible variation in $\overline{c_+c_-}$ under a slight misalignment of the setup decreases. Since relative differences between regions of the crystal are evaluated for the subsequent analysis, a higher value of $\overline{c_+c_-}$ is therefore favorable to suppress this effect. Thus, higher values of d_A than those used for the rocking curve scans are acceptable, provided they result in a more even illumination.

However, $\overline{c_+c_-}$ limits the sensitivity of the scan in the axial direction, as explained in Section 7.4.4.
The setting of d_A is therefore a tradeoff between sensitivity and the needed comparable brightness. Addtionally, a higher value of $\overline{c_+c_-}$ causes a higher probing depth, as discussed in Section 7.4.2, which could be desireable if a depth-dependence is suspected.

To rule out possible effects by a misalignment of a sample, every characterized optic is scanned, flipped and scanned again. Visible features on one side of the resulting map must change locations when evaluating the flipped scan. Otherwise, the feature in question is caused by the setup rather than the sample.
The described change of the location of clearly visible features in the maps was reliably observed in all measurements presented in the following. To compensate for any potential discrepancies that might not be immediately apparent, the resulting map from the second, fliped scan was rotated by 180° and averaged with the map from the first scan.

Since it was not possible to produce a full, defocused image of the focus of any of the aluminum optic samples of batch 1 and 2, they are not included in the following results. In the following, the same 50 µm HAPG and 200 µm HOPG optics for which a rocking curve was measured are used to demonstrate the crystal map results.
The maps in Figure 7.9 are shown as three-dimensional plots, where the half-cylindric shape exactly matches the inner surface of the respective optic in terms of axial length, radius and the 180° azimuthal coverage. The intensity is normalized to the highest respective

value of the averaged, integrated detector count rate along the ROI for both maps.



(a) HOPG **(b)** HAPG

Figure 7.9: Three-dimensional plots of the crystal maps obtained with crystal scans of a 200 µm HOPG (a) and a 50 µm HAPG (b) optic half. The half-cylindric shape of the plots exactly matches the inner surface of the respective optic in terms of axial length, radius and the 180° azimuthal coverage. The plotted color and height toward the cylinder axis, normal to the surface at a point, corresponds to the intensity of reflection at this point. Both plots are normalized to the highest respective intensity.
Both samples show a pronounced location-dependence of the reflected intensities over the crystal, indicating varying crystal properties. The HOPG sample shows a streak-like pattern in the high-intensity areas, while the HAPG sample shows a well-defined area of highest intensity around $z = 5\,\text{mm}$ to $z = 15\,\text{mm}$.

In Figure 7.9, the plotted color and the height toward the cylinder axis, normal to the surface of the underlying cylinder, corresponds to the intensity of reflection at this point. Thus, a spatial resolution of the intensity of the reflections from different areas is shown. The HOPG sample was scanned with an aperture setting that corresponds to an illuminated width of $\overline{c_+c_-} = 3\,\text{mm}$, the HAPG sample was scanned with $\overline{c_+c_-} = 4.2\,\text{mm}$. Therefore, the sensitivity of the crystal scan of the HOPG sample was higher. Note that the aperture was indiviudally set to ensure an even illumination in both scans. The necessary width to provide this prerequisite varies depending on the reflectivity of the respective sample.

Both maps show a pronounced location-dependence of the reflected intensity over the respective crystal surface, which indicates varying properties over the surface. Since the lengths of $\overline{c_+c_-}$ in the mm range are far greater than the crystallite sizes in the µm range,

the varying reflectivity is not caused by the random distribution of the crystallites.

The illuminated areas correspond to incident angular coverages of $\Delta\theta = 0.14°$ for the HOPG sample, and $\Delta\theta = 0.2°$ for the HAPG sample. Since the surface scans are performed using the intial case of the setup, the aperture essentially "cuts out" the central part of the crystals' rocking curves with the respective angular ranges as the cut width. As an example, the illuminated area of the HOPG samples therefore corresponds to an angular range of $[\theta_B - 0.07°, \theta_B + 0.07°]$.

The varying intensity can have two conceptually different causes.
The first possible explanation is that the adhesion of the graphite layers to the substrate or underlying layers is inconsistent across a single optic. Consequently, the surface normal of different areas of the overall optic do not point toward the optic's central axis. Rather than the assumed smooth cylindrical surface, the inner surface of the optic would consist of individual areas that only approximate the exact shape.
The more a single area deviates from the ideal shape, the more its surface normal is tilted with respect to its ideal direction toward the cylinder axis. As a result, the incidence angle onto the assumed ideal cylinder surface deviates from the actual incidence angle onto the area. Thus, the part of the underlying mosaic distribution that is cut out by the illuminated area is effectively shifted by the deviation between the ideal normal and the actual normal, which reduces the integrated reflecitivity.
If a whole optic is illuminated and used for the reflection, as in the SCOTTI beamline, the additional random tilts of certain crystal areas accounts for a broader curve of the optic's reflectivity over the incidence angle. This effect is not expected to follow a pattern comparable to that of a mosaic distribution. Thus, it does not enhance the integral reflectivity of the respective optic, but worsens its focusing properties.

The characterization setup can be used to measure the rocking curves of multiple points on the optic in order to obtain a spatial resolution of this property. In a spatially-resolved scan, shifts between rocking curves relative to a selected scan point, set as the reference configuration, would be visible. Thus, the resulting unsystematic broadening of the intrinsic mosaicity could be estimated while maintaining the spatial resolution of the mosaic spread over the crystal.

The effectively broadened rocking curve in the azimuthal direction can also be measured directly by using a focused setup to perform a rocking curve scan. The resulting focal point is the sum of all contributions along the azimuthal coverage of a single illuminated strip. However, as explained in Section 7.1, using the focused setup introduces additional

challenges when defining an ROI that only includes the K_α lines.

The second possible explanation does not lie in the variation of the rocking curves' means in different areas, but rather in the variability of their amplitudes. The amplitude of a rocking curve is the peak reflectivity of the crystal at the respective point of measurement on its surface.
In principle, mosaic spread and peak reflectivity do not have to be coupled. In the calculation model used throughout this work, a lower peak reflectivity, while maintaining a constant mosaic spread, corresponds to a higher modeled crystallite thickness.
At the same time, a higher mosaic spread with a constant modeled crystallite thickness also account for a lower peak reflectivity, as less crystallites are oriented with no tilt. The results of the first rocking curve scans, presented in Section 7.5.1, did not show a significant variation of the mosaic spread. However, since only a single illuminated area in the axial direction was evaluated per scan, a reliable statement is not possible.
Lastly, the overall layer thickness of a mosaic crystal also influences the peak reflectivity. However, a significant variation of the layer thickness of the samples is not expected.

For a precisely tuned setup with a highly constant value of $\overline{c_+ c_-}$ thoughout the whole scan, the differences in peak reflectivity can also be accessed by spatially-resolved rocking curve measurements over the whole optic surface. Therefore, such a scan can differntiate between both effects that can cause the variation in reflectivity. However, it is time-consuming and highly dependent on an exact alignment, as the results of the rocking curve scans depend on the exact knowledge of $\overline{c_+ c_-}$.

The reason for the deviating reflecitivities is likely caused by a combination of both explanations. The perfomance of an optic is not dependent on the exact causes of the deviating reflectivity. An optimal optic would have a constant reflectivity over the whole reflecting surface. Therefore, the quality of an optic can be evaluated by its spatially-resolved variation in reflectivity as the result of single surface scan.

The results of the crystal measurements provide a possible explanation for the varying flux observed when using the graphite-based optics in the SCOTTI beamline. The automated alignment uses the summed detector counts in the focus to rate a current alignment. Thus, it aligns the position of the optic in a way, that the K_α line of the used tungsten X-ray tube is best reflected. For an optic of constant quality, this is fulfilled at a symmetric setup, where the Bragg condition of the K_α line is fulfilled for non-tilted crystallites, roughly at the middle of the optic, as explained in Section 3.4.1.

If the optic exhibits a variable quality across its surface, it is aligned to a position where the K_α line is reflected by the area of the crystal's surface with the highest reflectivity because this setting maximizes the flux. If multiple points on the crystal surface show local maxima of the reflectivity, the automatic alignment could optimize the position to a local maximum of the flux instead of the desired global maximum.

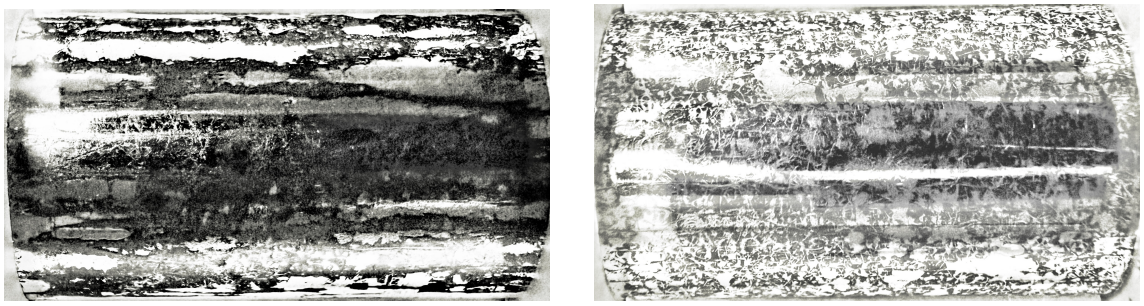
Additionally, two optics of the same specification (material, length, thickness) could not only vary by their mean reflectivity, but also in the axial location of possible reflection maxima. Therefore, an optic that maximizes the flux when it is aligned to symmetrically reflect the K_α line at one of its ends cannot use the entire geometrically available Rowland circle for reflection. Thus, two optics with the same mean reflectivity may exhibit different focusing properties depending on the location of their reflectivity maximum. This increases the likelihood of differences in the performance of optics with the same specifications, which was observed in measurements of various graphite optics used in the SCOTTI beamline.

Furthermore, a single graphite optic consists of two half cylinders. The relative orientation of these two parts can result in two maxima being located at the same axial position, which results in a higher performance of the entire optic than if the two maxima were located at different axial positions. Thus, an optic consisting of two half cylinders can exhibit different performance characteristics depending on the relative orientation of its two halves. After characterizing the two half-cylinders that comprise a single optic using the presented crystal scan, the optimal orientation and position of the optic within the SCOTTI beamline can be determined to maximize the flux. This could lead to more stable fluxes using the graphite optics. However, it will likely not change the maximum achievable flux.

Both samples in Figure 7.9 show streak-like patterns of high intensity areas, that are oriented along the axial direction of the optic. The HOPG sample's map in Figure 7.9a shows a more pronounced pattern with wider streaks.
The photos of the same samples' surfaces in Figure 6.1 also reveal a mosaic-like texture, which is likely caused by the manufacturing process of the graphite optics that involves the step-by-step application of exfoliated graphite layers. Figure 6.1a also shows that the HOPG optic shows a visibly rougher surface with more pronounced creases than the HAPG optic in Figure 6.1b, which also relates to the difference in the reflectivity maps in Figure 7.9. Thus, it is likely that the manufacturing step in which the graphite layers are applied is the main cause for the deviating reflectivity.

To support this hypothesis, Figure 7.10 additionally shows photos of the backsides of the HOPG and HAPG samples, taken through their transparent glass substrate, which

highlights the uneven adhesion of both coatings to their respective substrate. Light areas correspond to a good adhesion, black areas to a bad adhesion.



(a) HOPG optic **(b)** HAPG optic

Figure 7.10: Photos of a 200 µm HOPG-coated optic half (a) and a 50 µm HAPG-coated optic half (b) with a respective length of 33 mm, and an inner radius of the substrate of 10 mm. Both photos were taken from the backside through the transparent glass substrates and show the uneven adhesion of the coatings to the substrate of both optics. The HOPG optic sample shows a streak-like pattern, and the HAPG optic sample a dotted pattern. Light areas correspond to a good adhesion, black areas to a bad adhesion. The photos were converted to black and white to enhance the visibility of the adhesion patterns.

Figure 7.10a shows the adhesion of the HOPG coating, which displays the same streak-like pattern as seen in its reflectivity map in Figure 7.9a, and the photo of its front surface in Figure 6.1a. This relates to the possible explanation of the positional dependence of the reflectivity being caused by deviations of individual areas on the optic's surface from the perfect cylindrical shape.
The visible pattern and the differences of the surface between both types of pyrolytic graphite are typical for all HOPG and HAPG optics, and are prominent in all optics produced for use in SCOTTI so far.
Figure 7.10 also shows that the adhesion pattern of the HAPG sample is more uniform and shows finer features than the HOPG sample. This is consistent with its more uniform crystal map in Figure 7.9b and the less pronounced creases on its front surface, visible in Figure 6.1b.

However, the visibly observed effect of adhesion does not rule out the second possible explanation of location-dependent reflectivity, which is based on differences in peak reflectivities that can occur additionally.

The HAPG map in Figure 7.9b shows a clear peak of the reflectivity in an axial position at about $z = 5\,\text{mm}$ to $z = 15\,\text{mm}$. Following the discussed procedure for maximizing the flux, this area should be aligned to the Bragg angle of the K_α line when the optic is in use. The HAPG sample also shows a more constant reflectivity over the surface, when compared to the HOPG sample. Future characterizations of multiple samples could be

used to investigate if this difference is systematic for all HAPG and HOPG optics.

The reflectivity map of the HOPG optic in Figure 7.9a shows a higher variation of the reflectivity with no clear global maximum. However, the results imply, that the optic's quality is higher toward its edges at y values around $y = 0$. The strongly deviating reflectivity is consistent with the poorer performance of the optic when used in the SCOTTI beamline and compared to the best performing HOPG optic, which has the same specifications.

The evaluations presented in this chapter show that the characterization setup enables a thorough, spatially-resolved investigation of the properties of von Hámos optics. The reflectivity maps can be used to compare the qualitative differences among multiple optics and can also be used to improve the alignment of an optic in SCOTTI. Additionally, based on these measurements, recommendations can be made for combining different optic halves to maximize the overall optic's performance.
For a more in-depth study of the causes of varying reflectivities that are visible in the crystal maps, a more time-consuming, spatially-resolved rocking curve measurement can be performed. This requires a precise alignment of the setup. Additionally, the rocking curve measurements provide good estimates of the intrinsic mosaic spreads of the samples. Based on these results, more precise simulations of the focusing and defocusing properties of the optics can be performed, which can ultimately be used for further enhancements of the optics as well as other parts of the SCOTTI beamline, mainly the apertures.
It was also demonstrated that the characterization setup can be applied to the novel aluminum optics. The setup proved to be better suited for investigating the relevant properties of the specific samples than initially employed grazing incidence X-ray scattering measurements at the P03 beamline (PETRA III, DESY, Hamburg, Germany [156])

7.6 Future Adaptations of the Characterization Setup

In the current iteration, aligning the setup is very time consuming because only the sample's position in the axial direction can be adjusted by a motorized stage. The other two directions must be aligned manually using spacers and plastic screws to hold the samples in place. The aperture width is also adjusted manually.
Since the measurements depend on a good alignment, and the rocking curve evaluation requires precise knowledge of $\overline{c_+c_-}$, the setup would benefit from motorized stages to align a sample accurately in all axes.
Especially for samples with a small mosaic spread, the exact knowledge of $\overline{c_+c_-}$ is important for the point evaluation of the measurements, which yield the estimated values of the intrinsic mosaic spread. A motorized control of d_A could further increase the accuracy.

Additionally, a rocking curve measurement of a sample with a known mosaic spread can be conducted to confirm that all broadening effects are considered in the evaluation and simulation of the setup. This measurement would provide an instrumental broadening, which is the sum of all relevant effects.

A key weakness of the characterization setup is its inability to investigate the depth dependence of mosaicity. To study this relationship, the mosaic spread of a sample could be measured at different distances between its inner surface and the setup's axis. This would alter the depth of the Rowland circle on which the focusing crystallites must lie to be focused onto F.
However, doing so causes the bending axis of the optic and the axis of the setup to no longer align exactly. Consequently, only one azimuthal point can be evaluated, preferably at the upper edge of the defocused image.
Furthermore, the maximum probing depth should remain within the linear correlation range of the crystals' reflectivity versus layer thickness, as illustrated and discussed in Section 2.4.3. Otherwise, the attenuation of parts of the Rowland circle at different depths must be considered.
Such a study of the depth-dependence of the mosaicity requires a precise control of the distance between sample and setup axis. Note that a rocking curve scan is always an average over the different depths in which the Rowland circle lies.

8 Filtering Optics-Based X-ray Imaging (FOXI)

The main use of X-ray optics, discussed so far, is to focus X-rays from an X-ray tube, with the requirements described in Section 3.3. In this application, the optic provides a focus that is essentially a filtered image of the focal spot of the used X-ray tube. The result is a pencil-like beam with a small spectral width and a small divergence, which is ideal for XFI experiments.
Chapter 6 shows, that the conventional graphite as well as the newly developed aluminum von Hámos optics are capable of providing this functionality.

Within the focusing properties of the optic, lies another feature: The possibility to deliver a projection of an extended source, as demonstrated in Figure 3.5 in Section 3.2.5, while remaining its filtering properties. As a focusing optic in SCOTTI, this property is only used indirectly, as it produces an image of the focal spot of the X-ray tube. However, it can be utilized by using an optic on the detector side of the SCOTTI setup. The method was named Filtering Optics-Based X-ray Imaging (FOXI), and will be referred to as such hereinafter.

The main purpose of SCOTTI is to provide a compact platform for performing XFI experiments [24, 25]. A typical XFI signal is greatly simplified in the following.

As shown in Section 3.3, two main, interesting signal types in a SCOTTI measurement can be distinguished: A fluorescence signal, for example generated by nanoparticles to be detected, and a Compton scattering signal, generated by any kind of material, most pronounced in high-Z materials.
When combined with a fluorescence signal, it is potentially possible to achieve spatial resolution in the SCOTTI beam direction using a single pixelated detector in a FOXI setup.
Using Compton the signals of a probe opens a new field of possible experiments that can be performed using the SCOTTI setup to track voids in the SCOTTI beam pathway. The data obtained from such measurements could, for example, be used in non-destructive material science testing to detect trapped air bubbles or other material gaps.

This chapter will give a first impression of the possible potential of using an optic on the detector side of a SCOTTI setup. The main difficulty of this technique lies in the small solid angle coverage of the von Hámos optics, and consequently, in achieving a signal with a high enough flux to produce significant data. When comparing both types of described signals that the technique could be used for, Compton scattering is much more likely than fluorescence for available samples at the central SCOTTI energy of 59.32 keV. First-order Compton scattering accounts for the largest individual component of the total signal in a typical XFI spectrum, as illustrated in Figure 3.6.

In order to verify the general feasibility of using an optic on the detector side, the analysis will therefore initially be limited to first-order Compton scattering. This chapter shows a conceptual illustration of the technique, a simulation-based feasibility and performance assessment, and a first experimental realization of FOXI using the SCOTTI setup and an HOPG optic, followed by an outlook on ongoing efforts. All fit-calculations of this chapter are performed using the least squares method included in the `curve_fit` function of the `scipy` `Python`-package [153]. All integrals in the fits are approximated by a Riemann sum with at least 100 integration steps.

8.1 Test Scenario

As described in Section 4, the SCOTTI setup produces a pencil-like focused beam with a FWHM of about 1 mm, a small spectral width and a small divergence. Both latter properties are dependent on the X-ray optic used for the focusing of the beam. The central energy of the beam is tuned to the energy of the K_α line of tungsten of 59.32 keV.

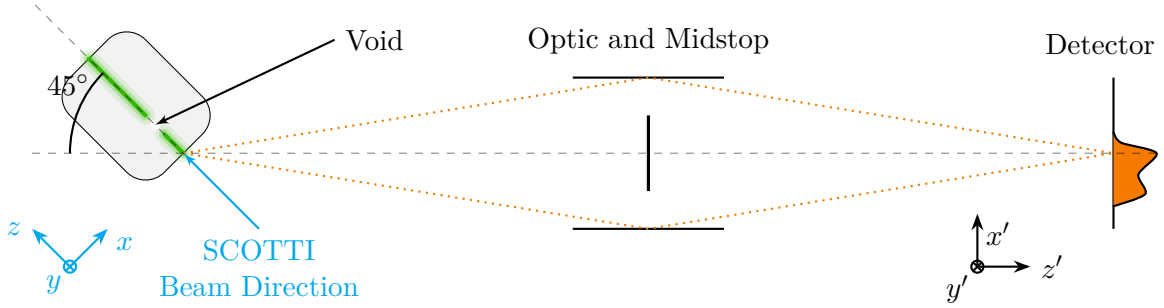


Figure 8.1: Conceptual illustration of the use of a von Hámos optic on the detector side for use in Compton imaging. The beam from the SCOTTI beamline enters from the bottom right and hits a sample, where it is scattered along its pathway through the sample. The sample exhibits an air-filled void in its bulk, where much less Compton scattering occurs. The detector-sided optic under an angle of 45° to the beam produces a projection of the beam pathway through the sample, where the void can be identified as a dip in the integrated signal. The projection defines a second coordinate system $[x', y', z']$. The optic is tuned to focus the Compton-scattered energy under the corresponding Compton scattering angle of 135°.

Figure 8.1 shows this beam, in blue color, hitting a sample. The green line illustrates the beam's path through the sample. Its divergence is not drawn in Figure 8.1. The beam triggers Compton scattering as it passes through the sample. This is illustrated by a green glow along the beam's pathway in the z-direction, except for a void in the sample, where no scattering occurs. In this chapter, only single Compton scatterings are considered. Coherent scattering processes or multiple successive Compton scattering events are not taken into account.

Under an angle of 45° to the beam, a von Hámos optic is placed and tuned to focus the Compton-scattered energy under the corresponding Compton scattering angle of 135°. Following Equation 2.6, the resulting Compton spectrum under this angle is shifted to a central energy of about 49.3 keV. The von Hámos optic is tuned to this energy, as described in Section 3.5.
Since the optic has a projection property with a certain field of view (FOV), part of the pathway, or the whole pathway of the beam, can be projected onto the detector. The mosaic crystal properties ensure that small energetic deviations from the central energy of the Compton spectrum as well as small angular deviations from the central point are still focused onto the detector. The focusing of the central point is illustrated by the dotted orange lines in Figure 8.1. The central point can be tuned by varying the optic's position along x' and y'. The angle between the SCOTTI beamline axis and the detector-sided optic defines a new coordinate system, indicated by $[x', y', z']$.

An angle of 45° between the SCOTTI beamline and the FOXI axes is chosen to be able to place the FOXI optic on the same side of the sample as the SCOTTI beamline. This enables the setup to scan various sized objects, while not interfering with the SCOTTI beamline itself. The angle accounts for a projection of a pathway of length l in z onto an image of a length of $l \cdot \sin(45°)$ in x'. Smaller angles decrease the projected image size, making it harder to resolve the void, which also speaks for the choice of 45°.
The following section describes the expected performance of a FOXI setup, based on simulations with `xrt`.

8.2 Ray Tracing-Based Feasibility and Performance Assessment

All simulations in this section are performed using the `xrt` ray tracing code, described in Chapter 5. Since `xrt` does not provide the possibility to include scattering processes, the simulation of the Compton scattering signal has to be approximated. This is done by simulating an extended, isotropic source in the dimension of the beam pathway through the sample, with a spectrum corresponding to the Compton spectrum under the given scattering angle. The spectrum is calculated numerically from the simulated SCOTTI

spectrum of an HOPG von Hámos optic with a radius of $R = 10\,\text{mm}$ and a layer thickness of $200\,\mu\text{m}$ by applying the Klein-Nishina formula (see Equation 2.6). This way, the ray tracing can not account for the exact x, y form of the SCOTTI beam's pathway. It is approximated by a fixed thickness, which corresponds to a constant FWHM of the SCOTTI beam with no divergence. Furthermore, deviations in the Compton-scattered spectrum due to slightly different scattering angles within the FOV of the optic are not included. However, the broadening of the spectrum is expected to be about $\Delta E \approx 0.2\,\text{keV}$ for a possible deviation of $\pm 2°$ of the Compton scattering direction, following the Klein-Nishina formula 2.6. The broadening is small enough to not significantly affect the results of the simulation. The geometrically possible deviation of the Compton scattering direction is determined by the FOV of the optic, which is further discussed in Section 8.2.1.

The attenuation of the SCOTTI beam in the original z-direction is included by applying an exponential decay of the intensity of the extended source in z-dircetion, following the Lambert-Beer law 2.5. The attenuation of the Compton-scattered signal within the sample, between the scattering site and the sample surface, before it reaches the FOXI optic, can not be included in the used ray tracing package `xrt`. The simulated signals of Compton photons produced at greater depths in the sample are therefore overestimated.

The flux of the simulated Compton signal is estimated by the flux of the SCOTTI beam and the probability of Compton scattering along the beam pathway. The SCOTTI beam flux was measured immediately before the FOXI demonstration measurements, using the same method as in Chapter 6, which yielded a value of $\Phi \approx (3.5 \pm 0.3) \times 10^8\,\text{ph}\,\text{s}^{-1}$.
The experiment described in Section 8.3 uses an aluminum sample. To estimate the flux of the Compton signal, the SCOTTI beam is assumed to be monoenergetic with an energy of 59.32 keV. At this energy, the mass attenuation coefficient due to incoherent scattering is approximately $\frac{\mu_C}{\rho} = 0.148\,\text{cm}^2\,\text{g}^{-1}$ for aluminum [157]. With a density of $\rho = 2.7\,\text{g}\,\text{cm}^{-3}$ [158] this results in a linear attenuation coefficient of $\mu_C = 0.4\,\text{cm}^{-1}$ for Compton scattering. According to the Lambert-Beer law (2.5), the probability that a photon will undergo Compton scattering along a pathway of length l can be calculated as [159]:

$$P_C = 1 - e^{-\mu_C \cdot l}. \tag{8.1}$$

The value is intended to provide a rough estimate of the orders of magnitude of the fluxes. Therefore, an isotropic probability distribution of the Compton scattering direction is assumed here.

The standard length from which the Compton photons in the simulation can originate was set to the thickness of the sample used in the experiment described in Section 8.3,

which is $l = 4.8\,\mathrm{mm}$. Using Equation 8.1, this yields a Compton scattering probability of about $P_C \approx 18\,\%$. The flux along the beam path is therefore estimated to be about $\Phi = 6.3 \times 10^7\,\mathrm{ph\,s^{-1}}$. The flux is adjusted accordingly for simulations that include a void in the sample, use a different propagation length, or use a different modeled SCOTTI spot size.

The simulated detector-sided optic is an HOPG von Hámos optic with a radius of $R = 10\,\mathrm{mm}$, an assumed mosaic spread of 0.46°, and a layer thickness of 100 µm.

In the ray tracing simulation, the detector is an ideal pixelated detector with a pixel size of 100 µm × 100 µm. For the feasibility simulations, the detector is not strictly limited to a certain size.
The simulation is an idealized case and does not include background signals, particularly those arising from scattering throughout the SCOTTI beamline. The SCOTTI beam is modeled as an ideal pencil-beam with no divergence in the simulation. Additionally, the optic's solid angle coverage, as defined by Equation 3.4 for a point source, is relatively small. This introduces a significant challenge to the experimental realization of the technique. Therefore, the following ray tracing calculations should be considered as a best-case scenario, providing an upper-limit estimate of the expected performance.

8.2.1 Field of View (FOV)

As described in the introduction of this chapter, FOXI relies on the imaging properties of the used von Hámos optic, which was originally designed to focus point-like sources that lie on the optic's cylinder axis. In the FOXI use case, the optic should also focus points that are displaced from this axis. The farther a point in the sample is from the FOXI axis, the more the imaging deviates from the original, cylindrically symmetric problem of focusing a point-like source. This results in decreased imaging performance of the FOXI optic as the distance from the axis increases in the (x', y') plane. The decrease is only dependent on the deviation from the FOXI axis and is not direction-dependent. The FOV was examined using ray tracing simulations with a basic setup similar to the experimental setup described in Section 8.3. However, the simulations employed a virtually infinite simulated beam path with a constant, isotropic flux. Projecting the resulting signal onto the x'-axis yields the FOV of the optic. The simulation results can be well approximated by a Gaussian G_{FOV} with a standard deviation of $\sigma_{\mathrm{FOV}} = 3.5\,\mathrm{mm}$.

Generally, the FOV of the used optics scales linearly with its radius. It is also directly related to the mosaicity of the optic. A higher mosaic spread results in a wider FOV. To maximize the FOV of an optic, its length should also be sufficient to satisfy Equation 3.3. The length, radius, and orientation of the optic determine the geometrically possible angles

of incidence onto it. The mosaicity then determines which angles can be Bragg-reflected and ultimately focused at a given energy.
To limit the FOV, the optic's midstop can also be enlarged to manually restrict the geometrically possible range of incidence angles.

Due to the described projection, the FOV of the optic in x' translates to an FOV of $\frac{1}{\sin\alpha}$ times its size in the z-direction, where α is the angle between the SCOTTI and FOXI axes. Note that the FOV of an optic is likely underestimated by the ray tracing, since it only simulates the Compton spectrum of the 135° scattering direction. Also note that if the optic used for FOXI has a Lorentzian mosaicity, the FOV is best approximated by a Lorentzian or Pseudo-Voigt profile.

8.2.2 Evaluation Approach

The main objective of the FOXI setup in this chapter is to detect a void in a sample's bulk and model its size. This section outlines the method to fit the void's signal using a ray tracing simulation of the demonstration experiment described in Section 8.3. Since the void is located on the z-axis of the setup and is projected onto the x'-axis of the detector, the signal is also projected onto the x'-axis for evaluation. The simulated focus on the detector is shown in Figure 8.5d, where it is compared to the experimental results.

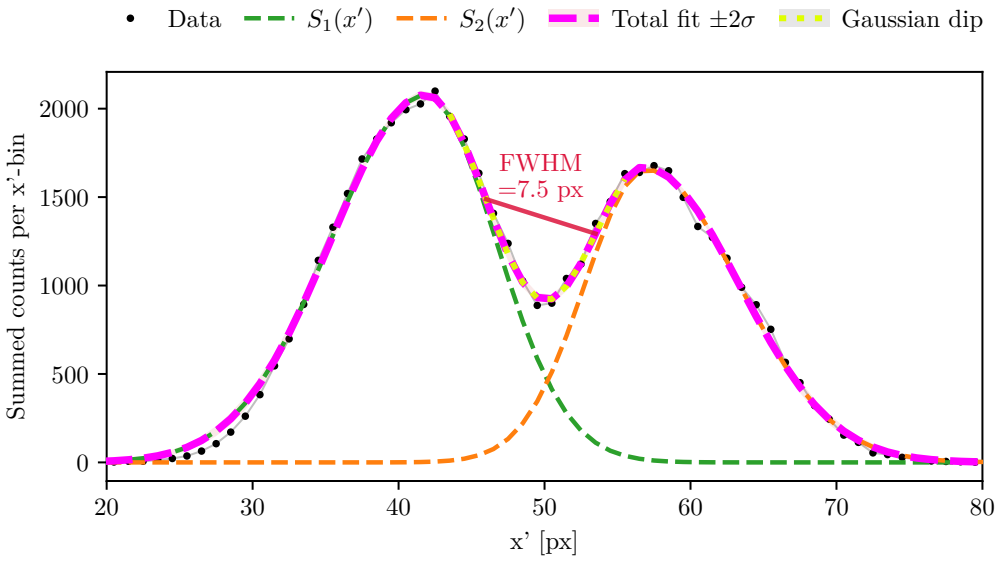


Figure 8.2: Projection of the focus of a FOXI ray tracing simulation onto the x'-axis, showing a dip in the signal. The signal is fitted with model 8.2, drawn in pink. Plotted on top in yellow is the fit of a negative Gaussian describing the width of the dip that can be used to calculate the width of the void it originates from.

The simulation excludes nearly all optical defocusing effects and the attenuation. Section 8.3.2 discusses why this approach yields the most meaningful simulated data for comparison with the experiment. This allows for a simple model to be used for the fit:

$$y'(x') = \big(S_1(x') + S_2(x')\big) \cdot G_{\mathrm{FOV}}, \tag{8.2}$$

where G_{FOV} denotes the Gaussian approximation of the FOV of the optic, as described in Section 8.2.1. $S_1(x')$ and $S_2(x')$ are also Gaussians describing the Compton scattering origins on both sides of the void. The relevance of G_{FOV} is described in detail in Section 8.3.2. In contrast to the more complex model 8.11, model 8.2 does not present the physical relationships accurately. However, it can be used to fit the simple simulation example. This is done because the parameters of the model 8.11 can not be included in an `xrt` simulation.

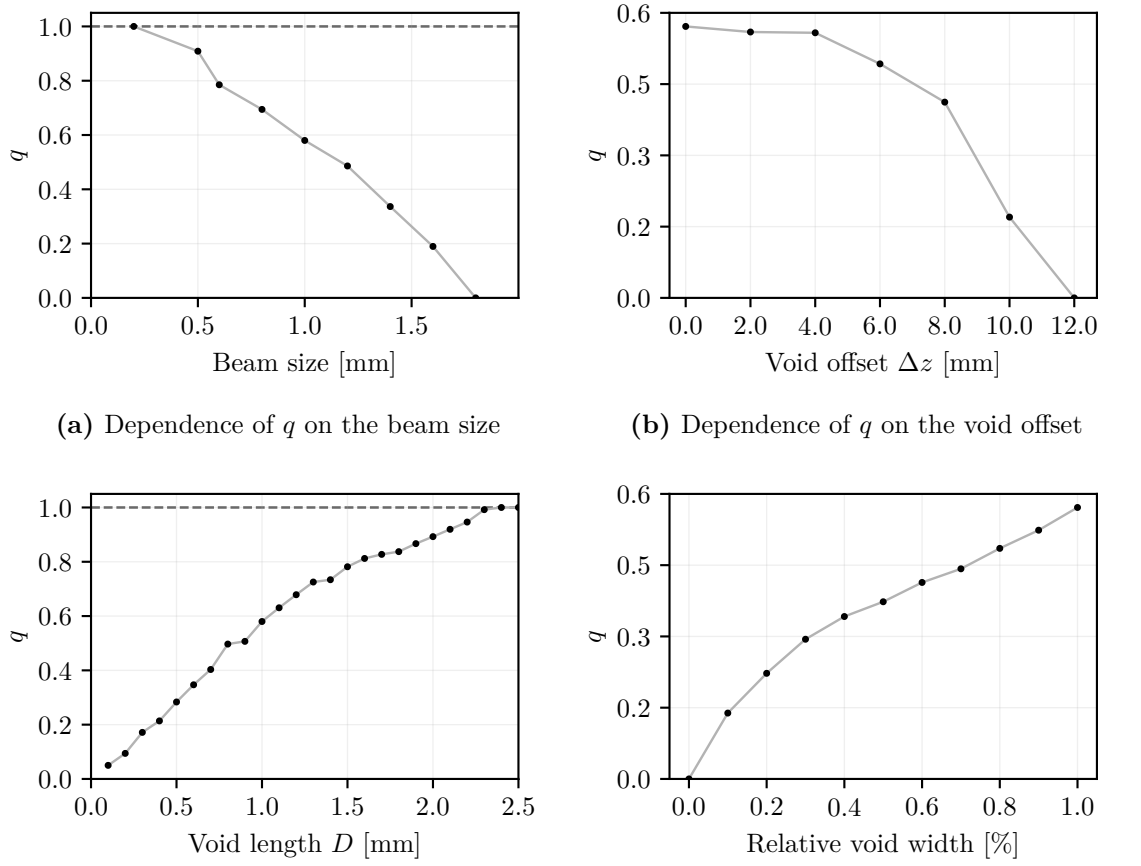
Figure 8.2 shows a clear dip around $x' = 50\,\mathrm{px}$. This dip can be well approximated by a negative Gaussian function (yellow curve) that is fitted to the curve based on model 8.2 (pink curve). The FWHM of the dip is fitted to FWHM=$(7.5 \pm 0.1)\,\mathrm{px}$ and is a good measurement for the projected void width. It can be translated to an estimate of the original dip width D in z using the known property of the projection and the pixel size of $100\,\mu\mathrm{m} \times 100\,\mu\mathrm{m}$ via:

$$D = \frac{(7.5 \pm 0.1)\,\mathrm{px}}{\sin(45°)} \cdot 0.1\,\mathrm{mm\,px^{-1}} = (1.06 \pm 0.01)\,\mathrm{mm}, \tag{8.3}$$

which is good approximation of the actual dip width of 1 mm. Note that the defocusing effect caused by crystallites outside the Rowland circle (see Figure 3.2b) is not excludable, as it is inherent to the mosaicity. It leads to an overestimation of D. This effect is corrected in Equation 8.14.

Generally, the depth of a dip in a signal can be quantified by comparing the absolute value of the amplitude $|A_{\mathrm{dip}}|$ of the negative Gaussian fit of the dip to the signal's behavior if the dip would not be present. This can be approximated by $y'(x' = \mu_{\mathrm{dip}}) + |A_{\mathrm{dip}}|$, with μ_{dip} denoting the median of the Gaussian fit of the dip, and $y'(x')$ describing the fitted total signal (pink curve in Figure 8.2).
The quotient $q = \frac{|A_{\mathrm{dip}}|}{y(x'=\mu_{\mathrm{dip}})+|A_{\mathrm{dip}}|}$ is a good measurement for ray tracing simulations because it is independent of the simulated flux. It also allows a detected ray to effectively carry less than one photon, which is physically impossible, but is used as a weighting factor in the `xrt` simulations.
Ray tracing simulations show, that the amplitude of the dip is influenced by the width of the reflected spectrum, while the dip's width is not dependent on it. Since the ray tracing

simulations can only account for one Compton scattering direction and thus underestimate the energy range, no evaluation can be made in this regard.
Furthermore, the dip amplitude depends on the size of the void, the position of the void within the optic's FOV, the size of the SCOTTI beam, and the characteristics of the optic that define the FOV. All factors are briefly discussed in the following.



(a) Dependence of q on the beam size

(b) Dependence of q on the void offset

(c) Dependence of q on the void size

(d) Dependence of q on the void width relative to the beam width

Figure 8.3: Dependence of the quotient q on different parameters of the ray tracing simulation. The standard values for the parameters, if not varied in the respective simulation, are a beam size of 1 mm × 1 mm, a void offset of $\Delta z = 0$ mm, a void size of 1 mm and a relative void width of 1.

Therefore, the example simulation described in Section 8.2.2 is adapted to the respective variable parameter. Figure 8.3 summarizes the results of the dips' analysis regarding q as a function of the discussed parameters. As can be seen in Figure 8.3c, if the void length D in z is increased, q initially begins to rise linearly, flattens out slightly and eventually approaches the value $q = 1$. In the simulated experiment, the transition to saturation occurs when the void length in z exceeds 1.5 mm. Consequently, the same behavior can also be observed in Figure 8.3a for a decreasing beam size.

As a void of constant size is shifted within the FOV or its z-position, q is monotonically convex and decreases with an increasing slope, as shown in Figure 8.3b. The formation

of a double peak and the resulting dip can be observed approximately up to the position in the FOV that corresponds to about 1.5 times its half-width. In the simulated case it can be observed up to about $\Delta x' = 6.3\,\mathrm{mm}$ in both directions from the center of the FOV, which correspond to $\Delta z \approx 8.9\,\mathrm{mm}$ in both directions in z from the central focused point of the SCOTTI beam path through the sample. This defines a second FOV for the detection of a 1 mm void, which is smaller than the 2σ range of the original FOV for detecting a Compton signal without a void.

The dip width also depends on the relative width of the void compared to the SCOTTI beam. A void that has not the same width as the SCOTTI beam produces a shallower dip signal, as illustrated in Figure 8.3d.

In addition to the void itself, q is influenced by the rest of the experimental setup. It decreases with increasing size of the SCOTTI beam, as can be seen in Figure 8.3a. A smaller focused beam is therefore beneficial for the resolution of FOXI.

When comparing two optics with regard to their use in a FOXI setup, mosaicity and thickness of the reflecting material play a significant role. A higher mosaic spread leads to a higher integral reflectivity and therefore a generally stronger signal. The same is true for higher reflecting material thicknesses. However, as explained in Section 3.2, they also introduce a higher degree of defocusing, which leads to blurring of the signal and a resulting decrease of q. This is further amplified by a broader reflected spectrum at higher mosaicities. At the same time, the total FOV profile of the optic is flattened by a higher mosaicity, which enlarges the FOV for the detection of a void.

Therefore, the final choice of an optic is a balance between signal strength and sharpness, which has to be adapted to the features to be detected and to the rest of the setup.

8.3 First Experimental Realization

Figure 8.4 shows the first experimental implementation of a FOXI technique setup using a detector-sided HOPG von Hámos optic. The focused SCOTTI beam, illustrated in blue, is incident from the left and hits an aluminum sample. The beam has a near Gaussian profile with a FWHM of about 1 mm and a central energy of 59.32 keV. Before the start of the experiment, its flux was measured to be about $\Phi \approx (3.5 \pm 0.2) \times 10^8\,\mathrm{ph\,s^{-1}}$. It is produced using an HOPG von Hámos optic with a radius of $R = 10\,\mathrm{mm}$, a mosaicity of 0.46° and a layer thickness of 200 µm.

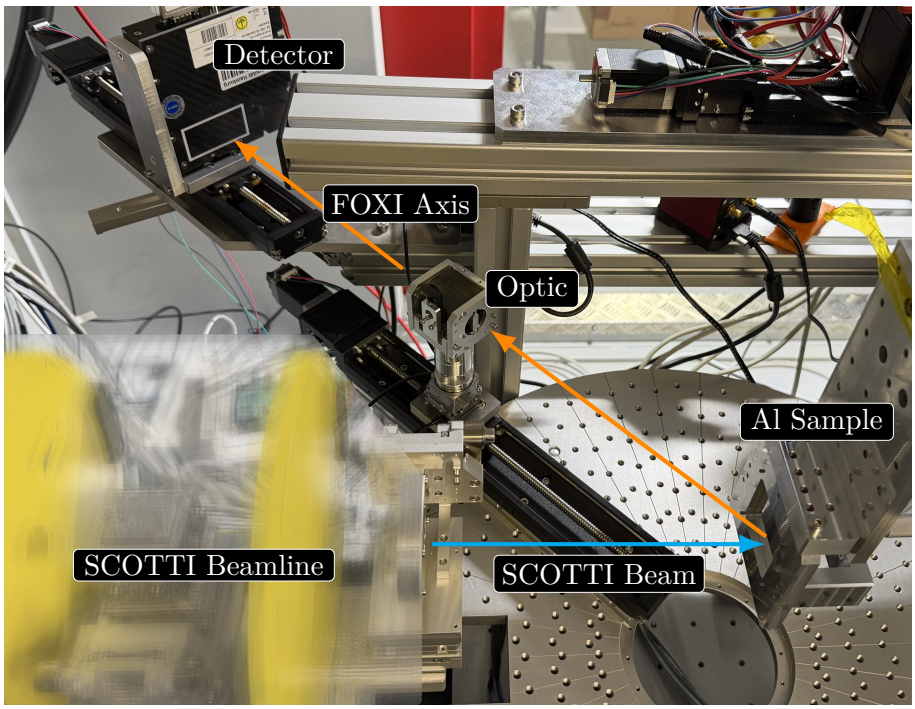


Figure 8.4: Experimental FOXI setup using the SCOTTI beamline and an HOPG von Hámos optic. The beam from the SCOTTI beamline is incident from the left and hits an aluminum sample, where it is scattered. The detector-sided optic, under an angle of 45° to the beam, produces a projection of the beam pathway on the detector.

The sample consist of a 4.8 mm thick aluminum plate with a drilled hole of 2.4 mm depth at the backside of the sample. An aluminum pin with a diameter exactly matching the width of the hole can be inserted, creating a precise, controllable void between the pin and the front plate. The void size is varied via a millimeter screw. If the pin is fully inserted, the sample can be treated as a solid aluminum sheet. The complete removal of the pin creates an aluminum sheet of 2.4 mm thickness at the location of the drilled hole.

The position of the sample is tuned to align the front of the plate and the position of the drilled hole with the SCOTTI focus point.
As described in Section 8.1, the beam is expected to trigger constant Compton scattering along its pathway through the sample. The Compton photons scattered under a scattering angle of $\approx 135°$ are aligned with the FOXI axis, illustrated in orange. The FOXI optic is a von Hámos optic with a radius of $R = 10\,\text{mm}$, a mosaicity of $\beta \approx 0.46°$ and a layer thickness of 100 µm.
Its distance to the front of the sample is tuned to focus the Compton-scattered energy of about 49.3 keV onto the detector, which is placed at the end of the FOXI axis at a central distance of about 532 mm to the front of the sample, as explained in Section 3.5.

The optic tilt is tuned to align exactly with the FOXI axis. An Actaeon FX5 pixel detector, which is described in Section 4.3.1, is used as the FOXI detector.

8.3.1 FOXI Alignment

The experiment has several degrees of freedom in the alignment: x, y, z of the sample, x', y', z' of both the optic and the detector, as well as the tilt ω of the optic around its y'-axis.

At the start of the experiment, the (x, y) position of the sample was aligned with the use of an Amptek XR-100CdTe X-ray and Gamma ray detector, which is described in Section 4.3.2, by positioning it at a 135° scattering angle on the opposite side of the FOXI setup. The pin of the sample was removed to reveal the full drilled hole at the backside of the sample. An area of 10 mm × 10 mm was scanned, while measuring the Compton signal with the Amptek detector. The resulting map of the Compton signal showed a clearly defined minimum, indicating the position of the drilled hole, where less material is traversed by the SCOTTI beam and therefore less Compton signal is generated. At this position, the sample essentially presents an aluminum sheet of 2.4 mm thickness at the SCOTTI beam position.
Afterwards, the FOXI optic was first aligned manually to the motor axis below the FOXI beam direction using a visible laser. The z'-position of the optic was adjusted to a distance of about 266 mm from the front of the sample. The detector was placed at about twice the distance, ensuring the best possible focus on the detector.

The first measurements taken with the FOXI detector and the optic in place revealed a strong noise signal originating from the SCOTTI beamline. Due to its design, SCOTTI is only shielded along its z-axis, but not toward the FOXI axis. To overcome this issue, tantalum sheets were used to shield all parts of the SCOTTI beamline, as well as the side of the FOXI detector facing z.
In the described setup, the FOXI optic has a small solid angle coverage of about 1.1×10^{-3} sr for the central focused point. Thus, a high integration time of at least 1000 s was used for all measurements to be able to obtain a significant signal. This made the alignment process time-consuming and only allowed for large motor steps between measuring points during the optimization process.

Furthermore, the motorized stages for x', y' and ω of the FOXI optic showed a strong nonlinearity. Therefore, scanning through the different settings of these parameters is pointless because their exact positions are unknown once they are moved. The alignment of these parameters therefore only relied on manual tuning with a laser and subsequent manual fine-tuning of the motors. To align ω, the shadow of the midstop of the optic was used. The presence of a circular shadow on the detector indicates that this parameter is properly aligned.

The strongest achievable signal was generated by varying x', y' and ω as described. Afterwards, the z-position of the sample was varied for fine-tuning. A variation of $\pm 5\,\text{mm}$ in $0.5\,\text{mm}$ steps showed only minor variations in the signal, which became more pronounced toward the edges. In accordance with Figure 8.3b, this confirmed that the thin sample was aligned to the center of the FOV of the optic. The sample was now aligned to the intersection of the SCOTTI and the FOXI axes.

8.3.2 Measurements

As a first measurement, the sample was used as in the alignment process, with the pin removed, creating a plate of $2.4\,\text{mm}$ thickness. The measurement was performed with an integration time of $5000\,\text{s}$.
Due to a power outage after the first experiment, the alignment had to be redone, resulting in a different position of the signal on the detector than for both other measurements, as can be seen in Figure 8.5.
Before the second measurement the pin was installed and fully inserted, creating a solid aluminum sheet of $4.8\,\text{mm}$ thickness. Note that the pin is longer than the depth of the drilled hole and is also held by an aluminum millimeter screw. Therefore, the actual SCOTTI beam path is longer than the thickness of the sample. The third measurement was performed with the pin moved backwards, creating a void of $1\,\text{mm}$ thickness in the sample. As the goal of the first measurement campaign was to verify the ability of the setup to reproduce the expected signal, and given the alignment issues, this void size was chosen.
To further reduce the background, reference measurements with an integration time of $10\,000\,\text{s}$ were recorded. This required the optic's HOPG-coated substrate to be replaced with an uncoated glass substrate, which naturally does not produce a focused signal on the detector. Its position was adjusted to align as closely as possible with the HOPG optic's alignment, considering the nonlinear motor stages.

Due to varying integration times, the sample measurement and the used reference measurement are both normalized to their respective global maximum before they are subtracted from each other to obtain the final signal, which is therefore defined as:

$$\Delta I_{\text{norm}}(x', y') = \frac{I_{\text{sample}}(x', y')}{max(I_{\text{sample}})} - \frac{I_{\text{reference}}(x', y')}{max(I_{\text{reference}})}, \tag{8.4}$$

where $I(x', y')$ denotes the value of a pixel.

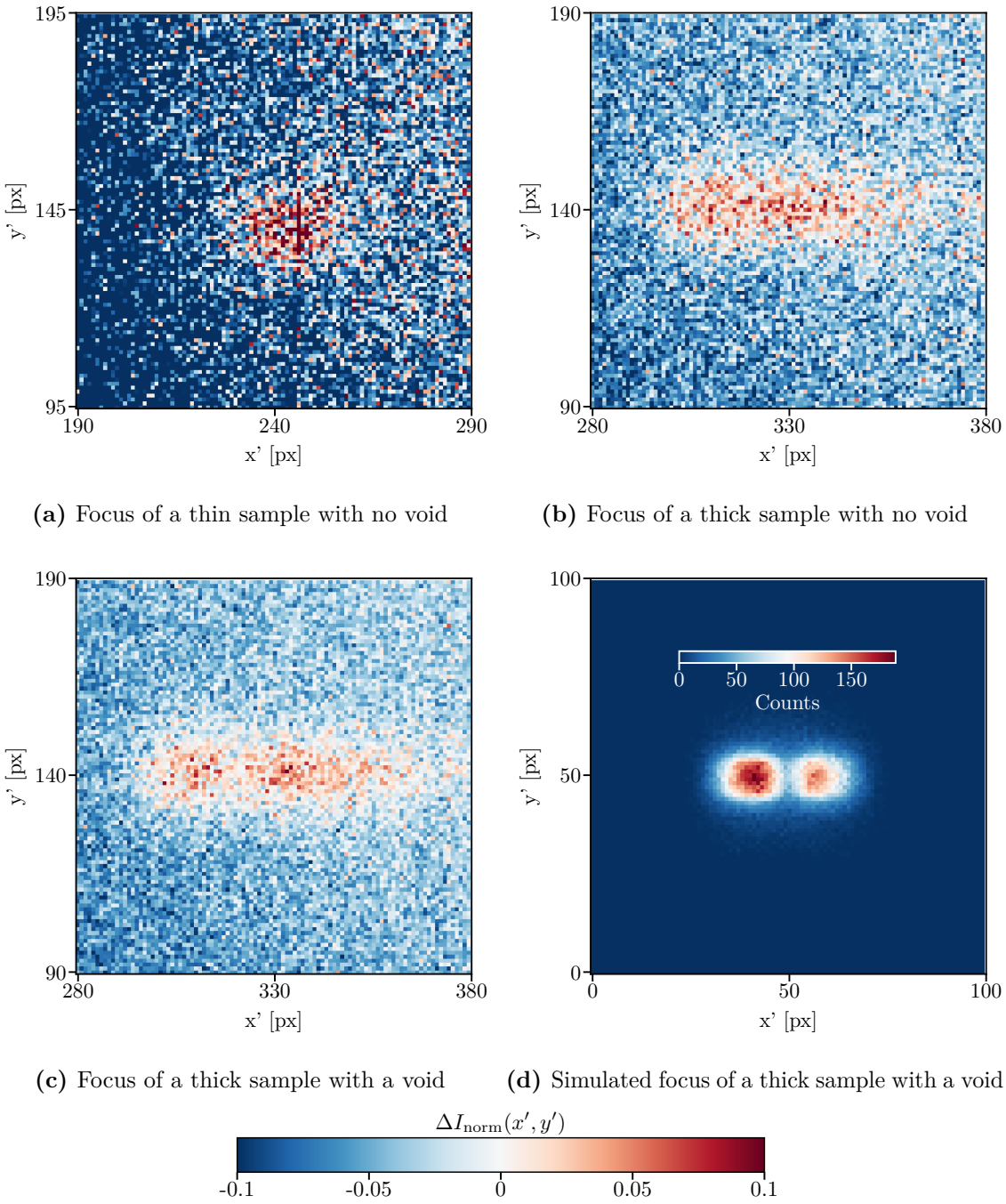
This enabled the use of the reference measurement to produce a live-view of the subtracted detector image for the alignment process of the sample measurements, which improved the

signal visibility and, therefore, the alignment. Note that the measurements were taken over the course of several days. The improvised shielding was removed each night to prevent damage to the equipment. Additionally, the nonlinear motors do not allow for precise reconstruction of the used optic's position prior to the reference measurements. The motor stages are also not protected against a possible drift in between measurements.

The experimental limitations could have caused variations in the noise signal. Additionally, pixel-accurate spatial registration of the images was not reliably possible with the recorded data. As a result of the possible geometric deviations, different local image regions may be compared with one another. Section 8.3.3 discusses how the limitations can be overcome in future measurements.
The data analysis presented in Section 8.2.2 is based on the relative trend of the x'-projection, particularly the positions, separations, and characteristic widths of features, rather than its absolute intensity level. The fit model accounts for the linear contributions resulting from normalization and image subtraction, as well as any remaining noise not eliminated by subtraction, via a linear background term. This is appropriate because the x'-projections of the reference measurements exhibit approximately linear trends over the relevant regions.

The respective ordinate axes of the projections are given as $\Delta I_{\mathrm{norm},x'}(x') = \sum_{y'} \Delta I_{\mathrm{norm}}(x', y')$ for the projections onto the x'-axis and as $\Delta I_{\mathrm{norm},y'}(y') = \sum_{x'} \Delta I_{\mathrm{norm}}(x', y')$ for the projections onto the y'-axis, both in arbitrary units (a.u).
Due to the normalization and the possibly different noise in the measurements, the absolute ordinate values in the following evaluations have no relevance and are not comparable between measurements. The described normalization procedure also explains the negative values in Figures 8.5a to 8.5c.

Figure 8.5 shows the resulting signals $\Delta I_{\mathrm{norm}}(x', y')$ as well as the detector image of an idealized ray tracing simulation (Figure 8.5d) using the same sample- and beam parameters, as described in Section 8.2.2. The simulation includes no background. Therefore, no reference measurement was subtracted, and the signal is not normalized.
All measurements show clear signals with the expected shapes. Figure 8.5a shows a relatively narrow focus in the x'-direction. In contrast, Figure 8.5b shows a focus, extended in the horizontal direction, which is expected due to the larger thickness of the sample. Figure 8.5c shows a focus similar to that of Figure 8.5b, but with a clear void in the horizontal direction, as anticipated due to the void in the sample.
The idealized ray tracing simulation in Figure 8.5d shows the same features, but with smaller extensions in both horizontal and vertical direction, which is consistent with expectations due to the idealized nature of the simulation, as described in Section 8.2.



(a) Focus of a thin sample with no void

(b) Focus of a thick sample with no void

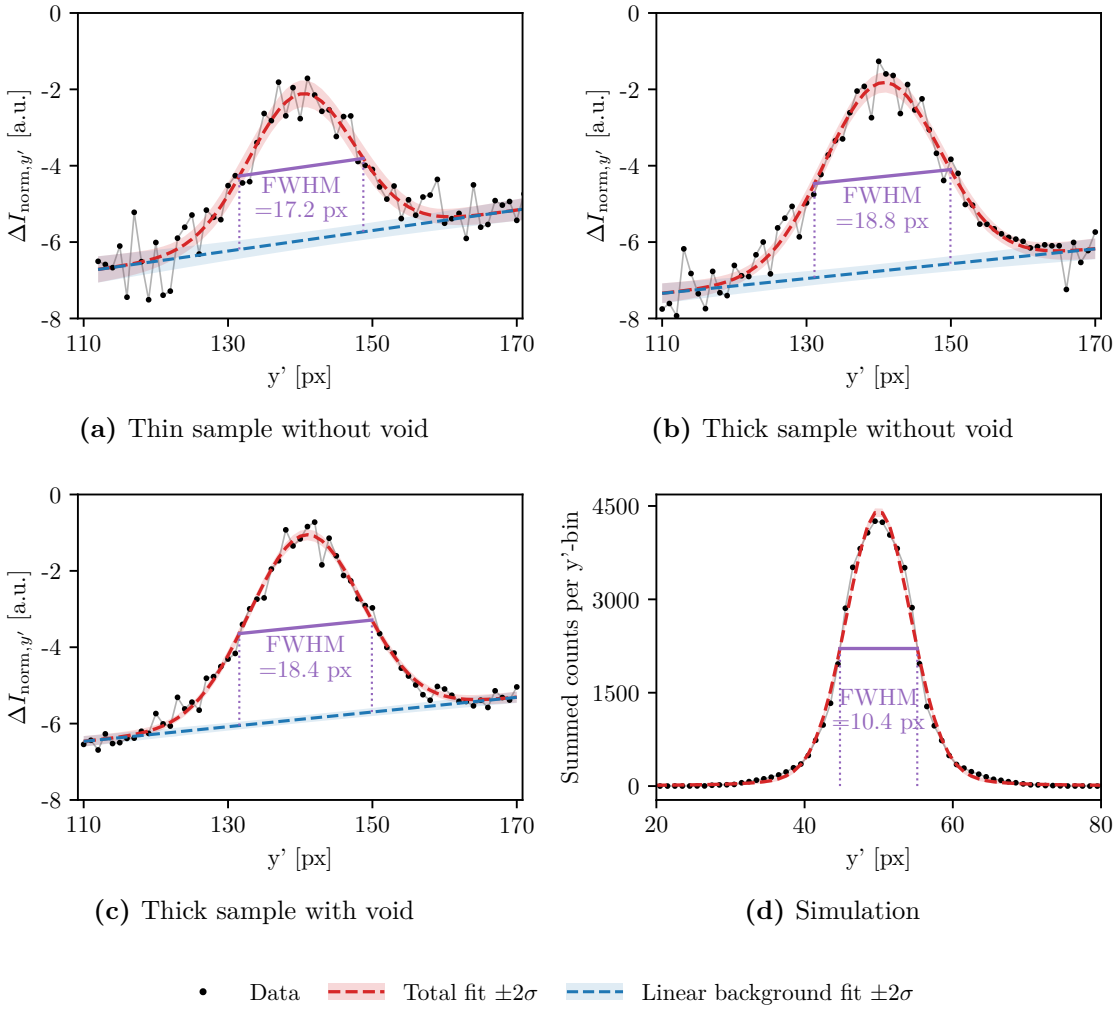
(c) Focus of a thick sample with a void

(d) Simulated focus of a thick sample with a void

Figure 8.5: Experimentally recorded, normalized, reference-subtracted (a, b, c) and simulated (d) focal points on the FOXI pixel detector using the setup described in 8.1 and 8.3. (a, b, c) share a color bar at the bottom. (d) has its own color bar. Due to the necessary normalization, described in Section 8.3.2, the focal points can only be compared qualitatively.

The foci in Figures 8.5a to 8.5c show the same vertical width. This is consistent with the expectation of a nearly constant extent of the focused beam size in the vertical direction (y or y') through the sample, regardless of the extent of the beam in z. Furthermore, the vertical beam size is not influenced by the projection caused by the angle between the SCOTTI and the FOXI axis, as described in Section 8.1. The original size of the beam in vertical direction is known to have a FWHM of about 1 mm [134]. Therefore, it can be used

to define a magnification factor M. This factor accounts for all sources of beam broadening. These include the defocusing effects described in Chapter 3.2, a possible deviation of the z' position of the detector from the perfect focus, as well as broadening effects due to the focusing of Compton-scattered photons from directions other than the assumed sole 135° scattering angle direction. Due to the cylinder-symmetry of the optic, the magnification factor M is expected to be the same in both horizontal and vertical direction.



(a) Thin sample without void

(b) Thick sample without void

(c) Thick sample with void

(d) Simulation

Figure 8.6: Projection of the foci in Figure 8.5 onto the y'-axis. The signal is fitted with a Gaussian (red) and a linear background (blue) model 8.2. The FWHM values of all projections are illustrated.

Figure 8.6 shows a projection of all four signals from Figure 8.5 onto the y'-axis by summing up all values of $\Delta I_{\mathrm{norm}}(x', y')$ in the horizontal direction in a region of interest (ROI) around the focus. All ROIs are defined as a 140 px × 60 px area around the respective focus.
The resulting curves are fitted with a Gaussian function, which is used to determine the FWHM of the vertical beam extent on the detector. The values for the FWHM are illustrated in Figure 8.6. The mean FWHM of the signals in Figures 8.6a to 8.6c, taking into account the fit errors, is FWHM=(18.1 ± 0.5) px. As the pixel size is 100 µm, this corresponds to a magnification factor of $M = \frac{FWHM_{\mathrm{detector}}}{FWHM_{\mathrm{beam}}} = 1.81 \pm 0.05$.

As described in Section 8.2.2, the ray tracing simulation is idealized to show next to no magnification effects by suppressing the defocusing effects by the bulk, placing the detector exactly at the perfect focus and only simulating the Compton-scattered photons from the 135° scattering angle direction. Although the intrinsic defocusing effects of the optics could be included in the simulations in principle, the recorded experimental data contain the aforementioned additional inaccuracies. Since these contributions cannot be separated from the modelable, intrinsic defocusing, an idealized simulation is the most meaningful reference for comparison with the measurements.
The magnification factor of the idealized ray tracing simulation, calculated using the same principle, is $M \approx 1.04 \pm 0.01$.

In the following, the x' projections are is analyzed and fitted, starting with the signal of the extended plate with no void, which is best-suited to explain the fit model.

Thick sample with no void

Figure 8.7 shows a projection of the signal from Figure 8.5b onto the x'-axis by summing up all values of $\Delta I_{\text{norm}}(x', y')$ in the vertical direction for each horizontal point in an ROI around the focus. The signal is fitted with the following model:

$$y'_{\text{fit}} = \underbrace{(mx' + b)}_{\text{linear background}} + \underbrace{S\left(x'\right)}_{\text{core signal}} \cdot \underbrace{G_{\text{FOV}}}_{\text{globally enveloping Gaussian through the FOV}} . \tag{8.5}$$

The linear background fit, illustrated by the blue line in 8.7, accounts for the discussed limitation of the imperfect background subtraction. A linear fit to the background above the ROI yields the same slope value, indicating that the linear term is indeed caused by the aforementioned constraints rather than the relevant signal.
The globally enveloping Gaussian accounts for the FOV of the FOXI optic. The ray tracing simulations in Section 8.2.1 confirmed the Gaussian shape and revealed an estimated standard deviation of the FOV of $\sigma_{\text{FOV}} = 3.5\,\text{mm} = 35\,\text{px}$. This value is used for the fit via:

$$G_{\text{FOV}} = \exp\left(-\frac{(x - \mu_{\text{FOV}})^2}{2\sigma_{\text{FOV}}^2}\right). \tag{8.6}$$

The median of the Gaussian, μ_{FOV}, is expected to be at the center of the signal. This was confirmed during the alignment process, described in Section 8.3.1, and is also indicated by the visible plateau in the projected signal around $x' = 330\,\text{px}$.

The core signal is given by an integration of Gaussian contributions of all positions along the beam path:

$$S(x') = A \int_0^W e^{-\lambda_{z,z'}u}\, \mathcal{N}\left(x; \mu_0 + u, \sigma(u)\right) du, \tag{8.7}$$

where A is the amplitude of the signal, W represents the finite size of the sample in x', $\lambda_{z,z'}$ is an attenuation coefficient accounting for the attenuation of the FOXI beam in z-direction and the Compton signal in the z'-direction. $\mathcal{N}$ is a Gaussian distribution with median $\mu_0 + u$ and standard deviation $\sigma(u)$, where μ_0 is the center of the first Gaussian at $u = 0$. The variable of integration u corresponds to the projected position in the sample along the beam pathway.

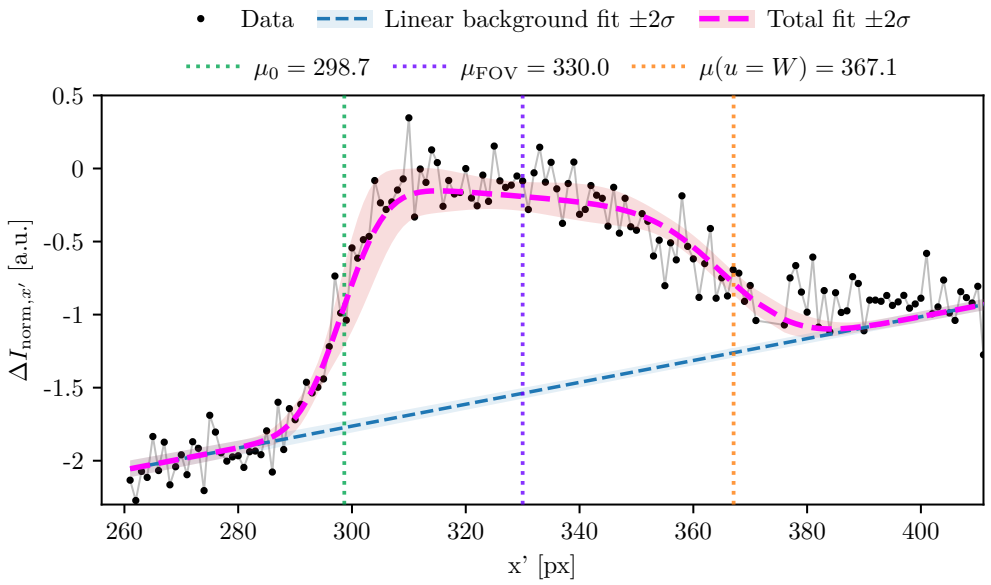


Figure 8.7: Projection of the focus of a thick sample with no void (8.5b) onto the x'-axis. The projected signal is fitted (pink dashed line) with the model given by Equation 8.5. The model consists of a linear background (blue, dashed line), and an integration of Gaussian contributions evaluated at sampled positions along the beam path. The median values of the first (μ_0) and the last ($\mu(u = W)$) partial signals are drawn, which represent the projected penetration depth into the sample in z. The signal is also influenced by the Gaussian FOV (G_{FOV}) of the FOXI optic, the median of which is plotted at μ_{FOV}.

The concept behind the fit model is that every infinitesimal point along the SCOTTI beam pathway through the sample can be seen as an individual point source, whose properties are determined by the underlying Compton scattering. Every partial signal is eventually focused by the optic and is treated by the fit as a normalized Gaussian. The focusing of a partial signal depends on its origin along z and its spectrum.

The total signal on the detector is a result of the overlapping of all partial signals, reflected by the integral in the fit model of $S(x')$. Since the sample, and therefore the pathway from which the total Compton signal arises, has a finite size, the upper integration border is set to a value W, which is part of the fit.

The point at which the SCOTTI beam enters the sample produces the partial signal $\mathcal{N}(x; \mu_0, \sigma_0)$. Its position on the detector is represented by its median μ_0, and its standard deviation is represented by σ_0. The incidence point also marks the lower limit of the integration variable u. Since this initial signal is not produced in the bulk of the sample, it is not attenuated. Figure 8.7 shows the plot in which the median value of the first signal was fitted to $\mu_0 = (298.7 \pm 1.3)\,\mathrm{px}$.

All signals produced at greater depths are represented by a higher value of u, which is a combination of the partial signal's origin depth in z, the magnification factor M, and the signal projection caused by the angle between the SCOTTI and FOXI axes. These signals are subject to attenuation. The attenuation is represented by the factor $e^{-\lambda_{z,z'}u}$ in accordance with the Lambert-Beer law, introduced in Section 2.2.1. It can not distinguish between the attenuation of the SCOTTI beam with $E \approx 60\,\mathrm{keV}$ along z prior to the generation of the Compton signal, and the attenuation of that signal with $E \approx 50\,\mathrm{keV}$ along the FOXI beam direction z'. In the fit, shown in Figure 8.7, it was fitted to $\lambda_{z,z'} = (0.008 \pm 0.003)\,\mathrm{px}^{-1} = (0.8 \pm 0.3)\,\mathrm{cm}^{-1}$, which is in the same order of magnitude as the values of $\lambda \approx 0.76\,\mathrm{cm}^{-1} - 1.00\,\mathrm{cm}^{-1}$ for aluminum at $50 - 60\,\mathrm{keV}$ [157, 158]. Note that $\lambda_{z,z'}$ represents the attenuation in u, which is caused by the consecutive attenuation along z and z' with the different energies of the SCOTTI beam and the FOXI signal. Possible future improvements are discussed in Section 8.3.3.
The standard deviation of every consecutive normalized Gaussian is given by a steady expansion model:

$$\sigma(u) = \sigma + \Delta\sigma \frac{u}{W}, \tag{8.8}$$

where $\Delta\sigma$ represents the expansion. This part of the model accounts for the fact that a partial signal becomes increasingly defocused the farther its origin is from the central point of ideal focusing of the FOXI optic. It also accounts for the divergence of the SCOTTI beam, which produces the Compton signal. As the SCOTTI beam diverges, its x, y expansion becomes broader with increasing distance from the ideal focusing point. This effect, which is not included in M, adds to the global defocusing and is quantified a by possible steady expansion of $\sigma(u)$. The maximum detuning occurs at the maximum distance in z from the optimal focal point, which is generally defined by the boundaries of the optic's FOV. For the used optic, the $2\sigma_{\mathrm{FOV}}$ limit lies at $z \approx \pm 10\,\mathrm{mm}$, depending on the orientation and expansion of the sample toward or away from the FOXI optic. The focal point from the FOV border has the same distance to the optimal focal point of the optic. The resulting maximum change in the width of the signal is given by:

$$\Delta\sigma_{\max} = 10\,\mathrm{mm} \cdot (\tan(\theta_{B\,\mathrm{SCOTTI}}) + \tan(\theta_{B\,\mathrm{FOXI}})) \approx 0.7\,\mathrm{mm} = 7\,\mathrm{px} \tag{8.9}$$

in both directions of the horizontal FOV, where $\theta_{B\,\mathrm{SCOTTI}}$ and $\theta_{B\,\mathrm{FOXI}}$ are the Bragg angles of the SCOTTI and the FOXI optics, respectively. Both angles quantify the respective divergence of the SCOTTI beam and the focused Compton signal. For the first experimental realization, as illustrated in Figure 8.3, only half the FOV was used. Furthermore, the front of the sample was assumed to align with the best-focused point. Therefore, it was assumed to correspond to the smallest possible value of σ and was defined as the central point of the steady extension.

The total fit matches the acquired data. On top of the linear background, the projected signal starts with a sharp increase, fitted by the first Gaussian in $S(x)$ with a median value of about $\mu_0 \approx 300\,\mathrm{px}$. Afterwards, it shows the formation of a plateau around $x' = 330\,\mathrm{px}$, which is fitted by the center of the FOV of the optic at μ_{FOV}. Subsequently, the curve declines mainly due to the attenuation of the signal, which is quantified by $\lambda_{z,z'}$. The decline is increased by the effect of the declining G_{FOV} and extended by the discussed effect of $\Delta\sigma$. Additionally, the projected signal shows a bend at about $x' = 355\,\mathrm{px}$, fitted by the finite size of the sample of $W = (68.4 \pm 2.1)\,\mathrm{px}$ in dimensions of u. The decline of the signal cannot be fully attributed to the finite sample size, the defocusing effect, or the FOV of the optic, because the sample has a more complex form that holds the described pin. The exact fraction of the entire sample assembly, including the pin and its holder, that lies within the optic's FOV cannot be determined with certainty. Therefore, the fitted result of W is not compared to the sample's dimension in z.

Note that the complex fit model 8.5 is sensitive to parameter correlations, especially between the parameters of the globally enveloping Gaussian, $\lambda_{z,z'}$ and $\Delta\sigma$ which all describe part of the decline of the signal in Figure 8.7. Section 8.3.3 briefly discusses how the uncertainty in the parameters could be overcome. Since the main goal of the demonstration experiment is to detect a void in the sample, the data acquired from this sample and the other two samples were nevertheless fitted to the corresponding models, to ensure their suitability for future measurements.

Thin sample with no void

Figure 8.8 shows a projection of the signal from Figure 8.5a onto the x'-axis by summing up all values of $\Delta I_{\mathrm{norm}}(x', y')$ in the vertical direction for each horizontal point in an ROI around the focus. The measurement represents a sample state, in which the pin and its holding mechanism have been fully removed. This leaves a 2.4 mm-thick aluminum plate in the beam path. Unlike all other ROIs used for the analysis of the experimental data, an ROI width of 100 px in the x'-direction was chosen here to improve the visualization of the thinner sample's signal.

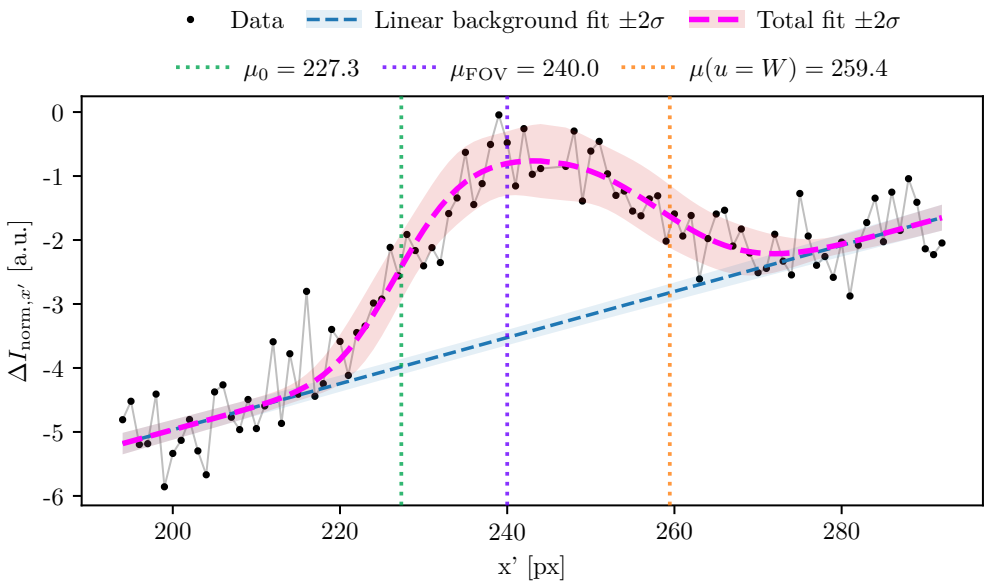


Figure 8.8: Projection of the focus of a thin sample with no void (8.5b) onto the x'-axis. The projected signal is fitted (pink dashed line) with the model given by Equation 8.5. The model consists of a linear background (blue, dashed line), and an integration of Gaussian contributions evaluated at sampled positions along the beam path. The median values of the first (μ_0) and the last ($\mu(u = W)$) partial signals are drawn, which represent the projected size in z of the sample. The signal is also influenced by the Gaussian FOV (G_{FOV}) of the FOXI optic, the median of which is plotted at μ_{FOV}.

The fit uses the exact same model as the thicker sample, given by Equation 8.5. In contrast to the ticker sample, the beam path length is exactly known and can be compared to the fitted value of the sample width in x' of $W = (32.1 \pm 6.8)\,\mathrm{px}$.

The value of W can be translated to a fitted thickness in z taking into account the magnification factor $M = 1.81 \pm 0.05$, the projection of z onto x', and the pixel size of 100 µm via:

$$W(z) = \frac{W(u)}{M \sin(45°)} \cdot 0.1\,\mathrm{mm\,px^{-1}} = (2.51 \pm 0.54)\,\mathrm{mm}. \tag{8.10}$$

Thus, the fitted value and the actual thickness of the sample of 2.4 mm match well.

Thick sample with void

Figure 8.9 shows a projection of the signal from Figure 8.5c onto the x'-axis by summing up all values of $\Delta I_{\mathrm{norm}}(x', y')$ in the vertical direction for each horizontal point in an ROI around the focus. It represents a sample state in which the pin is inserted into the hole in such a way that along the beam path lies a 2.4 mm-thick aluminum plate, followed by a 1 mm void and the pin with its holding mechanism. Figure 8.9 shows a clear dip in the projected signal around $x' = 325\,\mathrm{px}$.

To correctly fit the dip, the model must be adapted by combining the two signals from both sides of the void in the material to:

$$y'_{\text{fit}} = \underbrace{(mx' + b)}_{\text{linear background}} + \underbrace{\left(S_1\left(x'\right) + S_2\left(x'\right)\right)}_{\text{two core signal blocks}} \cdot \underbrace{G_{\text{FOV}}}_{\text{globally enveloping Gaussian through the FOV}} . \quad (8.11)$$

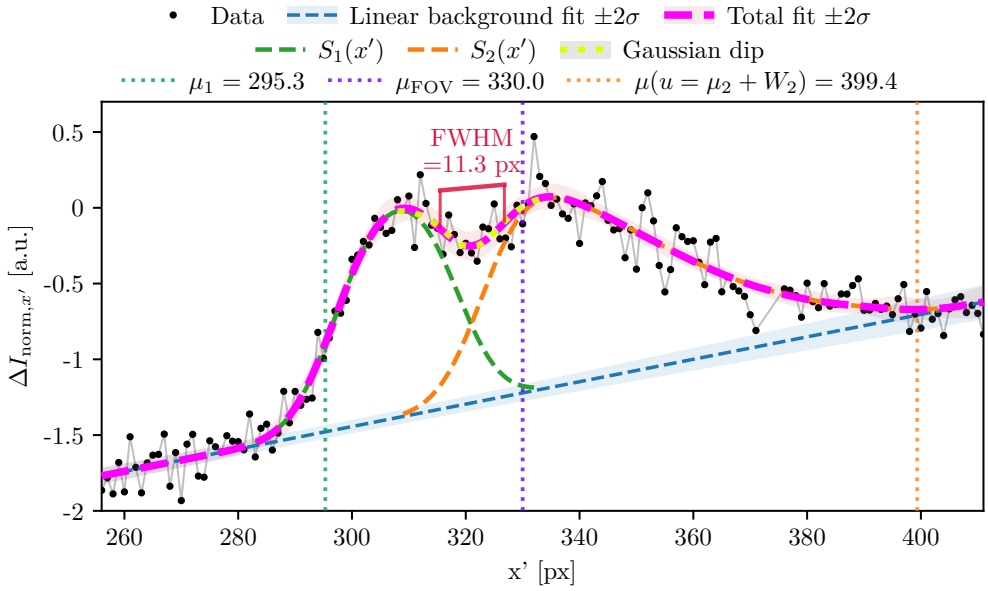


Figure 8.9: Projection of the focus of a thick sample with a 1 mm void (8.5c) onto the x'-axis. The projected signal is fitted (pink dashed line) with the model given by Equation 8.11. The model consists of a linear background (blue, dashed line), and an integration of Gaussian contributions evaluated at sampled positions along the beam path. The void in the sample in z is projected onto the screen and fitted by appropriate integration limits, which divide the signal into two distinct blocks $S_1(x')$ and $S_2(x')$. The median values of the first (μ_1) and the last ($\mu(u = \mu_2 + W_2)$) individual Gaussians are drawn, which represent the projected penetration depth into the sample in z. Fitted on top in yellow is a negative Gaussian, whose FWHM describes the width of the dip that can be used to calculate the width of the void it originates from. The signal is also influenced by the Gaussian FOV (G_{FOV}) of the FOXI optic, the median of which is plotted at μ_{FOV}.

In this adapted model, the linear fit of the background as well as the globally enveloping Gaussian, caused by the FOV of the optic, remain unchanged. The values of μ_{FOV} and σ_{FOV} are the same as those in the fit of the sample with the fully inserted pin. The two signal blocks are given by:

$$S_1(x') = A_1 \int_0^{W_1} e^{-\lambda u} \mathcal{N}\left(x' \mid \mu_1 + u, \sigma(u)\right) du, \quad (8.12a)$$

$$S_2(x') = A_2 \int_0^{W_2} e^{-\lambda(W_1+g+u)} \mathcal{N}\left(x' \mid \mu_2 + u, \sigma\left(W_1 + g + u\right)\right) du, \quad (8.12b)$$

with $\mu_2 = \mu_1 + W_1 + g$ and g accounting for the void. The steady expansion of σ is given by a global model via $\sigma(d) = \sigma_0 + \Delta\sigma \cdot \frac{d}{W_1+g+W_2}$ with d representing a length across the entire signal ranging from 0 to $W_1 + g + W_2$. The attenuation is also defined across the entire signal, which does not account for the fact that the SCOTTI beam is not attenuated within the sample void. However, the thickness of the material through which the Compton signal must pass remains constant, even across the void. The error resulting from overestimating the attenuation of the SCOTTI beam can be neglected for small voids.
The total fit matches the acquired data. The quotient q, which describes the depth of the dip as defined in Section 8.2.2, is calculated to $q = 0.28$.
Again, the projected signal starts with a sharp increase, fitted by the first Gaussian in $S_1(x')$ with a median value of $\mu_1 = (295.3 \pm 2.2)\,\mathrm{px}$. The fitted signal $S_1(x')$ is illustrated in green in Figure 8.9. In theory, $S_1(x')$ should be identical to the projected signal of the sample with no pin inserted. The width of the signal $S_1(x')$ is calculated by the fitting algorithm to $W_1 = (22.6 \pm 3.4)\,\mathrm{px}$, which is lower than the value acquired from the sample with no pin inserted, and does therefore not represent the 2.4 mm front part of the sample as good as the first measurement. Future measurements with an improved setup will determine whether this effect is systematic or caused by inaccuracies in the experiment or its evaluation.

For the same reasons described for the sample with the fully inserted pin, the width of the signal $S_2(x')$ cannot be compared to the sample dimensions. However, the fitted upper boundary of the underlying signal, $\mu(\mu_2 + W_2)$, seems too large. This deviation might be attributed to the background signal's deviation from the assumed linear behavior.
The attenuation coefficient value is calculated by the fitting algorithm as: $\lambda_{z,z'} = (0.012 \pm 0.01)\,\mathrm{px}^{-1}$. This result is again in a plausible order of magnitude.

As discussed in the evaluation of the sample with the fully inserted pin, the model is sensitive to parameter correlations, which is why the parameter g should not be used as an estimate for the void in the sample. Instead, the procedure presented in Section 8.2.2 for estimating the void size by fitting the dip in the total projected signal is employed.
The negative Gaussian, which is fitted to the main fit of the data, is plotted in yellow in Figure 8.9. It has a FWHM of $(11.3 \pm 0.6)\,\mathrm{px}$.
The value of the dip's FWHM can be translated to a fitted void size D in z by taking into account the magnification factor M and the projection of z onto x' via:

$$D = \frac{\mathrm{FWHM_{void}}}{M\ \sin(45°)} \cdot 0.1\,\mathrm{mm\,px^{-1}} = \frac{(11.3 \pm 0.6)\,\mathrm{px}}{(1.81 \pm 0.05)\ \sin(45°)} \cdot 0.1\,\mathrm{mm\,px^{-1}} = (0.88 \pm 0.05)\,\mathrm{mm}. \tag{8.13}$$

The resulting estimate has a slightly lower value than the actual width of 1.0 mm. However, taking the fit error into account, the deviation is only about 10 %. This confirms the principle suitability of the FOXI setup for detecting a void in a sample, quantifying its

position, and determining its size in a single measurement. Therefore, the demonstration experiment can be regarded as a success, especially considering the described difficulties with alignment and shielding.

The value of D_{sim} for the simulation, which was originally calculated in 8.3, can be corrected using the magnification factor M of the ray tracing in the same way:

$$D_{\mathrm{sim}} = \frac{\mathrm{FWHM}_{\mathrm{void}}}{M \sin(45°)} = \frac{(7.5 \pm 0.1)\,\mathrm{px}}{(1.04 \pm 0.01)\sin(45°)} \cdot 0.1\,\mathrm{mm\,px^{-1}} = (1.02 \pm 0.01)\,\mathrm{mm}, \quad (8.14)$$

which fits the actual simulated void width of 1.0 mm even better.

One way to estimate the significance[1] Z_{dip} of a dip is to divide its fitted amplitude A by its fit error σ_A. Therefore, the negative Gaussian that fits the dip must be fitted directly to the data, rather than to the model of the signal. This fit is not shown in Figure 8.9, but gives similar results for D. The significance of the fitted dip can be calculated to:

$$Z_{\mathrm{dip}} \approx \frac{A}{\sigma_A} = \frac{0.372}{0.065} \approx 5.7, \quad (8.15)$$

which confirms a statistically significant detection of the void.

8.3.3 Future Improvements and Outlook

As described in Sections 8.3.1 and 8.3.2, the first experimental realization of FOXI has some issues that need to be overcome. The shielding of the SCOTTI beamline, designed to suppress scattered radiation on the FOXI detector, should be upgraded. This would also make the results more comparable, because the normalization and subtraction of the detector data, as described in Section 8.3.2, might no longer be necessary. The reduced noise would also significantly reduce the necessary scan time.
Different motorized stages should be used to make the alignment reproducible and enable scanning through the range of the optic's degrees of freedom. This would also lead to an improved comparability between the measurements.

Furthermore, different optics can be used as a FOXI optic. This includes optics with parameters tailored to the needs of the concrete FOXI setup, regarding, for example, the needed FOV. The novel von Hámos optics, using aluminum as the Bragg-reflecting material, could also be used. Given the greater Bragg angles when using aluminum instead of graphite-based optics, this would decrease the overall FOXI setup length, as quantified

[1] The significance Z is a quantity that corresponds to the number of standard deviations by which a result deviates from the null hypothesis of no signal. In this case, the null hypothesis is that there is no dip ($A = 0$). Values of $Z \approx 3$ indicate evidence of a signal, while $Z \geq 5$ is typically considered a significant observation of a signal [160].

by Equation 3.2, and increase the optic's solid angle coverage.

Apart from the experimental setup, the data acquisition can also be improved by additional measurements. Most importantly, the FOV of the used optic in the FOXI setup should be studied. This can be realized by using a small sample that is used as a Compton signal source. During such a measurement, the position of the sample in the z-direction would be varied while the signal on the detector is recorded as a function of z or x'. The result would be an experimental measurement of the FOV of the FOXI optic, including the focusing of energies from Compton scattering directions that are not included in the simulations. This would allow the subsequent samples to be aligned within the FOV of the optic as desired. The same measurement could also be used to experimentally quantify the broadening of σ as suggested by Equation 8.8.

Furthermore, in a well-adjusted setup, the depth of the dips could also be related to the width of the void in the x, y plane. This would enable the study of voids that are smaller than the SCOTTI beam width.

Using multiple samples of known thickness and material can help study and improve the fit of the attenuation. This could add an attenuation reconstruction potential to the FOXI setup. Otherwise, if the material is known, an analytical model could be used for $\lambda_{z,z'}$ to improve the fit.

Improved simulations could also help to study properties of the setup, especially additional parameters describing the depth of the dip in a FOXI signal.
Lastly, the FOXI principle is applicable to different kinds of signals, like fluorescence, which opens a broad range of possible applications that can be studied further. It is also not limited to SCOTTI as its primary source for exciting the signals to be detected. Any kind of pencil-like source is generally suitable.

9 Summary and Outlook

Based on a compilation of theoretical preliminary considerations, it was demonstrated that Bragg reflections from mosaic crystals are suitable for focusing X-rays in the SCOTTI setup within a tunable energy range from $E = 30\,\mathrm{keV}$ to $E = 85\,\mathrm{keV}$. The requirements for an optic were compiled, confirming that the use of von Hámos optics is the best option for meeting them.

To perform realistic simulations of the focusing and defocusing properties of the von Hámos optics, the ray-tracing code `xrt` was adapted to account for the full extinction model according to Zachariasen. This allowed for a good agreement between simulated and experimentally measured fluxes, and the qualitative properties of the focus at the SCOTTI beamline.

The use of alternative materials, aluminum and magnesium oxide, was compared to the conventionally used HAPG and HOPG optics in various optic designs, based on ray tracing simulations. Concepts using both curved and non-curved crystals were discussed. Curved aluminum optics were identified as the best alternative, theoretically.
In a series of experiments with samples of such an optic, the ideal surface treatment and the ideal crystal thickness of 0.3 to 0.4 mm were identified, based on the flux achieved at their focus. The corresponding measurements were performed at the SCOTTI beamline under the same conditions as those for the graphite optics used to date. They showed a scaled improvement in flux by a factor of up to 5.2 compared to the previously best-performing HOPG optics.

A characterization setup dedicated to von Hámos optics was designed and experimentally implemented. This setup enables spatially resolved measurements of rocking curves and spatially resolved surface reflectivity mappings. Initial measurements confirm the suitability of the setup for both types of scans and provide explanations for observed fluctuations in the flux at the SCOTTI focus.

Finally, another application of von Hámos's mosaic crystal optics, referred to as FOXI, was presented. In this configuration, the optics are used for imaging in a detector-sided application instead of generating a focused, energy-filtered incident beam. Test measurements

demonstrated the setup's ability to detect a 1 mm wide void within an approximately 5 mm thick aluminum plate, based on the Compton signal from an exciting SCOTTI beam, which confirms the suitability of von Hámos optics for detector-sided applications.

Based on the results of this work, multiple aluminum von Hámos optics are currently being produced for their application in the SCOTTI beamline. The expected increase in flux by a factor of more than five is an important step toward enabling in vivo measurements with SCOTTI.

The characterization setup enables the investigation of the microscopic effects resulting from the bending process in the manufacturing of the novel aluminum optics. This serves as a benchmark for further enhancing the optics. Additionally, the spatially resolved reflectivity mapping of all optics is expected to lead to more reliable alignment procedures and reduced flux fluctuations. The results of the rocking curve scans will improve simulations of the optics' focusing and defocusing properties.

Finally, follow-up experiments with the FOXI setup are planned to study and improve its sensitivity and reduce the necessary scan time. The use of novel aluminum optics is expected to lead to significant improvements in this regard. Additionally, future experiments will expand FOXI to include fluorescence signals.

List of Figures

2.1 Refraction of visible light 5
2.2 Angular dependence of 60 keV Compton scattering 8
2.3 Scattering geometry for an atom 14
2.4 Definition of primitive and conventional lattice vector sets 18
2.5 Construction of a (2 1) lattice plane 21
2.6 Geometric representation of a Bragg reflection 25
2.7 Laue and Bragg geometry 27
2.8 Saturation thickness for Bragg reflections 31
2.9 Bragg reflection by a small crystallite 33
2.10 Darwin mosaic crystal model 39
2.11 Primitive triclinic unit cell 46

3.1 Divergent incident beams on a perfect and a mosaic crystal 50
3.2 Defocusing by crystal depth and width 52
3.3 Wavelength defocusing at perfect and mosaic crystals 53
3.4 Azimuthal mosaic crystal defocusing 54
3.5 Focusing of an extended divergent source 56
3.6 Typical XFI spectrum 58
3.7 Johann and Johansson optic geometry 61
3.8 Focusing of parallel X-rays by perfect Bragg and Laue crystals 63
3.9 Focusing of polychromatic incidence in Laue geometry 63
3.10 Von Hámos optic 66

4.1 SCOTTI: conceptual illustration 71
4.2 SCOTTI: source spectrum 72

5.1 Measured and simulated SCOTTI focus 81

6.1 Photos of HOPG and HAPG optic half 84
6.2 Tile optic approximating a von Hámos optic 90
6.3 Simulated performance of a tile optics approximating von Hámos optics as a function of used number of tiles 91
6.4 Simulated performance of an aluminum von Hámos optic as a function of layer thickness 93
6.5 Simulated performance of a von Hámos optic approximated by 30 bent tiles vs. 30 straight tiles vs. a perfect optic 94
6.6 Photo of bent aluminum samples of batches 1 and 2 96
6.7 Foci produced by bent aluminum crystals of batches 1 and 2 98
6.8 Comparison of aluminum crystals bent with different bending setups 99
6.9 Photo of bent aluminum samples of batch 3 100

6.10 Foci produced by bent aluminum crystals of batch 3 101
6.11 Flux in focus over aluminum sample thickness 103
6.12 Comparison of spectra of HOPG and aluminum optics 105

7.1 Schematic illustration of optic characterization setup 112
7.2 Defocused detector image during a rocking curve scan 116
7.3 Comparison of focused and defocused characterization setup 127
7.4 Experimental characterization setup 131
7.5 Rocking curve of HAPG optic sample 133
7.6 Rocking curve of HOPG optic sample 136
7.7 Zoomed defocused detector image of characterization setup (HOPG) 137
7.8 Detector image and plotted rocking curve of aluminum sample 3 138
7.9 Crystal map scans of HOPG and HAPG optics 141
7.10 Photos of HOPG and HAPG optic half backsides 145

8.1 FOXI: conceptual illustration 149
8.2 Horizontal-axis projection of the FOXI ray tracing simulation 153
8.3 Dependence of FOXI signal strength on simulation parameters 155
8.4 FOXI: Experimental setup 157
8.5 Experimentally recorded and simulated FOXI foci 161
8.6 Vertical-axis projection of the foci 162
8.7 Horizontal-axis projection of the focus for the thick sample with no void . . 164
8.8 Horizontal-axis projection of the focus for the thin sample with no void . . 167
8.9 Horizontal-axis projection of the focus for the thick sample with a void . . . 168

List of Tables

2.1 Overview of all possible Bravais lattices 47

6.1 Experimentally obtained mosaic spread and crystallite size 88
6.2 Reconstructed flux of aluminum optic samples 102

Bibliography

[1] T. Staufer and F. Grüner, "Review of Development and Recent Advances in Biomedical X-ray Fluorescence Imaging," International Journal of Molecular Sciences **24**, 10990 (2023).

[2] F. Grüner, J. Scheunemann, C. Hoeschen, T. Frenzel, and T. Staufer, "Comparing the Achievable Sensitivity Limits of Synchrotron-based X-ray Fluorescence Imaging versus conventional X-ray absorption imaging and comparing absorbed dose levels including PET/SPECT," Zeitschrift für Medizinische Physik **36**, 212–225 (2026).

[3] O. Schmutzler, S. Graf, N. Behm, W. Y. Mansour, F. Blumendorf, T. Staufer, C. Körnig, D. Salah, Y. Kang, J. N. Peters, Y. Liu, N. Feliu, W. J. Parak, A. Burkhardt, E. Gargioni, S. Gennis, S. Chandralingam, F. Höeg, W. Maison, K. Rothkamm, F. Schulz, and F. Grüner, "X-ray Fluorescence Uptake Measurement of Functionalized Gold Nanoparticles in Tumor Cell Microsamples," International Journal of Molecular Sciences **22**, 3691 (2021).

[4] C. Körnig, T. Staufer, O. Schmutzler, T. Bedke, A. Machicote, B. Liu, Y. Liu, E. Gargioni, N. Feliu, W. J. Parak, S. Huber, and F. Grüner, "In-situ x-ray fluorescence imaging of the endogenous iodine distribution in murine thyroids," Scientific Reports **12**, 2903 (2022).

[5] World Health Organization, *Global Status Report on Cancer 2026: The Future We Choose Together* (Geneva, Switzerland, 2026).

[6] G. M. Saladino, P.-H. Chao, B. Brodin, S.-D. Li, and H. M. Hertz, "Liposome biodistribution mapping with in vivo X-ray fluorescence imaging," Nanoscale **16**, 17404–17411 (2024).

[7] T. Staufer, V. Kopatz, A. Pradel, T. Brodie, R. Kuhrwahl, D. Stroka, J. Wallner, L. Kenner, V. Pichler, F. Grüner, and D. M. Mitrano, "Biodistribution of nanoplastics in mice: advancing analytical techniques using metal-doped plastics," Communications Biology **8**, 1247 (2025).

[8] F. Grüner, F. Blumendorf, O. Schmutzler, T. Staufer, M. Bradbury, U. Wiesner, T. Rosentreter, G. Loers, D. Lutz, B. Richter, M. Fischer, F. Schulz, S. Steiner, M. Warmer, A. Burkhardt, A. Meents, M. Kupinski, and C. Hoeschen, "Localising functionalised gold-nanoparticles in murine spinal cords by X-ray fluorescence imaging and background-reduction through spatial filtering for human-sized objects," Scientific Reports **8**, 16561 (2018).

[9] A. Ungerer, T. Staufer, O. Schmutzler, C. Körnig, K. Rothkamm, and F. Grüner, "X-ray-Fluorescence Imaging for In Vivo Detection of Gold-Nanoparticle-Labeled Immune Cells: A GEANT4 Based Feasibility Study," Cancers **13**, 5759 (2021).

[10] M. J. Pushie, I. J. Pickering, M. Korbas, M. J. Hackett, and G. N. George, "Elemental and Chemically Specific X-ray Fluorescence Imaging of Biological Systems," Chemical Reviews **114**, 8499–8541 (2014).

[11] C. Vanhoof, J. R. Bacon, U. E. A. Fittschen, and L. Vincze, "Atomic spectrometry update: review of advances in X-ray fluorescence spectrometry and its special applications," Journal of Analytical Atomic Spectrometry **39**, 2152–2164 (2024).

[12] F. Grüner, Redaktion Universität Hamburg, *Neuartiges Röntgenverfahren für Materialtests bei Elektromotoren*, University of Hamburg, (2024) https://www.uni-hamburg.de/newsroom/presse/2024/pm49.html (visited on 07/07/2026).

[13] I. O. Romero, Y. Fang, M. Lun, and C. Li, "X-ray Fluorescence Computed Tomography (XFCT) Imaging with a Superfine Pencil Beam X-ray Source," Photonics **8**, 236 (2021).

[14] K. Shaker, C. Vogt, Y. Katsu-Jimenez, R. V. Kuiper, K. Andersson, Y. Li, J. C. Larsson, A. Rodriguez-Garcia, M. S. Toprak, M. Arsenian-Henriksson, and H. M. Hertz, "Longitudinal In-Vivo X-Ray Fluorescence Computed Tomography With Molybdenum Nanoparticles," IEEE Transactions on Medical Imaging **39**, 3910–3919 (2020).

[15] J. Baumann, C. Kornig, T. Staufer, C. Schlesiger, O. Schmutzler, F. Gruner, W. Malzer, and B. Kanngiesser, "Enabling Coarse X-ray Fluorescence Imaging Scans with Enlarged Synchrotron Beam by Means of Mosaic Crystal Defocusing Optics," Int J Mol Sci **23**, 4673 (2022).

[16] T. Brümmer, A. Debus, R. Pausch, J. Osterhoff, and F. Grüner, "Design study for a compact laser-driven source for medical x-ray fluorescence imaging," Physical Review Accelerators and Beams **23**, 031601 (2020).

[17] T. M. Staufer, *X-Ray Fluorescence Imaging with a Laser-Driven X-Ray Source*, PhD thesis (University of Hamburg, 2020).

[18] M. v. Zimmermann, O. Ivashko, F. Igoa Saldaña, J. Liu, P. Glaevecke, O. Gutowski, R. Nowak, K. Köhler, B. Winkler, A. Schöps, H. Schulte-Schrepping, and A.-C. Dippel, "P21.1 at PETRA III – a high-energy X-ray diffraction beamline for physics and chemistry," Journal of Synchrotron Radiation **32**, 802–814 (2025).

[19] Deutsches Elektronen-Synchrotron (DESY), *Unified Data Sheet P21.1*, (2023) https://photon-science.desy.de/facilities/petra_iii/beamlines/p211_high_energy_x_ray_diffraction/unified_data_sheet_p211/index_eng.html (visited on 08/01/2025).

[20] N. Manohar, F. J. Reynoso, P. Diagaradjane, S. Krishnan, and S. H. Cho, "Quantitative imaging of gold nanoparticle distribution in a tumor-bearing mouse using benchtop x-ray fluorescence computed tomography," Scientific Reports **6**, 22079 (2016).

[21] A. Maier, S. Steidl, V. Christlein, and J. Hornegger, *Medical Imaging Systems: An Introductory Guide* (Springer International Publishing, 2018).

[22] J. Als-Nielsen and D. McMorrow, *Elements of Modern X-ray Physics* (Wiley, Mar. 2011).

[23] K. Kumar, M. Fachet, and C. Hoeschen, "High-Spatial-Resolution Benchtop X-ray Fluorescence Imaging through Bragg-Diffraction-Based Focusing with Bent Mosaic Graphite Crystals: A Simulation Study," International Journal of Molecular Sciences **25**, 4733 (2024).

[24] J. Baumann, C. P. Schlesiger, F. Gruener, T. Staufer, O. Schmutzler, and C. Koernig, *X-Ray Irradiation Apparatus, Including a Spectrally Shaping X-Ray Optic and a Spectral Filter Aperture Device, for X-Ray Imaging*, US Patent Application US20250062048A1 (Feb. 20, 2025).

[25] F. Grüner, Redaktion Universität Hamburg, *Der Beschleunigerring passt nicht ins Labor: Neues Bildgebungsverfahren zeigt das Immunsystem bei der Arbeit*, University of Hamburg, (Feb. 5, 2026) https://www.uni-hamburg.de/newsroom/forschung/2026/0205-fv-ha-min-bildgebung.html (visited on 07/07/2026).

[26] L. Elbrecht, *Numerical and experimental studies on a novel X-ray optic for X-ray fluorescence-based biomedical imaging*, unpublished, Master's thesis (University of Hamburg, 2023).

[27] M. Born and E. Wolf, *Principles of optics: Electromagnetic theory of propagation, interference and diffraction of light; 7th expand. ed.* (Cambridge Univ. Pr., Cambridge, 1999), 952 pages.

[28] Center for X-Ray Optics, *X-Ray Interactions with Matter: Optical Constants Database*, https://henke.lbl.gov/optical_constants/, Accessed: 2026-01-26, 2026.

[29] A. Fresnel, H. de Senarmont, and É. Verdet, *Oeuvres complètes d'Augustin Fresnel*, Oeuvres complètes d'Augustin Fresnel Bd. 1 (Impr. Impériale, 1866).

[30] A. C. Thompson, D. T. Attwood, E. M. Gullikson, M. R. Howells, J. B. Kortright, A. L. Robinson, J. H. Underwood, G. P. Williams, and H. Winick, eds., *X-Ray Data Booklet*, 3rd, Online edition, accessed 2026-01-26 (Lawrence Berkeley National Laboratory, 2009).

[31] D. Attwood, *Soft X-Rays and Extreme Ultraviolet Radiation: Principles and Applications* (Cambridge University Press, Aug. 1999).

[32] J. H. Lambert, *Photometria sive de mensura et gradibus luminis, colorum et umbrae* (Eberhard Klett, Augsburg, 1760).

[33] A. H. Compton, "A Quantum Theory of the Scattering of X-rays by Light Elements," Phys. Rev. **21**, 483–502 (1923).

[34] O. Klein and Y. Nishina, "Über die Streuung von Strahlung durch freie Elektronen nach der neuen relativistischen Quantendynamik von Dirac," Zeitschrift für Physik **52**, 853–868 (1929).

[35] J. D. Jackson, *Classical electrodynamics; Third edition* (John Wiley & Sons, Inc., New York, 1999), xxi, 808 pages : illustrations, diagrams.

[36] J. Thomson, "XLVI. On the scattering of light by unsymmetrical atoms and molecules," The London, Edinburgh, and Dublin Philosophical Magazine and Journal of Science **40**, 393–413 (1920).

[37] M. E. Peskin and D. V. Schroeder, *An introduction to quantum field theory*, The advanced book program (Addison-Wesley, Reading, 1995), 842 pages.

[38] R. Fitzpatrick, *Maxwell's equations and the principles of electromagnetism* (Jones and Bartlett, Sudbury, MA, Jan. 2008).

[39] J. Larmor, "LXIII. On the theory of the magnetic influence on spectra; and on the radiation from moving ions," The London, Edinburgh, and Dublin Philosophical Magazine and Journal of Science **44**, 503–512 (1897).

[40] J. H. Poynting, "XV. On the transfer of energy in the electromagnetic field," Philosophical Transactions of the Royal Society of London, 343–361 (1884).

[41] A. Guinier, *X-ray diffraction*, Books in Physics S. (W.H. Freeman, New York, NY, Dec. 1963).

[42] C. T. Chantler, "Detailed Tabulation of Atomic Form Factors, Photoelectric Absorption and Scattering Cross Section, and Mass Attenuation Coefficients in the Vicinity of Absorption Edges in the Soft X-Ray (Z=30–36, Z=60–89, E=0.1 keV–10 keV), Addressing Convergence Issues of Earlier Work," Journal of Physical and Chemical Reference Data **29**, 597–1056 (2000).

[43] C. Chantler, K. Olsen, R. Dragoset, A. Kishore, S. Kotochigova, and D. Zucker, *X-Ray form factor, attenuation, and scattering tables*, en, (Jan. 2003) http://physics.nist.gov/FFast.

[44] P. Debye, "Interferenz von Röntgenstrahlen und Wärmebewegung," Annalen der Physik **348**, 49–92 (1913).

[45] B. E. Warren, *X-ray Diffraction* (Dover Publications, 1990).

[46] International Union of Crystallography, *Online Dictionary of Crystallography - Crystal*, https://dictionary.iucr.org/Crystal (visited on 08/16/2023).

[47] C. Kittel, *Introduction to Solid State Physics*, 8th ed. (John Wiley & Sons, New York, 2005).

[48] International Union of Crystallography, *International Tables for Crystallography Volume A: Space-group symmetry* (International Union of Crystallography, Dec. 2016).

[49] W. Zachariasen, *Theory of X-ray Diffraction in Crystals* (Dover, 1967).

[50] A. Bravais, "Mémoire sur les systèmes formés par des points distribués régulièrement sur un plan ou dans l'espace," Journal de l'École Polytechnique **19**, 1–128 (1850).

[51] N. W. Ashcroft and N. D. Mermin, *Solid State Physics* (Holt, Rinehart and Winston, New York, 1976).

[52] W. Friedrich, P. Knipping, and M. Laue, "Interferenzerscheinungen bei Röntgenstrahlen," Annalen der Physik **346**, 971–988 (1913).

[53] M. Laue, "Eine quantitative Prüfung der Theorie für die Interferenzerscheinungen bei Röntgenstrahlen," Annalen der Physik **346**, 989–1002 (1913).

[54] A. 1.-2. Authier, *Dynamical theory of x-ray diffraction*, Rev. ed, International Union of Crystallography monographs on crystallography (Oxford Univ. Press, 2004).

[55] F. Masiello, G. Cembali, A. I. Chumakov, S. H. Connell, C. Ferrero, J. Härtwig, I. Sergeev, and P. Van Vaerenbergh, "Rocking curve measurements revisited," Journal of Applied Crystallography **47**, 1304–1314 (2014).

[56] International Union of Crystallography, *International Tables for Crystallography Volume B: Reciprocal space* (International Union of Crystallography, Jan. 2010).

[57] W. H. Bragg and W. L. Bragg, "The reflection of X-rays by crystals," Proceedings of the Royal Society of London. Series A, Containing Papers of a Mathematical and Physical Character **88**, 428–438 (1913).

[58] V. Sears, "Bragg Reflection in Mosaic Crystals. I. General Solution of the Darwin Equations," Acta Crystallographica Section A **53**, 35–45 (1997).

[59] W. H. Zachariasen, "A general theory of X-ray diffraction in crystals," Acta Crystallographica **23**, 558–564 (1967).

[60] C. G. Darwin, "XXXIV. The theory of X-ray reflexion," The London, Edinburgh, and Dublin Philosophical Magazine and Journal of Science **27**, 315–333 (1914).

[61] C. G. Darwin, "LXXVIII. The theory of X-ray reflexion. Part II," The London, Edinburgh, and Dublin Philosophical Magazine and Journal of Science **27**, 675–690 (1914).

[62] S. Takagi, "Dynamical theory of diffraction applicable to crystals with any kind of small distortion," Acta Crystallographica **15**, 1311–1312 (1962).

[63] D. Taupin, "Théorie dynamique de la diffraction des rayons X par les cristaux déformés," Bulletin de Minéralogie **87**, 469–511 (1964).

[64] S. Takagi, "A Dynamical Theory of Diffraction for a Distorted Crystal," Journal of the Physical Society of Japan **26**, 1239–1253 (1969).

[65] A. Authier, "Dynamical theory of X-ray diffraction," in *International Tables for Crystallography* (International Union of Crystallography, Oct. 2006), pp. 534–551.

[66] W. Friedrich, P. Knipping, and M. Laue, "Interferenzerscheinungen bei Röntgenstrahlen," Annalen der Physik **346**, 971–988 (1913).

[67] R. P. Feynman, *Quantum mechanics*, edited by R. B. Leighton and M. L. Sands, 11. print, The lectures on physics (Addison-Wesley, 1979).

[68] M. O. Krause and J. H. Oliver, "Natural widths of atomic K and L levels, Kα X-ray lines and several KLL Auger lines," Journal of Physical and Chemical Reference Data **8**, 329–338 (1979).

[69] F. Livet and M. Sutton, "X-ray coherent scattering in metal physics," Comptes Rendus. Physique **13**, 227–236 (2012).

[70] C. Darwin, "XCII. The reflexion of X-rays from imperfect crystals," The London, Edinburgh, and Dublin Philosophical Magazine and Journal of Science **43**, 800–829 (1922).

[71] M. Gerlach, L. Anklamm, A. Antonov, I. Grigorieva, I. Holfelder, B. Kanngießer, H. Legall, W. Malzer, C. Schlesiger, and B. Beckhoff, "Characterization of HAPG mosaic crystals using synchrotron radiation," Journal of Applied Crystallography **48**, 1381–1390 (2015).

[72] M. Sanchez del Rio, N. Canestrari, F. Jiang, and F. Cerrina, "*SHADOW3*: a new version of the synchrotron X-ray optics modelling package," Journal of Synchrotron Radiation **18**, 708–716 (2011).

[73] M. S. del Río and R. J. Dejus, "XOP v2.4: recent developments of the x-ray optics software toolkit," in Advances in Computational Methods for X-Ray Optics II, Vol. 8141, edited by M. S. del Rio and O. Chubar (International Society for Optics and Photonics, 2011), p. 814115.

[74] H. Halloin and P. Bastie, "Laue diffraction lenses for astrophysics: Theoretical concepts," Experimental Astronomy **20**, 151–170 (2006).

[75] P. Debye and P. Scherrer, "Interferenzen an regellos orientierten Teilchen im Röntgenlicht. I.," Nachrichten von der Gesellschaft der Wissenschaften zu Göttingen, Mathematisch-Physikalische Klasse **1916**, 1–15 (1916).

[76] S. Stoupin, J. P. C. Ruff, T. Krawczyk, and K. D. Finkelstein, "X-ray reflectivity of chemically vapor-deposited diamond single crystals in the Laue geometry," Acta Crystallographica Section A Foundations and Advances **74**, 567–577 (2018).

[77] J.-P. Guigay and M. Sanchez del Rio, "Formulation of perfect-crystal diffraction from Takagi–Taupin equations: numerical implementation in the *crystalpy* library," Journal of Synchrotron Radiation **31**, 1469–1480 (2024).

[78] K. Klementiev and R. Chernikov, "Powerful scriptable ray tracing package xrt," in Advances in Computational Methods for X-Ray Optics III, Vol. 9209, edited by M. S. del Rio and O. Chubar (International Society for Optics and Photonics, 2014), 92090A.

[79] S. Gražulis, D. Chateigner, R. T. Downs, A. F. T. Yokochi, M. Quirós, L. Lutterotti, E. Manakova, J. Butkus, P. Moeck, and A. Le Bail, "Crystallography Open Database – an open-access collection of crystal structures," Journal of Applied Crystallography **42**, 726–729 (2009).

[80] F. Frontera and P. von Ballmoos, "Laue Gamma-Ray Lenses for Space Astrophysics: Status and Prospects," X-Ray Optics and Instrumentation **2010**, 1–18 (2010).

[81] R. Camattari, V. Bellucci, V. Guidi, and I. Neri, "Quasi-mosaic crystals for high-resolution focusing of hard x-rays through a Laue lens," in Optics for EUV, X-Ray, and Gamma-Ray Astronomy V, Vol. 8147, edited by S. L. O'Dell and G. Pareschi (2011), 81471G.

[82] M. S. del Rio, M. Gambaccini, G. Pareschi, A. Taibi, A. Tuffanelli, and A. K. Freund, "Focusing properties of mosaic crystals," **3448**, edited by A. T. Macrander, A. K. Freund, T. Ishikawa, and D. M. Mills, 246–255 (1998).

[83] H. Legall, H. Stiel, V. Arkadiev, and A. Bjeoumikhov, "High spectral resolution x-ray optics with highly oriented pyrolytic graphite," Optics Express **14**, 4570–4576 (2006).

[84] C. Schlesiger, L. Anklamm, H. Stiel, W. Malzer, and B. Kanngießer, "XAFS spectroscopy by an X-ray tube based spectrometer using a novel type of HOPG mosaic crystal and optimized image processing," Journal of Analytical Atomic Spectrometry **30**, 1080–1085 (2015).

[85] H. A. Rowland, "XXIX. On concave gratings for optical purposes," The London, Edinburgh, and Dublin Philosophical Magazine and Journal of Science **16**, 197–210 (1883).

[86] H. Winick and S. Doniach, eds., *Synchrotron radiation research* (Plenum Press, New York, 1980), 754 pages.

[87] D. Anagnostopoulos, A. Siozios, and P. Patsalas, "Characterization of aluminum nitride based films with high resolution X-ray fluorescence spectroscopy," Journal of Applied Physics **123**, 065105 (2018).

[88] Comet AG, *MXR-225HP/11 X-Ray Tube*, Product datasheet, Comet AG (2023).

[89] D. Attwood, *Soft X-Rays and Extreme Ultraviolet Radiation: Principles and Applications* (Cambridge University Press, 1999).

[90] Amptek Inc., *X-123 FAST SDD®Ultra High Performance Silicon Drift Detector*, Product description, Amptek Inc. (2026).

[91] T. Staufer, C. Körnig, B. Liu, Y. Liu, C. Lanzloth, O. Schmutzler, T. Bedke, A. Machicote, W. J. Parak, N. Feliu, L. Bosurgi, S. Huber, and F. Grüner, "Enabling X-ray fluorescence imaging for in vivo immune cell tracking," Scientific Reports **13**, 11505 (2023).

[92] L. v. Hámos, "Röntgenspektroskopie und Abbildung mittels gekrümmter Kristallreflektoren," Naturwissenschaften **20**, 705–706 (1932).

[93] P. Zimmermann, S. Peredkov, P. Abdala, S. DeBeer, M. Tromp, C. Müller, and J. Bokhoven, "Modern X-ray spectroscopy: XAS and XES in the laboratory," Coordination Chemistry Reviews **423**, 213466 (2020).

[94] P. Jagodziński, M. Pajek, D. Banaś, H. Beyer, M. Trassinelli, and T. Sto¨hlker, "Ray-tracing simulations of spherical Johann diffraction spectrometer for in-beam X-ray experiments," Nuclear Instruments and Methods in Physics Research Section A: Accelerators, Spectrometers, Detectors and Associated Equipment **753**, 121–130 (2014).

[95] J. K. Kowalska, F. A. Lima, C. J. Pollock, J. A. Rees, and S. DeBeer, "A Practical Guide to High-resolution X-ray Spectroscopic Measurements and their Applications in Bioinorganic Chemistry," Israel Journal of Chemistry **56**, 803–815 (2016).

[96] B. S. Fraenkel and M. Bitter, "The 2D curved crystal Johansson X-ray spectrometer for diagnostics of hot plasmas," Journal of X-Ray Science and Technology **9**, 29–33 (2001).

[97] R. Camattari, "Laue lens for astrophysics: Extensive comparison between mosaic, curved, and quasi-mosaic crystals," Astronomy & Astrophysics **587**, A21 (2016).

[98] E. Virgilli, F. Frontera, V. Valsan, V. Liccardo, E. Caroli, J. B. Stephen, F. Cassese, L. Recanatesi, M. Pecora, S. Mottini, P. Attiná, and B. Negri, "The LAUE project for broadband gamma-ray focusing lenses," in Optics for EUV, X-Ray, and Gamma-Ray Astronomy V, Vol. 8147, edited by S. L. O'Dell and G. Pareschi (International Society for Optics and Photonics, 2011), p. 81471C.

[99] N. Barrière, J. Tomsick, S. Boggs, J. Rousselle, and P. von Ballmoos, "Development of efficient Laue lenses: experimental results and projects," in Space Telescopes and Instrumentation 2010: Ultraviolet to Gamma Ray, Vol. 7732, edited by M. Arnaud, S. S. Murray, and T. Takahashi (2010), p. 773226.

[100] B. Lengeler, C. G. Schroer, M. Kuhlmann, B. Benner, T. Florian Günzler, O. Kurapova, F. Zontone, A. Snigirev, and I. Snigireva, "Refractive x-ray lenses," Journal of Physics D: Applied Physics **38**, A218 (2005).

[101] B. Lengeler, C. Schroer, J. Tümmler, B. Benner, M. Richwin, A. Snigirev, I. Snigireva, and M. Drakopoulos, "Imaging by parabolic refractive lenses in the hard X-ray range," Journal of Synchrotron Radiation **6**, 1153–1167 (1999).

[102] C. G. Schroer, O. Kurapova, J. Patommel, P. Boye, J. Feldkamp, B. Lengeler, M. Burghammer, C. Riekel, L. Vincze, A. van der Hart, and M. Küchler, "Hard x-ray nanoprobe based on refractive x-ray lenses," Applied Physics Letters **87**, 124103 (2005).

[103] S.-R. Wu, Y. Hwu, and G. Margaritondo, "Hard-X-ray Zone Plates: Recent Progress," Materials **5**, 1752–1773 (2012).

[104] V. V. Lider, "Zone Plates for X-Ray Focusing (Review)," Journal of Surface Investigation: X-ray, Synchrotron and Neutron Techniques **11**, 1113–1127 (2017).

[105] K. P. Singh, "Grazing incidence optics for X-ray astronomy: X-ray optics," Journal of Optics **40**, 88–95 (2011).

[106] P. Friedrich, *The Universe in X-Rays*, edited by J. E. Trümper and G. Hasinger (Springer Berlin Heidelberg, 2008).

[107] H. Wolter, "Spiegelsysteme streifenden Einfalls als abbildende Optiken für Röntgenstrahlen," Annalen der Physik **445**, 94–114 (1952).

[108] P. J. Schields, D. M. Gibson, W. M. Gibson, N. Gao, H. Huang, and I. Y. Ponomarev, "Overview of polycapillary X-ray optics," Powder Diffraction **17**, 70–80 (2002).

[109] V. V. Lider, "X-ray fluorescence imaging," Physics-Uspekhi **61**, 980–999 (2018).

[110] P. Kirkpatrick and A. V. Baez, "Formation of Optical Images by X-Rays," J. Opt. Soc. Am. **38**, 766–774 (1948).

[111] W. Liu, G. E. Ice, L. Assoufid, C. Liu, B. Shi, P. Zschack, J. Tischler, J. Qian, R. Khachartryan, and D. Shu, "Hard X-ray nano-focusing with Montel mirror optics," Nuclear Instruments and Methods in Physics Research Section A: Accelerators, Spectrometers, Detectors and Associated Equipment **649**, National Synchrotron Radiation Instrumentation conference in 2010, 169–171 (2011).

[112] K. Mundboth, J. Sutter, D. Laundy, S. Collins, S. Stoupin, and Y. Shvyd'ko, "Tests and characterization of a laterally graded multilayer Montel mirror," Journal of Synchrotron Radiation **21**, 16–23 (2014).

[113] W. Singhapong, C. Bowen, H. Wang, K. Sawhney, and A. J. G. Lunt, "Multilayer Optics for Synchrotron Applications," Advanced Materials Technologies **9**, 2302187 (2024).

[114] C. Chantler, "X-ray diffraction of bent crystals in Bragg geometry. I. Perfect-crystal modelling," Journal of Applied Crystallography - J APPL CRYST **25**, 674–693 (1992).

[115] R. Camattari, V. Guidi, V. Bellucci, and A. Mazzolari, "The 'quasi-mosaic' effect in crystals and its applications in modern physics," Journal of Applied Crystallography **48**, 977–989 (2015).

[116] J. Haak, *PhD dissertation*, Unpublished dissertation (manuscript in preparation) (University of Hamburg, 2026).

[117] F. Ziegler, *PhD dissertation*, Unpublished dissertation (manuscript in preparation) (University of Hamburg, 2026).

[118] R. Buchin, *Beam Characterization and Automation Techniques for a Compact X-Ray Fluorescence Imaging Platform*, unpublished, Master's thesis (University of Hamburg, 2024).

[119] G. Poludniowski, A. Omar, R. Bujila, and P. Andreo, "Technical Note: SpekPy v2.0—a software toolkit for modeling x-ray tube spectra," Medical Physics **48**, 3630–3637 (2021).

[120] Plansee SE, *DENSIMET®Tungsten Heavy Metal Alloys*, Material datasheet, Plansee SE, 2021.

[121] Direct Conversion AB, *XC-ACTAEON FX3/FX5 Technical Manual*, Revision D, Document No. 40-450-104, Direct Conversion AB (Danderyd, Sweden, 2020).

[122] A. Shankar, J. Krebs, D. R. Bednarek, and S. Rudin, "Evaluation of a new photon-counting imaging detector (PCD) with various acquisition modes," in Medical Imaging 2018: Physics of Medical Imaging, Vol. 10573, edited by J. Y. Lo, T. G. Schmidt, and G.-H. Chen (International Society for Optics and Photonics, 2018), 105734Y.

[123] Dectris Ltd., *PILATUS3 R 100K-M Hybrid Photon-Counting Detector*, Product description, Dectris Ltd. (2024).

[124] X. Llopart, R. Ballabriga, M. Campbell, L. Tlustos, and W. Wong, "Timepix, a 65k programmable pixel readout chip for arrival time, energy and/or photon counting measurements," Nuclear Instruments and Methods in Physics Research Section A: Accelerators, Spectrometers, Detectors and Associated Equipment **581**, VCI 2007, 485–494 (2007).

[125] ADVACAM s.r.o., *MiniPIX edu: Pixel detector for radiation imaging and spectroscopy*, Product documentation, ADVACAM (2023).

[126] J. Haak, F. Ziegler, T. Staufer, and F. Grüner, "XFI: recent applications and detector requirements," in Hard X-Ray, Gamma-Ray, and Neutron Detector Physics XXVI, Vol. 13151, edited by N. J. Cherepy, M. Fiederle, and R. B. James (International Society for Optics and Photonics, 2024), 131510J.

[127] J. Allison, K. Amako, J. Apostolakis, P. Arce, M. Asai, T. Aso, E. Bagli, A. Bagulya, S. Banerjee, G. Barrand, B. Beck, A. Bogdanov, D. Brandt, J. Brown, H. Burkhardt, P. Canal, D. Cano-Ott, S. Chauvie, K. Cho, G. Cirrone, G. Cooperman, M. Cortés-Giraldo, G. Cosmo, G. Cuttone, G. Depaola, L. Desorgher, X. Dong, A. Dotti, V. Elvira, G. Folger, Z. Francis, A. Galoyan, L. Garnier, M. Gayer, K. Genser, V. Grichine, S. Guatelli, P. Guèye, P. Gumplinger, A. Howard, I. Hřivnáčová, S. Hwang, S. Incerti, A. Ivanchenko, V. Ivanchenko, F. Jones, S. Jun, P. Kaitaniemi, N. Karakatsanis, M. Karamitros, M. Kelsey, A. Kimura, T. Koi, H. Kurashige, A. Lechner, S. Lee, F. Longo, M. Maire, D. Mancusi, A. Mantero, E. Mendoza, B. Morgan, K. Murakami, T. Nikitina, L. Pandola, P. Paprocki, J. Perl, I. Petrović, M. Pia, W. Pokorski, J. Quesada, M. Raine, M. Reis, A. Ribon, A. Ristić Fira, F. Romano, G. Russo, G. Santin, T. Sasaki, D. Sawkey, J. Shin, I. Strakovsky, A. Taborda, S. Tanaka, B. Tomé, T. Toshito, H. Tran, P. Truscott, L. Urban, V. Uzhinsky, J. Verbeke, M. Verderi, B. Wendt, H. Wenzel, D. Wright, D. Wright, T. Yamashita, J. Yarba, and H. Yoshida, "Recent developments in Geant4," Nuclear Instruments and Methods in Physics Research Section A: Accelerators, Spectrometers, Detectors and Associated Equipment **835**, 186–225 (2016).

[128] F. Guan, M. Asai, D. A. Bartkoski, M. Kleckner, Z. Harel, and M. Salehpour, "Adding the X-ray Bragg reflection physical process in crystal to the Geant4 Monte Carlo simulation toolkit, part I: reflection from a crystal slab," Precision Radiation Oncology **7**, 59–66 (2023).

[129] E. Bergbäck Knudsen, A. Prodi, J. Baltser, M. Thomsen, P. Kjær Willendrup, M. Sanchez del Rio, C. Ferrero, E. Farhi, K. Haldrup, A. Vickery, R. Feidenhans'l, K. Mortensen, M. Meedom Nielsen, H. Friis Poulsen, S. Schmidt, and K. Lefmann, "*McXtrace*: a Monte Carlo software package for simulating X-ray optics, beamlines and experiments," Journal of Applied Crystallography **46**, 679–696 (2013).

[130] M. Šmíd, X. Pan, and K. Falk, "X-ray spectrometer simulation code with a detailed support of mosaic crystals," Computer Physics Communications **262**, 107811 (2021).

[131] C. Schlesiger and J. Baumann, *Private communication for providing a X-ray tracing code and experiences with HAPG and HOPG crystals*, Private communication, 2023.

[132] C. Schlesiger, L. Anklamm, W. Malzer, R. Gnewkow, and B. Kanngießer, "A new model for the description of X-ray diffraction from mosaic crystals for ray-tracing calculations," Journal of Applied Crystallography **50**, 1490–1497 (2017).

[133] University of Hamburg, *PHYSnet Computing Cluster*, High-performance computing cluster, 2026.

[134] J. Haak and F. Ziegler, *Private communication on the focal spot asymmetry and different measured flux values observed in the SCOTTI setup*, Private communication on the focal spot asymmetry and differnt measured flux values observed in the SCOTTI setup, May 2026.

[135] C. G. Körnig, *Pilot studies for quantitative 2D and 3D X-ray fluorescence imaging*, PhD thesis (Staats-und Universitätsbibliothek Hamburg Carl von Ossietzky, 2022).

[136] Optigraph GmbH, *Graphite Optics*, Accessed: 2026-04-27, (2022) https://www.optigraph.eu/graphite-optics.

[137] Analytical X-ray Physics Group, *Analytical X-ray Physics*, Accessed: 2026-06-09, 2026.

[138] I. Grigorieva, A. Antonov, and G. Gudi, "Graphite Optics—Current Opportunities, Properties and Limits," Condensed Matter **4**, 18 (2019).

[139] Optigraph GmbH, *Private communication on HOPG and HAPG crystal optic manufacturing*, Private communication, 2024.

[140] M. Ohler, M. S. del Rio, A. Tuffanelli, M. Gambaccini, A. Taibi, A. Fantini, and G. Pareschi, "X-ray topographic determination of the granular structure in a graphite mosaic crystal: a three-dimensional reconstruction," Journal of Applied Crystallography **33**, 1023–1030 (2000).

[141] A. Tuffanelli, M. S. del Rio, G. Pareschi, M. Gambaccini, A. Taibi, A. Fantini, and M. Ohler, "Comparative characterization of highly oriented pyrolytic graphite by means of diffraction topography," in X-Ray Optics Design, Performance, and Applications, Vol. 3773, edited by A. M. Khounsary, A. K. Freund, T. Ishikawa, G. Srajer, and J. C. Lang (International Society for Optics and Photonics, 1999), pp. 192–198.

[142] D. A. Bartkoski, A. Bar-David, M. Kleckner, D. Mirkovic, R. Tailor, J. Moradi-Kurdestany, S. Borukhin, Z. Harel, Z. Burshtein, A. Zuck, and M. Salehpour, "Analysis of a novel X-ray lens for converging beam radiotherapy," Scientific Reports **11**, 19180 (2021).

[143] MaTecK Material-Technologie & Kristalle GmbH, *Product lineup*, Accessed: 2026-06-09, (2026) https://mateck.com.

[144] T. Fink, *Private communication on crystal properties and manufacturing*, Private communication, MaTecK Material-Technologie & Kristalle GmbH, 2024.

[145] T. Fink, *Private communication on bending setup for curved aluminum crystal samples*, Private communication, MaTecK Material-Technologie & Kristalle GmbH, 2026.

[146] K. Knowles, "The Plane Strain Young's Modulus in Cubic Materials," Journal of Elasticity **128**, 1–27 (2017).

[147] D. Grötzsch, J. Grage, and W. Malzer, *Implementation of the Experimental Characterization Setup and Control Software*, Private communication, 2026.

[148] rtw Röntgen-Technik Dr. Warrikhoff GmbH & Co. KG, *Metal-Ceramic X-Ray Tube: MCBI 50B-50 Rh 40°*, Data sheet, version dated 2025-01-28 (Jan. 2025).

[149] W. F. Guthrie, *NIST/SEMATECH e-Handbook of Statistical Methods (NIST Handbook 151)*, en, 2020.

[150] S. Brandt, *Data Analysis* (Springer International Publishing, 2014).

[151] J. Olivero and R. Longbothum, "Empirical fits to the Voigt line width: A brief review," Journal of Quantitative Spectroscopy and Radiative Transfer **17**, 233–236 (1977).

[152] D. M. Kipping, "Binning is sinning: morphological light-curve distortions due to finite integration time: Binning is sinning," Monthly Notices of the Royal Astronomical Society **408**, 1758–1769 (2010).

[153] P. Virtanen, R. Gommers, T. E. Oliphant, M. Haberland, T. Reddy, D. Cournapeau, E. Burovski, P. Peterson, W. Weckesser, J. Bright, S. J. van der Walt, M. Brett, J. Wilson, K. J. Millman, N. Mayorov, A. R. J. Nelson, E. Jones, R. Kern, E. Larson, C. J. Carey, İ. Polat, Y. Feng, E. W. Moore, J. VanderPlas, D. Laxalde, J. Perktold, R. Cimrman, I. Henriksen, E. A. Quintero, C. R. Harris, A. M. Archibald, A. H. Ribeiro, F. Pedregosa, P. van Mulbregt, A. Vijaykumar, A. P. Bardelli, A. Rothberg, A. Hilboll, A. Kloeckner, A. Scopatz, A. Lee, A. Rokem, C. N. Woods, C. Fulton, C. Masson, C. Häggström, C. Fitzgerald, D. A. Nicholson, D. R. Hagen, D. V. Pasechnik, E. Olivetti, E. Martin, E. Wieser, F. Silva, F. Lenders, F. Wilhelm, G. Young, G. A. Price, G.-L. Ingold, G. E. Allen, G. R. Lee, H. Audren, I. Probst, J. P. Dietrich, J. Silterra, J. T. Webber, J. Slavič, J. Nothman, J. Buchner, J. Kulick, J. L. Schönberger, J. V. de Miranda Cardoso, J. Reimer, J. Harrington, J. L. C. Rodríguez, J. Nunez-Iglesias, J. Kuczynski, K. Tritz, M. Thoma, M. Newville, M. Kümmerer, M. Bolingbroke, M. Tartre, M. Pak, N. J. Smith, N. Nowaczyk, N. Shebanov, O. Pavlyk, P. A. Brodtkorb, P. Lee, R. T. McGibbon, R. Feldbauer, S. Lewis, S. Tygier, S. Sievert, S. Vigna, S. Peterson, S. More, T. Pudlik, T. Oshima, T. J. Pingel, T. P. Robitaille, T. Spura, T. R. Jones, T. Cera, T. Leslie, T. Zito, T. Krauss, U. Upadhyay, Y. O. Halchenko, and Y. Vázquez-Baeza, "SciPy 1.0: fundamental algorithms for scientific computing in Python," Nature Methods **17**, 261–272 (2020).

[154] J. C. C. Chan and D. P. Kroese, *Statistical Modeling and Computation* (Springer US, 2025).

[155] Optigraph GmbH, *Private communication on measured mosaic spread of HAPG von Hámos optic samples*, Private communication, 2022.

[156] A. Buffet, A. Rothkirch, R. Döhrmann, V. Körstgens, M. M. Abul Kashem, J. Perlich, G. Herzog, M. Schwartzkopf, R. Gehrke, P. Müller-Buschbaum, and S. V. Roth, "P03, the microfocus and nanofocus X-ray scattering (MiNaXS) beamline of the PETRA III storage ring: the microfocus endstation," Journal of Synchrotron Radiation **19**, 647–653 (2012).

[157] S. Seltzer, *XCOM-Photon Cross Sections Database, NIST Standard Reference Database 8*, en, 1987.

[158] S. Seltzer, *Tables of X-Ray Mass Attenuation Coefficients and Mass Energy-Absorption Coefficients, NIST Standard Reference Database 126*, en, 1995.

[159] G. F. Knoll and D. K. Wehe, *Radiation detection and measurement: Student solutions manual; 4th ed.* (Wiley, Hoboken, 2012), 82 pages.

[160] G. Cowan, *Statistical data analysis [with applications from particle physics]*, Repr., Oxford science publications (Clarendon Press, 2004).

Appendix

A.1 Use of Large Language Models

Large Language Models (LLMs), specifically OpenAI's ChatGPT and Codex (available through an OpenAI Plus subscription), were used during this work. The author developed all research questions, analyses, interpretations, and conclusions and is responsible for them. The LLMs were therefore used solely as supportive tools to increase efficiency. The following remarks explain how the models were used and how the results were verified. Sample prompts are provided for each case. These prompts are illustrative and representative of their respective uses.

A.1.1 Coding

In this work, OpenAI's LLM Codex was used to provide programming assistance in `Python`. This assistance primarily involved implementing small code units that would have otherwise required more in-depth research. For instance, evaluating the measurements in Chapter 7.5.1 required defining the ROI as a circle segment. Rather than researching how to implement such a shape, the task of adapting the ROI from a rectangular shape to a circular segment was given to Codex. The change in the code was then checked and validated for correctness, functionality, and consistency with the intended change or addition. Thus, the LLM supported the step-by-step development of `Python` scripts to analyze the measurements presented in Chapters 7 and 8. The significant time savings made it possible to test different analysis ideas efficiently or react quickly to any necessary changes during a measurement campaign by rapidly analyzing the data.

This support was limited to implementing previously planned analysis procedures. The underlying algorithms, analysis strategies, and physical models were developed by the author. All script sections created by Codex were checked and validated after generation. In addition to generating `Python` code for analyzing measurements, Codex assisted in generating figures for this `LaTeX` document, particularly `TikZ` codes. The author always determined the content, design, and scientific message of the figures. The support provided by Codex was similar to that described above. For instance, Codex was instructed to provide code to blur the enclosed area after the edges of the blurred area in Figure 7.4 were defined.

Using the LLM in this context eliminated the need for a time-consuming search to implement custom visualizations. Finally, Codex was used to quickly identify and resolve errors that occurred during the compilation of `Python` and `LaTeX` scripts. Most of these errors were limited to typos or incompatible packages. The suggested changes were reviewed before final implementation. Both the OpenAI website and the Visual Studio Code IDE extension were used to access Codex.

A.1.2 Research

ChatGPT was only used to a limited extent for researching academic sources. Specifically, it was used to identify standard sources on particular topics and frequently cited academic publications on specific subjects. However, the results were often unreliable and always required verification and supplementation through further in-depth research. All statements in this work, supported by sources, were verified using physical or digital copies of the respective publications and are therefore based on the original sources. ChatGPT was not used to reproduce literature summaries, scientific statements, unverified citations, or sources.

A.1.3 Writing

This work does not contain any scientific content, interpretations, arguments, or conclusions generated by an LLM. In some cases, missing technical terms needed for further research were queried via ChatGPT by paraphrasing them. The results of these prompts were always verified. The same applies to searching for common phrasing. Additionally, ChatGPT was occasionally used to suggest or review phrasing, as well as for proofreading.

To translate passages, phrases, and word groups originally written in German, DeepL Pro, the tool recommended by the University of Hamburg for this purpose, was used. It was also used to check spelling, grammar, and punctuation, as well as to find synonyms. In these cases, only errors were corrected, and minor improvements to the wording were provided. DeepL was not used to generate or revise content.

The author bears sole responsibility for all content, including calculations, analyses, interpretations, conclusions, and illustrations. No sensitive data, confidential information within the group, or measurement values were shared with ChatGPT.

Danksagung

Ich möchte mich zunächst herzlich bei meinem Doktorvater Prof. Florian Grüner bedanken, der mich über die Zeit meiner Promotion hinweg immer wieder durch begeisternde Diskussionen motiviert und zu neuen Ideen angeregt hat. Ich schätze vor allem das mir entgegengebrachte Vertrauen und unser stets gutes Verhältnis auf Augenhöhe.

Mein weiterer besonderer Dank gebührt Dr. Theresa Staufer, die mich während meiner Zeit als Doktorand neben zahlreichen fachlichen Diskussionen auch bei organisatorischen Fragen umfangreich unterstützt hat. Ich danke ihr auch sehr für die zahlreichen Gruppenausflüge und das Organisieren von allen weiteren Dingen, die unsere Arbeitsgruppe zu einer Gemeinschaft machen, mit der man auch außerhalb der Arbeit gern seine Freizeit verbringt.

Ich danke Jannis Haak und Florian Ziegler für die großartige Unterstützung bei den Messungen an SCOTTI sowie für die vielen lustigen Momente im Labor, während der Strahlzeiten und auf Konferenzen.

Zudem bedanke ich mich bei Prof. Dr. Birgit Kanngießer, Dr. Wolfgang Malzer, Daniel Grötzsch und Jonas Grage von der TU Berlin für die Unterstützung bei den Messungen sowie den stets herzlichen Empfang.

Meinen tiefster Dank gilt meinen Eltern, Britt und Jens Elbrecht, die mich immer unterstützt, aufgemuntert und stets an mich geglaubt haben.

Zu guter Letzt möchte ich meiner Freundin danken, die immer ein offenes Ohr für meine Gedanken hatte, mir den Rücken freigehalten hat, wenn es mal stressig wurde, stets Verständnis aufgebracht hat, wenn es mal spät wurde, und unser gemeinsames Zuhause zu einem Ort gemacht hat, an dem ich abschalten konnte – etwas, das mir manchmal schwerfällt.
Danke, Ziena!

Eidesstattliche Versicherung

Hiermit versichere ich an Eides statt, die vorliegende Dissertationsschrift selbst verfasst und keine anderen als die angegebenen Hilfsmittel und Quellen benutzt zu haben.
Sofern im Zuge der Erstellung der vorliegenden Dissertationsschrift generative Künstliche Intelligenz (gKI) basierte elektronische Hilfsmittel verwendet wurden, versichere ich, dass meine eigene Leistung im Vordergrund stand und dass eine vollständige Dokumentation aller verwendeten Hilfsmittel gemäß der Guten wissenschaftlichen Praxis vorliegt. Ich trage die Verantwortung für eventuell durch die gKI generierte fehlerhafte oder verzerrte Inhalte, fehlerhafte Referenzen, Verstöße gegen das Datenschutz- und Urheberrecht oder Plagiate.

Affidavit

I hereby declare and affirm that this doctoral dissertation is my own work and that I have not used any aids and sources other than those indicated.
If electronic resources based on generative artificial intelligence (gAI) were used in the course of writing this dissertation, I confirm that my own work was the main and value-adding contribution and that complete documentation of all resources used is available in accordance with good scientific practice. I am responsible for any erroneous or distorted content, incorrect references, violations of data protection and copyright law or plagiarism that may have been generated by the gAI.

Hamburg, 29.07.2026 .....

Ort, Datum / City, date

Lukas Elbrecht